



**National Technical University of Athens**  
SCHOOL OF ELECTRICAL AND COMPUTER ENGINEERING  
DIVISION OF SIGNALS, CONTROL AND ROBOTICS  
INTELLIGENT ROBOTICS AND AUTOMATION LAB

**Reactive Motion Planning for Robotic  
Manipulators and Interaction Control with  
Deformable Environment: Application to Physical  
Human-Assistive Tasks**

Ph.D. Dissertation

**Athanasios C. Dometios**

*Dipl.-Ing. in Electrical and Computer Engineering, NTUA*

**Supervisor:** Assoc. Prof. Constantinos Tzafestas

Athens, May 2021







ΕΘΝΙΚΟ ΜΕΤΣΟΒΙΟ ΠΟΛΥΤΕΧΝΕΙΟ  
ΣΧΟΛΗ ΗΛΕΚΤΡΟΛΟΓΩΝ ΜΗΧΑΝΙΚΩΝ ΚΑΙ ΜΗΧΑΝΙΚΩΝ ΥΠΟΛΟΓΙΣΤΩΝ  
ΤΟΜΕΑΣ ΣΗΜΑΤΩΝ, ΕΛΕΓΧΟΥ ΚΑΙ ΡΟΜΠΟΤΙΚΗΣ  
ΕΡΓΑΣΤΗΡΙΟ ΡΟΜΠΟΤΙΚΗΣ ΚΑΙ ΑΥΤΟΜΑΤΙΣΜΟΥ

Διαδραστικός σχεδιασμός κίνησης ρομποτικών  
χειριστών και έλεγχος αλληλεπίδρασης με  
παραμορφώσιμο περιβάλλον: Εφαρμογή φυσικής  
υποβοήθησης του ανθρώπου

ΔΙΔΑΚΤΟΡΙΚΗ ΔΙΑΤΡΙΒΗ  
ΤΟΥ  
ΑΘΑΝΑΣΙΟΥ Χ. ΔΟΜΕΤΙΟΥ

Επιβλέπων: Κωνσταντίνος Τζαφέστας, Αναπλ. Καθηγητής Ε.Μ.Π.

Αθήνα, Μάιος 2021





Εθνικό Μετσόβιο Πολυτεχνείο  
Σχολή Ηλεκτρολόγων Μηχανικών και Μηχανικών Υπολογιστών  
Τομέας Σημάτων, Ελέγχου και Ρομποτικής  
Εργαστήριο Ρομποτικής και Αυτοματισμού

Διαδραστικός σχεδιασμός κίνησης ρομποτικών  
χειριστών και έλεγχος αλληλεπίδρασης με  
παραμορφώσιμο περιβάλλον: Εφαρμογή φυσικής  
υποβοήθησης του ανθρώπου

ΔΙΔΑΚΤΟΡΙΚΗ ΔΙΑΤΡΙΒΗ  
ΤΟΥ  
ΑΘΑΝΑΣΙΟΥ Χ. ΔΟΜΕΤΙΟΥ

Συμβουλευτική Επιτροπή: Κωνσταντίνος Τζαφέστας, Αναπλ. Καθηγητής  
Πέτρος Μαραγκός, Καθηγητής  
Γεώργιος Παπαβασιλόπουλος, Ομοτ. Καθηγητής

Εγκρίθηκε από την επταμελή εξεταστική επιτροπή την .....18/05/2021.....

(Υπογραφή)

(Υπογραφή)

(Υπογραφή)

(Υπογραφή)

.....  
Κωνσταντίνος Τζαφέστας  
Αναπλ. Καθηγητής  
Ε.Μ.Π.

(Υπογραφή)

.....  
Πέτρος Μαραγκός  
Καθηγητής  
Ε.Μ.Π.

(Υπογραφή)

.....  
Κωνσταντίνος Κυριακόπουλος  
Καθηγητής  
Ε.Μ.Π.

(Υπογραφή)

.....  
Στέφανος Κόλλιας  
Καθηγητής  
Ε.Μ.Π.

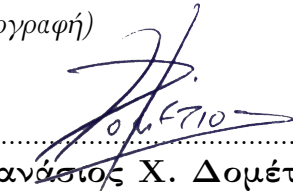
.....  
Αντώνιος Αργυρός  
Καθηγητής  
Πανεπιστημίου Κρήτης

.....  
Κωνσταντίνος Βλάχος  
Επίκουρος Καθηγητής  
Πανεπιστήμιο Ιωαννίνων

.....  
Αντώνιος Τζες  
Καθηγητής  
NYU Abu Dhabi

Αθήνα, Μάιος 2021

(Υπογραφή)



.....  
**Αθανάσιος Χ. Δομέτιος**

Διπλωματούχος Ηλεκτρολόγος Μηχανικός και Μηχανικός Υπολογιστών Ε.Μ.Π.

Copyright ©–All rights reserved Αθανάσιος Χ. Δομέτιος, 2021.

Με επιφύλαξη παντός δικαιώματος.

Απαγορεύεται η αντιγραφή, αποθήκευση και διανομή της παρούσας εργασίας, εξ' ολοκλήρου ή τμήματος αυτής, για εμπορικό σκοπό. Επιτρέπεται η ανατύπωση, αποθήκευση και διανομή για σκοπό μη κερδοσκοπικό, εκπαιδευτικής ή ερευνητικής φύσης, υπό την προϋπόθεση να αναφέρεται η πηγή προέλευσης και να διατηρείται το παρόν μήνυμα. Ερωτήματα που αφορούν τη χρήση της εργασίας για κερδοσκοπικό σκοπό πρέπει να απευθύνονται προς τον συγγραφέα.

Οι απόψεις και τα συμπεράσματα που περιέχονται σε αυτό το έγγραφο εκφράζουν το συγγραφέα και δεν πρέπει να ερμηνευθεί ότι αντιπροσωπεύουν τις επίσημες θέσεις του Εθνικού Μετσόβιου Πολυτεχνείου.





# Περίληψη

Η φυσική διεπαφή και αλληλεπίδραση ανθρώπου-ρομπότ διαδραματίζει κεντρικό ρόλο στην αποδοχή ρομποτικών εφαρμογών στην καθημερινή ζωή. Ειδικότερα στην περίπτωση εφαρμογών περίθαλψης και υποβοήθησης ανθρώπων με κινητικές ή άλλες δυσκολίες, η λειτουργική απαίτηση φυσικής επαφής ανθρώπου-ρομπότ αποτελεί και έναν από τους βασικούς παράγοντες που καθορίζουν την ασφάλεια του ρομποτικού συστήματος. Σε τέτοιες εφαρμογές αλληλεπίδρασης ανθρώπου-ρομπότ, απαιτείται ένα σύστημα διαδραστικού σχεδιασμού κίνησης βασιζόμενο σε μία διαρκή παρακολούθηση της κατάστασης του ανθρώπου, για να επιτευχθεί ένας πλήρως ασφαλής και συνεχώς προσαρμοζόμενος σχεδιασμός ρομποτικών κινήσεων και εργασιών.

Με βάση αυτήν τη γενική στόχευση, η παρούσα διατριβή πραγματεύεται τη διαδραστική παραγωγή και προσαρμογή ρομποτικών κινήσεων, οι οποίες έχουν προκύψει μέσω καταγραφής δεδομένων ανθρώπινης επίδειξης, κατάλληλες για εργασίες αλληλεπίδρασης με παραμορφώσιμες επιφάνειες, όπως μέρη του ανθρώπινου σώματος. Πιο συγκεκριμένα, στο πρώτο μέρος της διατριβής, και στο πλαίσιο μιας ευρύτερης ερευνητικής προσπάθειας που αποσκοπούσε στην κατασκευή ενός εύκαμπτου ρομποτικού μηχανισμού μπάνιου, αναπτύχθηκε ένας αλγόριθμος σχεδιασμού ρομποτικής κίνησης, ο οποίος χρησιμοποιεί την οπτική πληροφορία μιας κάμερας βάνους και την αντίστοιχη πληροφορία αντίληψης της σκληρής ρομποτικής δράσης, για να προσαρμόσει προκαθορισμένες και χωροχρονικά κλιμακούμενες τροχιές πάνω σε καμπύλες και παραμορφώσιμες επιφάνειες, όπως μέρη του ανθρώπινου σώματος, με ταυτόχρονη αποφυγή εμποδίων ή συγκεκριμένων υποπεριοχών της επιφάνειας αλληλεπίδρασης (για παράδειγμα, λόγω ύπαρξης τοπικών τραυματισμών, κ.α.). Η προσαρμογή επιτυγχάνεται με τη δημιουργία χωρικών μετασχηματισμών, με τις ιδιότητες του αμφιμονοσήμαντου και επί (bijection), οι οποίοι επιτυγχάνουν την έκφραση του προβλήματος παρακολούθησης σε ένα διδιάστατο κανονικοποιημένο χώρο. Η ακριβής παρακολούθηση τροχιάς πραγματοποιείται στη συνέχεια με έναν ελεγκτή συναρτήσεων πλοήγησης με αποδεδειγμένη καθολικά ομοιόμορφη ασυμπτωτική σύγκλιση στην επιθυμητή τροχιά. Η απόδοση του προτεινόμενου αλγορίθμου ελέγχθηκε τόσο σε συνθήκες εργαστηρίου όσο και σε πραγματικό κλινικό περιβάλλον με ηλικιωμένους χρήστες σε ξηρές συνθήκες και σε συνθήκες με χρήση νερού. Συμπληρωματικά πραγματοποιήθηκε μια κλινική μελέτη, η οποία αποσκοπούσε στην αξιολόγηση της αποδοχής και των δυνατοτήτων χρήσης ενός τέτοιου πολύπλοκου συστήματος από ηλικιωμένους χρήστες.

Στο επόμενο στάδιο της διατριβής, προτείνεται ένα ολοκληρωμένο σύστημα το οποίο, βασιζόμενο στην μέθοδο των Δυναμικών Πρωτογενών Κινήσεων (Dynamic Movement Primitives – DMPs), μπορεί να μάθει και να κωδικοποιήσει δράσεις χειρισμού και επαναληπτικές κινήσεις οι οποίες έχουν προκύψει κατόπιν επίδειξης από ειδικούς (εν προκειμένω, νοσηλευτικό προσωπικό) και να μιμηθεί τη συμπεριφορά τους. Οι συγκεκριμένες δράσεις καταγράφηκαν με χρήση συστημάτων οπτικής καταγραφής κίνησης, και ακολούθως αναλύθηκαν και αποσυντέθηκαν σε δυναμικές πρωτογενείς κινήσεις κατάλληλες για εκτέλεση από ρομποτικό σύστημα. Οι κωδικοποιημένες αυτές κινήσεις μπορούν στη συνέχεια να προσαρμοστούν στην επιφάνεια του σώματος του χρήστη, αντισταθμίζοντας την κίνηση ή την παραμόρφωσή του, καθώς και να μεταβληθούν ως προς συγκεκριμένες παραμέτρους της κίνησης κατά την εκτέλεση της εργα-

σίας, για να ικανοποιηθούν δεδομένες ανάγκες του χρήστη κατά τη διάρκεια της διαδικασίας ρομποτικής υποβοήθησης. Το προτεινόμενο σύστημα αξιολογήθηκε πειραματικά με τη χρήση ενός ανθρωποειδούς ρομπότ, το οποίο εκτέλεσε ένα σενάριο καθαρισμού επιφάνειας, καταδεικνύοντας την εφαρμοσιμότητα της μεθόδου σε πραγματικά σενάρια ρομποτικής υποβοήθησης. Επιπλέον της μεθόδου αυτής, προτείνεται και μία εναλλακτική μέθοδος εκμάθησης και αναπαγωγής σύνθετων κινήσεων από δεδομένα επίδειξης μέσω της διαμόρφωσης ενός απωστικού δυναμικού πεδίου συναρτήσεων πλοήγησης.

Στο τελευταίο στάδιο της παρούσας διατριβής, προτείνεται ένα πρωτότυπο σύστημα διαδραστικού σχεδιασμού κίνησης, με στόχο τον αποδοτικό και ακριβή έλεγχο ενός ρομποτικού χειριστή, ο οποίος εκτελεί διαδραστικές εργασίες στην επιφάνεια ενός παραμορφώσιμου αντικειμένου. Το προτεινόμενο σύστημα βασίζεται σε μία αναπαράσταση πλέγματος του αντικειμένου και ενσωματώνει τρία αποδοτικά στάδια προ-επεξεργασίας δεδομένων, τα οποία περιλαμβάνουν την οπτική κατάτμηση του αντικειμένου, την παρακολούθηση της παραμόρφωσης του αντικειμένου και την τοπική παραμετροποίηση του πλέγματος. Η χρήση βαρυκεντρικών συντεταγμένων, που ορίζονται στα τριγωνικά στοιχεία του πλέγματος, επιτρέπει τον ορισμό αμφιμονοσήμαντων μετασχηματισμών μεταξύ του εξεταζόμενου μέρους της επιφάνειας του αντικειμένου και της επίπεδης παραμετροποιημένης απεικόνισής του. Ο συνδυασμός αυτών των μετασχηματισμών με τα αρχικά στάδια επεξεργασίας και με ένα σχήμα ελέγχου ενεργούς ακαμψίας για τον ρομποτικό χειριστή, επιτρέπει τον ακριβή σχεδιασμό διαδραστικών τροχιών ακόμη και υπό συνθήκες οπτικής απόκρυψης μεγάλων τμημάτων της επιφάνειας. Παρουσιάζεται μία εκτενής πειραματική αξιολόγηση της μεθόδου, η οποία περιλαμβάνει ένα ρομποτικό χειριστή σε διάδραση με ένα ημισφαιρικό μοντέλο το οποίο υπόκειται σε ελέγξιμη παραμόρφωση. Σε αυτό το πλαίσιο, αξιολογείται η ακρίβεια του σχεδιασμού της κίνησης τόσο κατά την εκτέλεση διαδραστικών τροχιών όσο και κατά την συνεχή παρακολούθηση ενός σημείου στην επιφάνεια του αντικειμένου. Ελέγχθηκε επίσης η ικανότητα χρήσης της μεθόδου για προγραμματισμό κινήσεων από ανθρώπινη επίδειξη και για ρύθμιση των δυνάμεων επαφής με το αντικείμενο.



# Abstract

Natural human-robot physical interaction has a key role in the acceptance of robotic applications in everyday life. Especially in the case of applications for the care and assistance of people with mobility or other impairments, the functional requirement of physical contact between humans and robots is one of the key factors that determine the safety of the robotic system. Such human-robot interaction applications require an interactive motion planning system based on a continuous monitoring of the human condition, in order to achieve a completely safe and continuously adaptable robotic motion and task planning.

Towards this end, this dissertation deals with reactive adaptation and motion generation of human demonstrated interactive tasks with deformable surfaces, such as those of the human body parts. Particularly, in the first part of this thesis, and in the context of a broader research effort aimed at building a flexible robotic bath mechanism, a motion planning algorithm was developed, which uses the visual feedback from a depth camera and the corresponding scene perception information, in order to adapt predefined, time scalable trajectories on curved and deformable surfaces, such as the human body parts, with simultaneous avoidance of obstacle areas, such as injuries. The adaptation is achieved with the establishment of bijective transformations, which reformulate the tracking problem to a 2D Canonical Space. Accurate trajectory tracking is then realized with a Navigation Function (NF) controller with proven globally uniformly asymptotic convergence. The proposed algorithm was tested both in lab conditions and in a real clinical environment with elderly users in both dry and humid conditions. A clinical validation study was conducted, which focused on the acceptance and operation aspects of such a complex system by elderly users.

In the next phase of the thesis, an integrated system based on Dynamic Motion Primitives (DMP) approach is proposed, which can learn and encode demonstrated washing actions by professional nursing experts, imitating their actions. The washing actions were recorded with the use of optical motion tracker systems, analyzed and decomposed into primitive actions appropriate for robotic execution. The learned motions can then be adapted to the user's body parts, compensating their motion or deformation, as well as on-line modified with respect to their execution parameters, in order to meet the user's requirements during of the robotic assistance process. This system was experimentally validated with the use of a humanoid robot, which executed a wiping scenario, demonstrating the applicability of this method in real world scenarios of assistive robotics. Alternatively to the DMP approach, a NF method is proposed in order to learn and reproduce the way an expert clinical carer executes the bathing activities, by means of constructing artificial repulsive potential fields generated by virtual obstacles, which in essence represent the demonstrated motions.

In the final stage of this dissertation, an efficient interactive motion planning framework is proposed, to effectively and accurately control a robotic manipulator executing interactive tasks on the surface of a deformable object. The proposed interactive motion

planning framework is based on a mesh representation of the object, integrating three efficient preprocessing algorithmic steps, including visual object segmentation, FEM deformation tracking and local mesh parameterization. The use of barycentric coordinates, defined on the mesh triangles, enables the establishment of bijective transformations between the deformable part of an object surface and its planar (static and dynamic) parameterized mapping. By merging these spatial transformations with the preprocessing steps, in combination with an active stiffness scheme for robot manipulator control, we are able to achieve accurate and reactive motion planning of interactive trajectories, even under large and persistent visual occlusions. An extensive experimental evaluation study is presented, involving a robotic manipulator in interaction with a hemispherical model of controllable periodic active deformation, which permits precise ground truth derivation. Motion planning accuracy is evaluated in comparison with the previously described direct vision-based approach, showing clearly superior performance of the mesh-based approach under all experimental conditions. The performance of the proposed framework is also further highlighted in tasks involving physical point tracking, interactive programming by human demonstration, as well as contact force regulation.

# Ευχαριστίες

Η διδακτορική διατριβή προέρχεται ετυμολογικά από το ρήμα δια-τρίβω, που σημαίνει ασχολούμαι ιδιαίτερα ή μεθοδικά με κάτι. Είναι επομένως μια μεθοδική εργασία που απαιτεί καθημερινή τριβή με έννοιες και προβλήματα επιστημονικής ή τεχνολογικής φύσης και συμβάλει καθοριστικά στην νοητική ωρίμανση στον δρόμο ενός ανθρώπου από τον ρόλο του φοιτητή σε ολοκληρωμένο επιστήμονα-ερευνητή. Αυτή η πορεία πέρα από την επιμονή, την αφοσίωση και τον προσωπικό κόπο που απαιτεί, διακατέχεται και από μία πληθώρα συναισθημάτων, ανασφάλειας, λύπης, απογοητεύσεων αλλά και δυνατές στιγμές χαράς και έντονης ικανοποίησης, τα οποία σε διαμορφώνουν σαν άνθρωπο και αποτελούν την κινητήριο δύναμη για την συνέχεια. Ωστόσο, κοιτάζοντας πίσω αυτή την πορεία τώρα που αυτό το ταξίδι ολοκληρώνεται, δεν μπορώ να γράψω ότι ήταν μοναχικό, καθώς υπήρξαν πολλοί άνθρωποι που συνέβαλαν καθοριστικά και με υποστήριξαν τόσο σε προσωπικό όσο και σε επιστημονικό επίπεδο και τους οφείλω αμέριστη ευγνωμοσύνη στον κάθε ένα ξεχωριστά.

Ξεκινώντας, θα ήθελα να ευχαριστήσω τον μέντορα και βασικό επιβλέποντα της παρούσας διατριβής, καθηγητή Κωνσταντίνο Τζαφέστα, αρχικά για την αποδοχή ως μεταπτυχιακό ερευνητή υπό την επίβλεψή του, καθώς και για τις κατευθύνσεις και πολύτιμες συμβουλές και συνεχίζει να μου παρέχει γενναιόδωρα. Η συμβολή του με τον χρόνο και τον χώρο που μου έδωσε ώστε να έρθω σε επαφή με ένα μεγάλο εύρος ερευνητικών θεμάτων κατά την διάρκεια των διδακτορικών μου σπουδών, υπήρξε καθοριστική στην εξέλιξή μου σαν ερευνητή αλλά και σαν άνθρωπο με την αδιάκοπη υλική και ψυχολογική υποστήριξη που μου παρείχε όλα αυτά τα χρόνια για να καταφέρω να ολοκληρώσω την διδακτορική μου έρευνα.

Το ταξίδι στα μονοπάτια της ρομποτικής ξεκίνησε από νωρίς μαζί του στα μαθήματα των προπτυχιακών σπουδών στην Σχολή Ηλεκτρολόγων Μηχανικών και Μηχανικών Υπολογιστών και στην διαδικασία ολοκλήρωσης των σπουδών μου, στην οποία μέσω συνεπίβλεψης και του προγράμματος Erasmus μου έδωσε την δυνατότητα εκπόνησης της διπλωματικής εργασίας σε ένα μεγάλο ευρωπαϊκό πανεπιστήμιο. Στο Πολυτεχνείο του Μονάχου (TUM) είχα την ευκαιρία να έρθω σε επαφή με την ερευνητική διαδικασία στην ρομποτική, βάζοντας τον θεμέλιο λίθο για την μετέπειτα πορεία μου. Αυτά τα θεμέλια και η έμπνευση που μου δώθηκε διαμόρφωσαν σε μεγάλο βαθμό τις μετέπειτα επιλογές μου σε επαγγελματικό και ερευνητικό επίπεδο.

Ένα μεγάλο ευχαριστώ οφείλω και στον συνεπιβλέποντα καθηγητή Πέτρο Μαραγκό καθώς μέσα από τα μαθήματά του σε προπτυχιακό και μεταπτυχιακό επίπεδο μου έδωσε πολύτιμες γνώσεις στο πεδίο της επεξεργασίας σημάτων και όρασης υπολογιστών, διαμορφώνοντας την σκέψη μου σε θέματα που αφορούν την ρομποτική αντίληψη και μοντελοποίηση του περιβάλλοντος και δίνοντας μου έμπνευση στον συνδυασμό τους με τον ρομποτικό έλεγχο. Σε προσωπικό επίπεδο μέσα από συζητήσεις καθόλη την διάρκεια της διατριβής μου, ήταν πάντα παρών και πρόθυμος να βοηθήσει σε όποια καθημερινά και ερευνητικά προβλήματα προέκυπταν, παρέχοντας ουσιαστική στήριξη και κατανόηση. Αποτελεί για μένα παράδειγμα επιστήμονα και δασκάλου.

Συνεχίζοντας, θέλω να πω ένα τεράστιο ευχαριστώ στην Δρ. Ξανθή Παπαγεωργίου, με

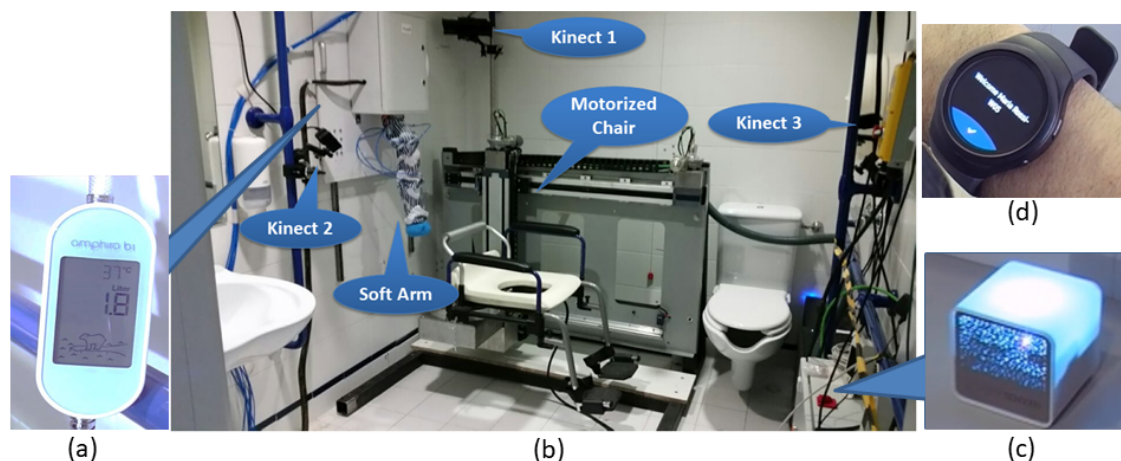
την οποία είχα την τύχη να συνεργαστώ τα πρώτα χρόνια των διδακτορικών μου σπουδών. Με βάση τον ρόλο της ως μεταδιδακτορική ερευνήτρια στο εργαστήριο Ρομποτικής και Αυτοματισμού ανέλαβε την καθημερινή μου επίβλεψη. Η Ξανθή είναι ο λόγος που κατάφερα να κάνω τα πρώτα μου ερευνητικά βήματα, καθώς με βοήθησε να σκέφτομαι και να συμπεριφέρομαι σαν ερευνητής, από την πρώτη αναζήτηση πηγών μέχρι την οργάνωση και εκτέλεση πειραματικών διαδικασιών και την εξαγωγή ασφαλών συμπερασμάτων. Την θαυμάζω σαν επιστήμονα για την άσβηστη ερευνητική φλόγα και το βαθύ επιστημονική της υπόβαθρο αλλά και την σέβομαι σαν άνθρωπο και γυναίκα για το ήθος και το μαχητικό πνεύμα που διαθέτει. Θα την έχω στο μυαλό και την καρδιά μου σε κάθε επόμενο βήμα που θα επιχειρώ.

Η οικογένειά μου και πιο συγκεκριμένα η μητέρα μου Βούλα, ο πατέρας μου Χρήστος και ο αδερφός μου Άγγελος αποτέλεσαν έναν βασικό πυλώνα στήριξης στην ζωή μου και σε όλες τις βαθμίδες της εκπαιδευτικής μου πορείας. Τους οφείλω το μεγαλύτερο ευχαριστώ για όλες τις θυσίες, την υπομονή, τις συμβουλές και την αγάπη τους που με στήριξαν μέχρι αυτό το σημείο. Ευγνώμων όμως είμαι και προς τα υπόλοιπα μέλη της οικογένειάς μου, την θεία μου Κική, την γιαγιά μου Μαρίκα και τα ξαδέφια μου Μαρία και Θανάση, που πάντοτε με υποστήριξαν, με επιβράβευαν και με παρακινούσαν να συνεχίζω τις προσπάθειές μου. Ιδιαίτερες ευχαριστίες θέλω να δώσω στους φίλους μου Παναγιώτη και Νίκο με τους οποίους μοιράστηκα πολλές στιγμές αυτής της διατριβής και ήταν οι καλύτεροι συνοδοιπόροι σε αυτή την διαδρομή, τον Χρήστο για την πολύτιμη βοήθεια σε επιστημονικές ερωτήσεις και την υποστήριξη μαζί με την Στέλλα έστω και από μακριά, την Τονια, τον Ηλία, την Κάτια και τον Μιχάλη με τους οποίους μοιράστηκα πολλές πτυχές της ζωής μου όλα αυτά τα χρόνια, προσφέροντάς μου τις απαραίτητες στιγμές χαράς και αξέχαστες συζητήσεις. Επίσης να ευχαριστήσω τον ξάδερφο μου Νίκο για την βοήθεια του ώστε να γίνει η δουλειά μου ομορφότερη και πιο κατανοητή μέσα από τις εικόνες και τα σχήματα των δημοσιεύσεων. Δεν μπορώ όμως να μην πω ένα μεγάλο ευχαριστώ μέσα από την καρδιά μου στην κοπέλα μου Στέλλα, με την οποία μοιράστηκα το μεγαλύτερο μέρος από τις σκέψεις, άγχη, απογοητεύσεις και επιτυχίες και κατάφερε με ένα μαγικό τρόπο να συγκεντρώνει την σκέψη μου και να μου δίνει δύναμη, κίνητρο και κουράγιο για την συνέχεια. Θα ήταν, ωστόσο, παράλειψή μου να μην ευχαριστήσω και τους γονείς της Στέλλας, Ιππολύτη και Δημοσθένη για την σιωπηλή και έμπρακτη υποστήριξη που μου πρόσφεραν απλόχερα από την πρώτη στιγμή.

Για τις ποικίλες επιστημονικές και προσωπικές συζητήσεις θέλω να ευχαριστήσω όλα τα μέλη και τους απόφοιτους του εργαστηρίου Ρομποτικής και Αυτοματισμού, για μένα είναι κάτι παραπάνω από συνάδελφοι καθώς με την στήριξη και τη φιλία τους έκαναν πιο όμορφες τις ώρες στο εργαστήριο. Θέλω ιδιαίτερα να ευχαριστήσω την Γεωργία Χαλβατζάκη, τον Πάρη Οικονόμου, τον Πέτρο Κούτρα, την Αντιγόνη Τσιάμη, τον Παναγιώτη Γιαννούλη, την Νίκη Ευθυμίου, τον Παναγιώτη Φιλντίση, τον Παναγιώτη Μέρμηγκα, τον Αντώνη Αρβανιτάκη και τον Γιώργο Ρετινά. Επίσης θα ήθελα να ευχαριστήσω τις συνεργάτιδες του εργαστηρίου Βασιλική Πλατίτσα, Φωτεινή Σταμέλου και τον σύζυγό της Παναγιώτη, αλλά και την Δέσποινα Κασσιανίδη για την φροντίδα και την βοήθεια που παρείχαν όλα τα χρόνια σε καθημερινά θέματα και μη. Θα ήθελα να ευχαριστήσω όλα τα μέλη της επιστημονικής κοινότητας που συμμετείχαν στην εξέταση της εργασίας και συνέβαλαν με τα εποικοδομητικά τους σχόλια και τις προτάσεις τους. Συγκεκριμένα ευχαριστώ τον Καθηγητή Κωνσταντίνο Κυριακόπουλο, τον Καθηγητή Στέφανο Κόλλια, τον Επικ. Καθηγητή Κωνσταντίνο Βλάχο, τον Καθηγητή Αντώνιο Αργυρό και τον Καθηγητή Αντώνιο Τζε, για τον χρόνο που αφιέρωσαν για την μελέτη και εξέταση της παρούσας διατριβής.

# Εκτεταμένη Περίληψη

Με την γήρανση του παγκόσμιου πληθυσμού, λόγω της αύξησης του προσδόκιμου ζωής, θα αυξηθούν και οι ανάγκες για φροντίδα στην εκτέλεση των δραστηριοτήτων καθημερινής διαβίωσης και νοσηλεία. Η επιμελής εκτέλεση της καθημερινής προσωπικής φροντίδας, η οποία είναι κρίσιμη για την υγιεινή ενός ατόμου, είναι από τις πρώτες δραστηριότητες καθημερινής διαβίωσης που δυσκολεύουν την καθημερινότητα ενός ηλικιωμένου ατόμου, καθώς απαιτεί ορθή σωματική κινητικότητα. Επιπλέον η παραμέληση της προσωπικής φροντίδας αποτελεί τον ισχυρότερο προγνωστικό παράγοντα για την ανάγκη κλινικής φροντίδας για έναν ηλικιωμένο άνθρωπο. Η έρευνα πάνω σε ρομποτικές εφαρμογές υποβοήθησης έχει ως στόχο την ανάπτυξη συστημάτων τα οποία θα βοηθούν ηλικιωμένους ανθρώπους ή άτομα με ειδικές ανάγκες στις καθημερινές τους δραστηριότητες, αλλά και θα μειώνουν δραστικά τον εργασιακό φόρτο του νοσηλευτικού προσωπικού καθιστώντας το αποτελεσματικότερο. Στο επίκεντρο αυτής της ερευνητικής στόχευσης και πιο συγκεκριμένα στο πλαίσιο του ερευνητικού προγράμματος I-Support (H2020-EU.3.1.4. “I-SUPPORT - ICT-Supported Bath Robots” - 643666) αναπτύχθηκε ένα καινοτόμο ρομποτικό σύστημα όπως φαίνεται στο Σχ. 1, το οποίο βοηθά ηλικιωμένους ανθρώπους να ολοκληρώσουν με ασφάλεια και ανεξαρτησία διάφορες σωματικά και γνωστικά απαιτητικές δραστηριότητες προσωπικής υγιεινής. Οι βασικές συσκευές που απαρτίζουν το σύστημα είναι μια ρομποτικά ελεγχόμενη κινούμενη καρέκλα για την ασφαλή



Σχήμα 1: Εγκατάσταση του συστήματος I-Support σε κλινικό περιβάλλον (Νοσοκομείο Fondazione Santa Lucia (FSL) στην Ρώμη, Ιταλία) για πειραματική αξιολόγηση. Οι συσκευές που απαρτίζουν το σύστημα απεικονίζονται με σειρά στο (a) Amphiro b1 αισθητήρας ροής και θερμοκρασίας νερού, (b) Το σύνολο του συστήματος με τα βασικά του υποσυστήματα όπως την αυτοκινούμενη καρέκλα, το ρομπότ από εύκαμπτα υλικά και η εγκατάσταση των καμερών Kinect, (c) Αισθητήρας θερμοκρασίας αέρα, υγρασίας και φωτισμού, (d) Έξυπνο ρολόι που βοηθάει στην ταυτοποίηση του χρήστη και στην παρακολούθηση της δραστηριότητάς του.

μετακίνηση του ηλικιωμένου στον χώρο του μπάνιου, ένας ρομποτικός χειριστής κατασκευασμένος από εύκαμπτα υλικά για ασφαλή επαφή με τον άνθρωπο και οι κάμερες Kinect οι οποίες δίνουν μια πολύπλευρη οπτική του χρήστη.

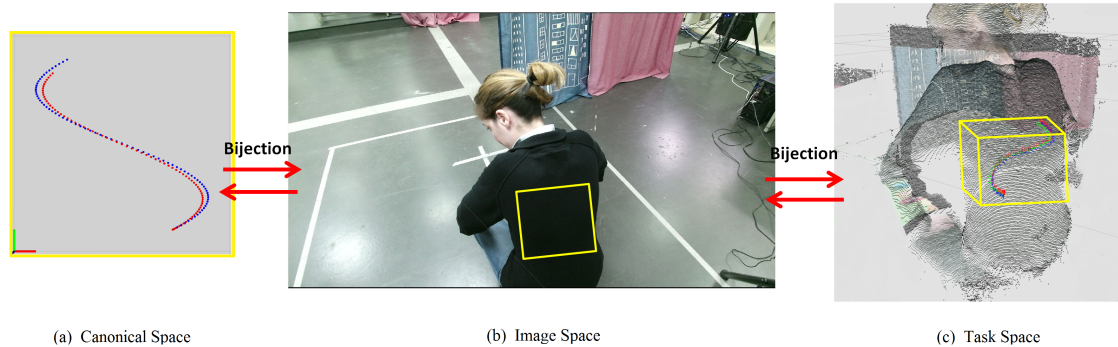
Η φυσική διεπαφή και αλληλεπίδραση ανθρώπου-ρομπότ διαδραματίζει κεντρικό ρόλο στην αποδοχή ρομποτικών εφαρμογών στην καθημερινή ζωή. Ειδικότερα στην περίπτωση εφαρμογών περίθαλψης και υποβοήθησης ανθρώπων με κινητικές ή άλλες δυσκολίες, η λειτουργική απαίτηση φυσικής επαφής ανθρώπου-ρομπότ αποτελεί και έναν από τους βασικούς παράγοντες που καθορίζουν την ασφάλεια του ρομποτικού συστήματος. Σε τέτοιες εφαρμογές αλληλεπίδρασης ανθρώπου-ρομπότ, απαιτείται ένα σύστημα διαδραστικού σχεδιασμού κίνησης βασιζόμενο σε μία διαρκή παρακολούθηση της κατάστασης του ανθρώπου, για να επιτευχθεί ένας πλήρως ασφαλής και συνεχώς προσαρμοζόμενος σχεδιασμός ρομποτικών κινήσεων και εργασιών. Ο σχεδιασμός θα πρέπει να λαμβάνει υπόψιν του την μορφολογία του κάθε σωματικού μέλους, αντισταθμίζοντας παράλληλα την φυσική του κίνηση, η οποία μπορεί να είναι είτε συστηματική λόγω της αναπνοής είτε τυχαία. Επίσης, μια βασική απαίτηση για τον σχεδιασμό των δράσεων πλυσίματος είναι να ακολουθούν τις οδηγίες και την επίδειξη κατάλληλων κινήσεων από ειδικούς νοσηλευτές, για να επιτευχθεί μια φιλική προς τον χρήστη ρομποτική λειτουργία.

## Εν Λειτουργία Διαδραστικός Σχεδιασμός Κίνησης Ρομποτικού Χειριστή

Εκφράζοντας το παραπάνω πρόβλημα υπό ένα τεχνικό πρίσμα, αυτό μετατρέπεται σε ένα πρόβλημα ρομποτικής παρακολούθησης και προσαρμογής προκαθορισμένων και χρονικά κλιμακούμενων τροχιών πάνω σε καμπύλες και παραμορφώσιμες επιφάνειες, όπως τα ανθρώπινα μέρη του σώματος. Επιπλέον, σε περίπτωση ύπαρξης τραυματισμού σε κάποια περιοχή του σώματος, τότε χρειάζεται η κατάλληλη μεταβολή της τροχιάς με στόχο την αποφυγή αυτής της περιοχής και την κάλυψη των υπολοίπων. Όπως φάνηκε και από τον παραπάνω σχεδιασμό του συστήματος I-Support κατασκευάστηκε ένας ρομποτικός χειριστής από εύκαμπτα υλικά, ο οποίος είναι ασφαλέστερος σε σχέση με ένα συμβατικό ρομπότ για την εκτέλεση των δράσεων πλυσίματος σε άμεση επαφή με τον χρήστη. Ωστόσο η πολυπλοκότητα του ελέγχου κίνησής του και η έλλειψη κινηματικού μοντέλου, οδήγησαν στην επιλογή ο αλγόριθμος σχεδιασμού να εκφράζει τα αποτελέσματά του στον χώρο εργασίας του ρομπότ με αλληλουχία επιθυμητών θέσεων για το τελικό στοιχείο δράσης. Βασιζόμενοι σε αυτούς τους περιορισμούς υποθέτουμε ότι το ρομπότ μπορεί να περιγραφεί κινηματικά από την παρακάτω σχέση:

$$\dot{q} = u \quad (1)$$

όπου  $q$  είναι το διάνυσμα της θέσης και τους προσανατολισμού του τελικού στοιχείου δράσης και  $u$  είναι το διάνυσμα των ταχυτήτων εισόδου. Για την προσαρμογή των τροχιών κατά την διάρκεια της εκτέλεσής τους προτάθηκε στο πρώτο μέρος αυτής της διατριβής η δημιουργία χωρικών μετασχηματισμών οι οποίοι κάθε χρονική στιγμή έχουν την ιδιότητα αμφιμονοσήμαντου και επί, μεταξύ του τρισδιάστατου χώρου εργασίας του ρομπότ, της περιοχής της εικόνας της κάμερας που απεικονίζει την επιφάνεια δράσης και ενός δισδιάστατου χώρου με κανονικοποιημένες διαστάσεις, όπως φαίνεται στο Σχ. 2. Πιο συγκεκριμένα, η σημασιολογική κατάτμηση των μερών του σώματος πάνω στην εικόνα γίνεται με αλγορίθμους βαθιάς μηχανικής μάθησης, το αποτέλεσμα των οποίων είναι το σύνολο των εικονοστοιχείων που απεικονίζουν το κάθε μέρος του σώματος κάθε χρονική στιγμή. Συνδυάζοντας την εκτίμηση βάθους των συγκεκριμένων εικονοστοιχείων της κάμερας με το αποτέλεσμα αυτών των αλγορίθμων, μπορούμε να



Σχήμα 2: Τρεις διαφορετικοί χώροι που περιγράφονται στην προτεινόμενη μεθοδολογία. (a) Δισδιάστατος χωρικά κανονικοποιημένος χώρος κατά τις  $x, y$  διαστάσεις ο οποίος αμφιφέρεται σαν ‘Κανονικοποιημένος’ χώρος (“Canonical” space). (b) Ο δισδιάστατος χώρος της εικόνας είναι η εικόνα της κάμερας Kinect με αρχικό μέγεθος  $512 \times 424$  εικονοστοιχεία. Η περιοχή που επισημαίνεται με ένα κίτρινο τετράγωνο είναι το αποτέλεσμα του αλγορίθμου κατάτμησης της εικόνας ο οποίος εντοπίζει το επιθυμητό μέρος του σώματος. (c) Ο τρισδιάστατος χώρος δράσης του ρομπότ (Task Space). Η ημιτονοειδής τροχιά από τον Κανονικοποιημένο χώρο αντιστοιχίζεται στην επιφάνεια της πλάτης της χρήστριας του συστήματος. Το κίτρινο κουτί αντιπροσωπεύει έναν υποχώρο, ο οποίος περιλαμβάνει τα σημεία προσαρμογής της τροχιάς.

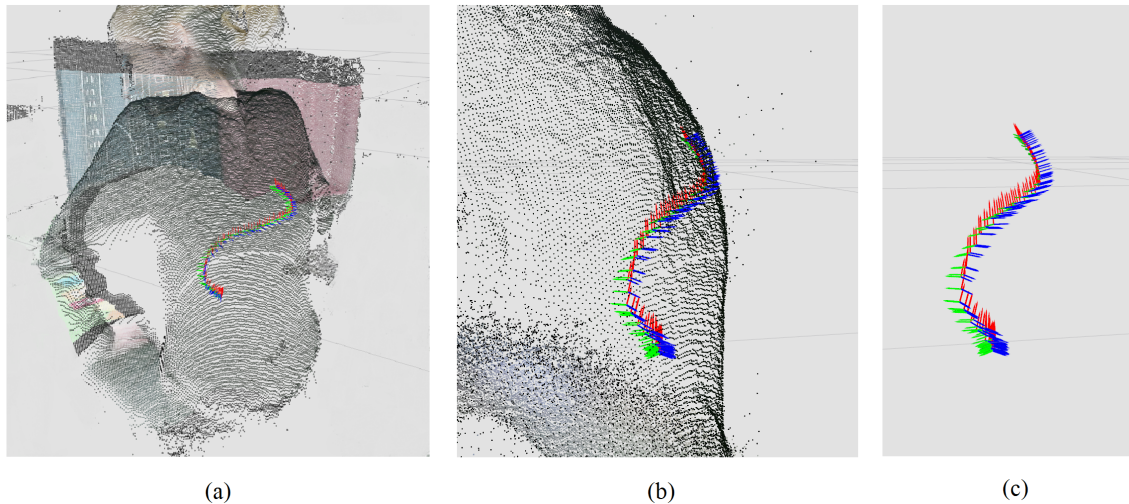
συνθέσουμε την τρισδιάστατη απεικόνιση της επιφάνειας του σώματος δειγματοληπτημένη με σημεία όπως φαίνεται στο Σχ. 2 (c).

Επομένως, η τροχιά που έχει προκύψει από την επίδειξη ενός νοσηλευτή μετασχηματίζεται στον Κανονικοποιημένο χώρο όπου και γίνεται η παρακολούθησή της. Το κάθε σημείο της τροχιάς στην συνέχεια μετασχηματίζεται χωρικά στο επίπεδο της εικόνας χρησιμοποιώντας ανισοτροπική κλιμάκωση σε σχέση με τα όρια της απεικόνισης σώματος στην εικόνα, όπως έχουν προκύψει από την κατάτμηση. Στην συνέχεια το ίδιο σημείο μετασχηματίζεται χωρικά στον χώρο δράσης του ρομπότ με την χρήση των τρισδιάστατων σημείων της επιφάνειας. Αναλυτικότερα από την εκτίμηση βάθους του εικονοστοιχείου και των γειτονικών του μπορούμε να εκτιμήσουμε τοπικά την κεντρική θέση και τον προσανατολισμό της επιφάνειας. Η επιθυμητή πόζα του ρομπότ απαρτίζεται από την κεντρική τρισδιάστατη θέση και τον κάθετο προσανατολισμό στην επιφάνεια για την εκτέλεση των δράσεων πλυσίματος όπως φαίνεται στο Σχ. 3. Για την παρακολούθηση της τροχιάς στον δισδιάστατο κανονικοποιημένο χώρο έγινε χρήση ενός ελεγκτή συναρτήσεων πλοήγησης (Navigation Functions) ο οποίος ακολουθεί την αρνητική κλίση της συνάρτησης πλοήγησης:

$$\varphi(q, t) = \frac{\gamma_d(q, t)}{[\gamma_d^\kappa(q, t) + \beta(q, t)]^{1/\kappa}} \quad (2)$$

όπου  $\kappa > 0$ ,  $\gamma_d(q, t)$  είναι η συνάρτηση απόστασης από την δισδιάστατα εκφρασμένη τροχιά πλυσίματος και  $\beta(q, t)$  είναι το γινόμενο των συναρτήσεων εμποδίων (περιοχή με τραύμα) όπως προκύπτουν από την οπτική πληροφορία. Ο ελεγκτής έχει αποδεδειγμένη καθολικά ομοιόμορφη ασυμπτωτική σύγκλιση στην επιθυμητή τροχιά. Η απόδοση του προτεινόμενου αλγορίθμου ελέγχθηκε τόσο σε συνθήκες εργαστηρίου όσο και σε πραγματικό κλινικό περιβάλλον με ηλικιωμένους χρήστες σε ξηρές συνθήκες και σε συνθήκες με χρήση νερού. Συμπληρωματικά πραγματοποιήθηκε μια κλινική μελέτη, η οποία αποσκοπούσε στην αξιολόγηση της αποδοχής και των δυνατοτήτων χρήσης ενός τέτοιου πολύπλοκου συστήματος από ηλικιωμένους χρήστες.

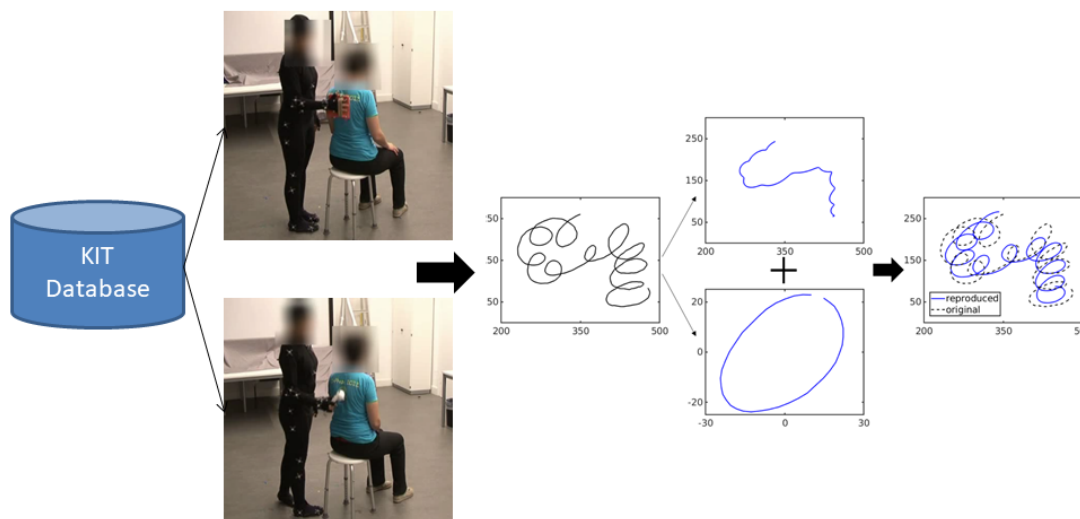




Σχήμα 3: (a) Πειραματική προσαρμογή σιγμοειδούς τροχιάς στην πλάτη μίας χρήτριας του συστήματος. (b) Κλιμάκωση της απεικόνισης της τροχιάς με έμφαση στην λεπτομερή οπτικοποίηση της προσαρμογής. (c) Απεικόνιση της τροχιάς χωρίς το νέφος σημείων της επιφάνειας της πλάτης.

## Προσαρμογή Πρωτογενών Κινήσεων σε Δυναμικές Επιφάνειες

Με στόχο την εκμάθηση δράσεων πλυσίματος φιλικών προς τον χρήστη, προτάθηκε στο επόμενο στάδιο της διατριβής ένα ενιαίο σύστημα, το οποίο βασιζόμενο στην μέθοδο των Δυναμικών Πρωτογενών Κινήσεων, μπορεί να μάθει και να κωδικοποιήσει δράσεις πλυσίμα-



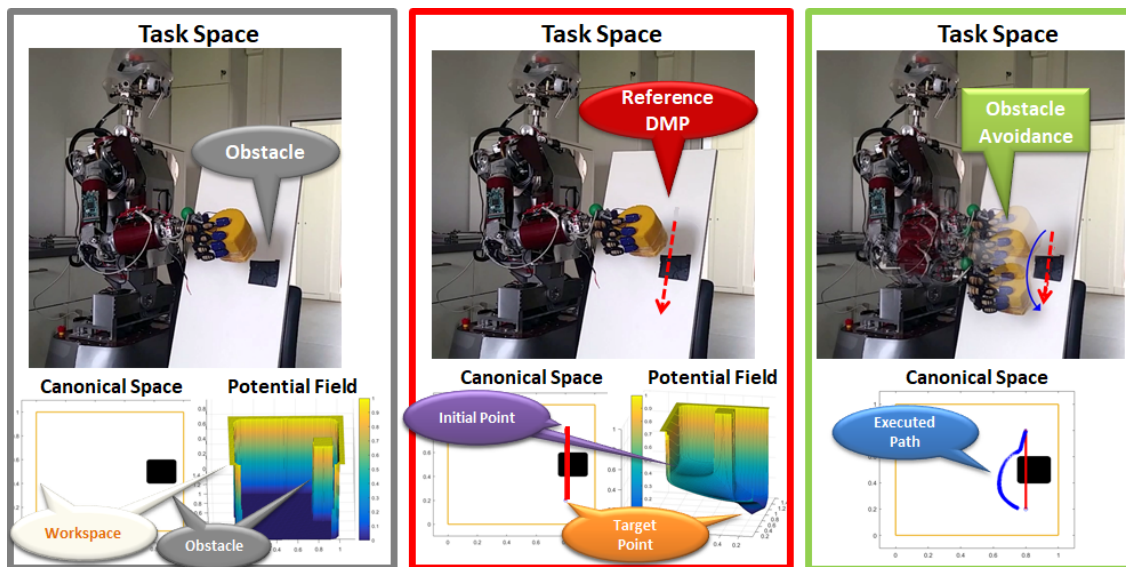
Σχήμα 4: Η διαδικασία εκμάθησης των παραμέτρων ενός συστήματος Δυναμικών Πρωτογενών Κινήσεων με αλλαγή συντεταγμένων CC-DMP περιλαμβάνει την αποσύνθεση της κίνησης σε διακριτό και περιοδικό μέρος. **Αριστερά:** Καταγραφή δράσης πλυσίματος από επίδειξη νοσηλεύτη. **Μέση:** Διαχωρισμός κίνησης σε πρωτογενείς διακριτές και περιοδικές κινήσεις. **Δεξιά:** Η αναπαραγόμενη κίνηση από την μέθοδο CC-DMP (με μπλέ χρώμα) είναι όμοια με την αρχική κίνηση (διακεκομμένη).



τος οι οποίες έχουν προκύψει κατόπιν επίδειξης από ειδικούς νοσηλευτές και να μιμηθεί την συμπεριφορά τους. Αρχικά έγινε καταγραφή μιας μεγάλης ποικιλίας δράσεων πλυσίματος με χρήση συστημάτων οπτικής καταγραφής κίνησης, δημιουργώντας μια βάση δεδομένων η οποία είναι δημόσια διαθέσιμη (KIT whole-body motion database). Ωστόσο, καταγράφηκαν λίγα παραδείγματα από κάθε κίνηση, καθιστώντας την εκμάθηση και γενίκευση της κάθε κίνησης δύσκολη. Στην συνέχεια έγινε αποσύνθεση των καταγεγραμμένων κινήσεων σε απλούστερες πρωτογενείς κινήσεις (π.χ. περιοδικές και διακριτές), οι οποίες είναι καταλληλότερες για ρομποτική εκτέλεση, όπως απεικονίζεται στο Σχ. 4. Η εκμάθηση κάθε πρωτογενούς κίνησης μπορεί να κωδικοποιηθεί σε αυτό το στάδιο στις παραμέτρους ενός μη-γραμμικού δυναμικού συστήματος της μορφής:

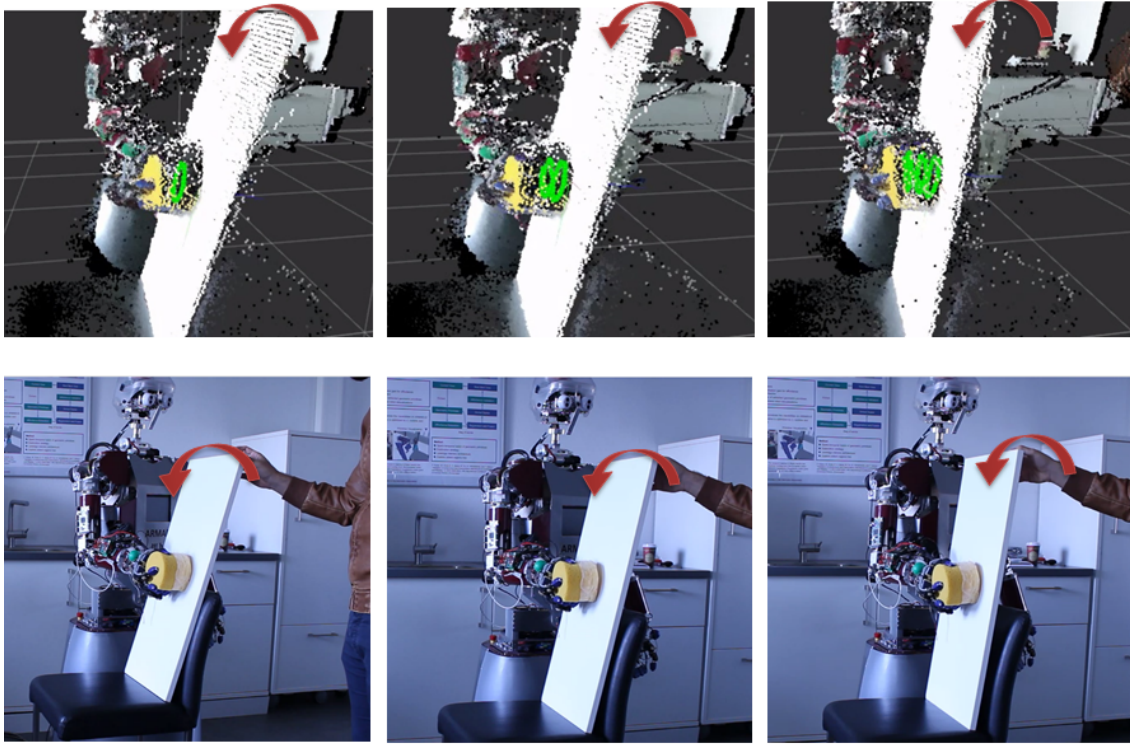
$$\begin{aligned}\tau \cdot \dot{v} &= K \cdot (g - y) - D \cdot v + scale \cdot f \\ \tau \cdot \dot{y} &= v,\end{aligned}\quad (3)$$

με το κέρδος του όρου θέσης  $K$ , το κέρδος του όρου ταχύτητας  $D$  και τον μη γραμμικό όρο δύναμης  $f$ , οι παράμετροι του οποίου προκύπτουν από εκμάθηση των δεδομένων επίδειξης.  $\tau$  είναι ο χρονικός παράγοντας της κίνησης, και  $g$  η θέση στόχος. Ακόμη,  $v$ ,  $\dot{v}$  και  $y$  προσδιορίζουν την τρέχουσα κατάσταση της κίνησης.  $scale$  είναι ένας παράγοντας κλιμάκωσης της κίνησης σε περίπτωση αλλαγής της αρχικής και τελικής κατάστασης. Η μέθοδος αυτή είναι γνωστή στην βιβλιογραφία ως μέθοδος των Πρωτογενών Δυναμικών Κινήσεων (Dynamic Movement Primitives).



Σχήμα 5: **Αριστερά:** Μία περιοχή εμποδίου (π.χ. ένας τραυματισμός που φαίνεται με μαυρο) εντοπίζεται στην επιφάνεια δράσης του ρομπότ Task Space και μετασχηματίζεται στον Κανονικοποιημένο χώρο Canonical Space. Το δυναμικό της συνάρτησης πλοήγησης μεγιστοποιείται στην περιοχή αυτή καθώς και στο σύνορο του χώρου εργασίας. **Μέση:** Η κίνηση οδηγός (κόκκινο) προσδιορίζεται και ένα ελκτικό δυναμικό πεδίο οδηγεί προς το σημείο στόχο. **Δεξιά:** Το αποτέλεσμα του ελεγκτή παρακολούθησης φαίνεται με το μπλε μονοπάτι, το οποίο εκτελείται από το ρομπότ, αποφεύγοντας την τραυματισμένη περιοχή. Μετά την αποφυγή εμποδίου η κίνηση του ρομπότ συγκλίνει και πάλι στην αρχικά σχεδιασμένη γραμμική κίνηση.

Η επανασύνθεση των πρωτογενών κινήσεων με διαφορετικές παραμέτρους κίνησης δίνει την δυνατότητα για μια πλουσιότερη αναπαραγωγή κινήσεων φιλικές προς τον χρήστη. Πιο συγκεκριμένα, για επανασύνθεση μίας πολύπλοκης δράσης πλυσίματος επιλέγεται μία πρω-



Σχήμα 6: Το ARMAR-III ανθρωποειδές ρομπότ εκτελεί μια κίνηση κυκλικού σκουπίσματος μιας τυχαία κινούμενης επιφάνειας. Το ρομπότ κρατάει ένα κίτρινο σφουγγάρι με το οποίο κρατάει συνεχή επαφή με την επιφάνεια, καθώς η κίνηση σκουπίσματος προσαρμόζεται στην κίνηση της επιφάνειας. **Πάνω:** Απεικόνιση με χρήση νέφους σημείων σε διαφορετικές στιγμές εξέλιξης της κίνησης. **Κάτω:** Απεικόνιση απο πλευρική κάμερα της κίνησης της επιφάνειας και της αντίστοιχης προσαρμογής απο το ρομπότ.

τογενής κίνηση σαν οδηγός και μία κίνηση σαν ακόλουθος. Η βασική διαφοροποίηση σε σχέση με την κλασική μέθοδο Πρωτογενών Δυναμικών Κινήσεων βασίζεται στην εκμάθηση των παραμέτρων του μη-γραμμικού όρου της κίνησης ακολούθου σχέση με το πλαίσιο αναφοράς της κίνησης οδηγού, διαμορφώνοντας την μέθοδο Πρωτογενών Δυναμικών Κινήσεων με Αλλαγή Συντεταγμένων (Coordinate Change Dynamic Movement Primitives CC-DMP). Έτσι για να εκφράσουμε την επιθυμητή κίνηση του ρομπότ με βάση την κίνηση ακόλουθο στο παγκόσμιο σύστημα συντεταγμένων χρειάζεται η προσθήκη του πίνακα μετασχηματισμού  $R_G^L$  από το τοπικό σύστημα συντεταγμένων  $L$  στο παγκόσμιο σύστημα δράσης του ρομπότ  $G$ . Έτσι το τελικό δυναμικό σύστημα προκύπτει ως εξής:

$$\begin{aligned} \tau \cdot R_{G,t+1}^L \cdot \dot{v}^G &= R_{G,t}^L \cdot (K \cdot (g^G - y^G) - D \cdot v^G + \\ &\quad \text{scale}^G \cdot f^G) \\ \tau \cdot R_{G,t+1}^L \cdot \dot{y}^G &= R_{G,t}^L \cdot v^G \end{aligned} \quad (4)$$

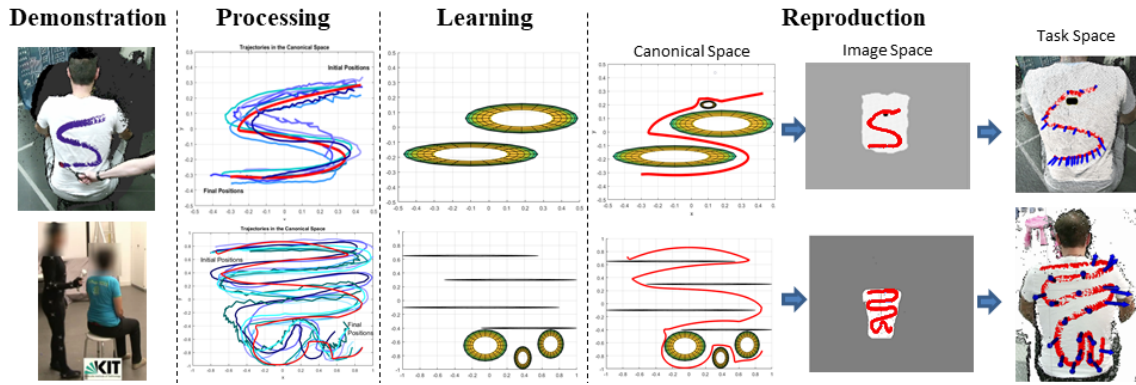
Εξετάζοντας την προσέγγιση οδηγού-ακόλουθου από μία ευρύτερη σκοπιά ως προς τις δράσεις πλυσίματος, το διακριτό μέρος της κίνησης περιγράφει την βασική κατεύθυνση της δράσης (π.χ. από το πάνω μέρος του σώματος προς το κάτω) ενώ το περιοδικό μέρος εκφράζει το λειτουργικό μέρος της κίνησης όπως μία ευθεία ή κυκλική περιοδική κίνηση. Με την προτεινόμενη αποσύνθεση των κινήσεων και την έκφραση του κάθε μέρους με την μέθοδο CC-DMP

υπάρχει η δυνατότητα αναπαραγωγής των αρχικών κινήσεων επίδειξης αλλά και προσαρμογή αυτών κατά την διάρκεια της λειτουργίας του ρομπότ, αλλάζοντας τις χρονικές παραμέτρους του δυναμικού συστήματος. Εντούτοις, η χρήση αποκλειστικά της μεθόδου CC-DMP δεν αρκεί για την δημιουργία ενός πλήρους συστήματος διαδραστικού σχεδιασμού δράσεων πλυσίματος, καθώς στην γενική περίπτωση ο μετασχηματισμός  $R_G^L$ , ο οποίος είναι απαραίτητος για την έκφραση της κίνησης ακολούθου στον χώρο, είναι άγνωστος ή μεταβάλλεται με τον χρόνο.

Επομένως είναι απαραίτητη η χρήση του συστήματος αισθητηριακής αντίληψης του χώρου δράσης και πιο συγκεκριμένα της οπτικής ανάδρασης από τις κάμερες του συστήματος για την παρακολούθηση της κίνησης του σώματος του χρήστη. Αναλυτικότερα με την χρήση του συστήματος προσαρμογής κίνησης, όπως περιγράφηκε παραπάνω, είναι δυνατή η αναπαραγωγή της κίνησης οδηγού στον Κανονικοποιημένων διαστάσεων δισδιάστατο χώρο και η προσαρμογή του στην κινούμενη και καμπύλη επιφάνεια του σώματος του χρήστη, όπως φαίνεται στο Σχ. 5. Στην περίπτωση ύπαρξης μιας τραυματισμένης περιοχής στην επιφάνεια του σώματος τότε ο ελεγκτής μεταβάλλει την αναπαραγώμενη κίνηση, αποφεύγοντας την συγκεκριμένη περιοχή. Επιπλέον, η αναπαραγωγή της κίνησης οδηγού στον κανονικοποιημένο χώρο, προσφέρει άμεση χωρική κλιμάκωση της κίνησης στο διαφορετικό μέγεθος των μερών του σώματος κάθε χρήστη, ανεξάρτητα από την κίνηση επίδειξης που χρησιμοποιήθηκε στην φάση εκμάθησης. Μετά το στάδιο της προσαρμογής και έκφρασης της κίνησης οδηγού στον χώρο εργασίας του ρομπότ, η επιθυμητή κίνηση του ρομπότ προκύπτει από την αναπαραγωγή της κίνησης ακολούθου ως προς το πλαίσιο της κίνησης οδηγού. Το προτεινόμενο σύστημα αξιολογήθηκε πειραματικά με τη χρήση ενός ανθρωποειδούς ρομπότ, το οποίο εκτέλεσε ένα σενάριο καθαρισμού επιφάνειας όπως φαίνεται στο παράδειγμα του Σχ. 6 όπου μία κυκλική κίνηση εκτελείται προσαρμοστικά στην κίνηση της επιφάνειας, διατηρώντας συνεχόμενη επαφή με αυτή. Τα παραδείγματα που εκτελέστηκαν καταδεικνύουν την εφαρμοσιμότητα της μεθόδου σε πραγματικά σενάρια ρομποτικής υποβοήθησης.

## Εκμάθηση Κινήσεων Από Επίδειξη Με Συναρτήσεις Πλοήγησης

Επιπλέον της μεθόδου των Δυναμικών Πρωτογενών Κινήσεων, προτάθηκε και μία εναλλακτική μέθοδος εκμάθησης και αναπαραγωγής σύνθετων κινήσεων από δεδομένα επίδειξης μέσω της διαμόρφωσης ενός απωστικού δυναμικού πεδίου συναρτήσεων πλοήγησης. Πιο συγκεκριμένα, η επίδειξη των κινήσεων πραγματοποιείται στον φυσικό τρισδιάστατο χώρο όπως φαίνεται στο Σχ. 7 και τα καταγραφόμενα δεδομένα κίνησης προβάλλονται πάνω στην επιφάνεια του σώματος και στην συνέχεια στον δισδιάστατο κανονικοποιημένο χώρο όπως περιγράφηκε παραπάνω. Σε αυτόν τον απλοποιημένο χώρο τα μονοπάτια επίδειξης αποθρομβοποιούνται και το διακριτό τους μέρος χρησιμοποιείται στην διαδικασία εκμάθησης. Η διαδικασία αυτή περιλαμβάνει τον υπολογισμό των συναρτήσεων εικονικών εμποδίων  $\beta$ , τα οποία συνδιαμορφώνουν μαζί με τα πραγματικά εμπόδια στην επιφάνεια, την συνάρτηση πλοήγησης  $\phi$  της Εξίσωσης 2 και υπολογίζονται με την μορφή έλλειψης όπως παρατηρείται στο Σχ. 7. Η έκφραση των παραμέτρων των εικονικών εμποδίων (κέντρο και μήκος βασικών αξόνων) υπολογίζεται από την επίλυση ενός μη-κυρτού προβλήματος βελτιστοποίησης με την βοήθεια ενός γενετικού αλγορίθμου επαυξημένου με μία μέθοδο κατάβασης κλίσης (Gradient Descent). Αναλυτικότερα, κάθε παράμετρος του εμποδίου αντιστοιχεί σε ένα γονίδιο του γενετικού αλγορίθμου και επηρεάζει διαφορετικά την μορφή της παραγόμενης τροχιάς από την συνάρτηση πλοήγησης και την τιμή της συνάρτησης κόστους, η οποία έχει την μορφή:



Σχήμα 7: Διαδικασίες Επίδειξης, Επεξεργασίας, Εκμάθησης και Αναπαραγωγής. Η διαδικασία της Επίδειξης εκφράζεται μέσω τροχιών που πραγματοποιούνται στον τρισδιάστατο φυσικό χώρο από νοσηλευτικό προσωπικό. Τα δεδομένα επίδειξης προβάλλονται στον δισδιάστατο κανονικοποιημένο χώρο όπου επεξεργάζονται. Στην φάση εκμάθησης με βάση την πληροφορία των δεδομένων κατασκευάζονται εικονικά εμπόδια σύμφωνα με την προτεινόμενη μέθοδο. Κατά την διαδικασία αναπαραγωγής της κίνησης ένας ελεγκτής συναρτήσεων πλοήγησης χρησιμοποιείται για την αναπαραγωγή της διαδικασίας πλυσίματος.

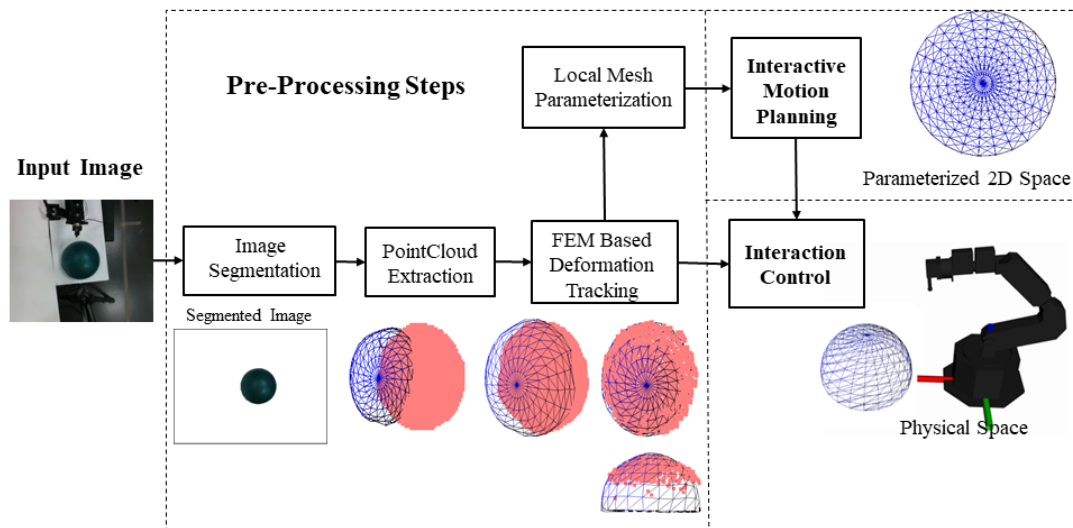
$$\mathbf{C} \triangleq \frac{1}{T_{exp}} \cdot \sum_{n \in N_{exp}} F(R, E_n) \quad (5)$$

όπου  $F$  είναι η απόσταση Fréchet μεταξύ της παραγόμενης τροχιάς  $R$  από την υποψήφια συνάρτηση εμποδίων  $\beta$  και μίας τροχιάς επίδειξης  $E_n$  για το σύνολο των τροχιών επίδειξης  $N_{exp}$ . Με αυτό τον τρόπο σε κάθε κύκλο εκπαίδευσης υπολογίζεται η ομοιότητα της παραγόμενης τροχιάς με τις τροχιές επίδειξης για όλη την χρονική διάρκεια της κίνησης  $T_{exp}$ . Επιπλέον, σε κάθε γενιά εκπαίδευσης η αναζήτηση του γενετικού αλγορίθμου επαυξάνεται με την χρήση της μεθόδου κατάβασης κλίσης για κάθε μέλος της τρέχουσας γενιάς εμποδίων, ώστε να βρεθεί μία τοπικά βέλτιστη λύση, χρησιμοποιώντας την ίδια συνάρτηση κόστους με στόχο την ταχύτερη σύγκλιση του αλγορίθμου εκπαίδευσης. Μετά την σύγκλιση, τα εικονικά εμπόδια που υπολογίστηκαν σε συνδυασμό με τα πραγματικά εμπόδια του χώρου εργασίας, διαμορφώνουν ένα δυναμικό, η κατάβαση του οποίου από μία αρχική σε μία τελική θέση κατάλληλα επιλεγμένες, παράγει μία τροχιά όμοια με την επίδειξη όπως φαίνεται στο Σχ. 7, προσδίδοντας στο ρομποτικό σύστημα τις απαραίτητες δεξιότητες για κάθε εργασία πλυσίματος.

## Έλεγχος Αλληλεπίδρασης Με Παραμορφώσιμες Επιφάνειες

Στο τελευταίο στάδιο της παρούσας διατριβής, προτάθηκε ένα σύστημα διαδραστικού σχεδιασμού κίνησης, το οποίο δύναται να αυξήσει την ακρίβεια σχεδιασμού των εργασιών αλληλεπίδρασης και να ρυθμίσει τις δυνάμεις επαφής κατά τις ρομποτικές δράσεις με φυσική επαφή. Πιο συγκεκριμένα, η αδυναμία εγκατάστασης ενός αξιόπιστου συστήματος μέτρησης της δύναμης επαφής σε πολλά ρομποτικά συστήματα όπως το I-Support, οδήγησε στην μελέτη ρομποτικών τεχνικών ελέγχου επαφής χωρίς άμεση ανάδραση. Τέτοια σχήματα αφορούν τον έλεγχο ακαμψίας του ρομποτικού μηχανισμού (stiffness control) μέσω του ελέγχου ροπής στους κινητήρες για αρθρωτούς ρομποτικούς χειριστές, ή έλεγχο συνδυασμού μηχανισμών κίνησης για εύκαμπτα ρομπότ. Παράλληλα η πρόοδος των τεχνικών όρασης υπολογιστών στην ανάλυση εικόνας και στις δυνατότητες αντίληψης του περιβάλλοντος με χωρική μοντελοποίηση τρισδιάστατου πλέγματος, έδωσε κίνητρο για την ανάπτυξη ενός αλγορίθμου διαδραστικού



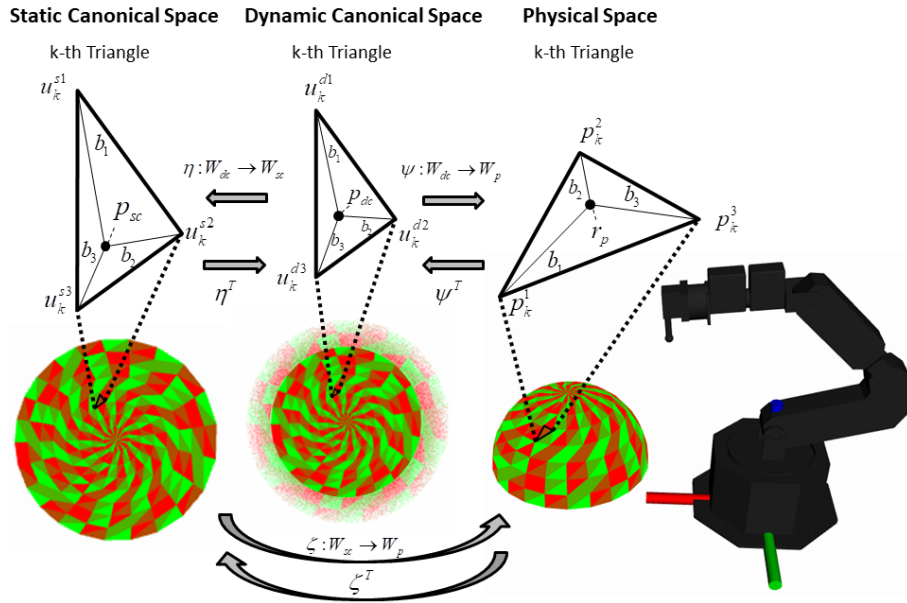


Σχήμα 8: Η συνολική αρχιτεκτονική του προτεινόμενης μεθόδου διαδραστικού σχεδιασμού κίνησης με βάση την αναπαράσταση πλέγματος του αντικειμένου. Η κατάτμηση της εικόνας εισόδου, η παρακολούθηση της παραμόρφωσης του αντικειμένου με τεχνικές διακριτών στοιχείων και η παραμετροποίηση του πλέγματος αποτελούν τα αλγοριθμικά βήματα προεπεξεργασίας. Αυτά τα βήματα παρέχουν μια αναπαράσταση πλέγματος του αντικειμένου τόσο στον Φυσικό χώρο, όπου εφαρμόζεται ένα σχήμα ελέγχου αλληλεπίδρασης δυσκαμψίας, όσο και σε 2Δ Παραμετρικούς χώρους, όπου πραγματοποιείται ο σχεδιασμός των διαδραστικών ενεργειών.

σχεδιασμού κίνησης βασιζόμενου σε μία δομή τρισδιάστατου πλέγματος (3D Mesh).

Όμοια με τις παραπάνω προσεγγίσεις ο βασικός στόχος του αλγορίθμου σχεδιασμού κίνησης είναι να επιτρέψει στον ρομποτικό χειριστή να πλοηγηθεί πάνω από ένα μέρος της επιφάνειας ενός αντικειμένου και να έρθει σε επαφή μαζί του, ενώ το αντικείμενο παραμορφώνεται ενεργά ή παθητικά. Η εξέλιξη της παραμόρφωσης του αντικειμένου δεν περιγράφεται από κάποιο χρονικό μοντέλο, επομένως η οπτική πληροφορία μίας κάμερας βάθους χρησιμοποιείται για την συνεχή εν λειτουργία μοντελοποίηση της παραμόρφωσης στον χρόνο. Παρά την πλούσια πληροφορία που παρέχεται από μία τέτοια κάμερα, χρειάζονται πολλαπλά επίπεδα επεξεργασίας των εισερχόμενων δεδομένων για να αντληθεί η χρήσιμη πληροφορία για τον προτεινόμενο αλγόριθμο.

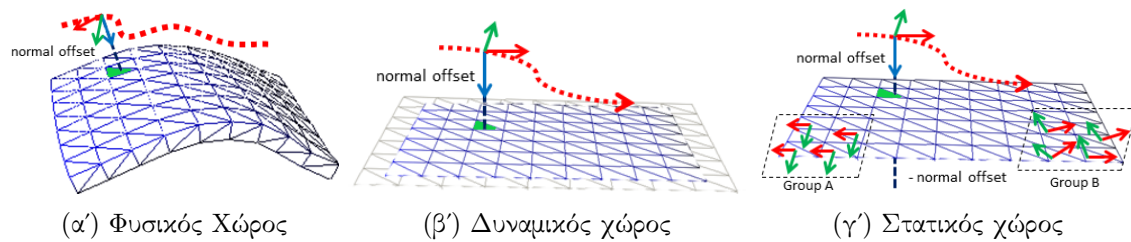
Αρχικά σαν πρώτο βήμα επεξεργασίας είναι απαραίτητος ο εντοπισμός του αντικειμένου ενδιαφέροντος στο επίπεδο της εικόνας. Όπως περιγράφηκε παραπάνω, ο συγκεκριμένος εντοπισμός πραγματοποιείται με τεχνικές κατάτμησης εικόνας. Το δεύτερο βήμα επεξεργασίας αποτελείται από έναν αλγόριθμο παρακολούθησης της παραμόρφωσης του αντικειμένου, ο οποίος χρησιμοποιεί σαν είσοδο τα τρισδιάστατα σημεία που παράγονται από την κάμερα βάθους κάθε χρονική στιγμή και προσαρμόζει ένα μοντέλο τρισδιάστατου πλέγματος στην μορφή τους, όπως φαίνεται στο Σχ. 8. Από την μελέτη των τεχνικών παραμόρφωσης της βιβλιογραφίας ξεχώρισαν οι τεχνικές που λαμβάνουν υπόψιν τους τα φυσικά χαρακτηριστικά του αντικειμένου και υλοποιούνται με μεθόδους πεπερασμένων στοιχείων (Finite Element Method). Η μοντελοποίηση των φυσικών παραμέτρων του αντικειμένου επιτρέπει τον υπολογισμό και την πρόβλεψη των εσωτερικών δυνάμεων που δημιουργούνται από την αλληλεπίδραση με το περιβάλλον του. Έτσι καθίσταται εφικτός ο σχεδιασμός και η εκτέλεση ρομποτικών εργασιών σε επαφή με το αντικείμενο. Επιπρόσθετα, παρακολούθηση της παραμόρφωσης του αντικειμένου βοηθάει στην αποτελεσματική αντιμετώπιση της απόκρυψης οπτικής επαφής της κάμερας με το αντικείμενο, η οποία συμβαίνει κατά την διάρκεια της ρομποτικής εργασίας.



Σχήμα 9: Έκφραση μετασχηματισμών αμφιμονοσήμαντο και επί μεταξύ του Στατικού Κανονικοποιημένου Χώρου, του Δυναμικού Κανονικοποιημένου Χώρου και του Φυσικού χώρου δράσης του ρομπότ με την χρήση βαρυκεντρικών συντεταγμένων μεταξύ των αντίστοιχων τριγώνων των τριών χώρων.

Παρά τα ακριβή αποτελέσματα παρακολούθησης της παραμόρφωσης του αντικειμένου, η πρόβλεψη της εξέλιξής της στον χρόνο είναι αδύνατη χωρίς ένα αντίστοιχο μαθηματικό μοντέλο. Έτσι είναι απαραίτητο ένα τρίτο βήμα επεξεργασίας το οποίο εφαρμόζει κάθε χρονική στιγμή ένα μη-γραμμικό μετασχηματισμό προβολής του τρισδιάστατου πλέγματος στον επίπεδο χώρο, ο οποίος ονομάζεται Δυναμικός Κανονικοποιημένος χώρος (Dynamic Canonical Space) και απεικονίζεται στην μέση του Σχ. 9. Ο Δυναμικός Κανονικοποιημένος χώρος παρακολουθεί τις αλλαγές στις γεωδαισικές αποστάσεις που συμβαίνουν στην επιφάνεια του αντικειμένου λόγω της παραμόρφωσης. Η έκφραση αυτού του μη-γραμμικού μετασχηματισμού προβολής σε μία σταθερή και κατάλληλα επιλεγμένη χρονική στιγμή δημιουργεί τον Στατικό Κανονικοποιημένο χώρο (αριστερά στο Σχ. 9). Αποδεικνύεται μέσω βαρυκεντρικών συντεταγμένων των τριγώνων του πλέγματος, ότι κάθε σημείο του Στατικού Κανονικοποιημένου χώρου αντιστοιχίζεται ένα-προς-ένα, με ένα σημείο του Δυναμικού Κανονικοποιημένου χώρου και ταυτόχρονα με ένα σημείο στην επιφάνεια του αντικειμένου στον Φυσικό χώρο δράσης του ρομπότ. Αυτή η αντιστοίχιση επιτρέπει τον σχεδιασμό κινήσεων στους επίπεδους χώρους και την άμεση έκφρασή τους στην επιφάνεια του αντικειμένου.

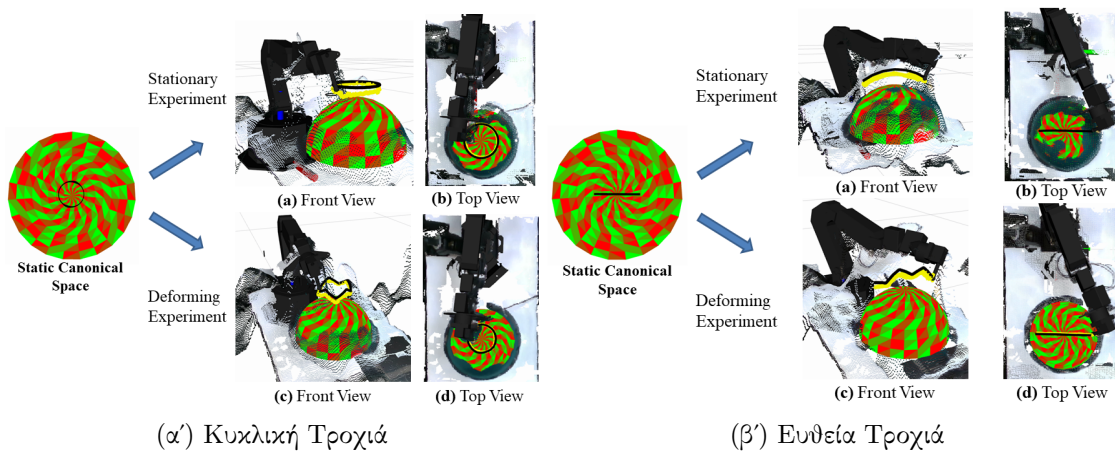
Ο στόχος του αλγορίθμου σχεδιασμού κίνησης είναι ο υπολογισμός της επιθυμητής πόζας του τελικού στοιχείου δράσης του ρομπότ. Η επιθυμητή τροχιά για μία ρομποτική εργασία αλληλεπίδρασης σχεδιάζεται αρχικά εντός των ορίων του Στατικού Κανονικοποιημένου χώρου όπως φαίνεται στο Σχ. 10γ'. Εκφράζοντας το κάθε σημείο της τροχιάς σε σχέση με τις κορυφές του αντίστοιχου τριγώνου (ενεργό τρίγωνο), μπορούμε στην συνέχεια να βρούμε μονοσήμαντα το αντίστοιχο σημείο του τόσο στον Δυναμικό Κανονικοποιημένο χώρο όσο και στον Φυσικό χώρο δράσης του ρομπότ 10α'. Η κάθετη απόσταση της σχεδιαζόμενης τροχιάς από το επίπεδο  $z = 0$  των διδιάστατων χώρων διατηρείται ίδια στον φυσικό χώρο δράσης σε σχέση με την επιφάνεια του αντικειμένου. Για να γίνει σχεδιασμός μίας ρομποτικής



Σχήμα 10: Η προτεινόμενη μέθοδος διαδραστικού σχεδιασμού κίνησης. Ο σχεδιασμός της κίνησης γίνεται στους διδιάστατους παραμετρικούς χώρους (Στατικό ή Δυναμικό) και κάθε χρονική στιγμή η κίνηση εκφράζεται στην επιφάνεια του αντικειμένου.

εργασίας με επαφή αρκεί να επιλεγεί μία θέση με αρνητική απόσταση από το μηδενικό επίπεδο. Επιπρόσθετα, ο επιθυμητός προσανατολισμός καθορίζεται με βάση το κάθετο διάνυσμα στους δύο διδιάστατους χώρους και αντίστοιχα στο τρίγωνο του τρισδιάστατου πλέγματος στον φυσικό χώρο.

Η απόδοση του συστήματος ελέγχθηκε πειραματικά σε συνθήκες εργαστηρίου, χρησιμοποιώντας ένα ρομποτικό χειριστή για την εκτέλεση διαδραστικών εργασιών με ένα παραμορφώσιμο μοντέλο. Μελετήθηκε η ακρίβεια του σχεδιασμού τέτοιων εργασιών συγκριτικά με προηγούμενες προσεγγίσεις οι οποίες στηρίζονται μόνο σε οπτική πληροφορία. Παρουσιάζονται επίσης αποτελέσματα ως προς την παρακολούθηση σημείου στην επιφάνεια ενός ενεργά παραμορφούμενου αντικειμένου και την ρύθμιση των δυνάμεων επαφής επί αυτού, καταδεικνύοντας την ακρίβεια και αποτελεσματικότητα του προτεινόμενου συστήματος ρομποτικού σχεδιασμού κίνησης και ελέγχου στην εκτέλεση διαδραστικών εργασιών χειρισμού επί παραμορφώσιμων επιφανειών.



Σχήμα 11: Παραδείγματα εκτέλεσης μίας κυκλικής και μίας ευθείας τροχιάς πάνω από ένα ημισφαιρικό παραμορφώσιμο μοντέλο, σε ένα στατικό σενάριο και ένα σενάριο ημιτονοειδούς παραμόρφωσης. Η παρακολούθηση της τροχιάς στον φυσικό χώρο από το ρομπότ γίνεται με συμμόρφωση στην παραμόρφωση του αντικειμένου και στις αλλαγές των γεωδαισικών αποστάσεων στην επιφάνειά του.





# Contents

<b>Contents</b>	<b>28</b>
<b>List of Figures</b>	<b>29</b>
<b>List of Tables</b>	<b>39</b>
<b>1 Introduction</b>	<b>41</b>
1.1 Motivation . . . . .	41
1.2 Problem formulation . . . . .	44
1.3 Related Work . . . . .	46
1.3.1 Assistive Nursing Care Robotic Systems . . . . .	46
1.3.2 Interactive Motion Planning Methods . . . . .	47
1.3.3 Interactive Motion Learning Methods . . . . .	48
1.3.4 Interactive Contact Force Regulation Methods . . . . .	50
1.4 Thesis Approach . . . . .	51
1.5 Contributions . . . . .	52
1.6 Thesis Structure . . . . .	54
<b>2 Theoretical Background</b>	<b>55</b>
2.1 Semantic Visual Segmentation and Human Pose Estimation . . . . .	55
2.2 Navigation Functions . . . . .	58
2.3 Dynamic Movement Primitives . . . . .	59
2.3.1 Discrete Motions . . . . .	60
2.3.2 Periodic Motions . . . . .	61
2.4 Deformation Tracking . . . . .	62
2.5 Mesh Parameterization . . . . .	64
<b>3 Perception-Based Motion Planning &amp; Learning from Demonstration</b>	<b>69</b>
3.1 Problem Statement . . . . .	69
3.2 Methodology & Mathematical Background . . . . .	71
3.2.1 Interactive Motion Learning & Generation . . . . .	71
3.2.2 Perception-Based Motion Planning . . . . .	73
3.3 Perception-Based Interaction System . . . . .	79
3.4 Learning from Demonstration Using Navigation Functions . . . . .	81
3.4.1 Learning of Discrete Interactive Motions . . . . .	81
3.4.2 Interactive Motion Reproduction . . . . .	85
3.5 Chapter Outcomes . . . . .	86

<b>4</b>	<b>Mesh-Based Motion Planning and Interaction Control</b>	<b>87</b>
4.1	Related Work . . . . .	87
4.2	Problem Formulation . . . . .	89
4.2.1	Mechanical stiffness . . . . .	90
4.2.2	Geometrically Consistent Active Stiffness . . . . .	91
4.3	Robot-Surface Interaction Control Framework . . . . .	94
4.3.1	Preprocessing Steps . . . . .	94
4.3.2	Mathematical Formulation . . . . .	97
4.3.3	Interactive Motion-Planning Approach . . . . .	99
<b>5</b>	<b>Experimental Validation of Perception-Based Interaction System</b>	<b>103</b>
5.1	Perception-Based Motion Planning . . . . .	103
5.1.1	Validation Strategy in Lab Conditions . . . . .	104
5.1.2	Validation Results and Discussion . . . . .	105
5.1.3	Clinical Validation Study . . . . .	107
5.1.4	Training and Comparison of Input Devices . . . . .	108
5.1.5	Water Pouring Experiments . . . . .	109
5.1.6	Clinical Validation Results and Discussion . . . . .	112
5.2	Learning from Demonstration Using Navigation Functions . . . . .	114
5.2.1	Validation Results & Discussion . . . . .	115
5.3	Adaptation of Motion Primitives to Dynamic Surfaces . . . . .	117
5.3.1	Experimental Scenarios . . . . .	118
5.3.2	Experimental Results & Discussion . . . . .	118
<b>6</b>	<b>Experiments of Interactive Motion Planning on Deformable Surface</b>	<b>125</b>
6.1	Pre-processing Steps . . . . .	125
6.2	Experimental Set-Up . . . . .	126
6.3	Experimental procedures and results . . . . .	128
6.3.1	Interactive Motion Planning Accuracy . . . . .	128
6.3.2	Interactive Motion Demonstration . . . . .	137
6.3.3	Contact Force Regulation . . . . .	139
<b>7</b>	<b>Conclusions &amp; Future Work</b>	<b>143</b>
7.1	Summary of Main Contributions . . . . .	143
7.2	Future Research Directions . . . . .	145
<b>A</b>	<b>Glossary</b>	<b>167</b>
<b>B</b>	<b>List of Publications</b>	<b>169</b>
B.1	Publications in Peer-reviewed International Journals . . . . .	169
B.2	Publications in Peer-reviewed International Conferences . . . . .	169

# List of Figures

- 1 Εγκατάσταση του συστήματος I-Support σε κλινικό περιβάλλον (Νοσοκομείο Fondazione Santa Lucia (FSL) στην Ρώμη, Ιταλία) για πειραματική αξιολόγηση. Οι συσκευές που απαρτίζουν το σύστημα απεικονίζονται με σειρά στο (a) Amphiro b1 αισθητήρας ροής και θερμοκρασίας νερού, (b) Το σύνολο του συστήματος με τα βασικά του υποσυστήματα όπως την αυτοκινούμενη καρέκλα, το ρομπότ απο εύκαμπτα υλικά και η εγκατάσταση των καμερών Kinect, (c) Αισθητήρας θερμοκρασίας αέρα, υγρασίας και φωτισμού, (d) Έξυπνο ρολόι που βοηθάει στην ταυτοποίηση του χρήστη και στην παρακολούθηση της δραστηριότητάς του. . . . . 15
  
- 2 Τρεις διαφορετικοί χώροι που περιγράφονται στην την προτεινόμενη μεθοδολογία. (a) Δισδιάστατος χωρικά κανονικοποιημένος χώρος κατά τις  $x, y$  διαστάσεις ο οποίος αμαφέρεται σαν ‘Κανονικοποιημένος’ χώρος (“Canonical” space). (b) Ο δισδιάστατος χώρος της εικόνας είναι η εικόνα της κάμερας Kinect με αρχικό μέγεθος  $512 \times 424$  εικονοστοιχεία. Η περιοχή που επισημαίνεται με ένα κίτρινο τετράγωνο είναι το αποτέλεσμα του αλγορίθμου κατάτμησης της εικόνας ο οποίος εντοπίζει το επιθυμητό μέρος του σώματος. (c) Ο τρισδιάστατος χώρος δράσης του ρομπότ (Task Space). Η ημιτονοειδής τροχία απο τον Κανονικοποιημένο χώρο αντιστοιχίζεται στην επιφάνεια της πλάτης της χρήστριας του συστήματος. Το κίτρινο κουτί αντιπροσωπεύει έναν υποχώρο, ο οποίος περιλαμβάνει τα σημεία προσαρμογής της τροχιάς. . . . . 17
  
- 3 (a) Πειραματική προσαρμογή σιγμοειδούς τροχιάς στην πλάτη μίας χρήστριας του συστήματος. (b) Κλιμάκωση της απεικόνισης της τροχιάς με έμφαση στην λεπτομερή οπτικοποίηση της προσαρμογής. (c) Απεικόνιση της τροχιάς χωρίς το νέφος σημείων της επιφάνειας της πλάτης. . . . . 18
  
- 4 Η διαδικασία εκμάθησης των παραμέτρων ενός συστήματος Δυναμικών Πρωτογενών Κινήσεων με αλλαγή συντεταγμένων CC-DMP περιλαμβάνει την αποσύνθεση της κίνησης σε διακριτό και περιοδικό μέρος. **Αριστερά:** Καταγραφή δράσης πλυσίματος απο επίδειξη νοσηλεύτη. **Μέση:** Διαχωρισμός κίνησης σε πρωτογενείς διακριτές και περιοδικές κινήσεις. **Δεξιά:** Η αναπαραγώμενη κίνηση από την μέθοδο CC-DMP (με μπλέ χρώμα) είναι όμοια με την αρχική κίνηση (διακεκομμένη). . . . . 18

- 5 **Αριστερά:** Μία περιοχή εμποδίου (π.χ. ένας τραυματισμός που φαίνεται με μαυρο) εντοπίζεται στην επιφάνεια δράσης του ρομπότ Task Space και μετασχηματίζεται στον Κανονικοποιημένο χώρο Canonical Space. Το δυναμικό της συνάρτησης πλοήγησης μεγιστοποιείται στην περιοχή αυτή καθώς και στο σύνορο του χώρου εργασίας. **Μέση:** Η κίνηση οδηγός (κόκκινο) προσδιορίζεται και ένα ελκτικό δυναμικό πεδίο οδηγεί προς το σημείο στόχο. **Δεξιά:** Το αποτέλεσμα του ελεγκτή παρακολούθησης φαίνεται με το μπλε μονοπάτι, το οποίο εκτελείται απο το ρομπότ, αποφεύγοντας την τραυματισμένη περιοχή. Μετα την αποφυγή εμποδίου η κίνηση του ρομπότ συγκλίνει και πάλι στην αρχικά σχεδιασμένη γραμμική κίνηση. . . . . 19
- 6 Το ARMAR-III ανθρωποειδές ρομπότ εκτελεί μια κίνηση κυκλικού σκουπίσματος μιας τυχαία κινούμενης επιφάνειας. Το ρομπότ κρατάει ένα κίτρινο σφουγγάρι με το οποίο κρατάει συνεχή επαφή με την επιφάνεια, καθώς η κίνηση σκουπίσματος προσαρμόζεται στην κίνηση της επιφάνειας. **Πάνω:** Απεικόνιση με χρήση νέφους σημείων σε διαφορετικές στιγμές εξέλιξης της κίνησης. **Κάτω:** Απεικόνιση απο πλευρική κάμερα της κίνησης της επιφάνειας και της αντίστοιχης προσαρμογής απο το ρομπότ. . . . . 20
- 7 Διαδικασίες Επίδειξης, Επεξεργασίας, Εκμάθησης και Αναπαραγωγής. Η διαδικασία της Επίδειξης εκφράζεται μέσω τροχιών που πραγματοποιούνται στον τρισδιάστατο φυσικό χώρο από νοσηλευτικό προσωπικό. Τα δεδομένα επίδειξης προβάλλονται στον δισδιάστατο κανονικοποιημένο χώρο όπου επεξεργάζονται. Στην φάση εκμάθησης με βάση την πληροφορία των δεδομένων κατασκευάζονται εικονικά εμπόδια σύμφωνα με την προτεινόμενη μέθοδο. Κατά την διαδικασία αναπαραγωγής της κίνησης ένας ελεγκτής συναρτήσεων πλοήγησης χρησιμοποιείται για την αναπαραγωγή της διαδικασίας πλυσίματος. . . . . 22
- 8 Η συνολική αρχιτεκτονική του προτεινόμενης μεθόδου διαδραστικού σχεδιασμού κίνησης με βάση την αναπαράσταση πλέγματος του αντικειμένου. Η κατάτμηση της εικόνας εισόδου, η παρακολούθηση της παραμόρφωσης του αντικειμένου με τεχνικές διακριτών στοιχείων και η παραμετροποίηση του πλέγματος αποτελούν τα αλγοριθμικά βήματα προεπεξεργασίας. Αυτά τα βήματα παρέχουν μια αναπαράσταση πλέγματος του αντικειμένου τόσο στον Φυσικό χώρο, όπου εφαρμόζεται ένα σχήμα ελέγχου αλληλεπίδρασης δυσκαμψίας, όσο και σε 2Δ Παραμετρικούς χώρους, όπου πραγματοποιείται ο σχεδιασμός των διαδραστικών ενεργειών. . . . . 23
- 9 Έκφραση μετασχηματισμών αμφιμονοσήμαντο και επί μεταξύ του Στατικού Κανονικοποιημένου Χώρου, του Δυναμικού Κανονικοποιημένου Χώρου και του Φυσικού χώρου δράσης του ρομπότ με την χρήση βαρυκεντρικών συντεταγμένων μεταξύ των αντίστοιχων τριγώνων των τριών χώρων. . . . . 24
- 10 Η προτεινόμενη μέθοδος διαδραστικού σχεδιασμού κίνησης. Ο σχεδιασμός της κίνησης γίνεται στους δισδιάστατους παραμετρικούς χώρους (Στατικό ή Δυναμικό) και κάθε χρονική στιγμή η κίνηση εκφράζεται στην επιφάνεια του αντικειμένου. . . . . 25
- 11 Παραδείγματα εκτέλεσης μίας κυκλικής και μίας ευθείας τροχιάς πάνω από ένα ημισφαιρικό παραμορφώσιμο μοντέλο, σε ένα στατικό σενάριο και ένα σενάριο ημιτονοειδούς παραμόρφωσης. Η παρακολούθηση της τροχιάς στον φυσικό χώρο από το ρομπότ γίνεται με συμμόρφωση στην παραμόρφωση του αντικειμένου και στις αλλαγές των γεωδαισικών αποστάσεων στην επιφάνειά του. . . . . 25

1.1	The envisioned transition from a (a) standardized clinical bathroom to (b) a bathing environment equipped with appropriate robotic and sensorial infrastructure. . . . .	42
1.2	Installation of the I-Support system in clinical environment (Fondazione Santa Lucia (FSL) Hospital in Rome, Italy) for experimental validation. The devices constituting the overall system are presented. (a) Amphiro b1 water flow and temperature sensor. (b) General aspect of the system showing the Motorized Chair, the Soft Robotic Arm and the installation of the Kinect sensors (for audio-gestural communication). (c) Air temperature, humidity and illumination sensors by CubeSensors. (d) Smartwatch for user identification and activity tracking. . . . .	44
1.3	Design of a soft-robotic arm performing bathing actions. . . . .	45
1.4	Examples of washing actions demonstrated from professional caregivers, available at KIT whole body database [1]. . . . .	52
2.1	Semantic segmentation of human torso visual results in multiple images of a human user in the I-Support system environment. Up: The segmented body parts labels shown in different colors. The torso is presented in light green color. Down: The original images obtained from the I-Support system's cameras. . . . .	56
2.2	Semantic segmentation of human legs visual results in multiple images of a human user in the I-Support system environment. Up: The segmented body parts labels shown in different colors. The legs are presented in orange color. Down: The original images obtained from the I-Support system's cameras. . . . .	56
2.3	Visualization of human pose estimation from multiple points of view from the cameras of the I-Support system. . . . .	57
2.4	Discrete Radial basis functions for $N = 11$ in the (a) time domain for $\tau = 1$ (b) $x$ phase variable domain for $\alpha_x = 4.6$ and $\tau = 1$ . . . . .	61
2.5	Parameterization of a 3D triangular mesh to a planar parameter domain [2].	65
3.1	Motion planning method evaluation through a series of clinical validation studies in realistic clinical validation scenarios of (a) Washing back and (b) Washing legs conducted in Bethanien Hospital in Heidelberg Germany and Fondazione Santa Lucia (FSL) Hospital in Rome Italy, respectively. . . . .	70
3.2	The procedure of learning CC-DMP by human demonstration includes the separation of the motion into discrete and periodic part. <b>Left:</b> A demonstrated washing action <b>Middle:</b> Separation of the demonstrated motion into primitive discrete and periodic motions. <b>Right:</b> The reproduced motion by the CC-DMP method (blue) is similar to the demonstrated one (dashed). . . . .	72
3.3	Three different spaces described in the proposed methodology. (a) 2D space normalized in x,y dimensions denoted as "Canonical" space. (b) 2D Image space is the actual image (of size 512 x 424 pixels) obtained from Kinect sensor. The yellow rectangular area marks the user's back region, as a result of a segmentation algorithm. (c) 3D Task Space is the operational space of the robot. The sinusoidal path from the Canonical space is fitted on the surface of a female subject's back region. The yellow box represents a Cartesian filter, including the points on which the robot will operate. . . . .	73

- 3.4 Adaptation of a showering motion demonstrated by a nursing expert to the back region of a subject. (a) Point-Cloud view from the system's depth cameras and a sequence of positions shown as green spheres, covering the surface of the detected back region. (b) The output of the visual semantic segmentation algorithm, which identifies the region of each body part on the image plane, is used in the planning process. . . . . 75
- 3.5 Execution of a leg showering scenario from the soft robotic arm. (a) User's point of view (b) I-Support depth camera Point-Cloud view. The result of human pose estimation algorithm is transformed to 3D space and depicted with red spheres. The green sphere show the result of the motion planning algorithm. . . . . 76
- 3.6 Perception-based motion planning. A leader DMP point (i,j) from the Canonical space is transformed with bijective transformation  $T_1$  to the point (u,v) of Image space and then with bijective transformation  $T_2$  to the point (x,y,z) of the body-part. From the neighborhood of (x,y,z) we are able to calculate the reference orientation. . . . . 77
- 3.7 **Left:** An obstacle area (e.g. injury depicted with black patch) is detected in the Task space and transformed back to the Canonical space. The Navigation Function potential field is maximized in the corresponding area and the boundary of the workspace. **Middle:** The leader DMP path (red) is defined and an attractive vector field leads to the target point. **Right:** The controllers output is the blue path and is executed by the robot, avoiding the sensitive injured area. After the obstacle avoidance the end-effector's motion converges again the indicated linear motion primitive. . . . . 78
- 3.8 Perception-based motion planning system (implementing a washing sequence). The output of the body-part visual segmentation and the depth data provided by the camera is the input of this system, while the output is the target washing action of the robot's end-effector. . . . . 79
- 3.9 Adaptation of a linear leader DMP (red) on a deformable surface (Point-Cloud view). The normal vector (blue) and the application of a follower periodic washing action is demonstrated on several segments of the path. Perspective and top views of a surface are depicted, subject to several unknown levels of deformation. **Top:** No deformation. **Middle:** Medium deformation. **Bottom:** High deformation. . . . . 80
- 3.10 Problem Statement: Find the obstacle functions based on the collected experimental human like trajectories  $\mathbf{q}(t_m)$ , to ensure that the new controller-based produced motion will always remain within the problem's domain. . . . . 82
- 3.11 Point robot motion planning problem on a 2D workspace that contains one cyclic obstacle. . . . . 83
- 3.12 The relation between the the obstacle's center on x-axis  $x_1$  and the distance of the resulted path from the y-axis  $x_2$ . . . . . 84

- 3.13 Demonstration, Processing, Learning and Reproduction procedures. The **Demonstration** trajectories are performed in physical space by professional nursing personnel. The demonstration data are projected into the 2D canonical space, in which are post-**Processed**. In the **Learning** phase virtual obstacles are learned using the demonstration data and the proposed NF approach. During the trajectory **Reproduction** phase a NF controller is employed to reproduce the washing action. The learned trajectory (red) is then adapted on the visually segmented back region (PointCloud view) of a subject, via the image space. **Top**: A simple showering sinusoidal trajectory is visually recorded, learned and reproduced. **Bottom**: A more complex showering trajectory is obtained from the KIT whole-body human motion database [1], learned and reproduced. . . . . 85
- 4.1 Human shape estimation from monocular camera. Human shape is presented in a textured mesh for different instances of human motion in (a) and (b). A multi-person instance is presented in (c). Detailed views of a mesh representation of human shape in (d) and (e). The depicted representation can easily be integrated in the proposed approach. Images used after written consent of the authors of [3]. . . . . 88
- 4.2 The overall architecture of the proposed planning framework. Visual object segmentation, FEM deformation tracking and local mesh parameterization are included in pre-processing algorithmic steps. These steps provide a mesh representation of the object both in Physical space, in which a stiffness interaction control scheme is implemented, and in 2D parameterized spaces, in which the planning of interactive actions is realized. . . . . 94
- 4.3 A robotic manipulator performing interactive tasks on a hemispherical deformable object. **(a) Left**: The experimental setup used to test the performance of the proposed approach, which includes an Intel®RealSense™ depth camera. **(b) Middle**: View from the system’s depth camera in PointCloud form. **(c) Right**: Tilted view from the system’s depth camera in Point-Cloud form, in which the missing scene information due to occlusions caused by the robot is apparent. . . . . 95
- 4.4 Establishment of bijective transformations between the Static Canonical Space (SCS), the Dynamic Canonical Space (DCS) and the Physical Space with the use of barycentric coordinates between the corresponding triangles. The position  $p_{dc}$  in the  $k^{th}$  active triangle of DCS corresponds to the position  $p_{sc}$  in the  $k^{th}$  active triangle of SCS through the transformation  $\eta$  and simultaneously on the other side to the position  $r_p$  in the  $k^{th}$  active triangle of the physical space through the transformation  $\psi$ . A direct transformation  $\zeta$  from the SCS to the Physical Space can also be defined similarly. . . . . 97

- 4.5 The proposed interaction control framework. **(a) Top Left:** The result of a deformation tracking preprocessing step is the mesh model of the object fitted in the Pointcloud data obtained by the depth camera. Each triangle provides information about the topology of the surface locally depicted with a blue normal vector and green-red tangential vectors. The planned path is fitted on the mesh surface depicted as red dots. The reference pose translated along the normal offset is depicted as a reference frame at a time instance. **(b) Top Right:** The flattened mesh surface is the result of the parameterization preprocessing step. For each time step the parameterization forming the Dynamic Canonical Space is calculated, which tracks the geodesic changes of the object's mesh model. If the object is not actively deforming the DCS equals to the SCS. **(c) Bottom:** At an initial time step the parameterized Static Canonical Space is obtained, in which the robot's reference motions are planned (depicted as a red path). The tangential directions can be computed axis aligned (Group A) or can follow the direction of the principal Gaussian curvatures (Group B). Each planned reference pose is depicted with a reference frame with the blue vector representing the normal direction and the green-red the tangential directions. The planning in the parameterized space includes a normal offset w.r.t. the mesh's surface. . . . . 100
- 5.1 Visualization of experimental results with the rectangular box. The blue arrows represent the normal vector to the surface, whereas the green and red arrows represent the tagential axes to the surface. (a) The rectangular box is stationary and the reference path is fitted on its surface. The orientation is calculated w.r.t the robot base frame. (b) A zoomed and segmented version of the box's front side providing a more clear aspect of the path fitted on the surface. (c) The box is rotated initially w.r.t. the z (blue) axis and then w.r.t. the y(green) axis and the calculated path adapts to this motion. . . . . 104
- 5.2 Experiment on a female subject. (a) Adaptation of the sinusoidal path on the curved surface of a female subject represented with PointCloud data. (b) A zoomed aspect of the experiment depicting in more detail the adaptation of the path. (c) A more clear view of the zoomed path without the PointCloud. . . . . 105
- 5.3 Experiment on a male subject. (a) Adaptation of the sinusoidal path on the curved surface of a female subject represented with PointCloud data. (b) A zoomed aspect of the experiment depicting in more detail the adaptation of the path. (c) A more clear view of the zoomed path without the PointCloud. 105
- 5.4 Perpendicular distance between the Katana end-effector and the experimental subject. . . . . 106
- 5.5 Evolution of the box's rotations and the reference trajectory orientation during (a) the first experiment that involves the static box and (b) the second experiment that involves the moving box. . . . . 107
- 5.6 a) Motion tracking hand-wearable device. b) Thimble with the embedded pressure sensor for activation). . . . . 109
- 5.7 Water pouring clinical validation study with the I-SUPPORT bathing robot installed in a typical bathroom of a rehabilitation clinic at a geriatric hospital. 110



5.8	Upper back region with the six target points for which the soft-arm provided water rinsing. The dark gray outlined cross represents the starting and final position for all operation modes, the dotted arrows indicate the optimal 6-step path for the water rinsing process on the upper back region. . . . .	111
5.9	Percentage (%) distribution of participants' ratings in the different SUS score categories . . . . .	114
5.10	Demonstration, Processing, Learning and Reproduction procedures in experimental validation. The <b>Demonstration</b> trajectories are performed in physical space by professional nursing personnel. The demonstration data are projected into the 2D canonical space, where they are post- <b>Processed</b> . In the <b>Learning</b> phase virtual obstacles are learned using the demonstration data and the proposed NF approach. During the trajectory <b>Reproduction</b> phase a NF controller is employed to reproduce the washing action. The learned trajectory (red) is then adapted on the visually segmented back region (PointCloud view) of a subject, via the image space. <b>Top:</b> A simple showering sinusoidal trajectory is visually recorded, learned and reproduced. <b>Bottom:</b> A more complex showering trajectory is obtained from the KIT whole-body human motion database [1], learned and reproduced. . . . .	115
5.11	Comparison of the NF-based produced trajectory (red line) w.r.t. the carer's demonstration (blue line) in the canonical space, based on the Fréchet distance metric. . . . .	116
5.12	Comparison of the NF-based produced trajectory (red line) w.r.t. the carer's demonstration (blue line) in the canonical space, based on the Fréchet distance metric. . . . .	117
5.13	The experimental setup includes a single Kinect-v2 camera providing depth data and an ARMAR-III robot developed at KIT. . . . .	118
5.14	<b>Scenario I:</b> ARMAR-III wipes a static whiteboard. <b>Left:</b> Execution of a wiping motion, which constitutes of a linear leader DMP path (red) and a periodic circular motion (green), depicted from the system's camera perspective in Point-Cloud view. <b>Right:</b> An obstacle area (e.g. injury depicted with black patch) is detected in the Task space and transformed back to the Canonical space. The leader DMP path (red) leads to the target point. The controllers output is the blue path and is executed by the robot, avoiding the sensitive injured area. After the obstacle avoidance the end-effector's motion converges to the indicated linear motion primitive. . . . .	119
5.15	<b>Scenario II:</b> ARMAR-III is wiping a dynamic whiteboard and a person moves the board. ARMAR-III is holding a yellow sponge, which keeps contact with the surface. The wiping movement is adapted to the surface's motion. <b>Top:</b> PointCloud view of the whiteboard and the robot's end-effector showing instances of the adaptation of the wiping motion with the green trajectory. <b>Bottom:</b> Side camera view of the wiping action indicating with the red arrow the motion of the whiteboard implied by the human. . . . .	120
5.16	Evolution of the reference position and orientation for the wiping motion and the executed robot end-effector position, during <b>Scenario I</b> that involves a static planar surface. . . . .	120
5.17	Evolution of the reference position and orientation for the wiping motion and the executed robot end-effector position, during <b>Scenario II</b> that involves a moving planar surface. . . . .	121

- 5.18 **Scenario III:** ARMAR-III is wiping a male subject's back region. The subject is moving to the right and the robot follows the motion. **Left:** Side camera view of the subject performing a translation to the right. **Right:** Zoomed Point cloud view of the experiment highlighting the adaptation of the wiping motion (green trajectory) to the movement of the subject. Safe distance is kept between the back and ARMAR-III's end-effector. . . . . 122
- 5.19 **Scenario III:** ARMAR-III is wiping a male subject's back region. The subject is moving backwards and the robot follows the motion. **Top:** Side camera view of the subject performing a translation backwards. **Bottom:** Point cloud view of the experiment highlighting the adaptation of the wiping motion (green trajectory) to the movement of the subject. Safe distance is kept between the back and ARMAR-III's end-effector. . . . . 123
- 6.1 Hemispherical model with known relative position and orientation with respect to the robot's base frame. This model is used to derive ground-truth data for position and orientation accuracy evaluation both of the planned and the executed motion by the robotic manipulator. . . . . 126
- 6.2 (a) The experimental setup used to test the performance of the proposed approach, which includes an Intel®RealSense™ depth camera, a Widow-XL robotic manipulator by Trossen Robotics and the top side of a balloon working as a hemispherical model. (b) Zoomed aspect of the Widow-XL robotic manipulator performing an physical interaction task with a hemispherical deformable object. (c) The deformation control mechanism is constructed with air pump providing proper airflow to deform a balloon model. The DC motor of the air pump is controlled via a PWM speed controller, whose potentiometer is controlled by a servo motor. The servo motor is accurately controlled by a Raspberry Pi 3 micro-computer. . . . . 127
- 6.3 Meridian path execution in **Up:** a stationary scenario and **Down:** a deforming scenario. The interactive task is planned in the Static Canonical Space (depicted with a black colored path) and is transformed to the Physical Space with the use of the proposed framework (also depicted with a black colored path). The yellow path is the executed interactive task by the robot. (a) Front view of the stationary experiment. (b) Top view of the stationary experiment. (c) Front view of the deforming experiment. (d) Top view of the deforming experiment. . . . . 128
- 6.4 Circular path execution in **Up:** a stationary scenario and **Down:** a deforming scenario. The interactive task is planned in the Static Canonical Space (depicted with a black colored path) and is transformed to the Physical Space with the use of the proposed framework (also depicted with a black colored path). The yellow path is the executed interactive task by the robot. (a) Front view of the stationary experiment. (b) Top view of the stationary experiment. (c) Front view of the deforming experiment. (d) Top view of the deforming experiment. . . . . 129

- 6.5 Random path execution in **Up:** a stationary scenario and **Down:** a deforming scenario. The interactive task is planned in the Static Canonical Space (depicted with a black colored path) and is transformed to the Physical Space with the use of the proposed framework (also depicted with a black colored path). The yellow path is the executed interactive task by the robot. (a) Front view of the stationary experiment. (b) Top view of the stationary experiment. (c) Side view of the deforming experiment. (d) Top view of the deforming experiment. . . . . 130
- 6.6 Evolution of the Ground Truth (red), the Planned (blue) and the Robot motion (green), during the execution of the **meridian** path in deforming scenario, expressed in (a) polar angle  $\theta$  representation which is indicative for the geodesic distance preservation from the pole of the hemispherical model and (b) radius  $r$  representation which is indicative for the perpendicular relative distance preservation from the surface of the hemispherical model. The orange line is the planned motion with direct transformation from the Static Canonical Space to the Physical Space. This planning strategy fails to follow the geodesic distance changes occurring in the object's surface. . . 134
- 6.7 Evolution of the Ground Truth (red), the Planned (blue) and the Robot motion (green), during the execution of the **circular** path in deforming scenario, expressed in (a) polar angle  $\theta$  representation which is indicative for the geodesic distance preservation from the pole of the hemispherical model and (b) radius  $r$  representation which is indicative for the perpendicular relative distance preservation from the surface of the hemispherical model. The orange line is the planned motion with direct transformation from the Static Canonical Space to the Physical Space. This planning strategy fails to follow the geodesic distance changes occurring in the object's surface. . . 135
- 6.8 Evolution of the Ground Truth (red), the Planned (blue) and the Robot motion (green), during the execution of the **circular** path in deforming scenario, expressed in (a) polar angle  $\theta$  representation which is indicative for the geodesic distance preservation from the pole of the hemispherical model and (b) radius  $r$  representation which is indicative for the perpendicular relative distance preservation from the surface of the hemispherical model. The orange line is the planned motion with direct transformation from the Static Canonical Space to the Physical Space. This planning strategy fails to follow the geodesic distance changes occurring in the object's surface. . . 135
- 6.9 Tracking of a physical point on the surface of a deformable object. The tracking accuracy is measured with the Ascension TrakStar ATC3DGT magnetic tracker with millimeter accuracy. . . . . 136
- 6.10 The interactive trajectory demonstration and transformation procedure procedure. **Left:** The user is shown to move the robot over the surface of a hemispherical deformable model, in a stationary instance with radius  $R=11\text{cm}$ , from the system's camera perspective. **Middle:** Visualization of the interactive trajectory with black line as recorded in the Physical space. At each time step the point of the trajectory is associated with the closest underlying triangle and using the proposed framework it is transformed to the Static Canonical Space. **Right:** Visualization of the interactive trajectory with black line transformed in the Static Canonical Space. . . . . 138

- 
- 6.11 Evolution over time of the Demonstrated Motion (blue) in the 3D Physical Space, compared to the reproduced motion over a stationary hemispherical model (with the same radius  $R=11\text{cm}$  for both motions). . . . . 139
- 6.12 Measurement of contact forces along the vertical direction (red arrow) to the object's surface with an ATI Mini-40 F/T sensor. The planning of a contact task is implemented in our approach by setting the normal offset  $d$  to negative values, instructing the robot to move below the object's surface. 140
- 6.13 Measurement of contact forces along the vertical direction to the object's surface for a range of normal offset  $d$ . A contact task is planned such that the reference orientation is vertical to the surface and the normal offset is linearly decreased until the 6 cm value, for the stationary scenario for hemispherical radius  $R_{max} = 11\text{cm}$  and  $R_{min} = 10\text{cm}$  (dashed blue and red lines respectively) and for the deforming scenario (green solid line) with deformation rate of 0,25Hz (left) & 0,5Hz (right). Several gain values for the stiffness controller were tested and a representative behaviour is shown for relative gain value  $k = 1$  (top) and  $k = 1.8$  (bottom). . . . . 142

# List of Tables

5.1	Mean Absolute Error in Orientation and Mean Distance . . . . .	106
5.2	Differences in the task effectiveness (coverage, step effectiveness) between the shared control and tele-manipulation modes . . . . .	112
5.3	Differences in the user satisfaction between the different operation modes . . . . .	113
6.1	Planning and execution accuracy errors for three interactive trajectories (Circular, Meridian, Combined), expressed in spherical coordinates, $r$ (cm), $\theta$ ( $\text{rad} \times 10^{-2}$ ), $\phi$ ( $\text{rad} \times 10^{-2}$ ), for the stationary object scenario with spherical radius values $R_{\max} = 11$ cm and $R_{\min} = 10$ cm. The planning errors of the current interactive mesh approach (denoted as <b>IMP</b> ) are compared to the planning errors of our previous direct visual planning approach (denoted as <b>DVP</b> ) and to the planning errors of our previous direct visual planning approach with occlusion from the robot motion (denoted as <b>DVPO</b> ). The robot execution errors (i.e. evaluated on the path actually executed by the robotic manipulator) are denoted as <b>Robot</b> . . . . .	131
6.2	Planning and execution accuracy errors for three interactive trajectories (Circular, Meridian, Combined), expressed in spherical coordinates, $r$ (cm), $\theta$ ( $\text{rad} \times 10^{-2}$ ), $\phi$ ( $\text{rad} \times 10^{-2}$ ), for the deforming object scenario with deformation rate $f = 0.25$ Hz & $f = 0.5$ Hz. The planning errors of the current interactive mesh approach (denoted as <b>IMP</b> ) are compared to the planning errors of our previous direct visual planning approach (denoted as <b>DVP</b> ) and to the planning errors of our previous direct visual planning approach with occlusion from the robot motion (denoted as <b>DVPO</b> ). The robot execution errors (i.e. evaluated on the path actually executed by the robotic manipulator) are denoted as <b>Robot</b> . . . . .	132
6.3	Physical point tracking errors presented along the axes of the Physical Space. The tracking error is calculated as the relative position between the magnetic tracker's probe attached on the deformable model and the tracker's probe attached on the robot's end-effector. . . . .	136
6.4	Motion reproduction errors of the demonstrated interactive trajectory, expressed in spherical coordinates ( $r, \theta, \phi$ ), for the whole duration of motion (RMSE $\pm$ standard deviation of the error values). The motion planning errors of the proposed approach (denoted as <b>IMP</b> ) are distinguished from the robot execution errors (evaluated on the trajectory actually executed by the robotic manipulator, denoted as <b>Robot</b> ). . . . .	138



# Chapter 1

## Introduction

Advanced countries with well organized and modern health care systems tend to become aging societies, according to World Health Organization's research on health and ageing [4]. The percentage of population with special needs for nursing attention (including people with mobility impairments) is significant and due to grow rapidly in the coming years. More specifically, the total population of older people (ages 65 and over) was 0.9 billion in 2015 and is expected to reach 1.4 billion by 2030 and 2.1 billion by 2050. The vulnerability of the elderly is most frequently reflected in cognitive, perception, stability and even functional disability problems [5]. Health care experts are called to support these people during the performance of Activities of Daily Living (**ADLs**) such as dressing, eating and showering, inducing great burden both to the families (mostly financial) [6] and to the caregivers [7]. Great research effort has been spent over the last decades [8, 9, 10] on studying and classifying the functional disabilities of older adults and associating the latter with basic factors of morbidity and mortality. Personal care (showering or bathing), which is crucial for a person's hygiene, is included among the first ADLs, which incommode an elderly's life [11] and ADL difficulties in bathing or showering represent the strongest predictor of subsequent institutionalization in older adults [12]. In addition it is among the last that are regained during post-surgery recovery. Older adults require assistance in bathing or showering more frequently than for any other ADL [13], since it has increased mobility requirements. Furthermore, since bathing is a highly intimate ADL, the wish for independence from personal bathing assistance of caregivers, as long as possible, is not unusual in older adults [14]. This clearly suggests that support in bathing activities, as an early marker of ADL disability, will foster independent living for persons prone to loss of autonomy and relieve the caring and nursing burden of the family, domiciliary services, medical centers and other assisted living environments. Therefore, as life expectancy continues to increase, care for the elderly is becoming an important issue in modern societies, given the shortage of nursing staff [15]. Therefore, the use of technology for medical and daily life support is vital. Robotics seems to naturally fit into the role of assistance, as it can incorporate features such as support for posture and stability, communication, health care, etc. This need has led to the emergence of a new field in robotics, that of Social Robotic Assistance Systems.

### 1.1 Motivation

Assistive Robotics is the main source of inspiration for this work. Past definitions of assistive robotics referred to robots that assisted people with physical disabilities through

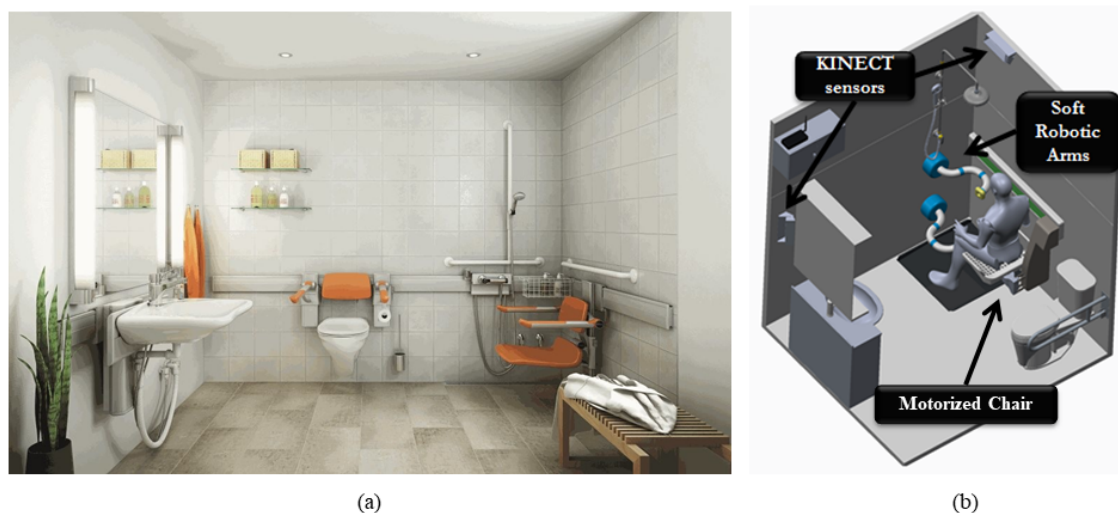


Figure 1.1: The envisioned transition from a (a) standardized clinical bathroom to (b) a bathing environment equipped with appropriate robotic and sensorial infrastructure.

physical interaction. The scope of this definition is no longer appropriate, since there is a large variety of robots that assist through non-contact interaction. Over the last two decades research on robotic assistive systems has included physical rehabilitation robots, robotic wheelchairs and other mobility assistance systems, robotic manipulators for people with disabilities, but also educational robots [16]. Moreover, the users' requirements for social interaction with the robots has led to a wider family of robotic systems, socially assistive robots. Therefore, an adequate definition of an assistive robot is a device that can collect and process sensory information and perform actions that benefit people with disabilities and older adults in the activities of their daily lives. These activities include: bath & shower, dressing, food preparation & feeding, mobility, personal hygiene & grooming, housekeeping, drug taking, money management, shopping, communication, home use, technology, Exercise, Reading, Relaxing, Socializing, etc. Social Robotics Assistance Systems aim to achieve effective social interaction with the user in order to provide assistance and achieve measurable improvement in recovery, rehabilitation, education, etc.

Bathing represents one of the most complex ADLs [17] for which older adults require personal assistance more frequently than for other ADLs. However, it is complex not only in terms of functional abilities, but also considering several other aspects as nicely presented in [18]. More specifically, there are factors affecting the bathing activity related to the person, such as physical (e.g., strength, balance, pain, limited range of motion), psychological (e.g., depression), attitudes and preferences about bathing, and cognition. Other factors are related to the environment, both physical including safety devices, bathroom hazards and materials, and social, focusing on the support from the family or caregivers, or related to the bathing task itself, such as specific sub-tasks, timing and actions required to perform the task. Apart from the aforementioned high level factors of analyzing the bathing activity, it is highly important for maintaining an individual's skin integrity and personal hygiene, thus reducing also the potential for infections and disease [19]. It also serves the social purpose of maintaining an acceptable standard of cleanliness for social interactions [20].

From the perspective of a caregiver, bathing of older people or people with a disability can be a time consuming and physically and psychologically demanding task [21]. At



the same time, some older adults might wish to be independent from personal assistance in bathing as long as possible [20], since it is considered by most of them a sensitive and intimate activity. A person's dependency in bathing and the caregiver burden in providing bathing assistance can be reduced through the use of assistive devices (Fig.1.1), such as grab bars, shower seats, bath chairs, and nonskid mats. However, these bath aids do not support the entire sequence of bathing tasks (i.e., bathing transfer, water rinsing, soaping, scrubbing, drying) and thus may often fail to enable users to independently complete the entire bathing process [22]. Furthermore, the evidence on the effectiveness of bath aids is still unclear [23]. In this context, assistive bathing robots that can support older adults in several bathing subtasks have been proposed [24].

The main motivation of this thesis is the use of intelligent robotic systems, which can monitor and understand the patient's state, infer the patients' intentions and needs, and decide independently to perform assistive actions during the entire bathing sequence. Such assistive bathing robots could help to preserve independence and privacy of older adults, but also reduce the burden of caregivers in providing bathing assistance and allow them to spend more time on other care tasks, which could increase their overall productivity and quality of care. A bathing robotic assistant needs to integrate important scientific and technological developments of multiple research fields. The main idea is to develop robotic assistants which can operate a) proactively and autonomously, performing specific human monitoring and decision making functions after recognizing user behavior patterns, and b) adaptively and interactively, analyzing and integrating the knowledge and experience of the nursing staff with multimodal modeling and learning, for both proper execution of the bathing sub-tasks and intuitive human-robot communication strategies. The reduction of cognitive effort for the operation of an assistive robot, especially for an elderly user, is crucial, not only for its effectiveness in task accomplishment [25], but also the acceptance and satisfaction of the user with the robot [26].

At the heart of this research targeting and more specifically within the context of the I-Support research project (H2020-EU.3.1.4. "I-SUPPORT - ICT-Supported Bath Robots" - 643666) an innovative, modular, ICT-supported robotic system was developed, depicted in Fig. 1.2, which successfully assists frail older adults to safely and independently complete various physically and cognitively demanding bathing tasks, such as properly washing their back and their lower limbs. The components of the I-Support system are the following:

- **Motorized Chair:** A motorized chair has been employed inside the shower to effectively assist the older adults during sit-to-stand and stand-to-sit tasks and for safely transfer from the exterior to the interior space of the shower cabin.
- **Human-Robot Interaction:** For the purpose of human-robot communication and perception, the I-Support system was equipped with Kinect V2 RGB-D cameras. These sensors are frequently used for visual analysis in assistive robotics [27], as they are inexpensive, reliable and simple to waterproof. This multi-view setup was designed so as to be able to deal with two technological tasks of the I-Support project, namely: a) audio-gestural command and action recognition and b) body pose estimation for robotic manipulation.
- **Context Awareness System:** Additional sensorial data coming from different types of sensors are analyzed by the system, in order to have full environmental awareness. More specifically, useful data regarding water flow and temperature are provided to the system (Fig. 1.2(a)), together with air temperature, humidity and illumination (Fig. 1.2(c)), which are environmental conditions indicative for the

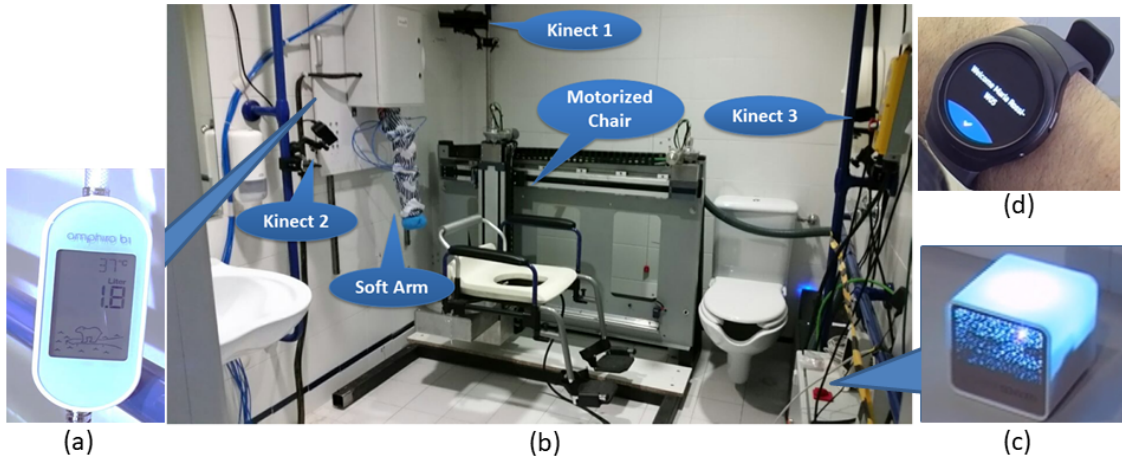


Figure 1.2: Installation of the I-Support system in clinical environment (Fondazione Santa Lucia (FSL) Hospital in Rome, Italy) for experimental validation. The devices constituting the overall system are presented. (a) Amphiro b1 water flow and temperature sensor. (b) General aspect of the system showing the Motorized Chair, the Soft Robotic Arm and the installation of the Kinect sensors (for audio-gestural communication). (c) Air temperature, humidity and illumination sensors by CubeSensors. (d) Smartwatch for user identification and activity tracking.

user's safety and comfort. A smartwatch similar to the one presented in Fig. 1.2(d) is integrated for user identification and activity tracking purposes.

- **Soft Robotic Arm:** A soft-arm (Fig. 1.2(b)) has been developed to assist elderly people in bathing tasks. Soft manipulators can be considered intrinsically safe thanks to the actuation technologies they are made of. One of their main features is their compliant body that can deform passively to adapt to environment changes, thus reducing the complexity of active control.

Among the multitude of research, technological and scientific issues that emerged from the design and development of I-Support system, this thesis focuses on the development of a reactive motion planning method which calculates the motion behavior of a robotic manipulator's end-effector, operating over a curved deformable surface. Such surfaces characterize the human body parts, which are systematically or randomly moving and deforming (e.g. due to users' breathing motion or due to users' voluntary motor activity). In particular, point-cloud data from the system's depth cameras, combined with enhanced visual perception data for area of interest segmentation, are used as input to the method. The design of robotic surface tasks has to adopt the expertise of professional carers for bathing sequences and appropriate motions, in order to achieve natural, physical human-robot interaction.

## 1.2 Problem formulation

In order for an assistive bathing robot to be capable of executing the whole bathing sequence, it is necessary to process and interpret multi-modal information from a variety of sensors mounted in the application environment (bathroom space). More specifically, the rich visual data, obtained from three Kinect v2 sensors of the I-Support system, has to be segmented into areas with rich semantic information, such as the human body



(a) Design of Soft-Robot performing Scrubbing (b) Design of Soft-Robot performing Showering

Figure 1.3: Design of a soft-robotic arm performing bathing actions.

parts or obstacles, resulting to full scene understanding. Especially for the bathing tasks, which require physical interaction of the robotic manipulator with the human body (e.g., showering or scrubbing), as depicted in Fig. 1.3, on-line accurate scene perception is crucial for appropriate action planning. In more detail, the robot should be able to execute showering or scrubbing tasks and at the same time to be compliant and safely interacting with with the body part.

Furthermore, those interaction tasks are required to be executed according to nursing expert's demonstration and directives and simultaneously according to user's preferences, to achieve proper and human-friendly motion behavior. This procedure might raise some requirements for each task, in terms of contact forces, execution time and motion complexity, which should be met by the motion planning strategy. More specifically, this work aims to provide a solution for the following problems:

1. Development of a motion planning algorithm, which uses the visual feedback from a depth camera and the corresponding scene perception information, in order to adapt predefined, time scalable trajectories on curved and deformable surfaces, such as the human body parts, while at the same time avoiding the interaction with obstacle areas, such as injuries.
2. Deployment of an integrated system, which can learn and encode complex, human-friendly interaction trajectories from demonstration of experts in elderly nursing care and apply the learned actions on real-life scenarios, imitating the human washing actions.
3. Apart from the human-friendly execution of interactive tasks, the applied contact forces are important for proper physical interaction tasks as well. Therefore, a system that can regulate the contact forces during a physical interaction task on a deformable surface is required, which should not necessarily rely on the use of force feedback.
4. Beyond the key motivation related to the development of efficient robotic assistive devices, a central goal of this thesis, in more general terms, envisions the development of a fully integrated perception-driven motion planning framework for effectively controlling a robotic manipulator in the execution of interactive tasks on the surface of a deformable object, efficiently handling both active and passive deformation conditions.

## 1.3 Related Work

### 1.3.1 Assistive Nursing Care Robotic Systems

During the last decades, the robotics society is attempting to tackle this challenge of unattended nursing by developing flexible and modular assistive devices that aim to cover the needs for support of everyday tasks involved in the caring of patients and elderly with moderate/low mobility, in both clinical and in-house environments. Regarding the latter, many innovative solutions have been developed, which can be mounted on a wheelchair or on static structures of the house. In particular, the system KARES-II is presented in [28], which consists of a mobile and a wheelchair platform with a cable-driven robotic arm with active compliance and visual servoing capability integrated with various human-robot interfaces. In addition, the MATS climbing service robot is developed in [29], which is a lightweight 5-DOF manipulator with on-board control and communications systems, able to move around the house climbing on multiple docking stations and perform assistance tasks such as eating and shaving. Various nursing tasks which involve human-robot physical interaction require sophisticated sensory infrastructure and control strategies. For example, in [30] the development of a four finger robot hand with a variable stiffness joint with simultaneous sensing of multidirectional external forces is described. This joint is made of two types of silicone rubber and enables safe and stable physical interactions with humans. Bedridden patient transfer is a very physically challenging task in nursing care, the burden of which is reduced by two robotic solutions. In [31, 32], Mukai et al. have developed a prototype robot RIBA, with human-type arms equipped with tactile sensors both for guidance and human posture adjustment, capable of performing heavy physical tasks requiring human contact. Similarly, in [33] a humanoid mobile robotic nurse assistant (RoNA) with bimanual dexterous manipulators, is presented.

On the other hand, several skincare and washing tasks require much more delicate actions by the the robot. A three finger system driven by a 3-DOF parallel translational mechanism is developed in [34], in order to perform skincare actions on the human body. The tree finger mechanism is attached on a seven-DOF Mitsubishi Heavy Industries PA-10 manipulator and is accompanied by a low-cost stereo vision camera for human body shape estimation. A multi-fingered robot [35] is also employed for washing hair in hospitals or care facilities. Several mechanisms with different end-effectors are controlled by compliance control, for providing an appropriate sense of pressure. A humanoid robotic nurse system named Cody [36] was created to assist individuals with disabilities. It was designed to support human-robot interaction tasks with an emphasis on tasks relevant to healthcare, such as bed baths. Automated showering assistance is provided by two commercially available solutions. Oasis system [37] has multiple shower jets and soap solutions distributed properly around a seat, achieving effective washing and rinsing of body parts without the risk of falls. To minimize the risk of fall, Poseidon system [38], apart from the showering system, is equipped with a motorized chair, for safe entrance into the shower cabin. On the downside, both of these solutions completely lack physical interaction with the user and therefore lack some basic functionalities of the bathing sequence such as scrubbing and wiping the senior.

The I-Support platform, developed in the context of a European Union funded project<sup>1</sup>, constitutes an innovative, modular, ICT-supported robotic system that successfully assists elderly people, to safely and independently complete various physically and cognitively demanding bathing tasks, such as properly washing their back and their lower limbs.

---

<sup>1</sup>I-SUPPORT EU Project, Grant number: H2020-643666, <http://www.i-support-project.eu/>

The main contributions of the project relate to the development and seamless integration of novel cognitive human-robot interaction technologies and to the evaluation of these technologies, as individual modules as well as an integrated assistive robotic platform as a whole, through a series of clinical validation studies in realistic scenarios and under real operating conditions. These technologies include: human activity monitoring and recognition, adaptation of a motorized chair for safe transfer of the elderly in and out the bathing cabin, a context awareness system that provides full environmental awareness, as well as a prototype soft robotic arm and a set of user-adaptive robot motion planning and control algorithms. Key features of this assistive robotic platform are supported by a multimodal modeling and learning system, which aims to enhance the human-robot communication making it natural, intuitive and easy to use, addressing aspects of smart assistive HRI.

### 1.3.2 Interactive Motion Planning Methods

Motion planning strategies should take into account a large variety of aspects of robotic interactive tasks, such as surface coverage, obstacle avoidance, surface perception and trajectory adaptation to different surfaces. The spectrum of applications, which involve a robotic manipulator executing surface interactive tasks with the environment using sensorial feedback, is wide. Application examples range from automotive industry, in which industrial manipulators are responsible for transferring or spraying actions on car parts [39] to service robotic systems interacting with household environment [40]. Another interesting application field concerns robotic surgery, particularly introducing semi-autonomy in specific tasks such as the beating heart motion compensation in robot-assisted cardiac surgery [41]. Considering the accuracy of task execution, many researchers have focused not only on deriving analytical inverse kinematics for a 5-DOF robot [42], but also on optimizing the null space of a redundant manipulator [43]. In the latter paper, the PR2 robot is confronted with the task of cleaning the previously known surface of a small car, implementing a coverage strategy, which is optimized with respect to cost functions defined in the joint-space. The control and trajectory tracking with obstacle avoidance on known surfaces is also addressed in [44], with the use of a Navigation function controller, which steers a manipulator while achieving limited joint velocities.

Various sensors are used as feedback for interactive task execution, such as capacitive sensing technique for human limb estimation [45]. More specifically, a multielectrode capacitive sensor, which is able to sense the limb through fabrics or wet cloth, is mounted on the end-effector of a robot and is combined with a neural network model to estimate the position of the closest point on a person's limb and the orientation of the limb's central axis. The robot is able, using these estimates, to plan a motion of its end-effector with respect to the limb and perform dressing and bathing tasks. Another bathing robot presented in [36], uses laser range data with a camera, both mounted on a tilting mechanism, to estimate the shape of the body part and at the same time locate a colored stain, in order to properly clean the designated area, using impedance control. A low cost stereo camera is used for human body part shape estimation, in a skincare interactive task proposed in [34]. The measurement of the body shape is performed in the beginning of the procedure and the measured area is divided into small segments, represented by a point. The robot's path is planned by connecting the representative points, while the depth data is interpolated by a spline function. In [46], Leidner et al. have used visual feedback and a generic particle distribution representation of different materials, in order to design proper motion plans for surface wiping actions and in [47] contact detection is used in combination with their

previous approach for task performance inference, incorporating appropriate re-planning strategies. Dragging actions for dirt removal are also planned in [48], using visual detection of the dirt distribution on a planar surface. The authors propose a stochastic action plan, with replanning every few actions exploiting new perception information. Adaptation to new environmental conditions is implemented with a learning heuristic that updates a rule model, used for planning. Scene modeling using a Kinect sensor and KinectFusion algorithm is employed in [49] for calculation of obstacle-avoidance objective functions in a GPU implementation.

Motion planning strategies for soft robotic manipulators are totally different from the rigid ones, since the large number and the complexity of possible configurations have to be taken into account during a task execution. The Kinect sensor is also used as a feedback in a planar setup [50], which includes a three segment continuum manipulator, for planning grasping actions of various objects. In particular, the objects and obstacles are visually detected and the feasible whole-arm wrapping around grasping and intermediate avoidance configurations are calculated. A reactive motion planning algorithm is proposed in [51], which is based on potential fields and achieves real-time dynamic obstacle avoidance for tendon-driven single-segment manipulator. Moreover, an electromagnetic sensor provides the manipulator's tip position and the estimation of the pose along its body is implemented with a non-linear observer based on an Extended Kalman Filter. A modification of this algorithm is proposed in [52], in such a way that makes it applicable to a constant-curvature kinematic model. Additionally, the mechanical constraints of the manipulator are taken into account by introducing a potential field for the actuator space, improving the smoothness of its motion.

### 1.3.3 Interactive Motion Learning Methods

Interactive tasks with the environment are usually very complex for robots, owing to their diversity and high variability of execution conditions. Consequently, many researchers have shifted their attention to learning-based approaches, to handle these problems. Learning a complicated motion from human demonstration includes both choosing appropriate motion representations and corresponding learning strategies. There are many methods that implement Learning from Demonstration (LfD) with the most common being: Gaussian mixture model (GMM), Hidden Markov model (HMM), Gaussian mixture regression (GMR) and Dynamic movement primitives (DMPs). A sum of weighted Gaussian kernels is used in [53] for learning rhythmic motion patterns, mapping an oscillator signal to the desired movement. The human demonstration is recorded via kinesthetic teaching to a robotic manipulator and an algorithm autonomously combines the learned movement, in order to wipe a planar surface. Kinesthetic teaching is also employed in [54] to develop an integrated method for a small humanoid robot to clean a whiteboard. The authors use an extension of DMP, described as superposition of basis motion fields, to encode the skill and extract variation and correlation information across demonstration data. A set of virtual attractors, learned by weighted least-squares regression, is used to reach a target. A combination of a modified HMM representation with a Gaussian regression is used in [55], to generate a continuous window wiping trajectory with online incremental kinesthetic learning.

Several methods of on-line robotic coaching are surveyed in [56] using second-order and third-order DMPs. The weights of a periodic DMP are adapted on-line, through different coaching methods, including visual or stiff force or compliant force feedback. The same extension of DMP is used in [57], to generate a sequencing of discrete motions, by modifying

the Gaussian kernel functions, for a wiping task. On-line adaptation of a periodic DMP for wiping tilted surfaces is presented in [58] and later in [59]. The robot initially establishes contact with a given surface, maintaining a predefined force of contact through force feedback. Using this type of feedback, the robot is able to comply with the constraints set by the environment and at the same time the human can act as tutor, modifying and correcting parts of the trajectories through physical contact, or through predefined gestures, transferring reliably knowledge to the robot, without the need of learning new trajectories from scratch. In [60] a predictive learning mechanism is proposed, which allows tightly coupled dual-agent systems (like human-robot or robot-robot) to learn an adaptive, sensor-driven interaction based on DMPs and execute collaborative tasks. Learning of interactive tasks by observing human-to-human engagement is proposed in [61] with interaction primitives build on the framework of DMPs by maintaining a distribution over the parameters of the DMP, learning the inherent correlations of cooperative activities. An alternative method for LfD is proposed in [62] based on Navigation Function approach with application to anthropomorphic grasping. In this approach, the authors propose a gradient descent method to construct an obstacle space which, when navigated using a Navigation Function based approach, produces trajectories similar to the learned trajectories. It is obvious from the papers presented above, that LfD techniques have been successful in mimicking human behavior and generating complex interactive trajectories. However, they have limited adaptability to interact with new environments without human intervention. Therefore, researchers have tried to enrich the learning datasets and turn to supervised learning techniques.

Supervised Learning is the machine learning task that directly derives a mapping between an input and an output based on a labeled set of training data. Most frequently, it is used in classification problems or regression processes, in order for the learned data to apply suitably to unseen situations. Representative methods of this type in robotic skill learning are the Artificial Neural Network (ANNs), Gaussian process regression (GPR) and support vector machines (SVMs). In [63], the authors combined learning from demonstration with supervised learning, to teach a humanoid robot to perform different types of wiping actions depending on the materials on the table. The authors developed an architecture of Convolutional Neural Networks (CNN), collecting data for training with the use of kinesthetic teaching. An imitation learning approach is proposed in [64], which allows teaching of a robot to observe, generalize, and reproduce interactive tasks from multiple demonstrations. The instructor manipulates several objects and the relations between its body parts and objects in the scene are learned. Then, proper actions are estimated by maximizing the joint probability distribution represented by a dynamic Bayesian network (DBN) training. A neural network controller with differential extrinsic synaptic plasticity was developed in [65] and applied to a muscle-tendon driven arm-shoulder system. The input data to the network comes from a force sensor attached to the robot and the training activation function is a h-tangent. The output consists of robot arm motion patterns for wiping a table.

Similarly in [66], the authors used hand-labeled force data to train a classifier, which is able to distinguish different contact events. The dataset comprised of 460 real-world robot wiping episodes using a table-mounted robotic manipulator equipped with a force sensor, training multidimensional time-series shapelets. A relation between the object and action is investigated in [67] and an internal nonparametric continuous model is generated using Support Vector Regression (SVR). A learning cycle is suggested linking object properties (softness and height) and action parameters defined by the interactive task and build the model from visual sensor data. This model can be used for predictions on the expected

effects for novel objects and consequently constrain the parameter exploration. Another class of objects, which presents large variability to interact with, comprises deformable objects. Langsfeld et al. [68] used a bi-manual robot setup for cleaning of deformable objects, in which one arm holds the part to be cleaned, while the other holds the cleaning tool. During interaction with the object, force and deflection data from the tool are collected, to build a stiffness model. The stains on the object are detected using visual feedback, with a k-means classifier, deriving three clusters as clean, dirty and background on image pixels. Normal forces applied to the surface during cleaning with an appropriate tool are predicted with the use of GPR. The same group of authors applied similar approach in [69], focusing on deriving proper planning algorithms for automated cleaning of hard paint stains on curved surfaces and rust on metal surfaces. Supervised learning shows some promising results for generalizing interactive tasks for new environmental conditions, but the training data usually overfit to the conditions that were collected.

### 1.3.4 Interactive Contact Force Regulation Methods

Direct interaction of a robotic device with the environment constitutes a research topic that the robotics society has been addressing for many years. There is a large literature variety in terms of control techniques, many of which rely on hybrid force/position schemes for rigid robotic manipulators [70]. Taking advantage of the abilities of redundant 7-DOF manipulators in decoupling force and position task execution, the authors of [71] proposed an impedance control scheme implemented as an outer-inner loop controller. The inner-loop is calculating the proper joint torque using joint-space inverse dynamics, whereas the outer-loop controller applies force feedback to control the end-effector. On the other hand, the on-line calculation of joint torques problem of a redundant robot is approached recently in [72], using projection recurrent neural networks (RNN). The reconstruction of motion-force control and redundancy resolution problem formulates it as quadratic-programming problem with an additional task of minimizing the joint torques. Then a convergence provable RNN is established to solve the modified problem online, satisfying multiple inequality constraints. Ortenzi et al. suggested a projected operational space dynamics solution [73], in order for a humanoid robot to perform various interactive tasks with proper contact force. This control technique, which uses force/torque sensor as feedback, minimizes joint torques by exploiting the environment contact constraints and enables full decoupling of motion and force control. However, in many cases force feedback is not available on the wrist of a robot, measuring the end-effector contact forces. For example, in the case of a standing humanoid robot [74] during wiping a vertical whiteboard, the decoupling between force and position control is implemented on the lower and upper body respectively. More specifically, the arms of the upper body are controlled with the use of a simple proportional derivative (PD) controller for motion tracking purposes, whereas a force tracking controller is proposed for the ankle of the lower body, which calculated the hand force using a foot pressure sensor. In another example on a robotic manipulator [75], the authors propose an algorithm, which combines the interoceptive information obtained from joint torque sensors with time delay estimation, to estimate external force exerted on the end-effector. The estimator, which does not require an accurate dynamics model of the robot, is used for a table wiping task.

Despite the large research effort presented above, interaction with a human being is a much more delicate action and is considered risky to be executed by a rigid robotic manipulator, even if it is equipped with the most sophisticated force/impedance control schemes. On the other hand, the advantage of soft robots [76] lies on their inherent or



structural compliance, which gives them the ability to actively interact with the environment and undergo large deformations. The term soft robotics is not only used to state that the devices are made of soft materials, but also to underline the shift from robots with rigid links (even hyper redundant ones [77]) to bio-inspired continuum robots. This shift is suggested to be gradual by the authors of [78], presenting a novel manipulator with variable stiffness links. In particular, they use a combination of fabric materials and silicone based structures for the development of stiffness-controllable links that are pneumatically actuated. The air pressure inside the structure regulates the stiffness of the links and the pressure readings from the pressure sensors inside the regulators can detect collisions between the manipulator body and a human. Another inflatable robotic manipulator is developed in [79], intended for safe human-robot physical interaction. It is built using membrane material and McKibben actuators and has contact detection capabilities based on its structural model. A contact reaction scheme is developed as well, which can cause the manipulator to move away from the external agent or to execute a wiping motion using the environment reaction forces. Contact sensing is achieved in [80] via a 3D printed soft skin with a built-in airtight cavity. In this cavity the air pressure can be sensed, enabling the robotic system to have very gentle physical interaction with soft objects. One basic problem of soft robots is the control of position and stiffness at the same time, given the available actuation [81]. Gillespie et al. in [82] use a Model Predictive Control (MPC) scheme to simultaneously control stiffness and position for a pneumatically actuated soft robot. By including the pressure in the soft robot actuation chambers as state variables, they improve their linearized state space model, achieving better performance in all control aspects.

## 1.4 Thesis Approach

In the context of a whole body bathing robot development, natural and effective human-robot physical interaction is a key characteristic both from system safety and from user acceptance point of view. To this end, accurate tracking of demonstrated trajectories from professional caregivers is required with simultaneous avoidance either of obstacle areas on user's body parts (such as injuries) or other body parts (such as the hands) of the user that may interfere to the robot's motion. Additionally, user friendly robotic action is not only achieved with proper execution of motions demonstrated by caregivers but also with on-line adaptation of the motion properties according to user preferences. In user's preferences are also included the contact forces experienced during the execution of contact tasks such as wiping or scrubbing.

Therefore, during the course of this thesis, a motion planning and adaptation system is developed, which uses the constant user state monitoring information obtained from the cameras and allows the robot to operate reactively to user's motion. More specifically, an on-line motion adaptation algorithm was proposed, which used body part segmentation visual data combined with Kinect camera's depth measurements to establish spatial transformations and simplify the motion tracking problem. For the latter, a trajectory tracking controller is used, which ensures globally uniformly asymptotic convergence to the demonstrated motions, while at the same time avoiding restricted areas, such as sensitive skin body areas. Using this approach, the washing actions can be adapted to various user's body parts size (e.g. back and legs) and surface shape.

Regarding the washing action learning from professional caregivers, a new dataset of washing actions was created, enhancing the publicly available KIT whole-body database [1]. A great variety of actions was recorded with the use of motion capture system, placing

appropriately markers to the washing tools, the caregiver and the user, as depicted in Fig. 1.4. These data were analyzed in a post-processing procedure and properly decomposed into simpler primitive motions, such as discrete and periodic, in order to enable robotic execution. The fusion of such primitive actions with different parameters (e.g. duration, amplitude e.t.c.) can reproduce more delicate and human-friendly actions. Even though a large variety of washing actions was recorded, each one of them was not demonstrated multiple times. Therefore, we compared several motion learning strategies from the literature and proposed two learning from demonstration methods, which can easily encode and generalize complex motions from a few demonstration examples.

Another important aspect of human-robot physical interaction are the contact forces exerted by the robot to the human body. However, the integration of a conventional 6-DOF force torque sensor to the structure of a soft-robotic arm operating in a highly humid bathroom environment is unattainable. Consequently, robotic control techniques without the use of force feedback were investigated, which are based on stiffness control of the robot. Simultaneously, in order to achieve high precision both on task execution and force, enhanced environment perception abilities had to be incorporated to the system. Deformable object modeling with mesh structures has been a common practice in computer graphics society for decades. Additionally, the development of computer vision techniques that can accurately determine the shape of the human body from a monocular camera [3, 83], has provided a wide spectrum of visual perception abilities to robotic devices. Capitalizing on recent advances regarding real-time deformation modeling, a fully integrated perception-driven motion planning framework is proposed for effectively controlling a robotic manipulator when executing interactive tasks on the surface of a deformable object. The proposed framework combines 3D perception and on-line deformation modeling, with real-time motion planning and interaction control, enabling the system to efficiently handle both active and passive deformation scenarios. The core of the approach is based on real-time FEM deformation tracking and efficient local mesh parameterization which, combined with stiffness control of the robotic manipulator, enables accurate reactive planning of interactive trajectories and contact force regulation on the surface of a dynamically deforming object, even in the presence of visual occlusions.

## 1.5 Contributions

The contributions of this thesis span a wide spectrum of research on interactive task planning with emphasis on reactive robotic action planning on the surface of deformable objects, such as the human body parts. Several motion planning methodologies for robotic

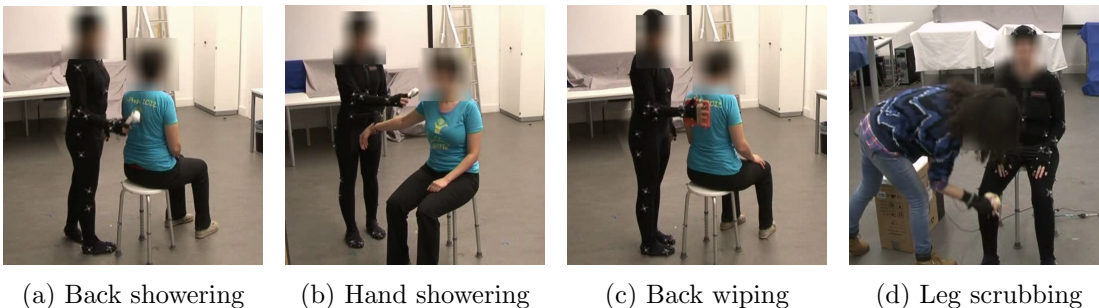


Figure 1.4: Examples of washing actions demonstrated from professional caregivers, available at KIT whole body database [1].

manipulators in interaction with their environment were investigated both analytic and learning based.

In the development process of a whole-body bathing robotic system, a motion planning algorithm was developed, which uses the visual feedback from a depth camera and the corresponding scene perception information, in order to adapt predefined, time scalable trajectories on curved and deformable surfaces, such as the human body parts, and at the same time avoid the interaction with obstacle areas, such as injuries. The proposed algorithm was tested both in lab conditions and in a real clinical environment with elderly users in both dry and humid conditions. A clinical validation study was conducted, which focused on the human-robot interaction aspects of the use of a bathing robot. More specifically it investigated the ability of elderly users to tele-operate the robot without direct visual contact and to complete a washing task with the motion adaptation assistance of the developed algorithm and without it. The majority of the users found the tele-operation without motion adaptation assistance very difficult and the operation of the system with it satisfying.

Furthermore, a database of washing actions demonstrated from professional caregivers was recorded with the use of optical motion trackers systems (Vicon), analyzed and decomposed into primitive actions appropriate for robotic execution. Using the analyzed data an integrated system based on Dynamic Motion Primitives approach was developed, which can learn and encode the demonstrated actions, imitating the human washing actions. The learned motions can then be adapted to the user's body parts compensating their motion or deformation and their execution parameters can be on-line modified in order to meet the user's requirements. This method was experimentally validated with the use of a humanoid robot, executing a wiping scenario. With the use of the same database, an alternative LfD method was proposed based on Navigation functions, in order to capture the way an expert clinical carer executes the bathing activities by means of constructing repulsive potential fields ("virtual obstacles"). Demonstration of bathing trajectories are realized in 3D physical space, and these trajectories are then transferred to a 2D spatially normalized space by establishing appropriate transformations. In this space, a set of virtual obstacles is calculated so that the trajectory produced by a NF based navigation resembles the human trajectories, in effect, the human trajectory is represented in the virtual obstacles.

In order to increase the accuracy of the interactive task planning and regulate the forces in contact tasks, we propose an interactive mesh-based framework integrating 3D perception and on-line deformation modeling, with real-time motion planning and interaction control. The goal is to effectively and accurately control a robotic manipulator when executing interactive tasks on the surface of a deformable object. The proposed motion planning framework is based on three efficient pre-processing algorithmic steps, including visual object segmentation, FEM deformation tracking, and local mesh parameterization. A central idea in our approach is the use of barycentric coordinates for the mesh triangles, in order to establish bijective transformations between the deformable part of the object's surface and its planar parameterized versions (static and dynamic). The combination of spatial transformations with the preprocessing steps and an active stiffness control scheme for the manipulator, allows for accurate reactive planning of interactive trajectories and contact force regulation, even in the presence of large and persistent visual occlusions, such as those caused by the presence of the robot manipulator in the visual scene. Extensive experimental evaluation results, involving interaction with a dynamically deforming model, validate the performance of the proposed framework in different experimental conditions.

## 1.6 Thesis Structure

In Chapter 2 the theoretical background and the mathematical formulations of several diverse techniques derived from the fields of motion planning, computer vision and graphics, required in the understanding of the proposed methodologies. Chapter 3 introduces an integrated framework, which is able to learn and encode complex, human-friendly washing actions from demonstration based on the DMP method and properly adapt the learned motions on the user's body parts. The use of DMP formulation enables the on-line modification of the motion parameters, fitting the user requirements. This learning method is combined with a perception-based motion planning strategy, which takes as an input the rich Point-Cloud information of a depth camera and the enhanced scene perception with human body part segmentation, in order to on-line adapt demonstrated interactive trajectories on the moving and deformable surface of the user's body. An alternative learning from demonstration method is presented at the end of the chapter, which aims to encode the same set of demonstrated actions into the construction of a repulsive potential field of Navigation functions. In Chapter 4 we propose an interactive mesh-based planning framework which combines: (a) enhanced visual perception, (b) reactive task planning and (c) contact force regulation, dealing with both active and passive deformation scenarios. This approach is based on real-time FEM deformation tracking and efficient local mesh parameterization which, combined with stiffness control of the robotic manipulator, enables accurate reactive planning of interactive trajectories and regulated contact on the surface of a dynamically deforming object, effectively handling visual occlusions.

In Chapter 5, we present an extensive experimental validation of the perception-based motion planning approach both in lab and clinical environment. Interactive motions learned by demonstration of human experts are executed both on the I-Support soft robotic platform and the ARMAR-III humanoid robotic platform in several experimental scenarios. This approach also serves as a baseline approach for comparative analysis with the interactive mesh-based planning framework, which is presumably more powerful in terms of better handling dynamic deformations and occlusions. Comparative experimental analysis results are presented in Chapter 6. The performance of the mesh-based framework is also further highlighted in tasks involving physical point tracking, interactive programming by human demonstration, as well as contact force regulation. Finally, in Chapter 7 we derive the conclusions from the available experimental results and the future research directions in the context of assistive robotics and physical interaction of robotic manipulators with deformable environment.

## Chapter 2

# Theoretical Background

### 2.1 Semantic Visual Segmentation and Human Pose Estimation

Image segmentation is a problem, which is widely analyzed in the computer vision society, and defines the process of partitioning a digital image into multiple segments (sets of pixels). The partitioning is implemented by assigning a label to every pixel in an image, which share certain common characteristics, changing the representation of an image into something that is more meaningful and easier to analyze. It is applied to a wide spectrum of applications such as medical imaging, object detection, face recognition, pedestrian detection and traffic control systems. The contextual importance of the characteristics shared in image segments (e.g. all pixels representing a car) allows for accomplishment of more complex visual tasks, leading to semantic visual representations. Most of the semantic segmentation systems, developed in the end of 00s decade, presented promising results based on on hand-crafted features combined with flat classifiers, such as Random Forests [84], Support Vector Machines [85], or Boosting [86]. Major performance boost have been achieved by containing richer semantic information [87] and structured prediction techniques [88, 89, 90]. However, their performance of has been limited, due to the use of features with poor expressive power.

The introduction of Deep Convolutional Neural Networks (DCNNs) in the past decade have pushed the boundaries of computer vision research in a large variety of high-level problems, achieving better performance, both in image classification [91, 92] and object recognition [93, 94, 95], than techniques relying on hand-crafted features. Their success mostly relies on the end-to-end training process, allowing them to learn increasingly abstract data representations. This performance leap has motivated the use of DCNN solutions, to identify the support of human body-parts in the image domain, which coupled with the depth information from the Kinect cameras of the I-Support system can allow the 3D pose estimation of body parts. This semantic segmentation task was addressed using the seminal work proposed in [96], in which a combination of CNNs with structured prediction techniques is proposed, yielding state of the art semantic segmentation results, as evaluated on the PASCAL semantic segmentation benchmark. A training a set of images containing humans was used [97], in which they were manually segmented into distinct human parts (head, torso, lower and upper arms, lower and upper legs), resulting in a pixel-wise labelling of the image in terms of the distinct object regions or background pixels. This approach was evaluated in the tasks of segmenting the torso (Fig. 2.1) and the legs (Fig. 2.2) of the user, using the mean Intersection over Union (IoU) metric. This

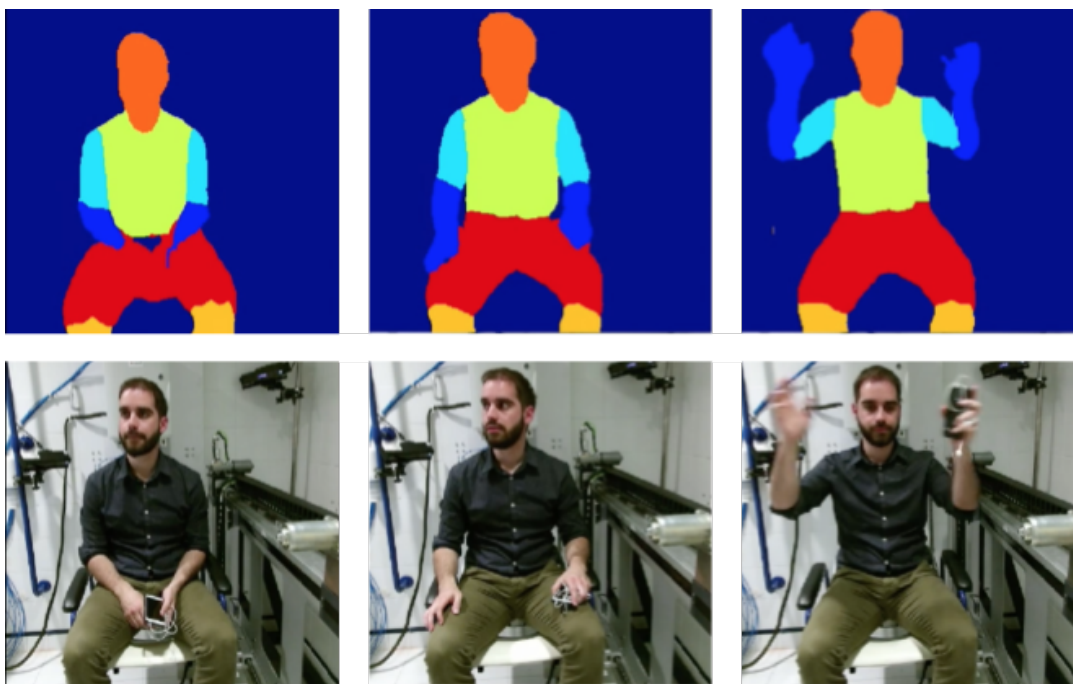


Figure 2.1: Semantic segmentation of human torso visual results in multiple images of a human user in the I-Support system environment. Up: The segmented body parts labels shown in different colors. The torso is presented in light green color. Down: The original images obtained from the I-Support system's cameras.

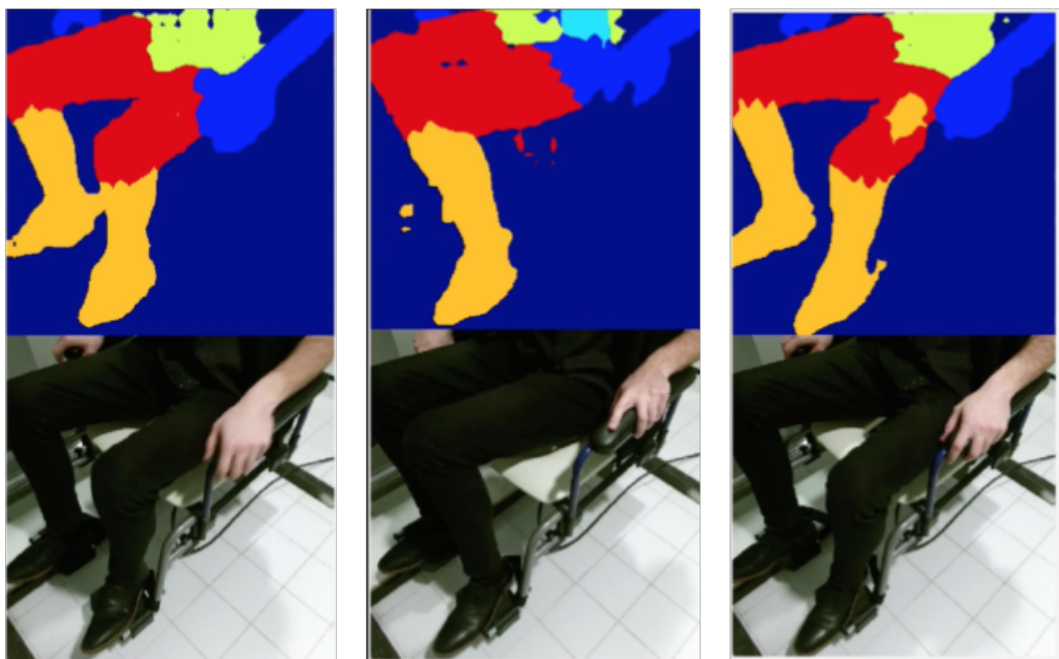


Figure 2.2: Semantic segmentation of human legs visual results in multiple images of a human user in the I-Support system environment. Up: The segmented body parts labels shown in different colors. The legs are presented in orange color. Down: The original images obtained from the I-Support system's cameras.



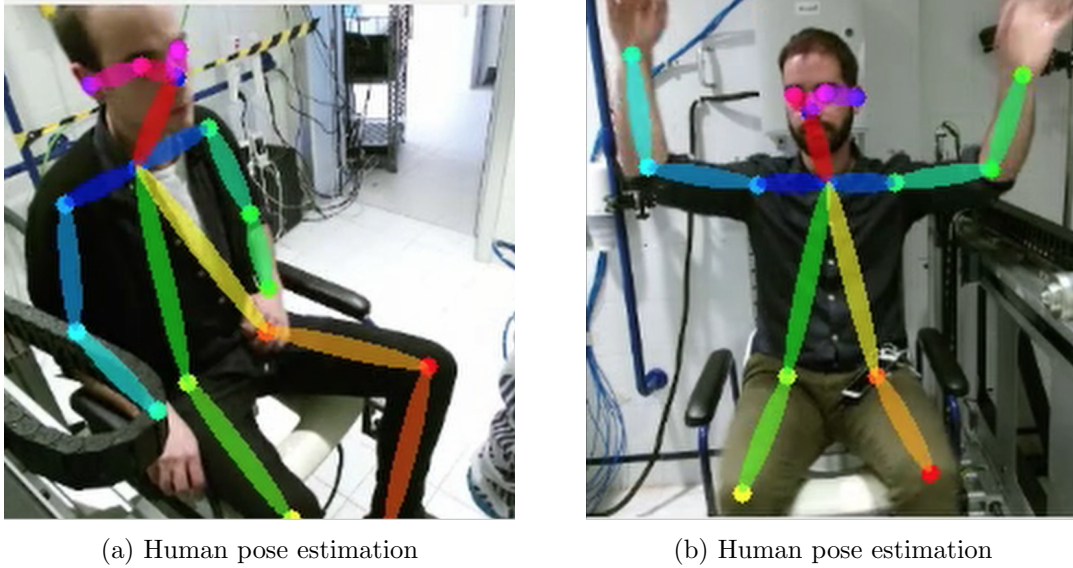


Figure 2.3: Visualization of human pose estimation from multiple points of view from the cameras of the I-Support system.

is obtained by evaluating the ratio of areas for intersection and union of predicted and groundtruth regions. The maximum value is 1, where the predicted and groundtruth regions are identical. Its pixel-wise accuracy in terms of IoU was reported 64.4% in [98] and later was improved to 66.1% in [96].

Another task in visual human perception that has been efficiently accomplished with the use of DCNNs is whole body pose estimation. More specifically, the goal of this task is to infer the locations of landmark points of the human body on the image plane. The accurate inference has a high relation to the whole image visual context, since locally there are no features distinguishing the left from the right knee, but it is through the propagation of mutual constraints that one can disambiguate their positions. CNN-based architectures have been shown able to exploit shape and context implicitly via stacked and learnable part localization operations, through both non-recurrent [99, 100, 101] and recurrent [102] refinements. The method integrated to I-Support system is based on the convolutional pose machines (CPM) approach [101], due to its simplicity and efficiency. The approach uses sequential prediction convolutional blocks that operate on image and intermediate belief maps and learn implicit image-dependent spatial models of the relationships between parts. The quality of the prediction is measured by metrics that involve comparing the predicted and the ground truth locations in the image plane. In particular, the performance of this system in pose estimation has been validated based the Percentage of Correctly estimated body Parts (PCP) commonly used in the pose estimation literature. An estimated body part is counted as correct if its segment endpoints lie within  $t\%$  of the length of the ground-truth segment from their annotated location. Overall performance is evaluated by a PCP-curve, obtained by varying the accuracy threshold  $t$ . The integrated system achieve a PCP measure of 85.8% and robustly estimates the body pose of the user (Fig. 2.3), operating at 10 frames per second.

## 2.2 Navigation Functions

The definition of robotic motion planning over continuous space can be summarized in finding a safe path from an initial to a desired configuration [103]. A safe plan not only includes obstacle avoidance but also convergence to the destination as well. As long as such a plan is available, trajectory generation and trajectory tracking can be integrated, by appropriately constructing a feedback control plan. Artificial Potential Fields, initially introduced by Khatib [104, 105], are a group of closed-loop feedback motion planning methods, which construct a scalar potential field over the workspace. Following the field's negated gradient a robotic agent is driven safely to the target configuration. A large number of works have followed, which use different ways of constructing potential fields, such as harmonic function combined with the panel method [106], harmonic functions constructed by solving partial differential equations [107] and superquadric potential fields [108]. However, it can be shown that for certain obstacle configurations in the workspace local minima arise, which can trap the robotic agent in a certain configuration.

Similar structure, i.e. scalar fields over the free space, have the methods of Navigation Functions (NF), which are proposed by Rimon and Koditschek in [109] and are shown to overcome the problem of local minima. Initially they show that it is unattainable for stationary points to disappear and they define an almost globally asymptotically stable scalar potential field. Under certain conditions, although they show that the existence of unstable equilibria is a subset of Lebesgue measure zero in the set of remaining saddle points, in real applications it is practically impossible for an agent to remain in a measure zero set. They have also proposed the rephrasing of motion planning problem from a purely geometric to a topological point of view. In particular, a convenient space, which is topologically equivalent to the original geometric structure, can be used to generate a safe path, avoiding geometrically complicated obstacles. The latter are diffeomorphically mapped to their simpler images in topological space, using the forward mapping, and inversely the generated path can be transformed to the original geometric space. This method was proposed in [110], in which navigation of mobile robot treated as spherical agent is achieved by defining the NF potential in on a sphere world and diffeomorphically mapped to real space. In the original navigation function formulation global knowledge of the geometric space is required, which is relaxed in [111, 112] by defining polynomial NFs.

In more detail, we can define the following sets in a sphere world  $\mathcal{W}$ :

1. Destination point  $\mathcal{F}_d \triangleq q_d$
2. Obstacle free subset  $\mathcal{F} \subseteq \mathcal{W}$
3. Obstacle free subset boundary  $\partial\mathcal{F}$
4. Set of obstacles  $\mathcal{O} \in \mathcal{W} \setminus \mathcal{F}$

. We consider the problem of a holonomic robotic agent in whose state  $q$  is governed by the control law:

$$\dot{q}(t) = -(\nabla_q \phi)q(t) \quad (2.1)$$

where  $\phi$  is a NF defined below. In [113] it is proven that this control law solves the motion planning problem in  $\mathcal{F}$ . A Navigation Functions is defined [113] on a compact connected analytic manifold with boundary  $\mathcal{M} \subset \mathbb{R}^n$  as a map  $\phi : \mathcal{M} \rightarrow [0, 1]$  which is:

1. Analytic on  $\mathcal{M}$ : locally convergent power series exists.



2. Polar on  $\mathcal{M}$ : unique minimum exists at  $q_d \in \mathcal{M}$ .
3. Morse on  $\mathcal{M}$ : all critical points are non-degenerate.
4. Admissible on  $\mathcal{M}$ : uniformly maximal on  $\partial\mathcal{F}$

. More specifically in [113] a NF for sphere worlds,  $\phi : \mathcal{F} \rightarrow [0, 1]$  is a composition of three functions:

$$\phi(q) \triangleq \sigma_d \circ \sigma \circ \hat{\phi} \quad (2.2)$$

Starting from the function  $\hat{\phi}$  it is defined as

$$\hat{\phi}(q) \triangleq \frac{\gamma(q)}{\beta(q)} \quad (2.3)$$

where  $\gamma(q) = \|q - q_d\|^{2k}$ ,  $k \in \mathbb{N} \setminus 0, 1$  is the function defining the distance from the target and  $\beta(q)$  is a product of obstacle functions. The image of  $\hat{\phi}$  is then modified by the diffeomorphism  $\sigma : [0, \infty) \rightarrow [0, 1]$  defined as

$$\sigma(x) \triangleq \frac{x}{1+x} \quad (2.4)$$

resulting in a polar, admissible, and analytic function which is non-degenerate on  $\mathcal{F}$  except at one point - the destination, which due to the parameter  $k$  in  $\hat{\phi}$  is a degenerate critical point. Therefore, the function  $\sigma_d : [0, 1] \rightarrow [0, 1]$  is added

$$\sigma_d(x) \triangleq (x)^{\frac{1}{k}}, k \in \mathbb{N} \setminus 0, 1 \quad (2.5)$$

resulting in the final form of a Navigation Function:

$$\varphi(q, t) = \frac{\gamma_d(q, t)}{[\gamma_d^\kappa(q, t) + \beta(q, t)]^{1/\kappa}} \quad (2.6)$$

The NF field is shaped by the tunable parameter  $k$ , for which there exists a lower bound as proven in [113], which clears the field of local minima other than the destination. Later in [114] an algorithm is proposed for online calculation of this tuning parameter. Furthermore, the sphere world requirement is relaxed in [115] to sufficiently curved worlds and to partially non-convex ones.

## 2.3 Dynamic Movement Primitives

Dynamic movement primitives, introduced by Ijspeert et al. [116, 117] are motion control policies, which are based on nonlinear dynamical system to describe a motion. The system comprises of second-order differential equations with well-defined attractor dynamics that contain information about the form and time evolution of a motion. In [118], the methodology has been developed for encoding and reproduction from multiple demonstrations of both discrete and periodic motions, whereas in [119] a single demonstration is required. Discrete are characterized the motions, which start from one point in space, follow a certain trajectory, ending at another point, without any repetition, whereas periodic are the motions, which are repeated at least once during their evolution and are constituted of oscillations of different widths and frequencies along the coordinate axes.

### 2.3.1 Discrete Motions

The formulation of [119] will be used to describe the basis of motion specification for a single degree of freedom denoted by  $y$ , which in a robotic system can be either a joint angle or one of the task-space coordinates, and is summarized in the following set of linear differential equations:

$$\tau \dot{z} = \alpha_z(\beta_z(g - y) - z) \quad (2.7)$$

$$\tau \dot{y} = z \quad (2.8)$$

where  $\alpha_z$  and  $\beta_z$  are constant coefficients and  $\tau$  is a time scaling coefficient, which determines the duration of the motion. This system has a unique attractor point at  $y = g$ ,  $z = 0$ , provided that  $\tau > 0$  and the parameters are selected appropriately, e.g.  $\alpha_z = 4\beta_z$ , for the system to be critically damped. Therefore, it can be used for the realization of discrete point-to-point motions. It is obvious from the form of Eq. (2.7)–(2.8) that the set of trajectories which can be encoded is rather limited. To increase this set of point-to-point trajectories a non-linear term  $f$  has to be added to the right hand side of Eq. (2.7). The function  $f$  is a weighted linear combination of  $N$  radial basis functions  $\Psi_i(x)$  as shown in the following equation:

$$f(x, g, y_0) = \frac{\sum_{i=1}^N w_i \Psi_i(x)}{\sum_{i=1}^N \Psi_i(x)} x(g - y_0) \quad , \quad \Psi_i(x) = \exp(-h_i(x - c_i)^2) \quad (2.9)$$

where  $y_0$  and  $g$  the starting and end point of the trajectory respectively,  $c_i$  and  $h_i$  are the centers and width of radial basis function  $\Psi_i(x)$  respectively. Despite the fact that Gaussian functions are used as basis functions, there are plenty of methods that use functions of other forms. The learning phase of the nonlinear term  $f$  constitutes of defining the weight  $w_i$  of each basis function. With a regression learning algorithm such as locally weighted regression proposed in [120], the weights of force term can be learned from a single demonstration. The center  $c_i$  and the width  $h_i$  of a Gaussian basis function for a specified number of functions  $N$  are calculated using

$$c_i = \exp\left(-\alpha_x \frac{i-1}{N-1}\right), \quad h_i = \frac{2}{(c_{i+1} - c_i)^2} \quad \text{and} \quad h_N = h_{N-1}, \quad i = 1, \dots, N. \quad (2.10)$$

A phase variable  $x$  is used in 2.9 instead of time to make the dependency of  $f$  on time more implicit. Its dynamics can be defined by

$$\tau \dot{x} = -\alpha_x x \quad (2.11)$$

which is defined as **canonical system**. Setting the initial value  $x(0) = 1$  the solution of (2.11) is  $x(t) = \exp(-\alpha_x t / \tau)$  where  $\alpha_x$  is a constant which determines the convergence rate of the variable  $x$  to 0. The use of this phase variable instead of explicit time gives the appealing property to DMPs, which can easily be temporally modulated without requiring an explicit time recalculation. This property can be effectively used for synchronization or stopping the evolution of time to account for perturbations during trajectory execution. This choice of phase variable results in the following system of differential equations:

$$\tau \dot{z} = \alpha_z(\beta_z(g - y) - z) + f(x) \quad (2.12)$$

$$\tau \dot{y} = z \quad (2.13)$$

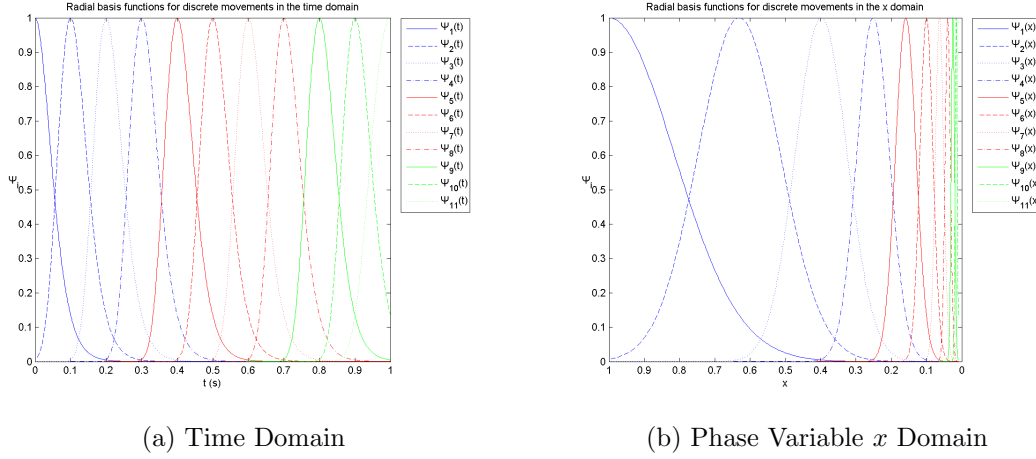


Figure 2.4: Discrete Radial basis functions for  $N = 11$  in the (a) time domain for  $\tau = 1$  (b)  $x$  phase variable domain for  $\alpha_x = 4.6$  and  $\tau = 1$ .

which is defined as **transformation system**. The general solution of the system (2.12) - (2.13), for  $a_z = 4b_z$ , is provided by the equation

$$y(t) = e^{-\frac{2b_z t}{\tau}} \left[ c_2 - \frac{1}{\tau^2} \int_0^t x e^{\frac{2b_z x}{\tau}} (4gb_z^2 + f(x)) dx + c_3 t + \frac{1}{\tau^2} \int_0^t e^{\frac{2b_z x}{\tau}} (4gb_z^2 + f(x)) dx \right], \quad (2.14)$$

where  $c_2$  and  $c_3$  constants with values depending on initial conditions. Chosing  $y(0) = y_0$  and  $\dot{y}(0) = 0$ , Eq. (2.14) is transformed to

$$y(t) = \frac{1}{\tau^2} e^{-\frac{2b_z t}{\tau}} \left[ - \int_0^t x e^{\frac{2b_z x}{\tau}} (4gb_z^2 + f(x)) dx + t \int_0^t e^{\frac{2b_z x}{\tau}} (4gb_z^2 + f(x)) dx + \tau^2 y_0 + 2b_z \tau y_{0t} \right]. \quad (2.15)$$

Since  $x$  tends to zero exponentially, the influence of the non-linear term  $f(x)$  decreases with time, as shown by the form of radial basis functions in Fig. 2.4, and the system (2.12)–(2.13) converges to  $[0, g]^T$  just like the system (2.7)–(2.8). The control policy specified by variable  $y$  defines what is called Dynamic Motion Primitive. This policy specified by Eq. (2.9)–(2.13) is time scalable, if the time constant  $\tau$  is replaced by  $c \cdot \tau$ , then the motion duration will be scaled by the factor  $c$ . Additionally, we can scale this policy in space by substituting the goal value  $g$  by  $c \cdot g$ , making the system to converge to  $c \cdot g$  with the same motion duration, without modifying the shape of motion. This property is very important not only for the generation of washing actions in the I-Support system but also to the adaptation of these actions to different users' needs.

### 2.3.2 Periodic Motions

One degree of freedom periodic motions can be generated with the form of an oscillation around a central value, with variable amplitude and frequency. A similar differential equations system to (2.12) - (2.13) is used to generate periodic motions, substituting the term  $\tau$ , which determines the duration of the motion, with the term  $\Omega = \frac{1}{\tau}$ , which determines the frequency of the oscillation. Moreover, the non-linear term  $f$  is changing to:

$$f(\phi, r) = \frac{\sum_{i=1}^N w_i \Gamma_i(\phi)}{\sum_{i=1}^N \Gamma_i(\phi)} r, \quad \Gamma_i(\phi) = \exp(h_i(\cos(\phi - c_i) - 1)) \quad (2.16)$$

where  $r$  is the amplitude of the oscillation,  $c_i$  and  $h_i$  is the center and the width of the radial basis function  $\Gamma_i(\phi)$  respectively. The phase variable  $\phi$  is used, just like  $x$  for

discrete motions, to make implicit the dependency of  $f$  on time and is calculated using the equation:

$$\dot{\phi} = \Omega \quad (2.17)$$

which is the respective canonical system of periodic DMPs. Using the initial value  $\phi(0) = 0$  in Eq. (2.17) we have

$$\phi(t) = \Omega t \quad (2.18)$$

Additionally, especially for periodic motions a different form of canonical system is propose in later works in the field [121, 122], which allows for on-line calculation of the frequency of a periodic motion during its execution. The center  $c_i$  and the width  $h_i$  of a radial basis function  $\Gamma_i(\phi)$  for a certain number of functions  $N$ , are defined according to [122] as

$$c_i = 2\pi \frac{i-1}{N} \quad \text{and} \quad h_i = 2,5N \quad \text{for} \quad i = 1, \dots, N \quad . \quad (2.19)$$

Comparing Eq. 2.19 with Eq. 2.18 we can see that the center  $c_i$  of radial basis functions are evenly distributed over the time domain and that of the variable  $\phi$ , having equal width, due to the linear form of the canonical system of periodic DMPs. Therefore we have the following system of differential equations

$$\dot{z} = \Omega (\alpha_z(\beta_z(g-y) - z) + f(\phi)) \quad (2.20)$$

$$\dot{y} = \Omega z \quad (2.21)$$

where  $g$  is the center of the oscillation. The system 2.20–2.21 is the respective transformation system of periodoc DMPs, which can equivalently take the form of second order differential equation:

$$\frac{1}{\Omega^2} \ddot{y} + \frac{\alpha_z}{\Omega} \dot{y} - \alpha_z \beta_z (g-y) = f(\phi) \quad . \quad (2.22)$$

The solution of the system 2.20–2.21, for  $a_z = 4b_z$ , is given by the equations 2.14–2.15 by substituting the terms  $\tau$  and  $x$  with the terms  $\frac{1}{\Omega}$  and  $\phi$  respectively.

## 2.4 Deformation Tracking

An object undergoes deformations, when its shape is changing during the excretion of external forces. Categorization of deformations depends on the object response when the external force is removed. If an object maintains the shape caused by a deforming force, then a plastic deformation occurred, whereas if its shape returns to its initial form, it is a case of elastic deformation. All the intermediate situations, in which the object does not return to its original shape, but it does not preserve its deformable form entirely, are defined as elasto-plastic. Early attempts to model the behaviour of deformable objects are made in the field of computer graphics, in order to produce more realistic animations. Nealen et al. in [123] and Moore et al. in [124] offer a comprehensive introduction to the computer graphics methodologies of the previous decade in their survey papers. More specifically, the deformation modeling can be done with a variety of techniques. In most cases, an object's shape representation (e.g. a set of particles or a mesh) and a deformation model synthesize a deformation estimation technique. A mesh representation consists of a set of points (vertices), edges and faces, which are usually triangles or quadrilaterals, or elements, the representation of which is commonly tetrahedra or hexahedra. The deformation models are essentially functions, which calculate at each time step the evolution of the position of every vertex, taking into account both their current state (position and

velocity) and an input force. In particular, the object deformation parameters, such as Young's modulus and the Poisson's ratio for isotropic objects, are taken into account, in order to approximate a displacement field through a set of partial differential equations solved through discretization techniques. This approximation transforms the effect of an external force into a distribution of internal forces acting on the mesh elements. There have also been developed deformation models, which do not require a mesh but work directly on particles either in 2D [125] or in 3D [126].

The categorization of the mesh-based models is formed either as continuous or as discrete variable models. The main representative of discrete methods is Mass-Spring-Damper (**MSD**) systems, in which the vertices of the mesh are treated as mass particles and the edges are considered as springs modeling the flexibility of the object. On the other hand, continuum models are usually set up with finite element methods (**FEM**), in which the object's shape is approximated by a set of discrete geometric parts called finite elements. Although FEM-based models produce more physically realistic deformation results, MSD models have gained a lot of researchers attention, since they are more intuitive and simpler to implement. However, the processing power has increased significantly due to the recent advances in computing and computer vision, making possible the real time simulation of realistic deformation (e.g. using FEM) of solid objects. This technological step has also shifted the interest of robotics researchers to the study of various interaction tasks, such as manipulation, grasping and object identification, with linear (e.g. ropes), planar (e.g. cloth, paper) and 3D objects (e.g. sponge, tissue). Recent survey papers [127, 128, 129] present thoroughly the works emerging from this research trend.

The evolution of cameras, especially RGB-D, along with computer vision algorithms has augmented the perception capabilities of deformable objects by robotic and computer systems. In [130] Zollhöfer et al. registers RGB-D data on a rigid template, in order to capture the deformations of general shapes, while recently Güller and Kokkinos demonstrated in [3] the power of Deep Learning in accurate human body shape reconstruction even with a monocular camera. Another template-based framework proposed in [131] is combined with visual features from the texture of the object to track the deformations of objects, which may undergo topological changes (e.g. paper tearing), whereas Famouri et al. [132] employ the same ideas for tracking deformations using monocular camera as an input. Additionally, Willimon et al. integrate classic computer vision techniques with energy function minimization in [133, 134], to estimate the configuration of a non-rigid cloth-like object. NURBS functions from computer graphics are also used together with visual features for deformation tracking in [135, 136]. Recent papers involve a robotic system into deformation tracking tasks. More specifically, in [137, 138] the authors characterize generic deformable objects by visually observing their interaction with a robotic hand and in [139] surface variations caused by the contact of a simulated robotic hand are measured visually on Point Cloud data. Tian and Jia in [140] extend their work on shape modelling of shell-like objects, which are grasped by a robotic hand. Visual depth data together with force-torque obtained from a sensor mounted on a probe, are fed into a neural gas network implemented in [141] to predict the deformation's characteristics of an object, without requiring knowledge of the object material. Real-time deformation tracking, which is the focus of [142] and more recently of [143, 144] is a prerequisite for closed-loop robotic manipulation of objects such as ropes, clothes or sponges.

Despite the large amount of work focusing on planar or even cloth-like objects, the robotic manipulation of solid deformable objects (e.g. sponges, plush toys and food) hasn't made the same progress, mainly due to the computational cost imposed by the simulation of 3D objects. However, the development of real-time deformation simulation techniques

such as FEM and MSD has changed this picture. Examples of such approaches are [145], in which a FEM-based model is combined with a vision system in order to enable the object's shape modification by a robotic arm, and [146], in which the object is modelled as a mass-spring-damper system undergoing deformations by a robotic system in order to bring an internal point to a desired position. Object's internal point control is the main focus of [147], the authors of which propose a model-free controller with visual feedback for the estimation of the deformation Jacobian matrix. Another model free method in [148] introduces the notion of diminishing rigidity in order to approximate the deformation Jacobian during manipulation tasks. Deformable object grasping is also a challenging robotic task, since the shape and consequently the grasping forces are modified during the grasping action. In order to address these problems, the authors of [149, 150] integrate the FEM modeling of the object with the tactile sensors of a multi-fingered robotic hand, to pick up objects from a table. Furthermore, visual and force data are combined with deformation modeling techniques in [151, 152, 153], to estimate with the use of a robotic arm the physical parameters of an object, which are very important for accurate modeling and interaction tasks. Caccamo et al. in [154] and Güler et al. in [155] use similar procedures with robotic probing on the surface of an object but they implement vision meshless techniques to estimate the deformability of objects.

Soft tissue is another solid deformable object, which has been extensively studied for robotic medical applications. The constraints of these applications (e.g. real-time interaction with moving organs and limited action space during surgical tasks) are not met in household or industrial applications. Therefore, the robotic actions during medical procedures have to be more precise, delicate and well-planned. In order to fulfill the aforementioned requirements in medical scenarios, robotic systems need an accurate perception layer, which is frequently based on vision, as described in [156]. The main goal of these vision-based systems is to augment the visualization capabilities of the surgeon during minimally invasive surgery, with the use of pre-operative CT-scan data combined with time-of-flight camera for the development of an organ's surface matching algorithm in [157], or a stereo endoscope and a biomechanical model for real-time motion tracking of the liver in [158]. The more challenging problem of monocular 3D reconstruction is faced in [159], in which a non-linear mechanical elastic model is proposed, to enable the reconstruction of highly deformable objects, presenting some promising results in computer assisted surgery scenarios, whereas in [160] and more recently in [161] the authors employ 3D template matching and Shape-from-Motion visual techniques for reconstruction of the peritoneal region and liver respectively. Non-rigid structure from motion is also used in [162] for tracking the surface of a beating heart, a task which is also studied in [163], by integrating a temporal heart motion model with visual data and presenting in vivo experiments. Other works [164] propose the combination of visual features with triangular meshes, to track tissue deformation using a monocular endoscope.

## 2.5 Mesh Parameterization

It is generally possible to calculate an one-to-one and onto mapping between two given surfaces with similar topology. This mapping computation problem is referred to as mesh parameterization, in case one of these surfaces is a piecewise linear triangular mesh. The other surface, in which the mesh is mapped, is typically mentioned as parameter domain. There are many different examples of parameter domains presented in literature, such as simplicial complexes [165, 166], spheres [167] and periodic planar regions [168, 169]. However, the main focus of of this thesis and of the literature, as presented in multiple

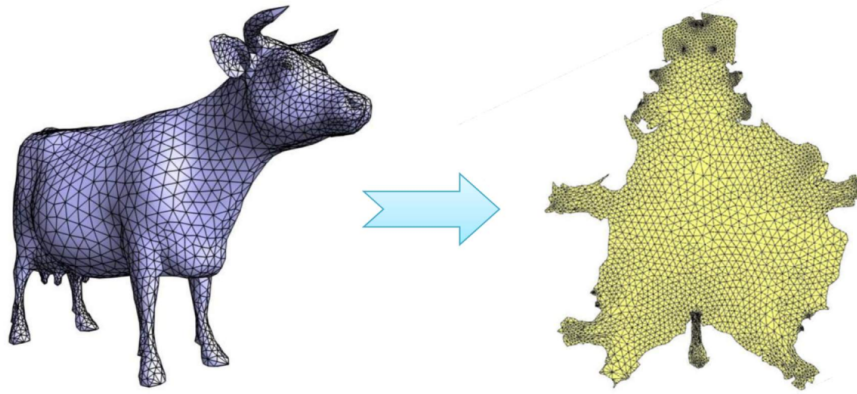


Figure 2.5: Parameterization of a 3D triangular mesh to a planar parameter domain [2].

surveys [170, 171, 172] is the planar parameter domain, an example of which is depicted in Fig. 2.5. Although the main motivation for the development of the first parameterization methods was the application to texture mapping [173] in the computer graphics society, other applications in engineering, geometry processing and medical visualization [174, 175] quickly emerged, including but not limited to mesh completion [176], mesh compression [177] for data transmission, surface remeshing [178], surface fitting [179] and material modeling [180].

Starting from a well-known result from differential geometry initially proven in [181] and mentions that for a general surface patch there is no distance-preserving (isometric) parameterization in the plane. Isometric parameterizations can be found only for surfaces with zero Gaussian curvature (e.g. cylindrical or conical sheets) commonly referred as developable. Therefore, parameterizations, except for the cases of developable surfaces, introduce distortions in either angles or areas. Most of the works proposed in the literature are minimizing angular distortion or shear and are called conformal, whereas less works presented a minimization of area distortion called authalic, since they have proven less useful in terms of application. Frequently, conformal maps are also referenced as harmonic, however as shown in [170] these terms are not equivalent. The previously mentioned terms are borrowed from differential geometry of smooth surfaces, in which the existence of conformal maps is guaranteed from a Riemann's theorem, mapping any infinitesimally small circle on the surface to a circle on the domain. This result shows the existence of an angle preserving mapping, but allows the scale factor of the transformation to vary across the map, introducing distortion. Furthermore, there are many applications which can tolerate a small amount of distortion of either type. Hence, many papers proposed some parameterization methods, that have a trade-off between angle preservation and area, or length preservation, called most-isometric parameterizations. Except for distortion, the evaluation of a parameterization method can be done in terms of boundary assumptions, robustness and computational cost. In particular, many methods assume a pre-defined convex boundary in the planar domain, making them simpler and faster in implementation, whereas boundary-free techniques are usually non-linear and slower computationally, but generally introduce significantly less distortion. Robustness of a parameterization regards the guarantee of local or global bijectivity (no triangle flips or boundary self-intersections).

A classic and old method, which shaped the workflow of many later parameterization methods, is Tutte's graph embedding method [182]. This method proposes a two stage procedure, in which the first one maps the boundary vertices of the mesh to a convex

boundary in 2D and the second one calculates the positions of the rest of the vertices solving a linear system independently for the 2D coordinates. Similar to this approach several conformal parameterization techniques [183, 184, 185] use the same boundary mapping step, but solve a system of equations with weights on each edge of the mesh. The choice of weights has an impact on both the distortion and the bijectivity of the parameterization. The solving of a single linear system makes these techniques efficient and simple, but they perform poorly if the boundaries of the 3D meshes differ significantly from the specified boundary of the planar domain. This drawback was one of the motivating factors for the development of boundary-free methods LCSM [186] and DCP [187]. They used different formulations of harmonic energy and managed to introduce significantly less distortion than fixed boundary approaches, especially near the domain boundaries. Later the HLSCM method [188] proposes a mechanism, which employs a hierarchical solver to speed up the solution process for LSCM. However, DCP/LSCM introduce more distance distortion than nonlinear conformal methods like the MIPS method [189], which optimizes a nonlinear functional that measures mesh conformality. Another popular nonlinear method is ABF [190], which defines planar parameterization in terms of angles of the planar triangles and specifies a set of constraints that these angle values have to satisfy. The resulting angles are converted into 2D vertex coordinates leading to a guaranteed local bijectivity without flipped triangles but can contain global overlaps. This problem was solved later in ABF++ [191] method providing at the same time a large boost in computational efficiency.

Area preserving parameterizations have not gained so much attention in literature by themselves, since they initiate large angular and linear distortion [192], but they are usually combined with angle preservation [193]. On the other hand, several distance preservation or stretch minimization parameterization techniques have been proposed without conformality properties. Several stretch metrics have been proposed, but the metrics of Sander et al. [194] are the more commonly used as standard measures of distance preservation. They were based on the fact that a linear map can be expressed as a translation, a rotation, and an anisotropic scale along two orthogonal axes. A minimization of a metric including the singular values of the transformation matrix, or the square roots of the eigenvalues of the integrated metric tensor, was proposed. Additionally in [195] the basic goal of the method is to preserve the distances between all pairs of vertices on the surface. Distances were calculated with the use of geodesics and the embedding of the mesh in the plane was implemented with multi-dimensional scaling. While this method works well for close to developable surfaces, it faces robustness issues for more complex ones. These issues were solved in the isomap method proposed in [196] achieving a computational speedup as well.

Many methods combine the above mentioned techniques in order to achieve a trade-off between angle and distance or area preservation. More specifically in [193] an extension of MIPS method is proposed, modifying the functional under minimization in order to take into account area deformation. Similarly in [190] the authors first applied the conformal ABF method and then computed the stretch of the resulting planar mesh and smoothed it out with an overlay grid. More recent methods referred as most-isometric, since they are trying to minimize both area and angle distortion, are using minimization of energy function and at the same time are guarantying the bijectivity of their solution. In [197] a parameterization algorithm is proposed, in which its local part minimizes the distortion of each triangle, while its global part uses efficient sparse linear solvers with factorization to fit together the 2D triangles in a coherent manner. Energy minimization functional is also used in [2], focusing more on the guaranty of a bijective and less on the search of a global solution close to isometry. Local parameterization solutions have found a large



---

spectrum of applications in computer graphics. For example, the Discrete Exponential Map (DEM) presented in [198] and later improved in [199] is an algorithm, which focuses on the computation of normal coordinates of a discrete surface (mesh) using the Dijkstra's algorithm with very high computational efficiency. In differential geometry, Euclidean normal coordinates can be calculated from radial coordinates, which constitute the natural parameterization of geodesic discs. The latter are an isometry near the center of the disc [200]. However, as one moves away from the center, the deviation from isometry depends on the variation in Gaussian curvature. For developable surfaces, the entire mapping is an isometry.



## Chapter 3

# Perception-Based Motion Planning & Learning from Demonstration

This chapter deals with reactive adaptation and motion generation of human demonstrated interactive tasks with deformable surfaces, such as those of the human body parts. Particularly, and in the context of a broader research effort aimed at building a flexible robotic bath mechanism, an integrated system based on Dynamic Motion Primitives approach was proposed, which can learn and encode demonstrated washing actions by professional nursing experts, imitating their actions. Encoding of nursing experts' skills allows for natural human-robot physical interaction, which plays a key role in the acceptance of an assistive robotic system by the users (Fig. 3.1). The interaction tasks were recorded with the use of optical motion tracker systems, analyzed and decomposed into primitive actions appropriate for robotic execution. The learned motions can then be adapted to the user's body parts with the use of a motion planning algorithm, which uses the visual feedback from a depth camera and the corresponding scene perception information, in order to achieve the adaptation with simultaneous avoidance of potential obstacle areas, corresponding for instance to injured or sensitive body parts to avoid. The adaptation is achieved with the establishment of bijective transformations, which reformulate the tracking problem to a 2D Canonical Space. Accurate trajectory tracking is then realized with a Navigation function controller with proven globally uniformly asymptotic convergence. The motion planning method is structured to be model free and can be adjusted to any robotic manipulator, provided that all the robot's workspace and velocity constraints are taken into account. Furthermore, an alternative to the DMP approach is proposed, which allows for learning and reproduction of interactive actions demonstrated by an expert clinical carer and is based on the established bijective transformations and a Navigation Function method, by means of construction of repulsive potential fields with "virtual obstacles".

### 3.1 Problem Statement

We consider the problem of generation of safe and human-friendly bathing actions with online adaptation on a moving, curved and deformable surface (e.g. user's body part). We assume that the generated washing actions will be executed by a robot which can be kinematically described by a general equation of the form:

$$\dot{q} = u \tag{3.1}$$

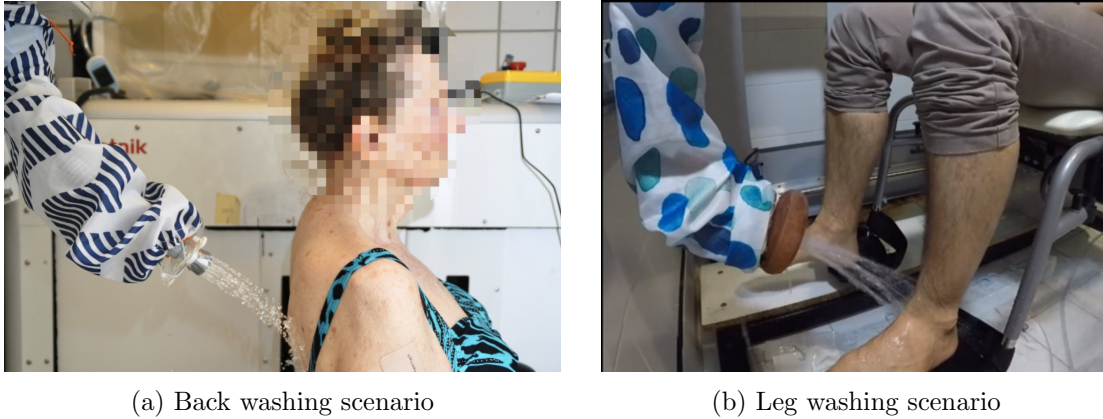


Figure 3.1: Motion planning method evaluation through a series of clinical validation studies in realistic clinical validation scenarios of (a) Washing back and (b) Washing legs conducted in Bethanien Hospital in Heidelberg Germany and Fondazione Santa Lucia (FSL) Hospital in Rome Italy, respectively.

where  $q$  is the vector of end-effector position and orientation, and  $u$  is the vector of velocity inputs. Let the admissible and feasible state space (workspace) for the robot be denoted as  $\mathcal{W} \subset \mathbb{R}^6$ . The obstacle free subset of the workspace is denoted  $\mathcal{W}_{free} \subseteq \mathcal{W}$ . Let  $\mathcal{O} \in \mathcal{W} \setminus \mathcal{W}_{free}$  be the set of all obstacles in 3-D workspace. These obstacles should be visible by a depth camera, whose field of view should include the workspace of the robot. Obstacle areas may regard restricted areas, either on the user’s body (e.g. local injury), which should be avoided during the washing sequence, or on other body parts that interfere to the robot’s motion (e.g. the hands of the user). Following this requirement, the core of this motion adaptation task is to calculate at each time step the reference pose for the end-effector, which will let the robotic manipulator execute proper human-friendly surface tasks (e.g. wiping the user’s back) and at the same time to be compliant with this body part. This is a challenging task, since all human body parts are non-planar surfaces, that are moving and deforming either systematically (e.g. user’s breathing motion) or randomly. Moreover, the user will have constant communication with the system (e.g. audio - gestural commands) and will be able to change the state and the parameters of the system with hand gestures, which may interfere to the robot’s operation. Adaptability to different users is also a very important feature of the system. Different users have dissimilar body areas and needs during the washing sequence.

Moreover, each human has unlike preferences and needs during the washing sequence. It is crucial for the user to feel comfortable and safe during the operation of an assistive robotic system. Therefore, proper and human friendly washing motions for each subtask should be learned by demonstrations of health care experts. In this process, a large variety of washing actions was recorded and are publicly available in KIT whole-body motion database [1]. However, a few demonstration examples were available for each motion, making the skill learning and generalization a demanding task. The learning and reproduction procedure might also raise some requirements for each task, in terms of execution time and motion complexity. However, decomposition into simpler primitive motions (e.g. periodic and discrete) is necessary for a robotic device for technical reasons. The fusion of such primitive actions with different parameters (e.g. duration, amplitude e.t.c.) can reproduce a large variety of more delicate and human-friendly actions.

In the next section, we will briefly provide the methodology and mathematical back-

ground, based on which, we develop an integrated perception-based motion planning and interactive control system, which is able to incorporate the recent advances of visual human perception algorithms (in particular on-line segmentation and reconstruction of human body parts) and can simultaneously, in the context of the envisaged assistive application, imitate and execute proper washing actions.

## 3.2 Methodology & Mathematical Background

A complete perception-based washing system consists of two main parts, a vision-based controller and an adaptable motion representation. The former one enables the system to perceive and handle the change of the environment, especially in our scenario the moving, curved and deformable washing surface. The latter one introduces the possibility of imitation learning and reinforcement learning by demonstration of health-care experts and generates adaptable washing actions.

### 3.2.1 Interactive Motion Learning & Generation

Instead of hard-coded trajectories, the robot can achieve more human friendly washing motion by observing human demonstrations. We choose DMP to represent washing movement primitives as mentioned before [201], which can learn and generalize complex washing skills from a few demonstrations. DMP is a damped-spring system coupled with a nonlinear term:

$$\begin{aligned}\tau \cdot \dot{v} &= K \cdot (g - y) - D \cdot v + scale \cdot f \\ \tau \cdot \dot{y} &= v,\end{aligned}\tag{3.2}$$

with the spring factor  $K$ , the damping factor  $D$  and the nonlinear force term  $f$ , which can be learned by observing demonstration examples.  $\tau$  is the temporal factor, and  $g$  is the goal for discrete movement or the anchor point for periodic movement. Also,  $v$ ,  $\dot{v}$  and  $y$  specify the current state of the motion.  $scale$  is the scaling factor for changed  $g$  or start position  $y_0$ .

However, the traditional DMP cannot handle interactive actions, such as wiping a dynamic surface. Hence, a leader-follower framework called Coordinate Change Dynamic Movement Primitive (CC-DMP) was developed in [202]. The idea of CC-DMP is that it incorporates the leader's dynamic motion by learning the follower's DMP in the leader's coordinate system. In order to get the follower's motion in the global coordinate system, a multiplication is required in both sides of the DMP transformation system with a coordinate transformation  $R_G^L$ , as in (3.3), where the superscript  $G$  denotes the global coordinate and  $L$  denotes the local coordinate. The leader's motion can also be encoded by another DMP, which, together with the follower's DMP, constructs a leader-follower framework realizing the adaptation of the follower's movements to the leader's behavior.

$$\begin{aligned}\tau \cdot R_{G,t+1}^L \cdot \dot{v}^G &= R_{G,t}^L \cdot (K \cdot (g^G - y^G) - D \cdot v^G + \\ &\quad scale^G \cdot f^G) \\ \tau \cdot R_{G,t+1}^L \cdot \dot{y}^G &= R_{G,t}^L \cdot v^G\end{aligned}\tag{3.3}$$

In order to learn a washing action and keep its capacity of generalization, the periodic pattern of motion is detected and separated from its discrete part by performing signal

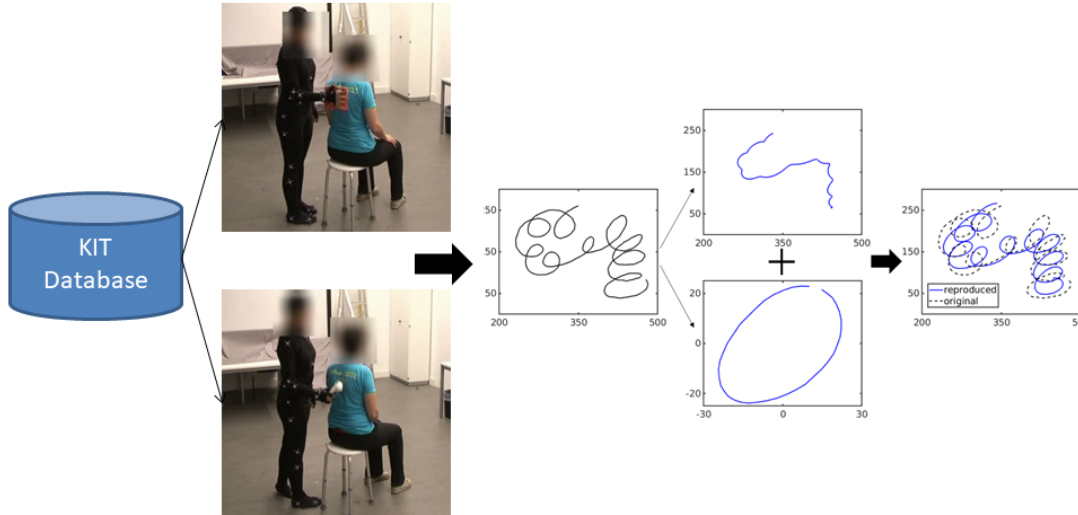


Figure 3.2: The procedure of learning CC-DMP by human demonstration includes the separation of the motion into discrete and periodic part. **Left:** A demonstrated washing action **Middle:** Separation of the demonstrated motion into primitive discrete and periodic motions. **Right:** The reproduced motion by the CC-DMP method (blue) is similar to the demonstrated one (dashed).

analysis. More specifically, as described in [202], the moving average method with appropriately chosen window size is employed for the extraction of the discrete part. Then the periodic part can be obtained by subtracting the discrete part from the trajectory. The rest of the signal contains the periodic parts, thus it is analyzed with Fourier transformation, to detect the dominating frequency, i.e. the frequency with the maximal spectrum. After frequency calculation, the rest part is cut into several small segments according to the inverse of the frequency and averaged, to reconstruct the approximated periodic pattern. In order to reproduce the original wiping trajectory, an amplitude profile is kept when extracting the periodic pattern. However, the main focus of this approach is the generalization and skill learning, rather than the exact reproduction of the original trajectory.

Examining the leader-follower approach from a more abstract point of view, the discrete part of a washing motion encodes the action direction such as top-down, left-right or some special movement. The periodic pattern encodes the functional primitive, which can be a cyclic motion, Fig. 3.2. In the extreme case, a motion whose periodic pattern has zero amplitude is a simple discrete motion. By this separation and representing both parts with DMPs, the motion can be modified according to the user's preference or task constraints. Fig. 3.2 shows one simple way to extract both parts of a washing action and reproduce it with CC-DMP. The accuracy of the reproduction is dependent on both separation and learning. Despite the accurate learning properties of DMP, signal splitting might cause information loss. Nevertheless, signal splitting can be avoided by customizing the expert's demonstration strategy.

Hence, a complete washing system based on CC-DMP has multiple leaders and followers. In the high level, the user's movement is the leader and a periodic motion is the follower. However, since the user's movement is not predictable in the general case, we need sensor feedback to perceive the change of the surface instead of learning user's movement with a DMP. In the low level, the discrete part of the motion is leader and

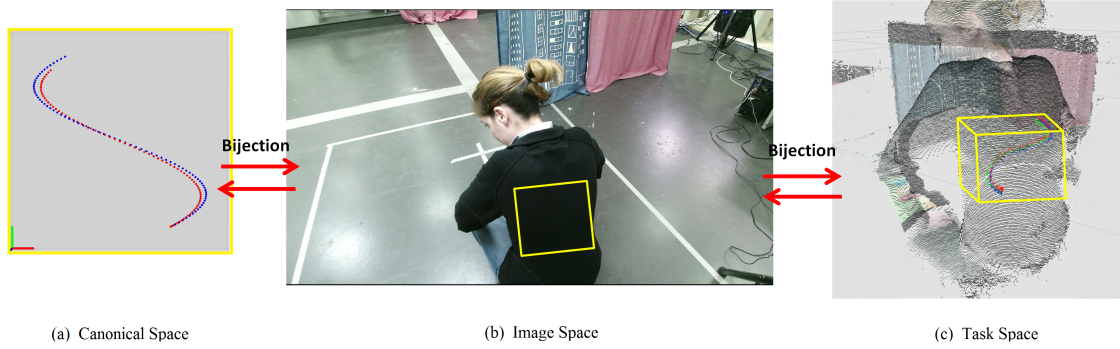


Figure 3.3: Three different spaces described in the proposed methodology. (a) 2D space normalized in  $x, y$  dimensions denoted as “Canonical” space. (b) 2D Image space is the actual image (of size  $512 \times 424$  pixels) obtained from Kinect sensor. The yellow rectangular area marks the user’s back region, as a result of a segmentation algorithm. (c) 3D Task Space is the operational space of the robot. The sinusoidal path from the Canonical space is fitted on the surface of a female subject’s back region. The yellow box represents a Cartesian filter, including the points on which the robot will operate.

the periodic pattern is the follower, both of which can be learned by demonstration with DMPs.

### 3.2.2 Perception-Based Motion Planning

The basic goal of the perception based motion planning is to adapt each interactive action on the surface of the user’s body by calculating on the fly the leader reference pose, around which each learned washing motion will be applied. The adaptation is achieved by integrating the visual perception of the user’s body parts into the planning procedure. with the establishment of three different spaces, which reformulate the problem of the leader motion tracking to the 2D space. More specifically, as shown in Fig. 3.3 we express the interactive motions in the following three spaces a) a 2D space denoted as “Canonical” space, b) the 2D Image space, corresponding to the actual image (of size  $512 \times 424$  pixels) captured by the Kinect image sensor and c) the 3D Task Space, corresponding to the operational space of the robot. The planning approach commences with the planning of the leader movement primitive’s path on a fixed 2D “**Canonical**” space, as depicted in the right of Fig. 3.3. This space can be considered as a canvas on which any path can be inscribed, in order for the robot to be able to navigate on any part of the surface that needs to be washed (e.g. the back of the user). The planned trajectories are tracked by the controller described in the next section.

#### Motion Tracking Controller

We make use of the following controller to satisfy both the time constraints imposed by the health-care specialist, or the user needs (e.g. the user prefers a quicker washing action than the predefined) and the spatial constraints imposed by the region of action (e.g. the back of the user) and the obstacle areas from the 3D operating scene. In what follows, we present the definition and the convergence proof of the motion tracking controller. In

more detail, we utilize a navigation function of the form:

$$\varphi(q, t) = \frac{\gamma_d(q, t)}{[\gamma_d^\kappa(q, t) + \beta(q, t)]^{1/\kappa}} \quad (3.4)$$

where  $\kappa > 0$ ,  $\gamma_d$  is the distance to the 2D time constrained washing motion, and  $\beta(q)$  is the product of obstacle functions coming from visual feedback, [109]. We consider convergence of the system to a small ball of radius  $r > 0$  containing the target.

Before defining the control we need some preliminary definitions. We can define the Hessian of function  $\varphi$ , as  $\nabla^2\varphi(q, t)$ . Let  $\lambda_{\min}$ ,  $\lambda_{\max}$ ,  $\hat{v}_{\lambda_{\min}}$ , and  $\hat{v}_{\lambda_{\max}}$ , be the minimum and the maximum eigenvalues of the Hessian, and the unit eigenvectors corresponding to the minimum and maximum eigenvalues of the Hessian, respectively. Then we assume the  $R$  region, as described in [44], to identify sets of points that contain sets of measure zero whose positive limit sets are saddle points:  $R = (\lambda_{\min} < 0) \wedge (\lambda_{\max} > 0) \wedge (|\hat{v}_{\lambda_{\min}} \cdot \nabla\varphi| < r_1)$ , where  $r_1 < \min_{S=\{q:\|q-q_d\|=r\}} (\|\nabla\varphi(S)\|)$ . If  $|\hat{v}_{\lambda_{\min}} \cdot \nabla\varphi| = 0$ . The set  $R$  consists of the measure zero set of initial conditions that lead to saddle point, [44]. Therefore,  $r_1$  can be chosen to be arbitrarily small so the sets defined by  $R$  eventually consist of thin sets containing sets of initial conditions that lead to saddle points.

**Proposition 1.** *The system (3.1), under the control law defined by the following vector field:*

$$u = -\nabla\varphi_\tau \quad (3.5)$$

*converges to the set where  $\|q - q_d\| < r$ , almost everywhere<sup>1</sup>. We can define  $\nabla\varphi_\tau$ , as:*

$$\nabla\varphi_\tau = a + b \cdot \frac{a}{f(\|a\|^2, r^2) - r^2 \cdot g(b) \cdot g(\|a\|^2)} \quad (3.6)$$

*with  $f(c, s) = \begin{cases} c, & c \geq s \\ s, & c < s \end{cases}$ , and  $g(c) = \frac{c}{1+|c|}$ , where  $a = \nabla\varphi$ ,  $b = \frac{\partial\varphi}{\partial t}$ , and  $\varphi$  is the defined navigation function (3.4).*

*Proof.* We form the Lyapunov function:

$$V = \varphi(q, t) \quad (3.7)$$

as described by (3.4), and we can take its derivative:

$$\dot{V} = \frac{\partial V}{\partial t} + u \cdot \nabla V = b + u \cdot a \quad (3.8)$$

After substituting the control law (3.5) by using (3.6), and since we pursue convergence in the set  $\|q - q_d\| < r$ , we get:

$$\dot{V} = -\|a\|^2 + b \cdot \left(1 - \frac{\|a\|^2}{\|a\|^2 - r^2 \cdot g(b) \cdot g(\|a\|^2)}\right)$$

Therefore, we can discriminate the following three cases:

1.  $b < 0 \Rightarrow -1 < g(b) < 0 \Rightarrow$   
 $\|a\|^2 < \|a\|^2 - r^2 \cdot g(b) \cdot g(\|a\|^2) < \|a\|^2 + r^2 \Rightarrow \dot{V} \leq 0$
2.  $b > 0 \Rightarrow 0 < g(b) < 1 \Rightarrow$   
 $\|a\|^2 - r^2 < \|a\|^2 - r^2 \cdot g(b) \cdot g(\|a\|^2) < \|a\|^2 \Rightarrow \dot{V} \leq 0$

---

<sup>1</sup>i.e. everywhere except a set of initial conditions of measure zero.



$$3. b = 0 \Rightarrow \dot{V} = -\|a\|^2 \leq 0$$

The sets defined by the set  $R$  are by construction repulsive. We make the assumption that the initial conditions of the system are in the set  $\{W\} \setminus \mathcal{E}$ , where the set  $\mathcal{E} = \{q : \|\nabla V\| < r_1\}$ .  $\square$

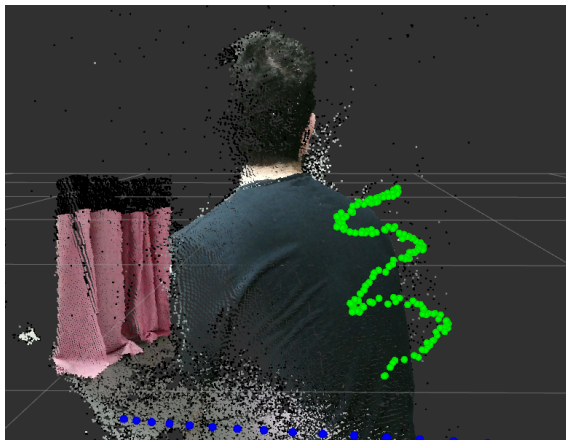
**Remark 1.** *Practically, we have the choice of an  $r_1$ , such that  $r_1 < \min\{r_0, \|\nabla V(q_0, t_0)\|\}$ , so we are sure that the system's initial conditions are not in  $\mathcal{E}$ .*

Based on this motion controller the next robot desired pose is extracted and propagated to 3D Task space for execution.

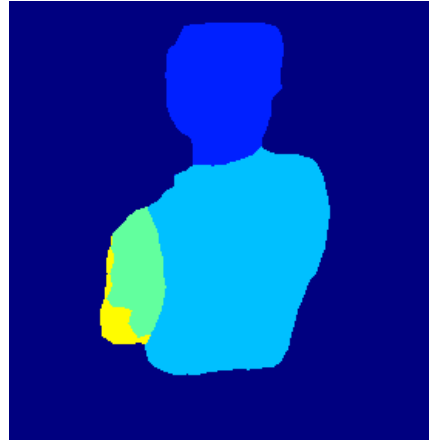
### Reference Motion Reactive Adaptation

In this proposed approach, we use as input the Point-Cloud data received from the depth sensors, and calculate on-line the reference motion, that the robot should execute in order to fulfill a washing task, Fig. 3.3. In particular, the data from Kinect depth sensors are processed initially by Deep learning based algorithms, which provide semantic visual segmentation of the user's body parts and human pose estimation, as described in Chapter 2.1. The output of segmentation algorithm is the calculation of human body-parts support in the image domain (denoted as valid pixels, Fig. 3.4b), which coupled with the depth information from the Kinect cameras of the I-Support system can allow the 3D pose estimation of body parts, on which the robot will operate (e.g. the back or the legs of the user), Fig. 3.3 (c). Additionally, the human pose estimation algorithm infers the locations of landmark points of the human body on the image plane.

Therefore, we can define the 2D extends of the body part on the image plane by simply calculating the minimum and maximum coordinates of the valid pixels along the image axes, or enhance the visual information by using the detected landmark points for each body part, as shown in Fig. 3.5b. The learned motion is followed by the controller and the result is transformed from the 2D "Canonical" space to the image space by performing



(a) Back Showering Motion Planning



(b) Visual Semantic Segmentation

Figure 3.4: Adaptation of a showering motion demonstrated by a nursing expert to the back region of a subject. (a) Point-Cloud view from the system's depth cameras and a sequence of positions shown as green spheres, covering the surface of the detected back region. (b) The output of the visual semantic segmentation algorithm, which identifies the region of each body part on the image plane, is used in the planning process.

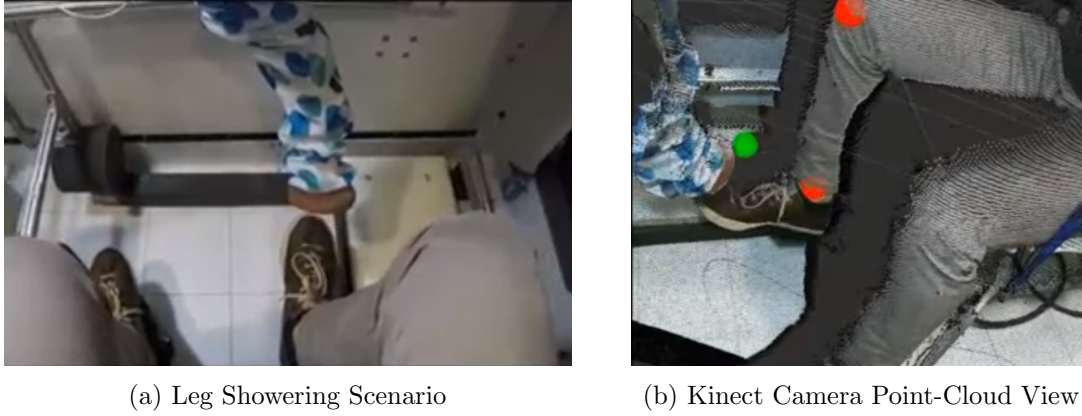


Figure 3.5: Execution of a leg showering scenario from the soft robotic arm. (a) User’s point of view (b) I-Support depth camera Point-Cloud view. The result of human pose estimation algorithm is transformed to 3D space and depicted with red spheres. The green sphere show the result of the motion planning algorithm.

an anisotropic scaling in order to fit to the projection limits calculated in the previous step, as depicted in up-left side of Fig. 3.6(up). Since scaling is a linear transformation we have one-to-one correspondence between the points of the motion on the “Canonical” space and the image space. At each time step one point of the motion is transformed from the “Canonical” space to the image space and then to the task space, i.e. the 3D space that the robot will normally operate, as shown in Fig. 3.6(bottom).

**Proposition 2.** *The transformation  $T_2$  (which is represented by the camera projection) from the Image space (i.e.  $IM = \{(u, v) : u \in [0, \mu], v \in [0, \nu]\}$ , where  $\mu, \nu$  are the image width and height respectively), to the Task space (i.e.  $V = \{(x, y, z) \in FOV\}$ ) at each time step is a bijection.*

*Proof:* We provide a descriptive and intuitive proof. The basic idea results from the fact that a ray starting from the camera’s optical center passes through the Image space and meets a point in the Task space. The latter is always true in an indoor environment, assuming that the areas of interest are visible by the camera. Therefore,  $\forall(\mathbf{u}, \mathbf{v}) \in IM \exists(\mathbf{x}, \mathbf{y}, \mathbf{z}) \in V$ . Using ray-casting technique it is easy to show that this point is unique, since the same ray cannot meet two points in the Task space at the same time. From the previous we can conclude that the transformation  $T_2 : IM \rightarrow V$  is one-to-one (injective) and onto (surjective), so it is bijective.

The latter stage of the reactive motion planning workflow is implemented by using the depth information from the image space. More specifically, from the depth data of the pixel, which corresponds to the motion point and of its neighboring pixels in the image space, we are able to directly calculate their 3D position. This group of points in the 3D task space form a small planar segment of the body part surface. Computing the mean of this group of points:

$$\mathbf{p}_k = [x_k \quad y_k \quad z_k]^T \triangleq [p_x^k \quad p_y^k \quad p_z^k]^T$$

where  $x_k, y_k, z_k$ , are the Cartesian coordinates for the number of points  $k = 1, \dots, n$ , and applying eigenvalue decomposition to the covariance matrix computed from these points, as follows:

$$C = \begin{bmatrix} C_{xx} & C_{xy} & C_{xz} \\ C_{yx} & C_{yy} & C_{yz} \\ C_{zx} & C_{zy} & C_{zz} \end{bmatrix},$$

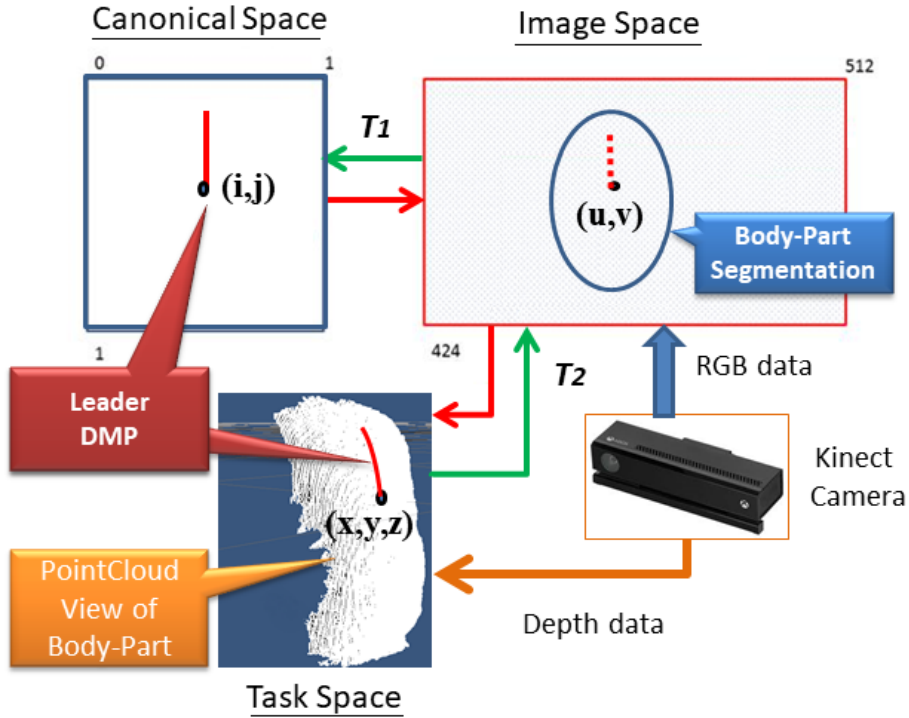


Figure 3.6: Perception-based motion planning. A leader DMP point  $(i,j)$  from the Canonical space is transformed with bijective transformation  $T_1$  to the point  $(u,v)$  of Image space and then with bijective transformation  $T_2$  to the point  $(x,y,z)$  of the body-part. From the neighborhood of  $(x,y,z)$  we are able to calculate the reference orientation.

where

$$C_{ij} = \frac{1}{n} \sum_{k=1}^n (p_i^k - m_i)(p_j^k - m_j),$$

and

$$\mathbf{m} = \frac{1}{n} \sum_{k=1}^n \mathbf{p}_k \triangleq [m_x \quad m_y \quad m_z]^T$$

with  $i, j = \{x, y, z\}$ , we are capable of determining the 6D reference pose for the robot. The 3D point, which the robot's end effector should meet, equals to the mean point of the group (presented with green spheres in Fig. 3.5b and 3.4a), whereas the orientation is calculated with the aid of the eigenvectors of the covariance matrix. The eigenvectors resulting from this decomposition correspond to the principal axis of the 3D data and more specifically, the normal direction of the planar segment is the axis that corresponds to the minimum eigenvalue, i.e. the direction of minimum variance of the data. Considering this set of vectors as the reference orientation for the end-effector of the robot, we are able to calculate the roll, pitch, yaw angles from the robot base frame, which the robotic manipulator should follow. The normal vector to the surface is used in the definition of the desired perpendicular distance, that the robot should keep according to the currently executed washing task. For showering tasks this distance is planned to be greater than zero, whereas for scrubbing or wiping tasks this distance should be zero or below zero adjusting in this way indirectly the contact force. Hence, the aim of this approach is to provide the appropriate reference position and orientation, in order for the robot to operate

in a perpendicular direction to the body part surface. The latter will allow smoother and accurate surface tracking techniques and proper force exertion to the human.

One major issue of this approach is the visual occlusion of the surface, which occurs during the robot's operation. This problem is tackled by adjusting the size of the neighborhood of pixels mentioned above. The larger occlusion occurs, the larger the neighborhood should be so we can locally reconstruct the missing depth information from the surrounding pixel's depth.

**Remark 2.** *The size of the robotic end-effector should be related to the curvature of the surface area. For example, if the robotic arm is large and causes a large visual occlusion, the local estimation of surface's curvature would be coarse in a highly curved area.*

**Remark 3.** *The reconstruction of the missing depth data from Kinect sensor can be solved with efficient image in-painting techniques presented in [203, 204]. The implementation of these computer vision algorithms is out of the scope of this thesis. In our implementation we apply a planar fit in the missing data. In addition, the problem of missing visual data is highly reduced in multi-camera systems such as the I-Support.*

Additionally, the described bijective transformations serve as a feedback to the controller as well. For example obstacle areas in the Task space (e.g. the hands of the user, or injuries on the back region) which are visible by the camera can be transformed back to the "Canonical" space by using the inverse procedure. In more detail, the black region in Fig. 3.7 represents a bandage on a body-part, which covers an injured region. This region is visually perceived and is transformed back and maximizes the values of the navigation function vector field in the corresponding coordinates. This modification will affect the

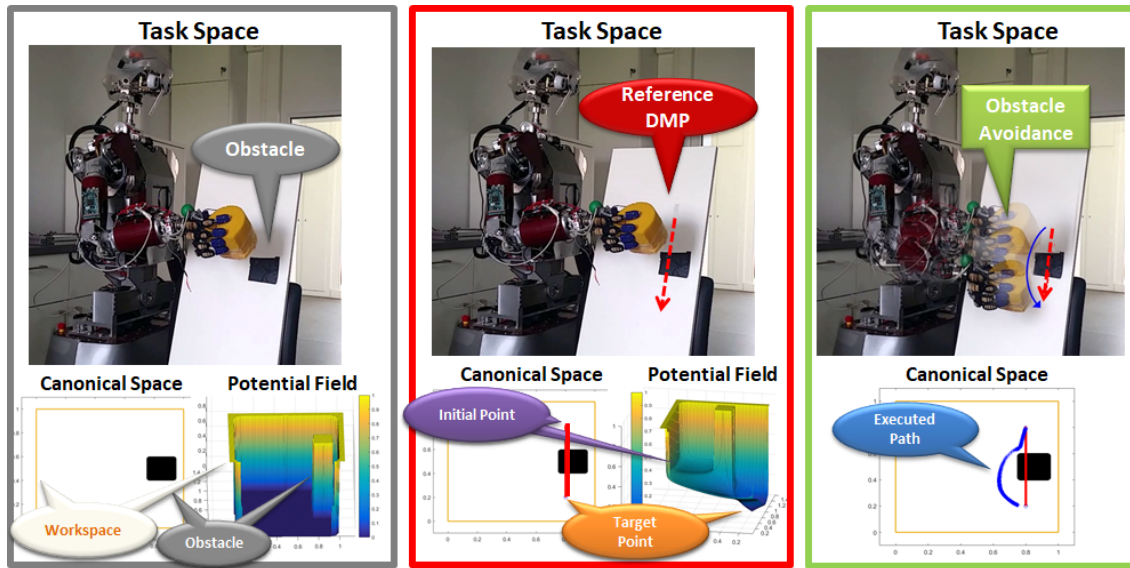


Figure 3.7: **Left:** An obstacle area (e.g. injury depicted with black patch) is detected in the Task space and transformed back to the Canonical space. The Navigation Function potential field is maximized in the corresponding area and the boundary of the workspace. **Middle:** The leader DMP path (red) is defined and an attractive vector field leads to the target point. **Right:** The controllers output is the blue path and is executed by the robot, avoiding the sensitive injured area. After the obstacle avoidance the end-effector's motion converges again the indicated linear motion primitive.

execution (blue path) of a demonstrated leader DMP (red path) which passes through this area, preventing the robot from washing this sensitive area. Therefore, the described approach provides augmented perception properties to the washing system, which include user motion compensation, adaptability to different body-part size together with obstacle avoidance.

### 3.3 Perception-Based Interaction System

If the desired washing movement is simple and predefined, a vision-based controller described in Sec. 3.2.2 can successfully adjust trajectory points one-by-one on a dynamical surface to generate a desired action. In the meantime, if the surface has known structure and does not change significantly during the motion evolution, CC-DMP described in Sec. 3.2.1 can flexibly generate complex trajectories learned by demonstration and adapt the movement to the surface's already modeled dynamic behavior.

However, in a washing case study, the size of each body-part differs among users and the body shape may change during the washing procedure, thus, we cannot generate an appropriate motion by pure imitation learning which cannot generalize for a relatively large change in the environment. On the other end, a pure perception-based controller cannot generate human-demonstrated washing trajectories. Furthermore, the preferences of each user may differ or change during the washing procedure, which requires the online modifications of motion parameters (e.g. amplitude, velocity). Therefore, this online motion modification requires the properties of a dynamical system such as CC-DMP.

To cope with the above requirements and constraints, we propose a hierarchical motion planning system, shown in Fig. 3.8, which merges the above DMP approach with an online visual perception loop, to achieve more robust behavior and to increase the capabilities of

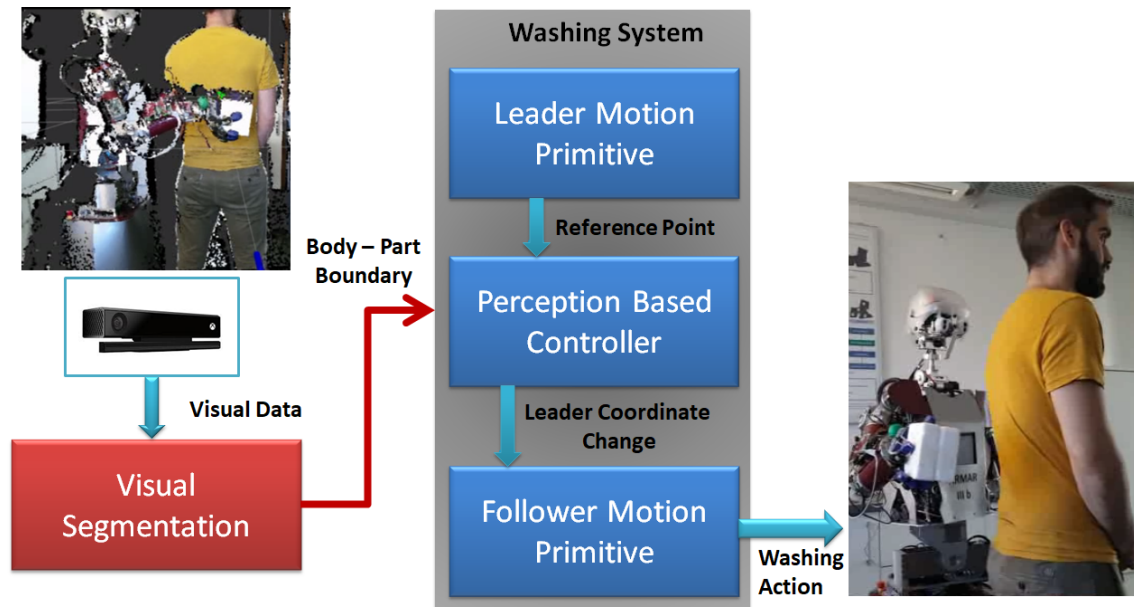


Figure 3.8: Perception-based motion planning system (implementing a washing sequence). The output of the body-part visual segmentation and the depth data provided by the camera is the input of this system, while the output is the target washing action of the robot's end-effector.



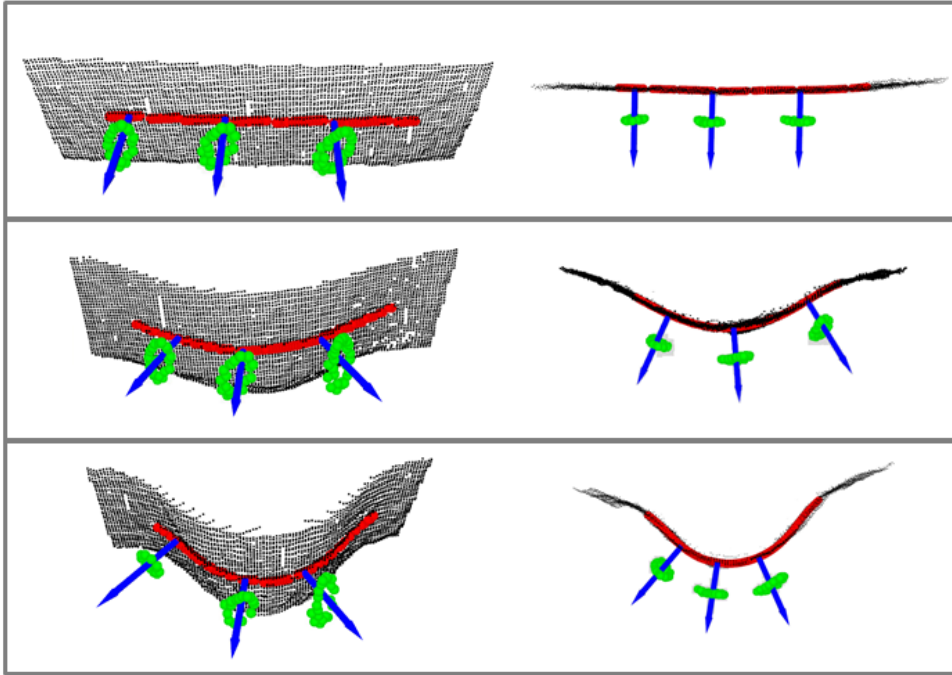


Figure 3.9: Adaptation of a linear leader DMP (red) on a deformable surface (PointCloud view). The normal vector (blue) and the application of a follower periodic washing action is demonstrated on several segments of the path. Perspective and top views of a surface are depicted, subject to several unknown levels of deformation. **Top:** No deformation. **Middle:** Medium deformation. **Bottom:** High deformation.

the system. In this system, we consider the discrete part of a washing action as the leader and the periodic pattern as the follower. The learned leader’s motion primitive outputs a reference point in the “Canonical” space, which is followed by the Navigation Function controller. The output is adjusted in the body-part extends and then transformed on its surface (see Fig. 3.6). The leader global pose is calculated by the analysis of camera’s depth data in a small neighborhood of the visually segmented target area as described in Sec. 3.2.2. In the latter step of this workflow, the follower movement primitive calculates the next point in the leader’s local coordinate system, then transforms it to the global or robot’s coordinate system. The final step is to use inverse kinematics to calculate the next required joint configurations of the robot and its low-level controller to drive the robot’s end-effector to the next desired pose.

The time and spatial adaptation, together with the decomposition of the learned washing actions allows for planning of a large repertoire of motions and adaptation on deformable surfaces as well. This repertoire includes different combinations of discrete and periodic actions, which may vary according to the washing sequence (e.g. pouring water, scrubbing, soaping etc.) decided by the user or the health-care expert. It also includes the capacity of the perception-based system for on-line adaptation on large and a-priori *unknown surface deformations* of the target part. An indicative example is presented in Fig. 3.9, in which a linear discrete motion (red) is adapted on a surface of unknown, but visually perceived curvature and deformation. The estimated local vector (blue) and the execution of a cyclic periodic pattern (green) are also demonstrated in several segments of the leader’s path. The local curvature estimation at each time step not only compensates for the surface’s motion and deformation, but also permits the regulation of the perpen-

dicular distance of the robot’s end-effector to the surface. This regulation enables the execution of actions that involve physical contact (e.g. scrubbing), thus also indirectly involving the application of forces without any additional feedback, as well as actions that involve no contact with the surface (e.g. pouring water).

### 3.4 Learning from Demonstration Using Navigation Functions

Washing action learning is an interactive task, which combines the execution of a complex motion relatively to the body part. In Section 3.2.1 a DMP a leader-follower framework has been described, which takes the environment’s motion into consideration. However, learning robotic actions with DMPs cannot incorporate multiple demonstrations and the subsequent planning does not consider the presence of obstacles in the workspace. In previous works [205, 206, 207] the authors combined DMP approach with Dynamic Potential Fields in order to achieve obstacle avoidance. However, the appearance of local minima can trap the agent before reaching its destination.

In this Section, a Navigation Function (NF) approach is proposed as an alternative approach for learning the way an expert clinical carer executes the bathing activities by means of constructing repulsive potential fields (“virtual obstacles”). The interactive trajectories demonstration is realized in 3D space and are transformed to the Canonical space by taking advantage of the appropriate transformations as shown in Section 3.2.2. In this space, a set of virtual obstacles is calculated so that the trajectory produced by a NF based navigation resembles the human trajectories, in effect, the human trajectory is represented in the virtual obstacles. Furthermore, we conclude this chapter by proposing an extension of our planning framework, in order to smoothly integrate our learning method into the system.

#### 3.4.1 Learning of Discrete Interactive Motions

In this Section we focus on deriving an alternative learning strategy for the discrete part of interactive actions, which constitutes the main part of the motion. Following the analysis presented in Section 3.2.2 analysis the control problem is reduced to an equivalent problem in the 2D Canonical space. Using this transformation, we shall use this 2D space for our control and learning schemes.

Assume that we have a set of  $T_{exp} \in \mathbb{N}^* \triangleq \mathbb{N} \setminus \{0\}$  demonstrated trajectories by nursing experts,  $E_n$ ,  $n \in N_{exp} \triangleq \{1, 2, \dots, T_{exp}\}$ . Each of them is a set  $E_n \triangleq \{\mathbf{q}_n(t_m)\}_{m \in N_n}$ ,  $N_n \triangleq \{1, 2, \dots, T_n\}$ ,  $n \in N_{exp}$  of  $T_n \in \mathbb{N}^*$  configurations  $\mathbf{q}_n(t_m) \in \mathcal{W} \subset \mathbb{R}^2$  recorded in subsequent time instants  $t_m \in [0, +\infty)$ , which are indexed in increasing order  $t_m < t_{m+1}$ ,  $\forall m \in N_n \setminus \{T_n\}$ ,  $\forall n \in N_{exp}$ . Also, assume that the desired destinations  $\mathbf{q}_{dn} \in \mathcal{W}$ ,  $n \in N_{exp}$  are provided.

The proposed solution is to produce a suitable vector field, the motion under which replicates the demonstrated data. This approach is clearly advantageous, as the incorporation of the learned data in a vector field allows their immediate combination with real obstacles detected by the perception system. The problem can then be stated as depicted in Fig. 3.10. We intent to use the experimental data  $E \triangleq \{E_n, \mathbf{q}_{dn}\}_{N_{exp}}$  in order to find the obstacle function  $\beta \in C^2(E^n, \mathbb{R})$ , so that the produced trajectory from the controller described in Section 3.2.2:

$$\dot{\mathbf{q}} = -\nabla_{\mathbf{q}}\varphi(\mathbf{q}) \quad (3.9)$$

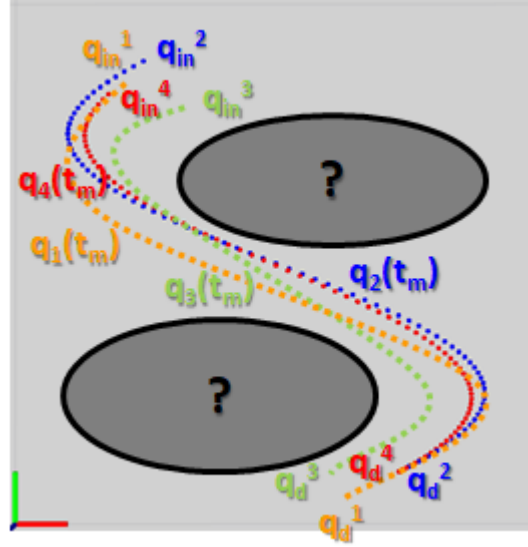


Figure 3.10: Problem Statement: Find the obstacle functions based on the collected experimental human like trajectories  $\mathbf{q}(t_m)$ , to ensure that the new controller-based produced motion will always remain within the problem's domain.

is similar to the experimental trajectories, defined by an appropriate similarity measure. Since it is not a simple path similarity problem, we propose to use the Fréchet distance [208], as the distance metric between two trajectories in the state space. This is a measure of similarity between two curves, that takes into account the flow of two curves, because the pairs of points whose distance contributes to the distance sweep continuously along their respective curves. This metric is defined as the maximum distance between two agents moving forward on the two trajectories and actively trying to keep their distance to a minimum and it is more “natural” way of estimating the distance of two curves, in a setting such as ours. In layman terms, the output of the controller should approximate the experimental trajectories. For ease of the reader, the definition of the Fréchet distance [208] is provided below:

**Definition 1.** Let  $S$  a metric space. A curve  $A \in S$  is a continuous map from the unit interval into  $S$ , i.e.  $A : [0, 1] \rightarrow S$ . A reparameterization  $\alpha$  is a continuous, non-decreasing, surjection  $\alpha : [0, 1] \rightarrow [0, 1]$ . Let  $A$  and  $\Lambda$  be two given curves in  $S$ . Then, the Fréchet distance between  $A$  and  $\Lambda$  is defined as the infimum over all reparameterizations  $\alpha, \lambda \in [0, 1]$  of the maximum over all  $t \in [0, 1]$  of the distance in  $S$  between  $A(\alpha(t))$  and  $\Lambda(\lambda(t))$ . In mathematical notation, the Fréchet distance  $F(A, \Lambda)$  is defined as:

$$F(A, \Lambda) = \inf_{\alpha, \lambda} \max_{t \in [0, 1]} \{d(A(\alpha(t)), \Lambda(\lambda(t)))\} \quad (3.10)$$

where  $d$  is the distance function of  $S$ . □

This coupling measure takes the value zero when the trajectories are equal and grows positively as the curves become more dissimilar.

### Obstacle Function Resolution Formulation

The main goal is to formulate an appropriate equation, the resolution of which will produce the unknown obstacle function  $\beta$  (the repulsive field). The proposed problem formulation



guarantees that the produced potential field, based on the constructed NF, models the carer's motions during the washing tasks. In other words, this approach creates the learning by demonstration procedure of washing models.

We can calculate the derivative of the NF (3.4):

$$\nabla_{\mathbf{q}}\varphi(\mathbf{q}, \mathbf{q}_d) = \frac{\partial\varphi}{\partial\gamma}(\gamma, \beta) \cdot \nabla_{\mathbf{q}}\gamma(\mathbf{q}, \mathbf{q}_d) + \frac{\partial\varphi}{\partial\beta}(\gamma, \beta) \cdot \nabla_{\mathbf{q}}\beta(\mathbf{q})$$

Therefore, it holds that:

$$\frac{\partial\varphi}{\partial\gamma} = \beta \cdot A, \quad \frac{\partial\varphi}{\partial\beta} = -\frac{\gamma}{\kappa} \cdot A, \quad \nabla\gamma = 2 \cdot (\mathbf{q} - \mathbf{q}_d)$$

where  $A = (\gamma^\kappa + \beta)^{-\left(\frac{\kappa+1}{\kappa}\right)}$ . Also, based on the obstacle function definition, it holds that:

$$\nabla\beta = \beta \cdot \sum_{i=0}^P \frac{\nabla\beta_i}{\beta_i}$$

In this work, we form an obstacle function structure  $\beta_i$ , for  $i = 1, \dots, Q$ , with  $Q < P$ , where  $P$  is the total number of obstacles, for simplicity as ellipsoid function and thus, the main goal is to compute the necessary parameters in order to construct these "virtual obstacles", i.e. their centers and the length of their principal axes.

In [62], the solution is based on a gradient descent method, that produces the obstacle function. Moreover, the authors use the gradient of the experimental trajectories in order to compute the cost function to be optimized. This resolution is feasible for convex case studies, otherwise the gradient descent method may be trapped in local minima.

### Non-Convexity of the Inverse Problem

When the workspace contains obstacles in its interior, the NF becomes highly entangled w.r.t. the position and the general form of the obstacles. Due to this aspect, the estimation of the appropriate set of parameters for the obstacles that generated a NF with the desired form equates into solving a problem that is non convex. The proof of this statement is presented next.

Assume the problem of a point robot motion planning on a 2D workspace. Let us assume for simplicity that the initial and desired configurations of the robot both lie on

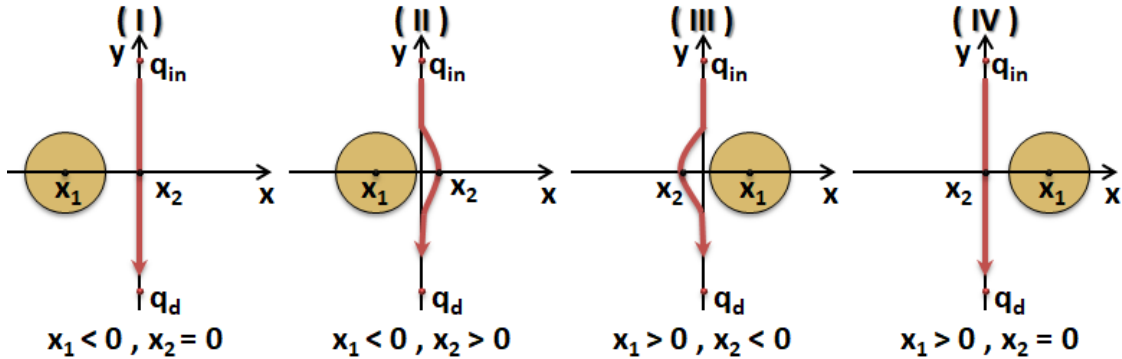


Figure 3.11: Point robot motion planning problem on a 2D workspace that contains one cyclic obstacle.

the y-axis, anti-symmetrically of the x-axis. The optimum path to resolve this motion planning problem is for the robot to follow a path that lies on the y-axis (following the line  $x = 0$ ). As one simple cyclic obstacle appears in the workspace, the motion planning resolution of this case depends on the relative position of the obstacle. Assuming that  $x_1$  is the obstacle's center on x-axis and  $x_2$  is the distance of the resulted path from the y-axis, we can distinguish four general cases for the obstacles relative position w.r.t y-axis, as described in Fig. 3.11. As the obstacle is away from the y-axis there are two cases, when the obstacle region is in negative side of y-axis (**I**), and when it is in the positive side of y-axis (**IV**), Fig. 3.11. In these cases the resulted optimal path remain on the y-axis and therefore the distance  $x_2 = 0$ . In the other two cases of Fig. 3.11, it holds that for case (**II**) the distance  $x_2 > 0$ , while for case (**III**) it switches  $x_2 < 0$ . Thus, the relation between  $x_1$  and  $x_2$  is described in Fig. 3.12. This figure demonstrates the highly non-convex character of the optimization problem. On that figure, a point on the left side of the diagram (with negative  $x_2$  deflection) cannot move, using gradient descent to the right side of the diagram (positive  $x_2$  deflection). If the initial position of the obstacle is point **Initial**, Fig. 3.12, a gradient descent will push away the obstacle towards point **Final**, i.e. will push the obstacle further away to the left. It is not possible for a gradient descent method to converge to point **Target**, i.e. an obstacle to the right of the y-axis. A gradient descent algorithm will result in the obstacle being “pushed away”. Therefore there is no way to resolve this problem with a simple gradient descent method.

### Non-Convex Inverse Problem Resolution

The recorded experimental data are usually very noisy, as it can be realized from the second column of Fig. 3.13. A numerical differentiation scheme would result in excessive noise added to the system. Thus, we propose to resolve the optimization problem in the entire recorded trajectory, by using the Fréchet distance metric (*Definition 1*).

Another important issue is that the problem is highly non-convex, as it is described in the previous subsection. Therefore, the optimization procedure, in order to resolve the inverse problem, that is based on a simple gradient descent method cannot result to a feasible solution and requires the use of some kind of heuristic approaches. In this approach, we used a Genetic Algorithm (GA) solution as the form of the problem is naturally suited for such an approach. In particular, the parameters of the obstacles are naturally suited genes for a GA, since, to an extent, the positions of the obstacle, the size

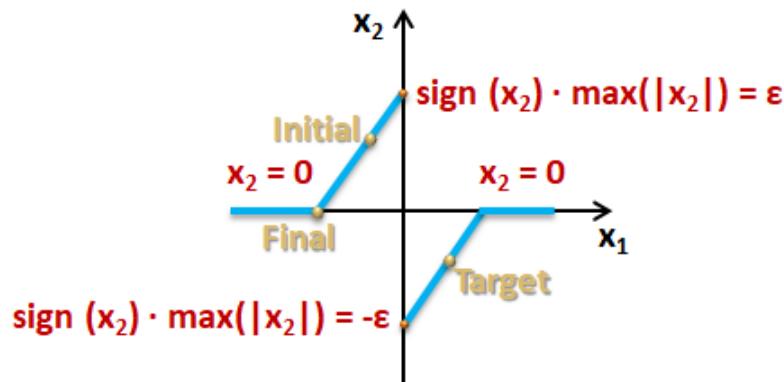


Figure 3.12: The relation between the the obstacle's center on x-axis  $x_1$  and the distance of the resulted path from the y-axis  $x_2$ .

and its form have a differential effect on the form of the NF trajectory and, therefore, to the cost of the optimization function.

In order to augment the GA search, a gradient descent method [209] is used, as local optimization scheme for every member of each generation, as:  $x^{(j+1)} = x^{(j)} - \omega \cdot \nabla \mathbf{C}$ , minimizing the cost function  $\mathbf{C}$ , where  $x^j$  denotes the obstacle parameter values at the  $j^{\text{th}}$  iteration of minimization procedure and  $\omega$  is the design space cost functional gradient step. Obviously, this augmentation will have the detrimental effect described above for some sets of solutions (will drive the obstacles away from the correct positions).

Then, it is necessary to formulate the optimization cost function  $\mathbf{C}$  for the discrete samples, as following:

$$\mathbf{C} \triangleq \frac{1}{T_{exp}} \cdot \sum_{n \in N_{exp}} F(R, E_n) \quad (3.11)$$

where  $F$  is the Fréchet distance defined by (3.10),  $E_n$  is an experimentally measured trajectory, while  $R$  is the estimated trajectory composed by the candidate obstacle function  $\beta$ . Each estimated point  $(\mu + 1)$  of the trajectory  $R$  is computed based on the previous point  $(\mu)$  by the equation:  $\mathbf{q}^{(\mu+1)} = \mathbf{q}^{(\mu)} + \Delta t \cdot \dot{\mathbf{q}}$ , where  $\Delta t$  is the time step between the points and  $\dot{\mathbf{q}}$  is calculated as in (3.9). The C code for the Discrete Fréchet Implementation was adopted from [210]. The GA [211] was also programmed in C/C++ and was adopted from [212].

### 3.4.2 Interactive Motion Reproduction

An indicative example of implementing this NF-based approach is illustrated in Fig. 3.13, where a whole sequence of the motion generation process is shown, including demonstration, pre-processing, learning, and reproduction, corresponding to a specific washing action such as water pouring. More specifically, the demonstration is performed in the physical

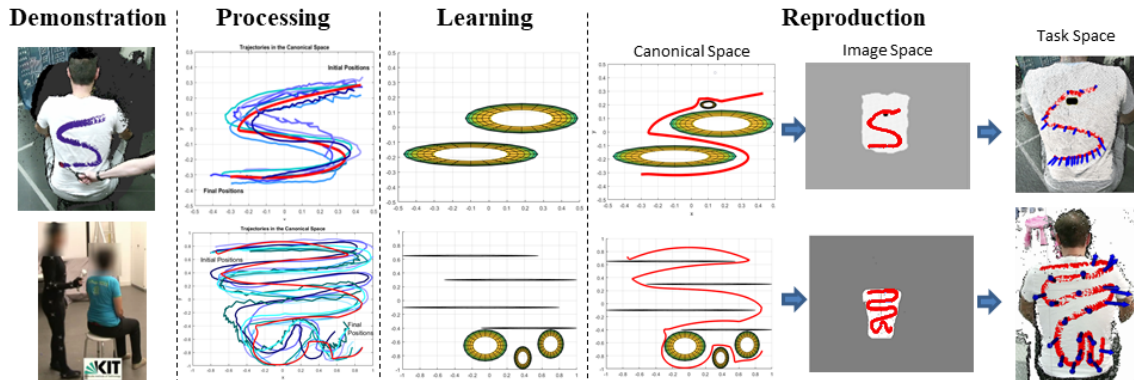


Figure 3.13: Demonstration, Processing, Learning and Reproduction procedures. The **Demonstration** trajectories are performed in physical space by professional nursing personnel. The demonstration data are projected into the  $2D$  canonical space, in which are post-**Processed**. In the **Learning** phase virtual obstacles are learned using the demonstration data and the proposed NF approach. During the trajectory **Reproduction** phase a NF controller is employed to reproduce the washing action. The learned trajectory (red) is then adapted on the visually segmented back region (PointCloud view) of a subject, via the image space. **Top**: A simple showering sinusoidal trajectory is visually recorded, learned and reproduced. **Bottom**: A more complex showering trajectory is obtained from the KIT whole-body human motion database [1], learned and reproduced.

space, hence a post-processing procedure follows, in which the demonstration examples are projected in a  $2D$  spatially normalized canonical space, following the notation of Section 3.2.2. In this simplified space the demonstration paths are denoised and the discrete part is separated from any periodic motion, as is described in the second column of Fig. 3.13. In this form the demonstration data are used in the learning procedure, in which a set of virtual obstacles is generated forming a repulsive landscape, which encodes the demonstrated washing skill.

The “virtual obstacle” function  $\beta$  (structure of repulsive potential field) is then used in the reproduction phase. At this stage an initial and goal configuration is provided to the system and fed into the motion tracking controller (Sec. 3.2.2) to generate a washing action, which satisfies the constraints imposed by the health-care specialist and the constraints imposed by the region of action (e.g. the back of the user). Based on the output of the controller, the next desired position is extracted in the  $2D$  canonical space and propagated to the  $3D$  task space for execution from the assistive robotic device.

### 3.5 Chapter Outcomes

In this Chapter, the theoretical contributions on learning interactive motions from demonstration and reactive motion adaptation on curved and deformable surfaces is presented. Particularly, we propose an integrated system based on DMP approach, which can learn and encode the demonstrated actions, imitating the human actions. The learned motions are then adapted to the user’s body parts compensating for their motion or deformation. The latter is achieved with a motion planning algorithm, which is based on visual perception with RGB-D cameras and the establishment of bijective transformations, redefining the motion tracking problem in a  $2D$  spatially normalized space. Accurate tracking of the learned actions is then realized with a Navigation function controller with proven globally uniformly asymptotic convergence.

The description of an alternative Learning from Demonstration method is concluding this chapter, which is based on Navigation functions, in order to capture the way an expert human performer (in our case, a clinical carer) executes the desired motions by means of construction repulsive potential fields (“virtual obstacles”). Demonstration of the desired trajectories is realized in  $3D$  space and these trajectories are then transformed to a  $2D$  spatially normalized space with the use of the bijective transformations. In this space, a set of virtual obstacles is calculated so that the trajectory produced by a NF based navigation resembles the human trajectories.

This perception-based motion planning approach (based on direct visual feedback from an RGB-D sensor) has been implemented on the I-Support soft robotic platform (depicted in Fig. 3.1), and has also been tested on the ARMAR-III humanoid robotic platform developed at KIT (depicted in Fig. 3.7). Experimental results of these implementations along with preliminary results of the learning with NF method are presented in Chapter 5. This approach also serves as a baseline direct visual planning (DVP) approach for comparative analysis with a more generic mesh-based interactive approach proposed in the following chapter, which is presumably more powerful in terms of better handling dynamic deformations and occlusions. Comparative experimental analysis results are presented in Chapter 6.

## Chapter 4

# Mesh-Based Motion Planning and Interaction Control

Aiming towards smoother and more robust contact not only with the human body but also with other deformable objects, we describe in this chapter a physical interaction framework based on deformable object modeling. Due to the fact that the integration of a conventional force torque sensor to the structure of I-Support system's soft-robotic arm, which operates under highly humid conditions in the bathroom environment, is not feasible, we investigated robotic control techniques without the use of force feedback, which are based on stiffness control of the robot. Simultaneously, in order to achieve high precision both on task execution and force, enhanced environment perception abilities has to be incorporated to the system. In particular, the use of visual information as presented in the previous chapters cannot guarantee the continuity of the generated motions across the whole duration of the motion. The bijectivity proof provided in Chapter 3 holds only for one time step, since the number of pixels associated with a body part will change if the user changes his position. This performance is acceptable for the purposes of a bathing robot. However, in an attempt to generalize interactive tasks execution in other applications, accurate real-time modeling of a deformable object is required. Deformable object modeling with mesh structures was a common practice in computer graphics society for decades. Additionally, the recent advances of computer vision techniques, which are able to accurately determine the shape of the human body from a monocular camera [3, 83] as depicted in Fig. 4.1, has provided a wide spectrum of visual perception abilities for human-robot physical interaction tasks. These technological advances have motivated the development of an algorithm, which effectively uses the results of object modeling techniques (Sec. 2.4) combined with mesh parameterization (Sec. 2.5) and is able to plan efficiently both non-contact and contact surface robotic actions.

### 4.1 Related Work

Autonomous interaction of robotic manipulation systems with various objects constitutes undoubtedly a vast research topic, which has attracted a lot of attention and research effort for nearly three decades now. Despite the fact that all these efforts have made significant progress in the direction of rigid object manipulation, which is now considered as a mature field in robotics [213], the study of deformable objects still remains limited and constitutes a challenging research field, as also described in a recent review paper [214]. In real world applications, the type of materials that a robot is called to interact

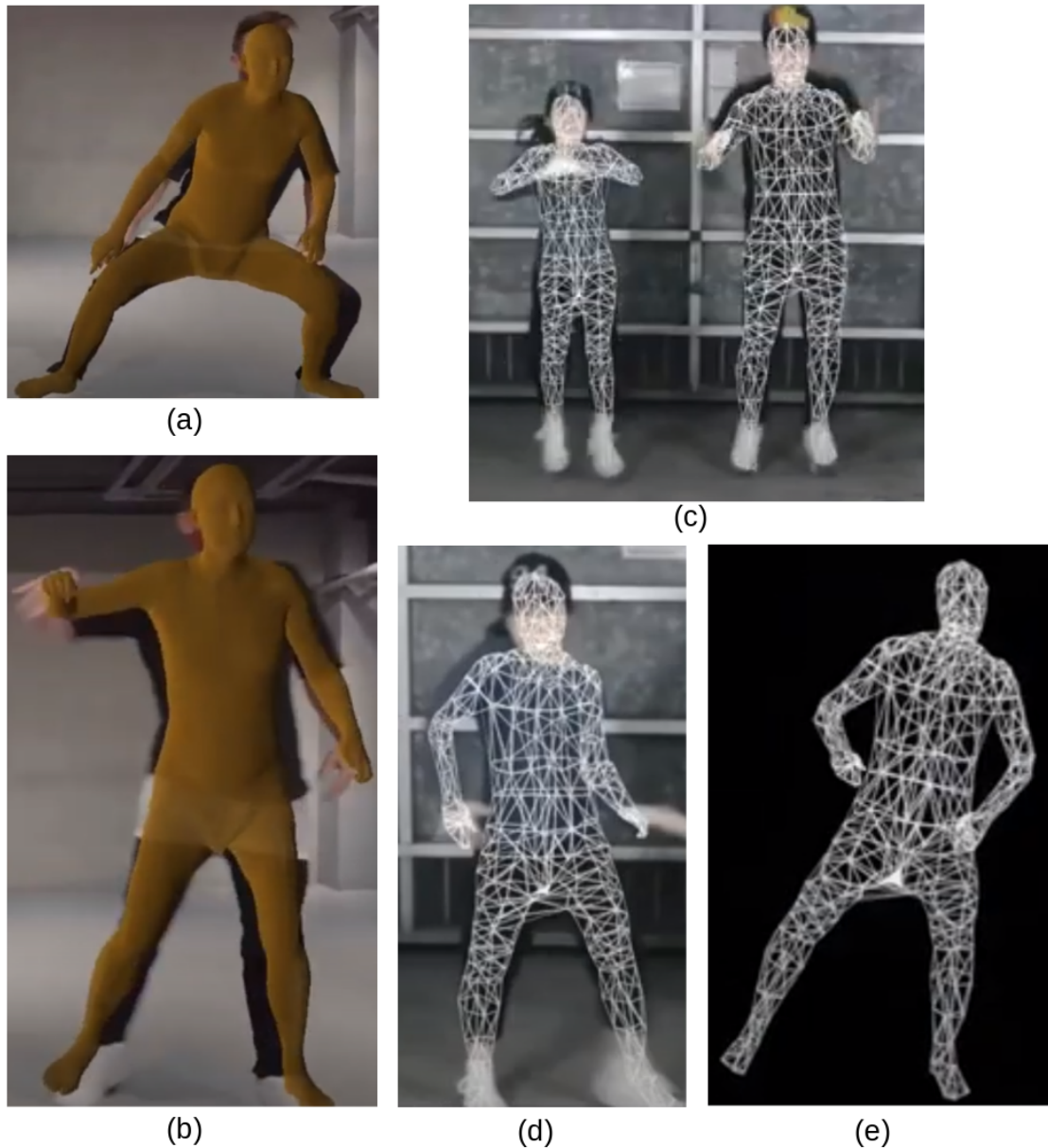


Figure 4.1: Human shape estimation from monocular camera. Human shape is presented in a textured mesh for different instances of human motion in (a) and (b). A multi-person instance is presented in (c). Detailed views of a mesh representation of human shape in (d) and (e). The depicted representation can easily be integrated in the proposed approach. Images used after written consent of the authors of [3].

with are usually non-rigid, since our world is formed mainly of deformable materials, the flexibility of which varies significantly. In order to achieve accurate and efficient robotic manipulation, a complete modelling of the manipulated object is required and this has to be coupled with the control process on-line. Different control and motion planning strategies have been developed for different kinds of objects. Early work of Tanner et al. in [215] and later in [216] study the control aspects of two mobile manipulators carrying a deformable cloth-like object. In general, garments and cloth-like objects have drawn a lot of research effort, due to their easier modeling than other 3D deformable objects and

clear visual structure. Yinxiao Li et al. in a series of papers propose solutions for various interaction tasks with garments such as real-time pose estimation [217], unfolding [218] and folding [219]. Moreover, a complete pipeline of the autonomous folding task is presented in [220], which includes a vision-based garment grasping from a pile of clothes by a dual arm robot, classification and proper unfolding on a table (previously presented in [221]) and a folding technique executed by the robotic system based on dynamic programming. Additionally, in [222] a geometric approach for garment unfolding is proposed, taking advantage of the clear visual structure of clothes to estimate appropriate grasping points. Another challenging task is the autonomous paper origami folding which was implemented in [223], employing a two-handed multi-fingered robot and depth vision system. A dual arm robot is also developed in [224] for industrial automatic electronic soldering tasks on flexible PCBs.

Many surgical tasks require the interaction of a robotic manipulator with the surface of an organ or tissue. Papers involving robotic manipulators combine visual techniques with FEM physical simulation and a force sensor [225], in order to develop real-time tracking system of soft tissues' deformation produced by a manipulator. However, non-visual techniques proposed in [226] exploit the motion of a robot and more specifically motion planning algorithms and a hybrid force-motion controller, to estimate the shape and impedance parameters of tissue. Motion plans are also computed in [227] for a 6DOF gripper for automated tissue retraction given the model of tissues in the vicinity of areas of interest. In a similar context concerning interaction with dynamically deforming organ tissues in surgical robotics, active motion compensation constitutes another open research topic, with a lot of effort focusing on beating heart surgery scenarios. In [228] a predictive force control algorithm is proposed to compensate priorly known motions generated both from breathing and beating heart, whereas a recent paper [229] proposes an impedance control scheme both for motion compensation in the slave robot and haptic feedback to the master robot in a tele-operation scenario. Another tele-operation approach, which integrates a visual system for motion perception, is presented in [230] using the da Vinci Research Kit (Intuitive Surgical Inc.). Its perception system estimates the distance from a rigid object (moved by an external device), which is used as reference for the da Vinci patient side manipulators to track motion in real time. Another example of visually guided surgical device is presented in [231]. Leonard et al. have developed STAR system, which includes a 7DOF robotic manipulator and a monocular camera and is dedicated to automate laparoscopic suturing. It uses vision guided system, through which the doctor can also determine the suturing points, and its accuracy and efficiency was tested on planar phantoms.

Relevant interactive tasks are also met in industrial applications, with some recent research work starting to focus on how to handle similar constraints involving real-time physical interaction with the surface of dynamically deforming objects in a robot cell, like in [232] where a one dimensional FEM model is used for bimanual robotic cleaning of a deformable object.

## 4.2 Problem Formulation

The problem considered in this chapter concerns interaction control of a robotic manipulator executing a task on the surface of a curved and deformable object. The main objective of the manipulator is to navigate over a part of an object's surface and physically interact with it, while the object is actively or passively deforming. Although, the initial shape of the object may be known, we assume that its deformation (active or passive) evolution over



time is unmodeled, i.e. there isn't a function of time describing its motion. There exists a large variety of typical examples that involve a robot executing a practical task over the surface or in contact with an object, either rigid (e.g. spraying, polishing, machining or assembly) or deformable (e.g. soft tissue manipulation, physical interaction with human body, beating heart robot assisted surgery).

In all the above cases of interactive tasks, the control of the (physical or non-physical) interaction between the robot manipulator and the surface of the dynamically deforming object is crucial for the success of the planned task. In particular during contact, the object sets constraints on the paths that the end-effector can follow. Hence, if the task is not accurately planned, the use of a pure motion control strategy in constrained motion scenarios may lead to failure. Accurate planning would, successively, require an accurate model both of the robot and the object. Although, modelling of the manipulator can be achieved with high precision based on kinematic and dynamic analysis, the motion model of a deformable object is difficult to obtain even if the original shape is described in detail. The modelling errors will give rise to planning errors along time and in turn, contact forces will be applied on the end-effector causing a deviation from the desired trajectory. At the same time, the robot's control system will react to reduce such deviation, resulting in a build-up of the contact force, until saturation of the actuators is reached or breakage of the parts in contact eventuates.

The effect of the phenomenon described above can be decreased if a compliant behaviour is ensured during the interaction. Compliant interaction behaviour can be achieved either passively or actively. Passive compliance can be realized via the structural compliance of robot's links, joints (e.g. soft robot arms [81, 76]) or end-effector (e.g. remote center of compliance for industrial applications [233]). Despite the fact that the passive approach is cheap and simple, it can only deal with small position and orientation deviations and cannot guarantee that high contact forces will never occur. On the other hand, active compliance can be established with either indirect force control schemes or direct force control schemes, which use as feedback force measurements describing the state of interaction. However, the lack of reliable force measurements in many real robotic systems has led us to the adoption of an indirect force control strategy. More specifically, the **geometrically consistent active stiffness** control method is adopted, described in [234], instead of other indirect force control methods such as impedance control, due to unavailability of an explicit deformation model. For the sake of completeness of this chapter we will briefly describe this method below.

#### 4.2.1 Mechanical stiffness

Consider the case in which two rigid bodies E representing the end-effector and D for the desired contact point on the surface are elastically coupled. The reference frames  $\Sigma_e$  and  $\Sigma_d$ , which are attached to E and D respectively, coincide at the equilibrium. The compliant behaviour near the equilibrium can be described by the linear mapping

$$h_d^d = K \delta x_{ed}^d = \begin{pmatrix} K_t & K_c \\ K_c & K_o \end{pmatrix} \delta x_{ed}^d \quad (4.1)$$

where  $h_d^d$  is the elastic wrench applied to body D, expressed in frame  $\Sigma_d$ , in case an infinitesimal twist displacement  $\delta x_{ed}^d$  of frame  $\Sigma_e$  with respect to frame  $\Sigma_d$  (expressed in frame  $\Sigma_d$ ) is present. Equivalently, the twist displacement of Eq. 4.1 can be expressed in frame  $\Sigma_e$ , since the two frames coincide at equilibrium. Therefore,  $h_d^d = h_d^e$  and  $\delta x_{ed}^d =$



$\delta x_{ed}^e$ ; moreover, for the elastic wrench applied to body E,  $h_e^e = K_t \delta x_{de}^e = -h_d^d$  being  $\delta x_{de}^e = -\delta x_{ed}^d$ . This property of Eq. 4.1 is called *port symmetry*.

In Eq. 4.1,  $K \in \mathbb{R}^{6 \times 6}$  is the stiffness matrix, which is symmetric and positive-semidefinite, consisting of  $K_t \in \mathbb{R}^{3 \times 3}$  and  $K_o \in \mathbb{R}^{3 \times 3}$ , which are called translational stiffness and rotational stiffness respectively and are symmetric as well. Additionally, it can be shown that if  $K_c \in \mathbb{R}^{3 \times 3}$ , which is the coupling stiffness, is symmetric, there is maximum decoupling between rotation and translation. In this case, the point corresponding to the coinciding origins of the frames  $\Sigma_e$  and  $\Sigma_d$  is called the center of stiffness. There are special cases in which no coupling exists between translation and rotation, i. e., a relative translation of the bodies results in a wrench corresponding to a pure force along an axis through the center of stiffness; also, a relative rotation of the bodies results in a wrench that is equivalent to a pure torque about an axis through the center of stiffness.

Since  $K_t$  and  $K_o$  are symmetric, there exists a decomposition  $K_t = R_t \Gamma_t R_t^T$ , where  $\Gamma_t$  is a diagonal matrix whose elements are the principal translational stiffnesses in the directions corresponding to the columns of the rotation matrix  $R_t$  expressed w.r.t the frame  $\Sigma_e = \Sigma_d$  at equilibrium, known as the principal axes of translational stiffness. Similarly,  $K_o$  can be written as  $K_o = R_o \Gamma_o R_o^T$ , with  $\Gamma_o$  expressing the principal rotational stiffnesses around the axes corresponding to the columns of rotation matrix  $R_o$ , representing the principal axes of rotational stiffness. Moreover, assuming that the origins of  $\Sigma_e$  and  $\Sigma_d$  at equilibrium coincide with the center of stiffness, the expression  $K_c = R_c \Gamma_c R_c^T$  can be found, where the diagonal elements of  $\Gamma_c$  are the principal coupling stiffnesses along the direction corresponding to the columns of the rotation matrix  $R_c$ , known as the principal axes of coupling stiffness.

It is important to mention that the mechanical stiffness defined in Eq. 4.1, describes an ideal 6-DOF spring, which stores potential energy. An ideal stiffness has a potential energy function, which depends only on the relative pose of the two attached bodies and is port symmetric. The predominant behaviour of a physical 6-DOF spring is similar to an ideal one, however there are always parasitic effects causing energy dissipation.

### 4.2.2 Geometrically Consistent Active Stiffness

In order to achieve a geometrically consistent 6-DOF active stiffness between the robot's end-effector and the deformable object, a suitable control law is required. This control law should define the behaviour of the end-effector, under the application of an elastic wrench from the object. The expression and the properties of the elastic wrench (Eq. 4.1) for small displacements should be extended to the case of finite displacements. A finite displacement can be expressed, in the problem of robot - surface interaction control, as the relative pose of a desired frame  $\Sigma_d$  with respect to the end-effector frame. We can distinguish two cases: (a) The desired frame is put above the object's surface and hence the robot is not in contact with the object and (b) the desired frame is put below the object's surface, therefore the robot has contact with the object. Additionally, a suitable potential elastic energy function must be defined, in order to guarantee asymptotic stability in the sense of Lyapunov for both cases.

Introducing the robot kinematics and dynamics notation we start with the joint configuration and its time derivative is  $q := [q_1, \dots, q_n]^T$ ,  $\dot{q} := [\dot{q}_1, \dots, \dot{q}_n]^T \in \mathbb{R}^n$ . The generalized velocity of the end-effector is denoted by the twist vector  $v_e = [\dot{p}_e^T \ \omega_e^T]^T \in \mathbb{R}^6$  where  $\dot{p}_e$  is the translational velocity and  $\omega_e$  the angular velocity. It can be computed through the differential kinematics  $v_e = J(q)\dot{q}$  [235], where  $J : \mathbb{R}^n \rightarrow \mathbb{R}^{6 \times n}$  is the robot's geometric Jacobian. We define also the set  $\mathbb{D} := q \in \mathbb{R}^n : \det(J(q)J(q)^T) > 0$  which contains

all the singularity free configurations. The force  $f_e$  and the moment  $\mu_e$  applied by the end-effector to the environment are the components of the wrench  $h_e = [f_e^T \mu_e^T]^T$ . In addition, the end-effector pose can be expressed as  $x_e = [p_e^T \zeta_e^T]^T \in \mathbb{R}^7$ , where  $p_e$  denotes the position and  $\zeta_e$  denotes the orientation as a unit quaternion  $\zeta_e = [\phi_e \ \epsilon_e^T] \in \mathbb{S}^3$  with  $\phi_e \in \mathbb{R}$  and  $\phi_e^2 + \epsilon_e^T \epsilon_e = 1$ , expressed with respect to the robot base frame.

Let us consider the operational space formulation of the dynamic model of a rigid robot manipulator in contact with the environment

$$M_x(q)\dot{v} + C_x(q, \dot{q})v + g_x(q) = h_c - h_e \quad (4.2)$$

where  $M_x(q) = (JM(q)^{-1}J^T)^{-1} : \mathbb{D} \rightarrow \mathbb{R}^{n \times n}$  is the positive definite inertia matrix,  $C_x = J^{-T}C(q, \dot{q})J^{-1} - M_x(q)\dot{J}J^{-1} : \mathbb{D} \times \mathbb{R}^n \rightarrow \mathbb{R}^{n \times n}$  is the matrix including centrifugal and Coriolis effects, and  $g_x = J^{-T}g(q) : \mathbb{D} \rightarrow \mathbb{R}^n$  is the gravity term.  $M(q)$ ,  $C(q, \dot{q})$  and  $g(q)$  are the corresponding quantities defined in joint space. The vector  $h_c = J^T \tau$  is the equivalent end-effector wrench corresponding to the input joint torques.

If we make the simplifying assumption that the coupling stiffness matrix is zero, we can decompose the potential elastic energy in its translational part and its rotational part. More specifically the translational potential energy can be defined as

$$V_t = \frac{1}{2} \Delta p_{de}^T K'_{Pt} \Delta p_{de} \quad (4.3)$$

with  $\Delta p_{de}$  denoting the position displacement of the end-effector w.r.t the desired position,  $K'_{Pt} = \frac{1}{2}R_d K_{Pt} R_d^T + \frac{1}{2}R_e K_{Pt} R_e^T$  and  $K_{Pt} \in \mathbb{R}^{3 \times 3}$  symmetric and positive-definite.  $R_d$  and  $R_e$  are the rotation matrices corresponding to the desired pose and the end-effector pose respectively. The use of  $K'_{Pt}$  instead of  $K_{Pt}$  in (4.3) guarantees that the potential energy is port symmetric in the presence of finite displacements as well.  $K'_{Pt}$  and  $K_{Pt}$  coincide at equilibrium (i.e., when  $R_d = R_e$ ) and in the case of isotropic translational stiffness (i.e., when  $K_{Pt} = \kappa \mathbf{I}$ ). Calculating the derivative of the potential energy we have

$$\dot{V}_t = \Delta \dot{p}_{de}^{eT} f_t^e + \Delta \omega_{de}^{eT} \mu_t^e \quad (4.4)$$

where  $\Delta \dot{p}_{de}^e$  being the time derivative of the position displacement  $\Delta p_{de}^e = R_e^T(p_d - p_e)$  and  $\Delta \omega_{de}^e = R_e^T(\omega_d - \omega_e)$ . The vectors  $f_t^e$ ,  $\mu_t^e$  constitute the elastic wrench applied to the end-effector in the presence of a finite position displacement  $\Delta p_{de}$ . Rewriting this wrench in the robot base frame we have  $h_t = [f_t^T, \mu_t^T]$  in which

$$f_t = K'_{Pt} \Delta p_{de} \quad \text{and} \quad \mu_t = K''_{Pt} \Delta p_{de} \quad (4.5)$$

with  $K'_{Pt}$  the same as (4.3) and  $K''_{Pt} = \frac{1}{2}S(\Delta p_{de})R_d K_{Pt} R_d^T$  where  $S(\cdot)$  is the skew-symmetric operator performing the vector product. The moment  $\mu_t$  is null in the case of isotropic translational stiffness.

The orientation potential energy can be computed similarly with the form

$$V_o = 2\epsilon_{de}^{eT} K_{Po} \epsilon_{de}^e \quad (4.6)$$

where  $K_{Po} \in \mathbb{R}^{3 \times 3}$  is symmetric and positive-definite and  $\epsilon_{de}^e$  is the vector part of the unit quaternion  $\zeta_{de}^e = [\phi_{de}^e, \epsilon_{de}^{eT}]$ , which can be extracted from the rotation matrix  $R_d^e = R_e^T R_d$ , expressing the orientation displacement between the frames  $\Sigma_d$  and  $\Sigma_e$ . The expression of  $V_o$  is port symmetric due to the property of conjugate unit quaternion  $\epsilon_{de}^e = -\epsilon_{ed}^d$ . The computation of the derivative yields

$$\dot{V}_o = \omega_{de}^{eT} m_o^e \quad \text{with} \quad m_o = K'_{Po} \epsilon_{de}^e \quad (4.7)$$

with  $K'_{P_o} = 2E^T(\phi_{de}, \epsilon_{de})R_e K_{P_o} R_e^T$  and  $E(\phi_{de}, \epsilon_{de}) = \phi_{de} \mathbf{I} - S(\epsilon_{de})$ . The aforementioned equations show that an elastic wrench  $h_o = [\mathbf{0}^T, \mu_o^T]^T$  is produced from a finite orientation displacement  $\epsilon_{de} = R_e^T \epsilon_{de}^{eT}$  expressed in the robot base frame.

Consequently, a finite position and orientation displacement of the desired frame  $\Sigma_d$  with respect to the end-effector frame  $\Sigma_e$  produced a total elastic wrench defined in the robot base frame as

$$h_\Delta = h_t + h_o \quad (4.8)$$

Using (4.8) for the computation of the elastic wrench in the case of an infinitesimal twist displacement  $\delta x_{de}^e$  near the equilibrium, and discarding the high-order infinitesimal terms, yields the linear mapping

$$h_e^e = K_P \delta x_{de}^e = \begin{pmatrix} K_{Pt} & \mathbf{0} \\ \mathbf{0} & K_{P_o} \end{pmatrix} \delta x_{de}^e \quad (4.9)$$

It is apparent that the matrix  $K_P$  represents the stiffness matrix of an ideal spring with respect to a frame  $\Sigma_e$  (coinciding with  $\Sigma_d$  at equilibrium) with the origin at the center of stiffness. Additionally, it can be shown, using (4.8), that the physical/geometrical meaning of the principal stiffnesses and of the principal axes for the matrices  $K_{Pt}$  and  $K_{P_o}$  are preserved also in the case of large displacements. The above discussion imply that the active stiffness matrix  $K_P$  can be set in a geometrically consistent way with respect to the task at hand.

Hence, if we denote the end-effector error in the operational space as  $\Delta x_{de} = x_d - x_e$  and the corresponding velocity error as  $\Delta \dot{x}_{de} = -\dot{x}_e$ , assuming constant  $x_d$  i.e. considering the surface's deformation as a quasi-static phenomenon, a smooth compliance control with a geometrically consistent active stiffness can be achieved with the use of the control law

$$h_c = h_\Delta - K_D v_e + \lambda(q) \quad (4.10)$$

where  $h_\Delta$  is calculated in Eq. 4.8,  $K_D \in \mathbb{R}^{6 \times 6}$  is symmetric, positive-definite and expresses the gain of a D term and  $\lambda(q)$  is the gravity compensation term which is known from the robot dynamic model (Eq. 4.2).

In the absence of interaction of the environment (i.e., when  $w_e = 0$ ), the equilibrium  $\Delta \dot{x}_{de} = 0$ ,  $\Delta x_{de} = 0$  for the closed-loop system is asymptotically stable. The proof of the stability is based on the positive-definite Lyapunov function

$$V = \frac{1}{2} v_e^T B(q) v_e + V_t + V_o \quad (4.11)$$

with  $V_t$  and  $V_o$  calculated in Eq. 4.3 and Eq. 4.6, whose time derivatives along the trajectories of the closed-loop system is the negative semidefinite function

$$\dot{V} = -v_e^T K_D v_e \quad (4.12)$$

in case the frame  $\Sigma_d$  is motionless. When the robot is interacting with the environment ( $h_e \neq 0$ ), a different asymptotically stable equilibrium can be found, corresponding to a non-null displacement of the desired frame  $\Sigma_d$  with respect to the end-effector frame  $\Sigma_e$ . The new equilibrium is the solution of the equation  $h_\Delta = h_e$ .

Considering the analysis above, for the problem of robotic interaction control with a deformable surface it is sufficient to define the desired frame  $\Sigma_d$ , which can be used to define the displacement vectors with respect to the end-effector. The desired frame  $\Sigma_d$  can be provided to the controller through the proposed framework described in Sec. 4.3.

### 4.3 Robot-Surface Interaction Control Framework

This Section presents the proposed interactive motion planning and control framework and describes in detail its main components. A general overview of the overall architecture of the proposed framework is provided in Fig. 4.2, which deals both with the on-line motion planning and the interaction force regulation aspects of the robot control system. Starting from the assumption that the initial position of the surface and its deformation evolution (active or passive) over time are unmodelled, a robust perception layer has to be integrated to the robotic system. The visual (RGB-D) information obtained from a camera (Fig. 4.2 left) is processed and combined with the mesh representation of the object in a sequence of preprocessing steps (Fig. 4.2 middle), in order to deduce reliably the configuration of the object in the physical space, where a stiffness interaction control scheme is implemented (Fig. 4.2 right-bottom). At the core of the system, a mesh-based version of object deformable surface is constructed and tracked over time in 2D parameterized spaces, where the actual planning of interactive actions is realized (Fig. 4.2 right-top). The rest of this section presents all the key algorithmic steps and components of the system, describing more in detail the mesh-based parameterization and associated interactive motion planning phases which constitute the core modules in the proposed framework.

#### 4.3.1 Preprocessing Steps

The initial key step of the whole system is to process, robustly and in real time, rich visual data in order to reliably extract information about the configuration of the deformable target object in the scene. Though this visual pre-processing step does not constitute the focus of this paper, some critical considerations are discussed hereafter, in order to high-

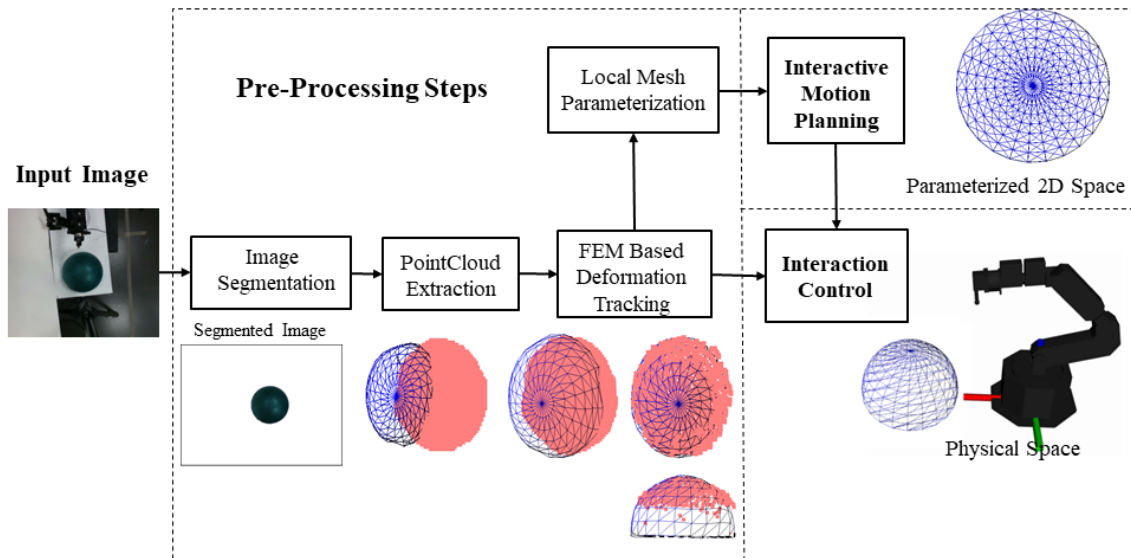


Figure 4.2: The overall architecture of the proposed planning framework. Visual object segmentation, FEM deformation tracking and local mesh parameterization are included in pre-processing algorithmic steps. These steps provide a mesh representation of the object both in Physical space, in which a stiffness interaction control scheme is implemented, and in 2D parameterized spaces, in which the planning of interactive actions is realized.

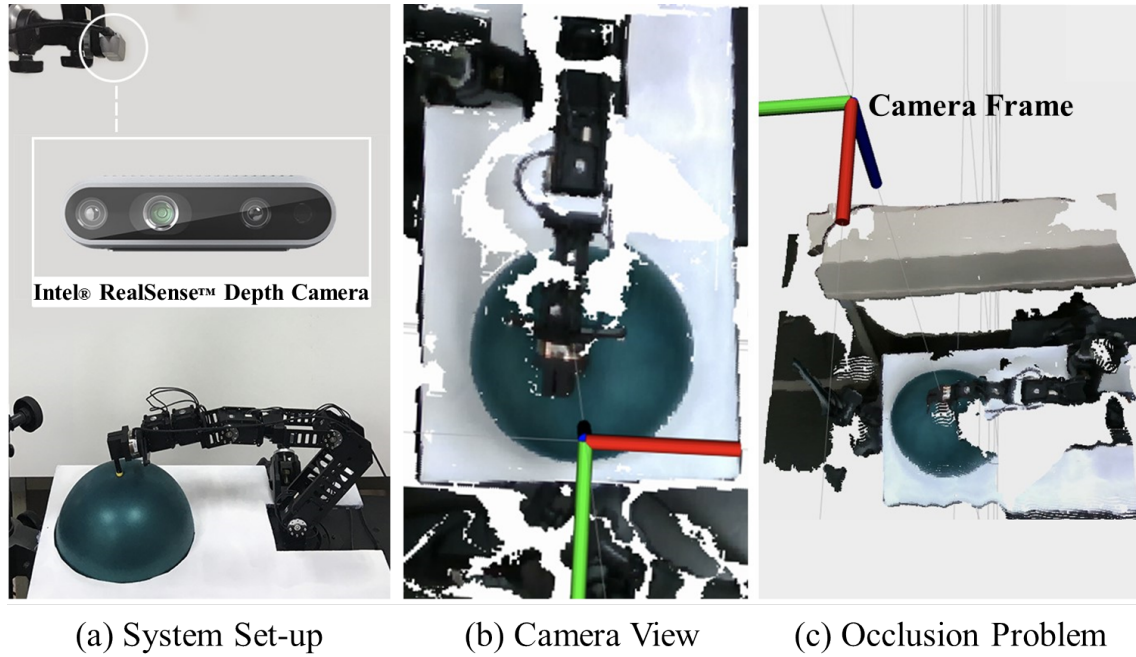


Figure 4.3: A robotic manipulator performing interactive tasks on a hemispherical deformable object. **(a) Left:** The experimental setup used to test the performance of the proposed approach, which includes an Intel®RealSense™depth camera. **(b) Middle:** View from the system’s depth camera in PointCloud form. **(c) Right:** Tilted view from the system’s depth camera in PointCloud form, in which the missing scene information due to occlusions caused by the robot is apparent.

light specific constraints and requirements related to the interactive robotic manipulation tasks addressed in this work. A camera can provide rich information about the structure of the surface at high frame rates, however the choice of the camera type is important for coping with some critical data robustness issues. For instance, tracking a physical landmark on the surface is not possible using only the input from a camera, as depicted in Fig. 4.3(a). Although some approaches have been proposed handling this tracking problem by taking advantage of the image texture [163, 164], these approaches are not suitable for interaction tasks since the visual information may not be available due to the presence of the robot in the scene. More specifically, during the execution of an interaction task, the robot itself might occlude the view of the surface (Fig. 4.3 (c)) or the nature of the task may modify its visual structure (e.g. polishing), thus disrupting some valuable visual information. On the other hand, the lack of visual features may infer some ambiguities in the process of pose identification of a surface in the 3D space. Therefore, in this work we assume textureless objects, which is a more generic case and more applicable to interaction control tasks, and consequently rely on an RGB-D sensor (Fig. 4.3 (a)), which can provide 3D visual information and be used to remove the described ambiguities.

Despite the rich 3D visual data obtained from an RGB-D sensor, some critical preprocessing layers of the input data are required. Firstly, an algorithmic layer performing object or region of interest detection and **visual segmentation** is a prerequisite for the purposes of input data reduction and accurate localization of the target object in the manipulation scene. Several algorithms exist in the literature which can be used to perform these preprocessing steps, such as the ones described in [236, 237], and constitute

a major topic in computer vision society. Hence, these algorithms fall outside the scope of this paper and will not be further analysed. Secondly, a **deformation tracking** algorithm, which can combine the visual information with the elasticity parameters of the object, constitutes another important preprocessing step. It is important to distinguish deformation tracking from non-rigid reconstruction performed by methods such as those proposed in [238, 239, 240], which reconstruct a single mesh at each frame provided by the vision sensor. This distinction is key to our proposed framework, as will be explained below, since typical non-rigid reconstruction methods provide no guarantee for constant cardinality of the reconstructed mesh elements.

On the other hand, the goal of tracking algorithms is to continuously estimate the deformations and rigid transformations undergone by an object, which is previously modeled by a known mesh. Among the deformation tracking algorithms, which use as an input the Point-Cloud data from an RGB-D sensor, there are some using NURBS parameterization [136, 130] and others using physics-based methods such as discrete mass-spring-damper system [142, 241] or Finite Element Method [158, 143, 144] based on continuum mechanics. These methods register the acquired Point-Cloud data to a mesh with suitable topology as depicted in Fig. 4.2. Physics-based methods are more suitable for robot-object interaction and manipulation applications, since an explicit physical modelling permits the reliable computation and prediction of internal forces undergone by the object and thus to plan and perform proper force control tasks. Furthermore, the tessellation of the region of interest that a mesh provides gives valuable information about the topology of the surface locally, both for normal vector estimation and for calculating geodesic distances between physical points, and is appropriate for the reduction of data noise inserted by the RGB-D sensor. Additionally, the physical simulation process of the tracking algorithms can handle efficiently the visual occlusion problem, since the position of the mesh elements, which correspond to the occluded areas, is continuously updated using the calculated internal forces, even when the Point-Cloud data are not available.

In spite of the accurate deformation estimation achieved with a tracking algorithm at each time frame, the problem of predicting the evolution of the deformation over time remains unsolved. This problem makes the definition of a motion planning strategy impossible, as explained above. Therefore, another pre-processing step is essential; that is, the calculation of a non-linear transformation which will project a set of triangles, representing the area of interaction, to a plane at each time step. We name this planar space as *Dynamic Canonical Space*  $\mathcal{W}_{dc}$ , graphically shown in the middle of Fig 4.4. In case we take an instance of this dynamic triangular set at an initial time frame, we can define a static version of the planar space as *Static Canonical Space*  $\mathcal{W}_{sc}$ , depicted in the left of Fig. 4.4.

An ideal property of this projection transformation concerns distance and angle preservation (isometry), which is though not true for general surfaces, since the Gaussian curvatures of an arbitrarily triangulated 3D surface and of a planar surface are not equal. However, extensive literature from computer graphics society exists, [170, 242, 197], proposing a variety of algorithmic approaches for constructing a global close-to-isometric **mesh parameterization**. Most of these approaches are though computationally expensive and thus not suited for real-time planning and control purposes. Nevertheless, local solutions also exist which parameterize a part of the object surface, such as the one presented in [198]. Such solutions have proven both efficient and accurate in terms of isometry, though applied in a completely different context than the one considered in this paper. In this work, we employ a local mesh parameterization approach, integrated in the core of the proposed interactive motion planning framework, ensuring the imposed performance re-

quirements (bijective transformation properties and computational efficiency), as will be explained in the rest of this Section.

### 4.3.2 Mathematical Formulation

The definition of two different parameterized spaces is useful for tracking differentially the changes of the geodesic distances on the object's surface, coming from the deformation. Hence, at this point, it is useful to present an explicit form of the projection transformation  $\psi^T$  which is based on the reference surface in the physical space  $\mathcal{W}_p$ . Practically, part of the object's surface in physical space represents a 2D manifold embedded in  $\mathbb{R}^3$ , in which the reference surface is expressed as a set of connected triangles  $\mathcal{T}_k^p, k = 1 \dots N$  (Fig. 4.4), whose vertices are given by the points  $p_k^1, p_k^2, p_k^3 \in \mathcal{W}_p$ . This triangular mesh is the result of the visual segmentation and the deformation tracking preprocessing steps. The above vertices are projected using a mesh parameterization algorithm to points  $u_k^{d1}, u_k^{d2}, u_k^{d3} \in \mathcal{W}_{dc}$  on the Dynamic Canonical Space (DCS), forming the set of triangles  $\mathcal{T}_k^{dc}, k = 1 \dots N$ . This projection procedure can be expressed as a coordinate transformation  $\psi$ , which can be geometrically constructed piecewise inside the  $\mathbb{R}^2$  subspace  $\mathcal{W}_{dc}$  with boundary defined by the parameterized mesh boundary edges.

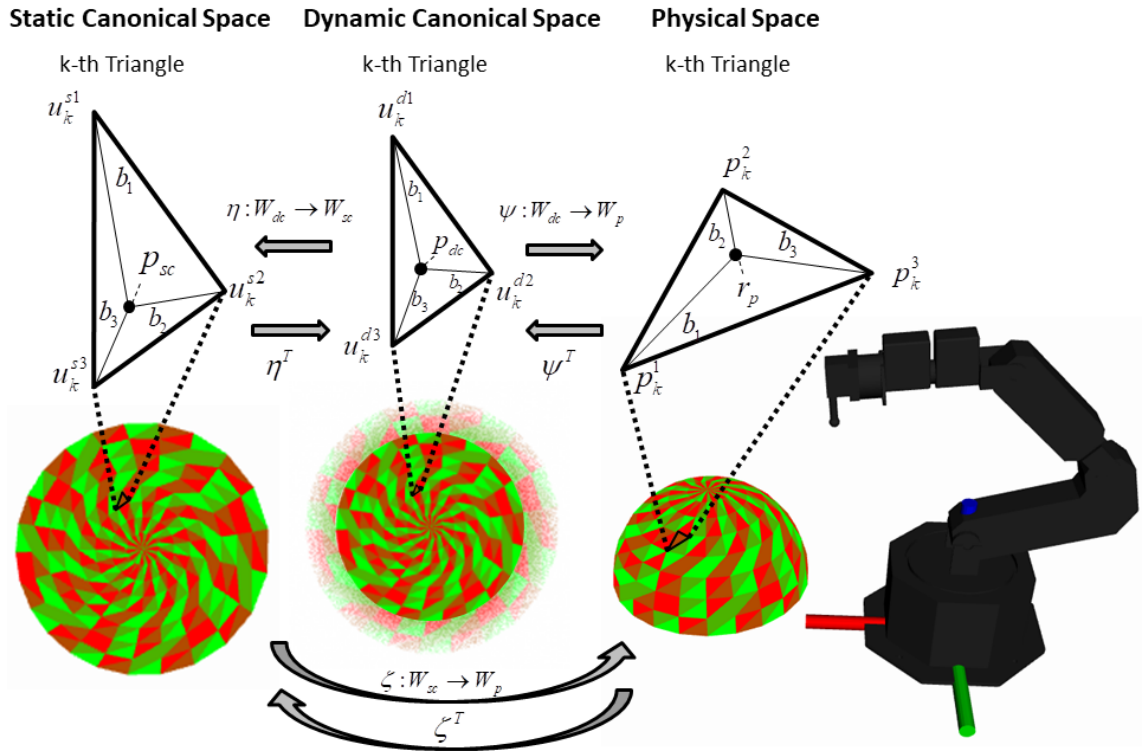


Figure 4.4: Establishment of bijective transformations between the Static Canonical Space (SCS), the Dynamic Canonical Space (DCS) and the Physical Space with the use of barycentric coordinates between the corresponding triangles. The position  $p_{dc}$  in the  $k^{th}$  active triangle of DCS corresponds to the position  $p_{sc}$  in the  $k^{th}$  active triangle of SCS through the transformation  $\eta$  and simultaneously on the other side to the position  $r_p$  in the  $k^{th}$  active triangle of the physical space through the transformation  $\psi$ . A direct transformation  $\zeta$  from the SCS to the Physical Space can also be defined similarly.

Let  $p_{dc} = (x_{dc}, y_{dc}) \in \mathcal{T}_k^{dc}$  be a point in DCS, which can be expressed in barycentric coordinates  $b_1, b_2, b_3$  of the triangle, in which it lies, as follows

$$p_{dc} = b_1 u_k^{d1} + b_2 u_k^{d2} + b_3 u_k^{d3} = [u_k^{d1}, u_k^{d2}, u_k^{d3}] \cdot \begin{bmatrix} b_1 \\ b_2 \\ b_3 \end{bmatrix} \quad (4.13)$$

with  $[u_k^{d1}, u_k^{d2}, u_k^{d3}]$  denoting the edges of the  $k$ -th triangle as shown in Fig. 4.4, written as a row vector. Using the property  $b_1 + b_2 + b_3 = 1$ , (4.13) can be rewritten in the form

$$\begin{bmatrix} b_1 \\ b_2 \end{bmatrix} = T_{[dc]k}^{-1} (p_{dc} - u_k^{d3}) \quad (4.14)$$

where the matrix  $T_{[dc]k} = (u_k^{d1} - u_k^{d3}, u_k^{d2} - u_k^{d3}) \in \mathbb{R}^{2 \times 2}$  is invertible since the vertices forming a triangle are linearly independent (as long as they are assumed not collinear). The corresponding point  $r_p \in \mathcal{T}_k^p$  in the physical space is calculated using the function  $\psi_k : \mathcal{T}_k^{dc} \rightarrow \mathcal{T}_k^p$

$$r_p = \psi_k(p_{dc}) = T_{[p]k} T_{[dc]k}^{-1} (p_{dc} - u_k^{d3}) + p_k^3 \quad (4.15)$$

where we define the matrix  $T_{[p]k} = (p_k^1 - p_k^3, p_k^2 - p_k^3) \in \mathbb{R}^{3 \times 2}$ , with the use of the  $k$ -th triangle's edges in physical space  $p_k^1, p_k^2, p_k^3$  (Fig. 4.4). Extending to the entire DSC we construct the coordinate transformation  $\psi : \cup_k \mathcal{T}_k^{dc} \rightarrow \cup_k \mathcal{T}_k^p$  as follows

$$r_p = \psi(p_{dc}) = \sum_{k=1}^N (T_{[p]k} T_{[dc]k}^{-1} (p_{dc} - u_k^{d3}) + p_k^3) \xi_k(p_{dc}) \quad (4.16)$$

where the selection function  $\xi_k(p_{dc})$  is defined as follows

$$\xi_k(p_{dc}) = \begin{cases} 1 & \text{if } p_{dc} \in \mathcal{T}_k^{dc} \\ 0 & \text{elsewhere} \end{cases} \quad (4.17)$$

Working similarly in physical space we can express  $r_p$  barycentric coordinates  $b_1, b_2, b_3$  of the  $k$ -th triangle, in which it lies Physical space, as follows

$$r_p = b_1 p_k^1 + b_2 p_k^2 + b_3 p_k^3 = [p_k^1, p_k^2, p_k^3] \cdot \begin{bmatrix} b_1 \\ b_2 \\ b_3 \end{bmatrix} \quad (4.18)$$

Since the matrix  $[p_k^1, p_k^2, p_k^3] \in \mathbb{R}^{3 \times 3}$  is invertible, we can rewrite (4.18) in the following form

$$[b_1, b_2, b_3]^T = [p_k^1, p_k^2, p_k^3]^{-1} r_p \quad (4.19)$$

Substituting (4.19) into (4.13) we can rewrite (4.13) as follows

$$p_{dc} = [u_k^{d1}, u_k^{d2}, u_k^{d3}] [p_k^1, p_k^2, p_k^3]^{-1} r_p \quad (4.20)$$

Extending to the entire Physical space we can construct the coordinate transformation  $\psi^{-1} : \cup_k \mathcal{T}_k^p \rightarrow \cup_k \mathcal{T}_k^{dc}$  as follows

$$p_{dc} = \psi^{-1}(r_p) = \sum_{k=1}^N [u_k^{d1}, u_k^{d2}, u_k^{d3}] \cdot [p_k^1, p_k^2, p_k^3]^{-1} \cdot r_p \cdot \xi_k(r_p) \quad (4.21)$$



where the selection function  $\xi_k(r_p)$  is defined as follows

$$\xi_k(r_p) = \begin{cases} 1 & \text{if } r_p \in \mathcal{T}_k^p \\ 0 & \text{elsewhere} \end{cases} \quad (4.22)$$

It is noteworthy that the summation of equations (4.16) and (4.21) is reduced to a single term, since  $p_{dc}$  and  $r_p$  respectively can lie on only one triangle, denoted as **active triangle**. In the edges and vertices which constitute the boundaries between two triangles the active triangle can easily be chosen with the use of a heuristic function. Additionally, the use of the deformation tracking algorithm described above allows for constant cardinality of triangles in the mesh structure across all the time frames, which is important for bijectivity preservation of the transformation  $\psi$  and continuity of the planned interactive tasks on the surface of the object. We can follow the same procedure to calculate a bijective coordinate transformation  $\zeta : \mathcal{W}_{sc} \rightarrow \mathcal{W}_p$  between the Static Canonical Space (SCS) and the physical space (not presented here for brevity). Using barycentric coordinates we can also define a bijective transformation  $\eta$  between  $\mathcal{W}_{sc}$ , which is a subspace of  $\mathbb{R}^2$  with boundary defined by the boundary edges of static parameterized mesh (Fig. 4.4), and  $\mathcal{W}_{dc}$  defined above. In order to express the transformation  $\eta$  we need to introduce a point in SCS,  $p_{sc} = (x_{sc}, y_{sc}) \in \mathcal{T}_k^{sc}$ , where  $\mathcal{T}_k^{sc}, k = 1 \dots N$  is a set of triangles with vertices defined by the points  $u_k^{s1}, u_k^{s2}, u_k^{s3} \in \mathcal{W}_{sc}$ . Reusing (4.14) we can express  $\eta : \mathcal{W}_{dc} \rightarrow \mathcal{W}_{sc}$  as follows

$$p_{sc} = \eta(p_{dc}) = \sum_{k=1}^N (T_{[sc]k} T_{[dc]k}^{-1} (p_{dc} - u_k^{d3}) + u_k^{s3}) \xi_k(p_{dc}) \quad (4.23)$$

where we define the matrix  $T_{[sc]k} = (u_k^{s1} - u_k^{s3}, u_k^{s2} - u_k^{s3}) \in \mathbb{R}^{2 \times 2}$ , which is invertible similarly to  $T_{[dc]k}$ , assuming non-collinear vertices for every triangle. Similar bijectivity properties have been proven for mesh structures in [243], however the authors have made the restrictive assumption, that the surface should have a terrain form (or 2.5D map), which is not appropriate for deformable objects.

### 4.3.3 Interactive Motion-Planning Approach

The core of our proposed framework for surface interaction control tasks is based on an online calculation of the desired frame  $\Sigma_d$ , which is used as an input to the stiffness controller, as described in Section 4.2. A central idea in this framework is to make use of the preprocessing steps, described in the previous paragraphs, in order to firstly construct the spaces denoted as physical and its planar parameterized versions denoted as static canonical and dynamic canonical. Through the respective coordinate transformations between these spaces, computed as defined above, it then becomes possible to continuously update the position and orientation of the desired stiffness control frame  $\Sigma_d$  at each time step.

Starting from the calculation of the position part in the desired control frame, the goal would be to achieve both motion planning on the interaction area and regulation of the interaction force. The first sub-goal can be accomplished by planning the trajectories in the Static Canonical Space. We take advantage of its 2D static nature and structure, in order to plan paths suitable for the interaction task, as shown in Fig. 4.5c. The planning procedure can be realized within the boundary of SCS, using well-known path planning algorithms [244] with integrated obstacle avoidance techniques, if some areas on the surface have to be avoided during the robotic interaction. Planning of the interaction

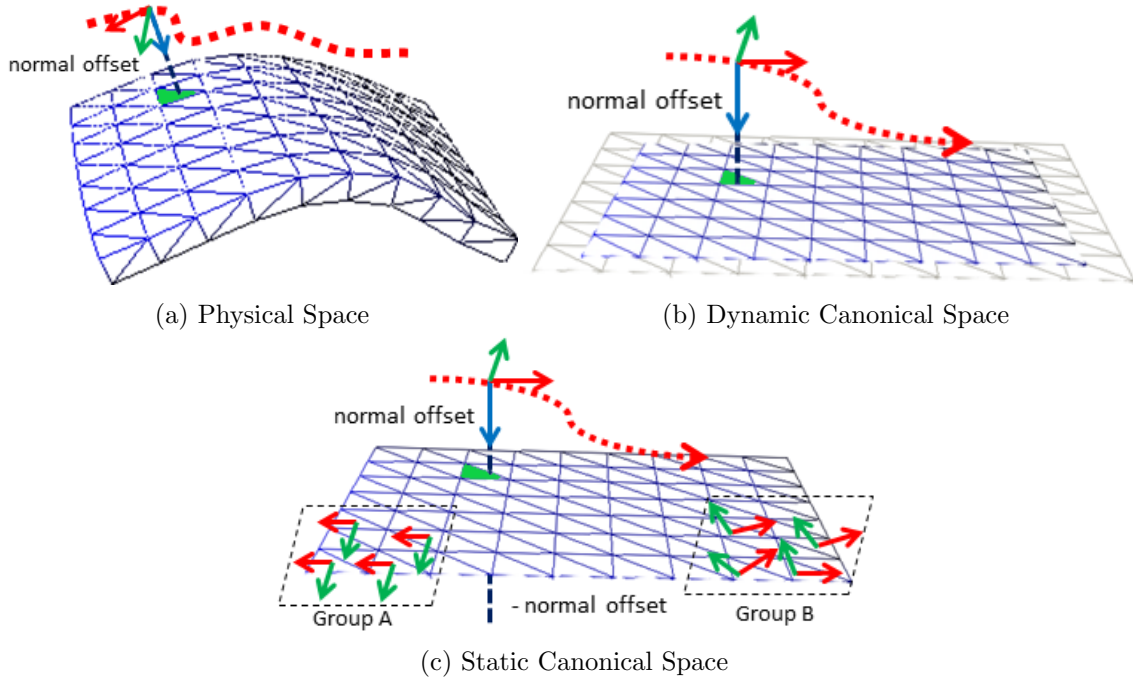


Figure 4.5: The proposed interaction control framework. **(a) Top Left:** The result of a deformation tracking preprocessing step is the mesh model of the object fitted in the Pointcloud data obtained by the depth camera. Each triangle provides information about the topology of the surface locally depicted with a blue normal vector and green-red tangential vectors. The planned path is fitted on the mesh surface depicted as red dots. The reference pose translated along the normal offset is depicted as a reference frame at a time instance. **(b) Top Right:** The flattened mesh surface is the result of the parameterization preprocessing step. For each time step the parameterization forming the Dynamic Canonical Space is calculated, which tracks the geodesic changes of the object’s mesh model. If the object is not actively deforming the DCS equals to the SCS. **(c) Bottom:** At an initial time step the parameterized Static Canonical Space is obtained, in which the robot’s reference motions are planned (depicted as a red path). The tangential directions can be computed axis aligned (Group A) or can follow the direction of the principal Gaussian curvatures (Group B). Each planned reference pose is depicted with a reference frame with the blue vector representing the normal direction and the green-red the tangential directions. The planning in the parameterized space includes a normal offset w.r.t. the mesh’s surface.

trajectory is then possible by sampling the paths at proper time steps. At each time step, the sampled point  $p_{sc}$  from the path will lie inside a triangle from the set  $\mathcal{T}_k^{sc}$ , defining the active triangle as described above and marked with green color in Fig. 4.5c. With the use of transformation  $\zeta : \mathcal{W}_{sc} \rightarrow \mathcal{W}_p$  we are able to calculate the corresponding point of the physical space. Hence, the interaction trajectory can be expressed in the physical space in real-time, since the computational cost of the transformation calculations is low, requiring only the calculation of barycentric coordinates.

However, the above strategy is sufficient for planning trajectories only on the reference surface, which would be sufficient only for contact tasks. For regulation of the contact force and planning of non-contact tasks, we add a vertical offset in the planning procedure, which is defined differently between the coordinate spaces. Namely, in SCS the offset is

set along the  $z$  axis of its inertial coordinate frame (Fig. 4.5c), whereas in physical space it is set along the direction of the normal vector of the active triangle, whose direction is calculated with the use of the local barycentric coordinates, as depicted in Fig. 4.5a. More specifically for the directional part, the mesh's normal vectors are calculated in its edges at each time frame by the mesh tracking algorithm as a linear combination of the neighbouring triangles' normals. Hence, the barycentric coordinates calculated by the transformation  $\zeta : \mathcal{W}_{sc} \rightarrow \mathcal{W}_p$  also provide a linear combination of the mesh's normals at each point inside a triangle, implementing a normal shading algorithm. In terms of offset values, for positive ones ( $\mathbf{z}_{sc} > 0$ ), the desired position is translated along the direction of the normal vector above the surface, thus resulting in a non-contact interaction task between the robot and the surface. In case of negative offset values, the desired position is set below the surface level, achieving contact with regulated interaction force by adjusting the offset value and hence the translational displacement error of (4.5). By planning smooth trajectories including the vertical offset, the robot can navigate across the whole area of interest, with desired motion and contact force properties defined by the interaction trajectory.

It is noteworthy that the geodesic distances on the surface of an object, which undergoes elastic deformations, are changing. This means in practice that the length of one step along a path planned in SCS is different than the corresponding step in physical space. It is obvious that, if the requirements of the interaction task include preservation of distance from a landmark point or of constant velocity on the surface, the motion planning strategy defined above is not sufficient. In this case, a different planning strategy has to be adopted, which involves the Dynamic Canonical Space 4.5b. In particular, we keep on planning the same interaction paths, but inside the DCS in this case, and then perform sampling along that path at proper time steps, for interaction trajectory planning according to the task requirements. At each time step, the sampled point  $p_{dc}$  from the path will lie inside a different triangle as compared to the SCS, defining a new active triangle, which is marked with green color in Fig. 4.5b. The continuous surface parameterization implemented with a close to isometric surface parameterization algorithm allows for continuous monitoring of the changes in the surface geodesic distances. In this way, the planned trajectories in DCS are then transformed to the physical space with the use of transformation  $\psi : \mathcal{W}_{dc} \rightarrow \mathcal{W}_p$ , incorporating the distance modifications imposed by the object's deformation. Moreover, the vertical offset will be set in DCS along the  $z$  axis of its inertial frame, similarly to SCS.

Regarding the calculation of the orientation part, besides computing the local normal vector, it is also necessary to define appropriately the tangent vectors. Since the path planning is implemented in SCS, we can set the reference tangent vectors of each triangle representing the local  $x$  and  $y$  axes, according to the planning strategy. For example, we can choose to set all the tangent vectors aligned to the SCS inertial frame, indicated in Fig. 4.5c as Group A, or to set them along the direction of the principal Gaussian curvatures (Group B in Fig. 4.5c), calculated locally from the reference surface at the time frame the SCS was captured. It is important, for the continuity of the planned motions, that the direction of reference tangent vectors in neighbouring triangles does not assume large deviations. The reason for this is that the orientation part of the desired frame  $\Sigma_d$  is calculated relatively to the local reference frame of the active triangle, formed by the reference tangent vectors and the vertical direction of each space (i.e., the  $z$  axis of SCS and DCS and the local normal vector in the physical space). Similarly to the position calculation, we plan the desired orientation in the planar spaces with respect to the local reference frame. By using the proper transformations, we then calculate the corresponding reference frame in the physical space, which consequently defines the desired orientation

of the stiffness control frame  $\Sigma_d$ . The computed desired orientation in physical space is then set as an input in (4.6), for the calculation of the orientation displacement error, as described in Sec.4.2.

## Chapter 5

# Experimental Validation of Perception-Based Interaction System

In this chapter we present experimental studies, which aim to validate the performance of the integrated perception-based interaction system presented in Chapter 3. This evaluation commences with experiments focusing on the perception based motion planning subsystem conducted both in the lab and in a clinical realistic environment. The goal of the former is to evaluate the performance and the accuracy of the proposed motion planning algorithm from a pure technical point of view, whereas the primary aim of the clinical study was to evaluate the task effectiveness and user satisfaction of older persons with different operation modes (autonomous operation, shared control, tele-manipulation) for a water rinsing task with the soft-robotic arm. The proposed clinical metrics are indicative for human-robot interaction (HRI) objective and subjective study in a cognitively demanding showering of the back region scenario, especially for older persons. Section 5.3, focuses on the evaluation of the integrated system, presenting experimental scenarios with generation and adaptation of more complex interactive primitive motions based on the leader-follower framework presented in 3.3. The generated motions in the presented scenarios are focusing on a wiping task, which is learned by demonstration, using data from the publicly available KIT whole-body motion database [1]. At the end of this Chapter, the ability of reproducing interactive washing actions from demonstration, for the alternative learning method with Navigation Functions described in Section 3.4, is validated experimentally with a water pouring scenario.

### 5.1 Perception-Based Motion Planning

The motion planning method described in 3.2.2 commences with the tracking of predefined, time scalable trajectories on a fixed 2D **“Canonical” space** and continues with the motion adaptation on curved and deformable surfaces, such as the human body parts, by means of two bijective transformations. In order to test and analyze the performance of the proposed approach in lab conditions, an experimental setup is used that includes a Kinect-v2 Camera providing depth data for the back region of a subject, with accuracy analyzed in [245]. The segmentation of the subjects’ back region is implemented, for the purposes of this experiment, by simply applying a Cartesian filter to the Point-Cloud data. The setup also includes a 5 DOF Katana arm by Neuronics, [246] and a HC-SR04 Ultrasonic Range

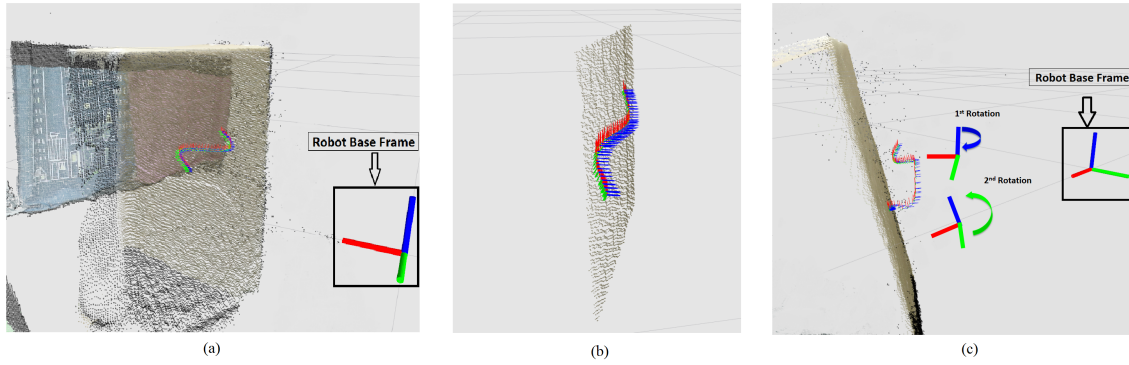


Figure 5.1: Visualization of experimental results with the rectangular box. The blue arrows represent the normal vector to the surface, whereas the green and red arrows represent the tangential axes to the surface. (a) The rectangular box is stationary and the reference path is fitted on its surface. The orientation is calculated w.r.t the robot base frame. (b) A zoomed and segmented version of the box’s front side providing a more clear aspect of the path fitted on the surface. (c) The box is rotated initially w.r.t. the z (blue) axis and then w.r.t. the y (green) axis and the calculated path adapts to this motion.

Finder for the distance measurements between the robot end-effector and the object or the subject. The distance measurement range of the latter is  $2\text{cm} - 400\text{cm}$  with accuracy  $0.3\text{cm}$ .

### 5.1.1 Validation Strategy in Lab Conditions

The experiments conducted include a trajectory tracking task, for a simple sinusoidal motion, keeping simultaneously a constant distance and perpendicular relative orientation to the surface of a rectangular box, that represents a rigid body. Also, the same experiments are conducted on a female and a male subject’s back region.

For the **first** and the **second** experiments we employ a rigid and rectangular object for the evaluation of the method (Fig. 5.1). In particular, we segment the side of the object facing the camera as shown in Fig. 5.1(b). The reference orientation of this planar segment is calculated with the same procedure described in Section 3.2.2, using in the calculations the total amount of points constituting the front side of the object. Since the chosen object is non-deformable, the calculated orientation is used as ground-truth, in order to validate the ability of the proposed algorithm to keep (on-line) perpendicular relative orientation between the robot’s end-effector and the operational surface. Both the ground-truth orientation and the on-line calculation of the reference pose subject to the same camera accuracy constraints (e.g. errors and noise), which are analyzed in more detail in [245].

During the **first** experiment the box is stationary, as shown in Fig. 5.1(a), whereas in the **second** experiment the box performs rotations around y and z axes, as shown in Fig. 5.1(c). Furthermore, for evaluation purposes we used an initial set-up including the Katana robot with the described distance sensor. In the **third** and **fourth** experiment, a female and a male subjects are involved (Fig. 5.2 and 5.3). In these cases, there is no ground truth data for total rotation of the subject, since the back region is a non-planar and deformable surface. These experiments were conducted, in order to highlight the adaptability of the algorithm to different users (a male and a female subject with a thinner silhouette).

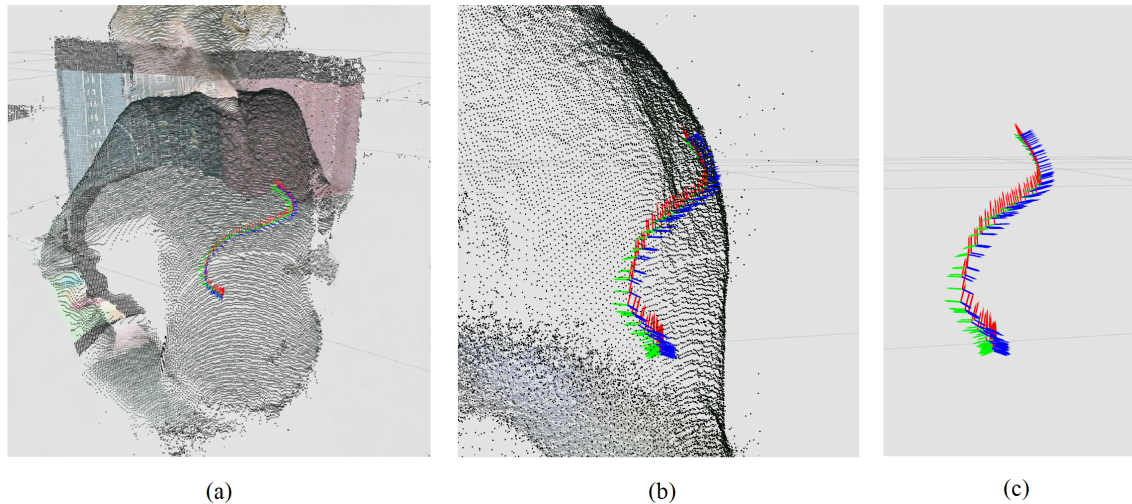


Figure 5.2: Experiment on a female subject. (a) Adaptation of the sinusoidal path on the curved surface of a female subject represented with PointCloud data. (b) A zoomed aspect of the experiment depicting in more detail the adaptation of the path. (c) A more clear view of the zoomed path without the PointCloud.

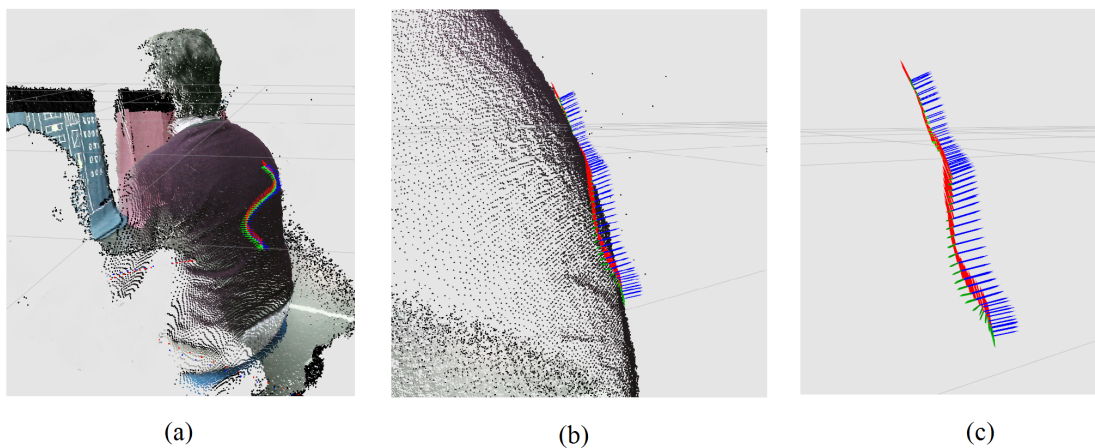


Figure 5.3: Experiment on a male subject. (a) Adaptation of the sinusoidal path on the curved surface of a male subject represented with PointCloud data. (b) A zoomed aspect of the experiment depicting in more detail the adaptation of the path. (c) A more clear view of the zoomed path without the PointCloud.

### 5.1.2 Validation Results and Discussion

Based on Fig. 5.1, Fig. 5.3 and Fig. 5.2, the experiments' resulting path is represented by orientation vectors. The blue arrows represent the normal vector to the surface, whereas the green and red arrows represent the tangential axes to the surface. These vectors are fitted on the object's front side and a female subject's back region. In Fig. 5.2(a) and Fig. 5.3(a) a general aspect of the experimental scene is shown, whereas in Fig. 5.2(b)(c) and Fig. 5.3(b)(c) a zoomed and more clear view of the same scene is depicted. It is more clear in the latter view, that the reference path is adapted to the subjects' back region, i.e. to the motion and the surface's deformation.



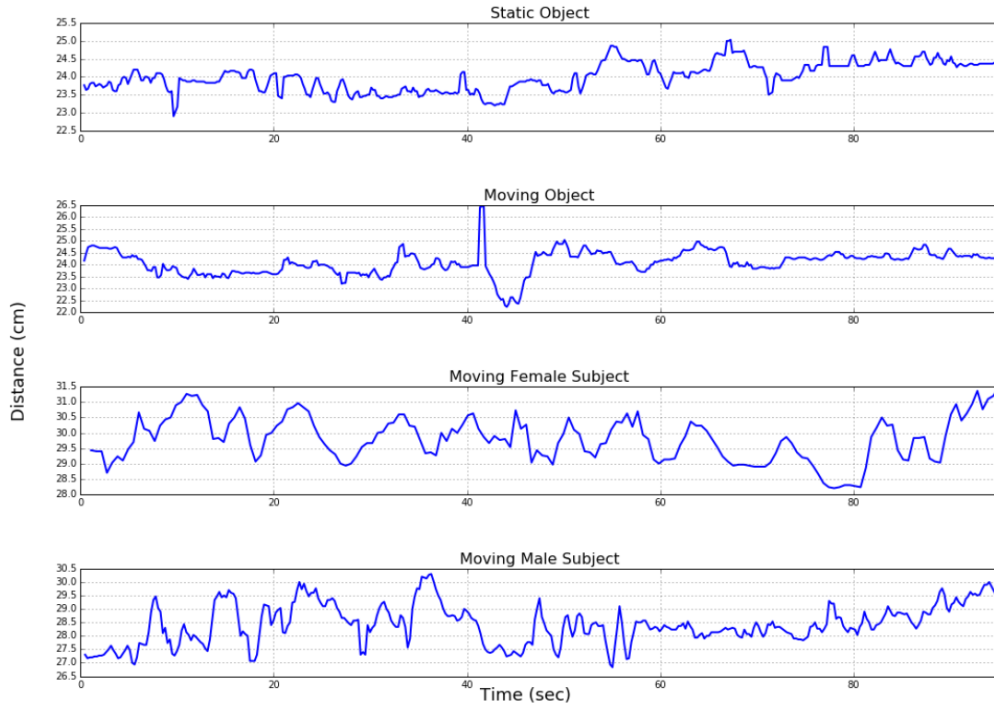


Figure 5.4: Perpendicular distance between the Katana end-effector and the experimental subject.

Therefore, in Fig. 5.5a, 5.5b, the roll, pitch and yaw rotations w.r.t. the robot base frame are shown. In these plots, the evolution of the object's rotations and the reference path orientation are depicted during the experimental procedure. In Table 5.1, the Mean Absolute Error of the object's rotations w.r.t. the reference path orientation are presented in degrees, along with the mean perpendicular distance between the end-effector and the experimental subject. It is obvious, that the calculated reference path manages to compensate with the object's motion, while the under-actuated robotic platform converges to the reference path. The variance of the Mean Absolute Error is primarily affected by the roughness of the object's material.

Table 5.1: Mean Absolute Error in Orientation and Mean Distance

	Roll (deg)	Pitch (deg)	Yaw (deg)	Distance (cm)
Static Object	$0.673 \pm 0.443$	$0.767 \pm 0.553$	$0.537 \pm 0.408$	$20.18 \pm 1.055$
Moving Object	$0.721 \pm 0.551$	$1.01 \pm 0.711$	$0.284 \pm 0.212$	$19.79 \pm 0.872$

Mean Absolute Error of the calculated reference orientation w.r.t the rotations of the object. The fourth column presents the mean and standard deviation of the perpendicular distances between the Katana end-effector and the object.

Moreover, in all experiments the perpendicular distance between the Katana end-effector and the experimental rectangular object is measured with the range-finder sensor and is presented in Fig. 5.4. Based on these results, the proposed method successfully keeps bounded distance taking into account the noise inserted by the accuracy of the sensor.



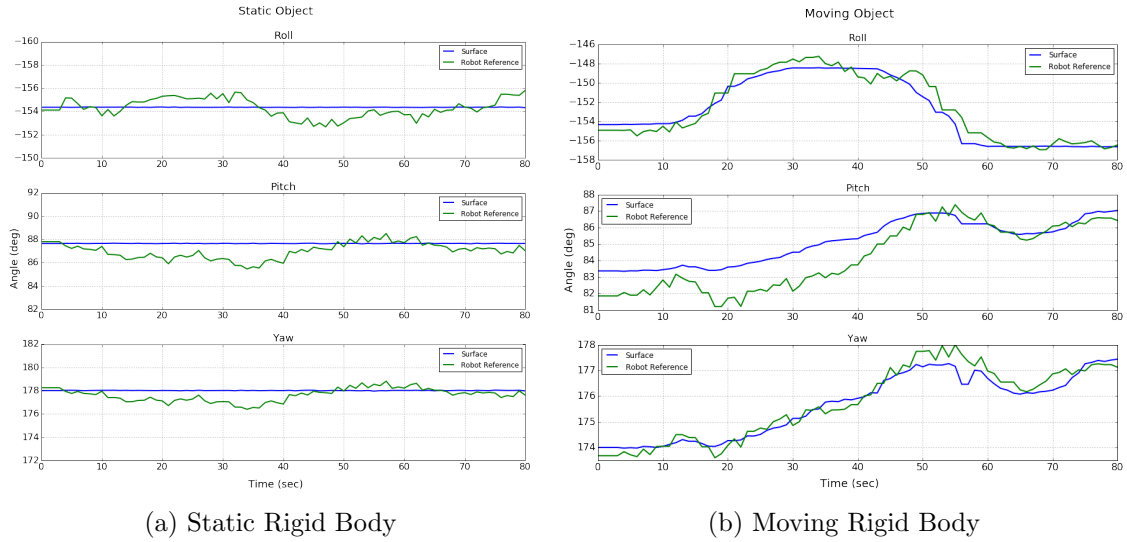


Figure 5.5: Evolution of the box's rotations and the reference trajectory orientation during (a) the first experiment that involves the static box and (b) the second experiment that involves the moving box.

The mean time performance of the proposed algorithm presented over the frames of the experimental procedure is **6ms**. The timing performance of the algorithm is high, making the proposed approach computationally efficient for on-line procedures. The execution times were measured in a computer system with Intel(R) Core(TM) i7-6700K CPU @ 4.00GHz and 16Gb RAM.

### 5.1.3 Clinical Validation Study

The main goal of the clinical validation study, conducted at Bethanien Geriatric Hospital in Heidelberg Germany, was to study the ability of the elderly to control the showering process using different operation modes of the I-Support system, which provide different amount of assistance during bathing the upper back region. More specifically, the **three operation modes** to be evaluated were:

- *Autonomous operation*: The soft-arm of the I-SUPPORT bathing robot provides water pouring fully automatically for a predefined body area (= upper back region) within a predefined time period and the user has no control over the motion of the soft-arm after starting the robot. The autonomous soft-arm motion in this operation mode was based on the proposed motion planning approach, which adapts the showering path in the limits and motion of the user's body part.
- *Shared control*: The participant could use an input device to issue simple motion commands (i.e. left vs. right and up vs. down), which were translated to a number of (high-level) discrete commands for the I-Support control system (i.e. soft-arm moved left/right or up/down), while the system provided assistance in terms of audio signals indicating that: (1) the participant's command was recognized and (2) the command was successfully executed, meaning that the participant could issue the next motion command. Further assistance was provided by the motion planning algorithm, in terms of restricting the motion of the soft-arm to the predefined body

area (i.e., upper back region cannot be exceeded). In this mode, the participant had predominant, but *not full control* over the robot motion.

- *Tele-manipulation*: The participant could issue motion commands (i.e. up vs. down and left vs. right) using the input device, similar to the shared control mode. In this mode, however, the system did not provide the audio signals for operating assistance, nor did it constrain the robot motion to the upper back region. Consequently, the participant had full control of the robot motion.

Having in mind these different levels of robot autonomy, it is reasonable to expect that different operation modes will have an effect on the task effectiveness and the user satisfaction with the assistive robot. No comparative studies between different operation modes within the research field of assistive bathing robots in older adults have been published. Previous studies with other assistive robots (e.g., telemedicine robot, robotic walker, robotic wheelchair) suggest that task effectiveness increases with increasing robot autonomy in young or older adults with physical impairments [247, 248, 249]. At the same time, the autonomous operation modes with the highest task effectiveness were not those with the highest user satisfaction, suggesting that users seem to prefer to retain as much control as possible when interacting with an assistive robot [247, 249]. Based on these studies, it was hypothesized that (1) task effectiveness with the bathing robot would be highest in the autonomous operation mode and would gradually decrease with lower levels of robot assistance, and (2) user satisfaction would be lower in the autonomous operation mode than in the more user-controlled operation modes (shared control, tele-manipulation). Potential users of the I-Support bathing robot are persons with (1) dependence in bathing activities, as defined by a score of 0 points (= person can use a bath tub, a shower, or take a complete sponge bath only with assistance or supervision from another person) for the bathing item of the Barthel Index (BI) [250], and (2) no severe cognitive impairment, as defined by a Mini-Mental State Examination (MMSE) score greater than 17 points [251]. The study was approved by the ethics committee of the Medical Faculty of the Heidelberg University on September 27, 2016 (S-382/2016) and was conducted in accordance with the Declaration of Helsinki. Written informed consent was obtained from all participants.

#### 5.1.4 Training and Comparison of Input Devices

The main question during the first stage of this study was the user satisfaction and acceptability of the input device for the elderly users of the I-Support system. A motion tracking input method involving technologies, which are available in any smartwatch versus a more typical button input device were examined. For the first input method a motion tracking hand-wearable device was constructed that was strapped on the external side of the palm (Fig. 5.6), containing an Inertial Measurement Unit (IMU) (including 3-axis accelerometers, 3-axis gyroscopes and 1 magnetometer), a micro-controller, and a bluetooth transmitter for wireless operation. The device could track the motion of the user's hand, which was transmitted to a central controller and those motions were then translated by the motion planner into the desired motion command for the control of the soft-arm. A thimble with an embedded pressure sensor acted as an activation switch for the tracker device (Fig. 5.6(b)) and only when the user pressed the thimble, the tracker was activated and the motion of the hand was recorded and translated into the desired motion command. The second input device was a commercial waterproof computer keyboard, where the user could issue a motion command for the soft-arm to be controlled by pressing the appropriate arrow button (e.g. upward movement = up-arrow button).



Figure 5.6: a) Motion tracking hand-wearable device. b) Thimble with the embedded pressure sensor for activation).

Both input methods were introduced to the participants as an option for controlling the soft-arm motion. Participants were initially trained in both options by a short computer game, which required to catch a red cube by a user-controlled green cube. If the red cube was caught then it would randomly jump to another field on the “game board” and the participant was instructed to catch it again as many times and as fast as he/she could for a time period of 1 min. The participants were asked, which option of the input device was found easier and thus would like to use in order to control the robot motion of the soft-arm during the water pouring scenario. After the training on the two input devices, and independently of the participants’ cognitive status, all (100%) mentioned that (1) providing motion commands was much easier with the computer keyboard than with the motion tracking hand-wearable device and (2) they prefer to use the computer keyboard for controlling the soft-arm in the water pouring scenario. Therefore, the following water pouring scenario was performed in all participants with the use of the waterproof computer keyboard.

### 5.1.5 Water Pouring Experiments

Initially, the participant wearing swimming clothes was seated on the motorized chair with the back towards the robotic soft-arm (Fig. 5.7) and the water temperature was set to his/her preferences. Subsequently, the test administrator explained to the participant that three different operation modes will be tested in the following order: (1) autonomous operation, (2) shared control and (3) tele-manipulation mode.

For the first, autonomous operation mode, the participant was informed that the soft-arm will provide water fully automatically for 1 min following a 6-step path on the upper back with the starting and end point at the top right of the upper body (Fig. 5.8). To illustrate the movement path of the water stream to the participant, the test administrator showed a poster that indicated the six target points on the upper back region.

After the water rinsing task with the autonomous operation mode was completed, the test administrator explained that in the next, shared control mode, the participant must control the motion of the soft-arm by his-/herself using the arrow keys of the waterproof computer keyboard, which was placed on the thighs such that the soft-arm motion related to the direction of the arrow keys. In addition, the participant was told that the I-Support bathing robot provides some audio assistance as described above (command registration



Figure 5.7: Water pouring clinical validation study with the I-SUPPORT bathing robot installed in a typical bathroom of a rehabilitation clinic at a geriatric hospital.

and execution) and that the motion of the soft-arm is restricted to the upper back region. The test administrator then instructed the participant to cover the entire upper back region (i.e., all six target points shown on the poster) with water and that 2 min would be provided to complete the task with the shared control mode. Finally, the participants were told to use the tele-manipulation mode to cover the entire upper back region with water. The test administrator explained that in this mode, the soft-arm motion is also controlled by the arrow keys of the waterproof computer keyboard placed on the participant's thighs; however, the I-Support bathing robot does not provide any audio assistance for command registration and execution, nor does it restrict the motion of the soft-arm to the upper back region. Also for this mode, each participant was informed that 2 min would be

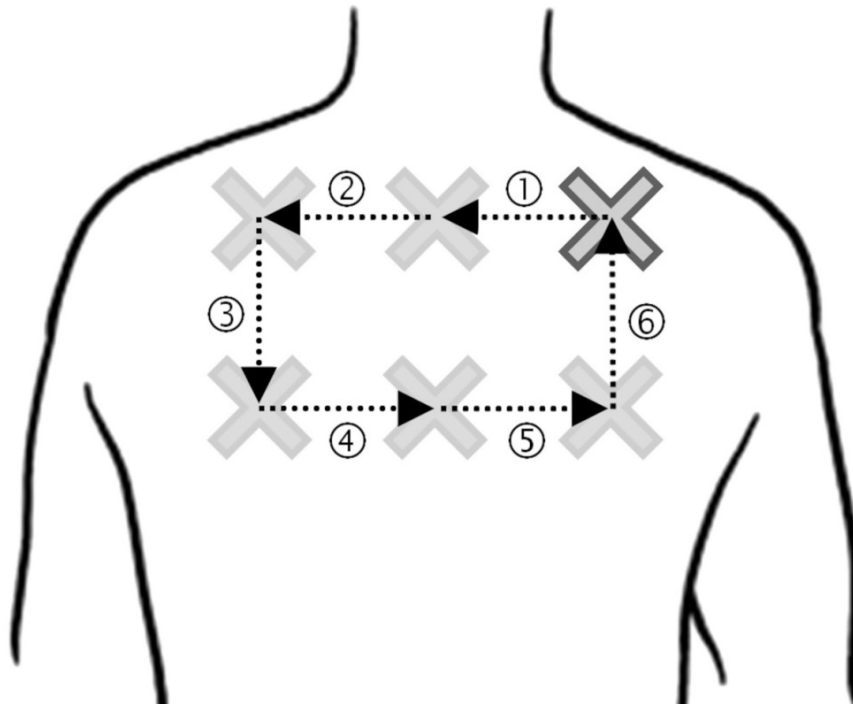


Figure 5.8: Upper back region with the six target points for which the soft-arm provided water rinsing. The dark gray outlined cross represents the starting and final position for all operation modes, the dotted arrows indicate the optimal 6-step path for the water rinsing process on the upper back region.

provided to complete the task.

Between testing each operation mode, a sufficient rest period was provided based on the feedback from the participant. For both user-controlled modes (shared control, tele-manipulation), the test administrator interrupted the test procedure either after the participant had successfully provided water for the entire upper back region (i.e., all six target points) or after 2 min even if the participant was not successful in water rinsing for the entire upper back region. The longer maximum processing time of 2 min in the user-control modes was chosen as for command issuing by the user and command recognition by the I-Support robot automatically more time is required than in the autonomous operation mode, in which the motion of the robotic soft-arm on the movement path is fully automatically controlled in smooth and constantly progressive way.

The effectiveness in rinsing water on the upper back region with the different operation modes was assessed by the following two outcome parameters: (1) coverage [%], defined as the percentage of the predefined upper back region covered with water (e.g., 3 out of 6 target points covered with water = 50 %) during the standardized time period (autonomous operation mode = 1 min, shared control and tele-manipulation mode = 2 min) and (2) step effectiveness [%], calculated as the ration of coverage to the number of steps required divided by the ratio of the maximum possible coverage to the minimum possible number of steps required for maximum possible coverage. The number of target points covered with water and the number of the steps performed during the standardized time periods were objectively calculated from the visual data obtained from the system's cameras and the kinematics combined with the behavioral-based motion controller of the

robotic soft-arm of the I-Support bathing robot.

The After-Scenario Questionnaire (ASQ) [252] was used to assess the user satisfaction with the three different operation modes. The questionnaire contains three statements that address the ease of completing the task, the time taken to complete the task, and the support available when completing the task. For each operation mode, the participants were asked to rate their level of agreement or disagreement on a 7-point scale, with lower scores indicating agreement (1 = strongly agree) and higher scores indicating disagreement (7 = strongly disagree). The scores for the three statements were averaged into a total ASQ score. The lower the ASQ score, the higher the participants' satisfaction with the operation mode. In addition, the participants completed the System Usability Scale (SUS) to evaluate their subjective perception of the overall usability of the I-Support bathing robot. The SUS is a well-established, reliable and valid 10-item scale, which can be quickly and easily administered to determine the user-perceived usability (effectiveness, efficacy, and satisfaction) of technical systems [253]. Its items are scored on a 5-point Likert-type scale ranging from "strongly agree" to "strongly disagree". The combined scores of the individual SUS items are converted into a total SUS score ranging from 0 to 100, with a higher score indicating better usability. SUS scores can be classified as "worst imaginable" (0–25 points), "poor" (25–39 points), "acceptable" (39–52 points), "good" (52–73 points), "excellent" (73–85 points), and "best imaginable" (85–100 points) perceived usability [254].

### 5.1.6 Clinical Validation Results and Discussion

The present study aimed to evaluate objectively and subjectively different operation modes of an assistive bathing robot from a human-robot interaction perspective. Being representative of potential users of this robot, we recruited older persons with bathing disability and analyzed the task effectiveness and user satisfaction with three operation modes providing different levels of assistance during a water rinsing task for the user's upper back region. In addition, we explored whether different subgroups of participants were most satisfied with a specific operation mode. Our results indicate that the autonomous operation mode for the robotic soft-arm of the bathing robot is highly effective and reliable in providing water rinsing for a predefined body area. Significantly lower task effectiveness was observed in the operation modes in which the robot autonomy was lower and the robotic soft-arm motion was predominantly controlled by the participants. Task effectiveness gradually decreased along with lower assistance provided by the bathing robot. Similar findings were observed for the user satisfaction, with the highest level of satisfaction observed for the autonomous operation mode and also a tendency to a gradually decreasing satisfaction with decreasing robot assistance. Preferences for a specific operation mode were not observed among different subgroups of participants.

Table 5.2: Differences in the task effectiveness (coverage, step effectiveness) between the shared control and tele-manipulation modes

	Autonomous operation (1)	Shared control (2)	Tele-manipulation (3)
Coverage (%)	100 ± 0.0	79.4 ± 18.2	64.4 ± 19.4
Step effectiveness (%)	100 ± 0.0	51.6 ± 10.3	43.9 ± 8.6

Data presented as mean and standard deviation.

In terms of **task effectiveness** in the autonomous operation mode, maximum coverage of the upper back region and maximum step effectiveness were achieved for all participants. Task effectiveness was substantially lower in the shared control and tele-manipulation modes than in the autonomous operation mode (Table 5.2). Only seven participants (33.3%) in the shared control mode and two participants (9.5%) in the tele-manipulation mode achieved the maximum possible coverage. Our results confirmed the primary hypothesis that task effectiveness with the bathing robot would be highest in the autonomous operation mode and gradually decrease with lower levels of robot assistance. This finding supports previous studies that compared different operation modes of other assistive robots in young or older adults and also found the highest task effectiveness in the most autonomous operation modes. Although the maximum possible time for completing the water rinsing task was allowed to be twice as long as in the autonomous operation mode, the body area covered in the user-controlled modes was significantly lower with only few participants able to provide water rinsing for the whole target body area. The lower task effectiveness in the user-controlled modes was also revealed by the significant lower step effectiveness. This suggests that participants issued several inefficient commands not increasing the body area covered by the water and that some target points on the upper back region were passed more than once or the water stream even exceeded this region (tele-manipulation mode).

As expected, among the user-controlled operation modes, task effectiveness was significantly higher in the shared control mode than in the tele-manipulation mode. This finding indicates that the audio signals of the I-Support robot given for command registration and execution as well as the restriction of the robotic soft-arm motion to the predefined upper back region effectively assisted the participants in completing the water rinsing task. However, as the task effectiveness in the shared control mode was still substantially lower than in the autonomous operation mode, it seems that the robot assistance in this mode was not optimal and the required interaction was too difficult to handle for the participants. This might be explained by the fact that participants did not directly see the robotic soft-arm behind their back during the test procedure but only could imagine its spatial position and movement based on the water stream felt on the skin of their upper back. As spatial and tactile sensory abilities decline with age [255], the position determination of the water stream on the upper back might have been particularly difficult in our sample of older adults and hampered their ability to accurately distinguish between the target points on the upper back and to perceive whether all of them were reached. Providing elderly users additional direct visual or audial assistance on the real-time position of the water stream might represent a potential option for increasing their task effectiveness in rinsing water on body parts which cannot be directly seen.

Based on previous studies on **user satisfaction**, suggesting that users of assistive robots seem to be more satisfied with operation modes for HRI in which they retain as much control as possible, we hypothesized that the user satisfaction would be lower in the autonomous operation than in the user-controlled operation modes (shared control,

Table 5.3: Differences in the user satisfaction between the different operation modes

	Autonomous operation (1)	Shared control (2)	Tele-manipulation (3)
ASQ (%)	$2.0 \pm 1.0$	$2.5 \pm 1.5$	$3.0 \pm 1.4$

Data presented as mean and standard deviation.



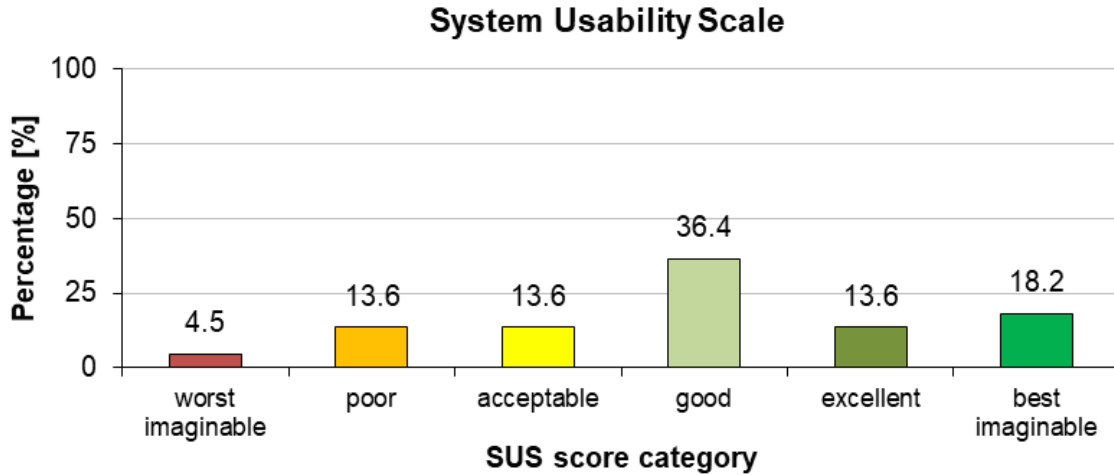


Figure 5.9: Percentage (%) distribution of participants' ratings in the different SUS score categories

tele-manipulation). Surprisingly and in contrast to this hypothesis, our results (Table 5.3) revealed that participants were, however, rather less satisfied with the user-controlled operation modes than with the autonomous operation mode, in which they had the least control and the I-Support robot fully autonomously completed the water rinsing task. A potential explanation for these findings might be the higher age of our participants, which may be associated with also a higher request for assistance when using technology than in younger populations, or the higher differences in the task effectiveness between the operation modes, which could have been perceived much more clearly by our participants during the test procedure. As the water rinsing task was interrupted by the test administrator after a maximum of 2 min in the user-controlled operation modes, participants who could not provide water for the whole target body area might have become aware of their low task effectiveness, potentially leading to a feeling of overload that may have affected their satisfaction with these operation modes [26].

Finally, the participants completed the **System Usability Scale** to evaluate their subjective perception of the overall usability of the I-Support bath robot system. The SUS score across participants that completed the “water pouring” scenario ( $n = 22$ ) averaged  $60.7 \pm 23.0$  points, indicating an overall “good” usability of the I-Support system tested during the validation experiments. The SUS scores ranged from the minimum of 0 points to the maximum of 100 points, suggesting a large heterogeneity in the SUS results. However, when averaging the scores into the different rating categories (Fig. 5.9) most of the participants gave a rather positive feedback on the I-Support usability. More than 81.8% of the participants rated the I-Support system between “acceptable” to “best imaginable”, while less than 18.2% rated the I-Support system between “poor” and “worst imaginable”.

## 5.2 Learning from Demonstration Using Navigation Functions

Using similar experimental setup that includes a Kinect-v2 camera, we aim in this Section to test and analyze the performance of the learning with Navigation Functions approach.



For an initial demonstration procedure in the lab, simple sinusoidal trajectories were visually captured by the camera. In this setup, the human expert holds a red marker and performs a pouring water like motion on the specific body part. The subject is seated and is free to move their back (twist, slight turn, etc.). The only constraint is to remain seated during the recordings and to avoid extreme movements, in order to keep the body part region inside the camera’s field of view, top row of Fig. 5.10. A more complex demonstration example obtained from the publicly available KIT whole-body human motion database [1], shown in bottom row of Fig. 5.10, is also employed to demonstrate the performance of the learning approach in a more realistic scenario. During this validation study the main goal is to imitate the way that the expert clinical carer executes the task. Therefore, our goal is to reproduce this execution no matter how effective the carer’s motion is or how complex and comprehensive this activity is (e.g. coverage percentage).

### 5.2.1 Validation Results & Discussion

The experimental data consists of trajectory data from demonstration by professional clinical carers for pouring water sequence in the 3D task space that have been transformed for learning purposes in the 2D canonical space. In the second column of Fig. 5.10, these trajectories in the canonical space are depicted with blue scaled colours.

After the proposed learning from the demonstration data approach in the canonical space (i.e. the “virtual” obstacles have been incorporated), the NF controller estimates the feasible and optimal trajectory again in the canonical space, by providing to it, just the initial and destination position and by taking into account the users body structure and restrictions (i.e. the real obstacles that have been recognized in the task space and they

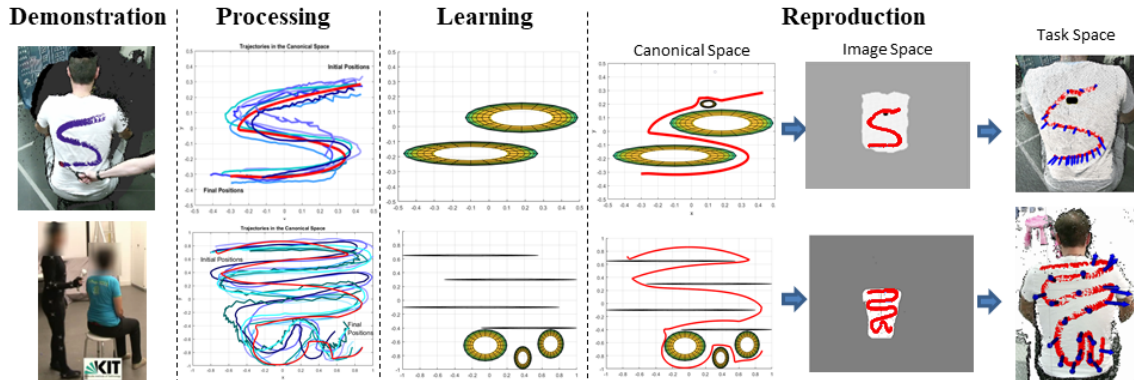


Figure 5.10: Demonstration, Processing, Learning and Reproduction procedures in experimental validation. The **Demonstration** trajectories are performed in physical space by professional nursing personnel. The demonstration data are projected into the 2D canonical space, where they are post-**Processed**. In the **Learning** phase virtual obstacles are learned using the demonstration data and the proposed NF approach. During the trajectory **Reproduction** phase a NF controller is employed to reproduce the washing action. The learned trajectory (red) is then adapted on the visually segmented back region (PointCloud view) of a subject, via the image space. **Top:** A simple showering sinusoidal trajectory is visually recorded, learned and reproduced. **Bottom:** A more complex showering trajectory is obtained from the KIT whole-body human motion database [1], learned and reproduced.

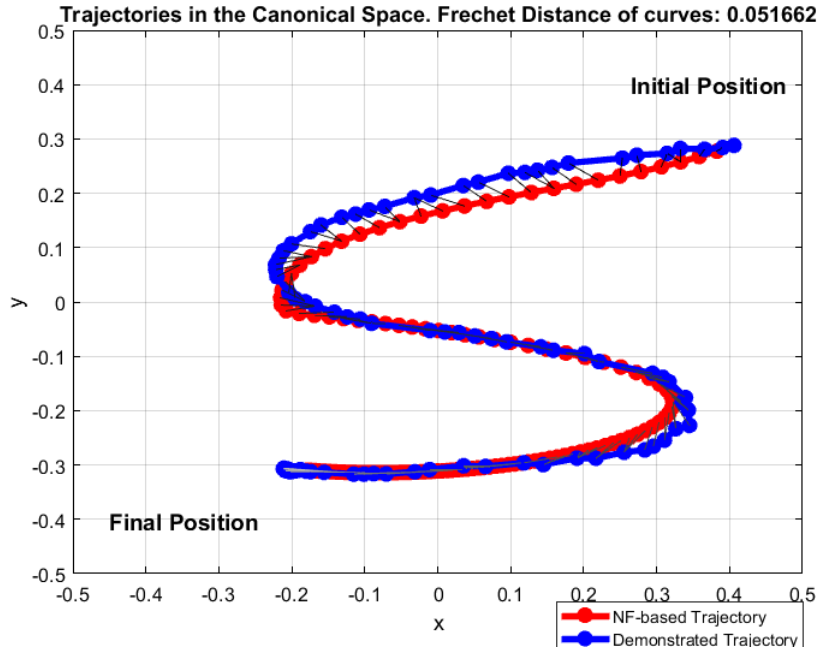


Figure 5.11: Comparison of the NF-based produced trajectory (red line) w.r.t. the carer’s demonstration (blue line) in the canonical space, based on the Fréchet distance metric.

have been also transformed to the canonical space). The evaluation procedure imposes the decision of random initial and destination positions in the canonical space.

For testing purposes we decide to use the recorded data in order to compare the NF-based produced trajectory w.r.t. the carer’s demonstration in the canonical space. In Fig. 5.11-5.12, both trajectories are plotted. The red lines represent the controller-based trajectory while with the blue lines are the demonstrated washing task execution. The discrete Fréchet distances is zero when the two trajectories are equal and grows positively as the curves become more dissimilar. Based on these results, these trajectories are very similar (based on the Fréchet distance metric), since this metric take values 0.052 and 0.198, respectively. Furthermore, another qualitative finding is that the resulted trajectories are very smooth, highly appropriate for execution by any assistive robotic device.

In the right part of Fig. 5.10 (Reproduction), a learned trajectory (red) is adapted on a 3D deformable back region of a subject, which is visually perceived by the camera (Point-Cloud view). The estimated local perpendicular vectors (blue) are also demonstrated in several segments of the executed path. Based on them, the ability of the proposed approach to apply any learned trajectory in the canonical space to any 3D subject’s body part surface with unknown curvature, motion and deformation is demonstrated. In Fig. 5.10 (top part of Reproduction), a learned trajectory (red) is adapted on a 3D deformable male’s subject back region, which is visually perceived by the camera, and also properly compensates for the presence of a real obstacle (e.g. a restricted area) of a subject’s body part (PointCloud view).

In conclusion, the experimental results show that the planning system is able to learn the expert’s skills by producing similar paths with the respective demonstrated trajectories, providing very smooth, highly appropriate for execution of demonstrated paths by any assistive robotic device. This approach is also suitable for adapting the variable subject’s preferences w.r.t. to time constraints of washing tasks execution. Hence we can conclude

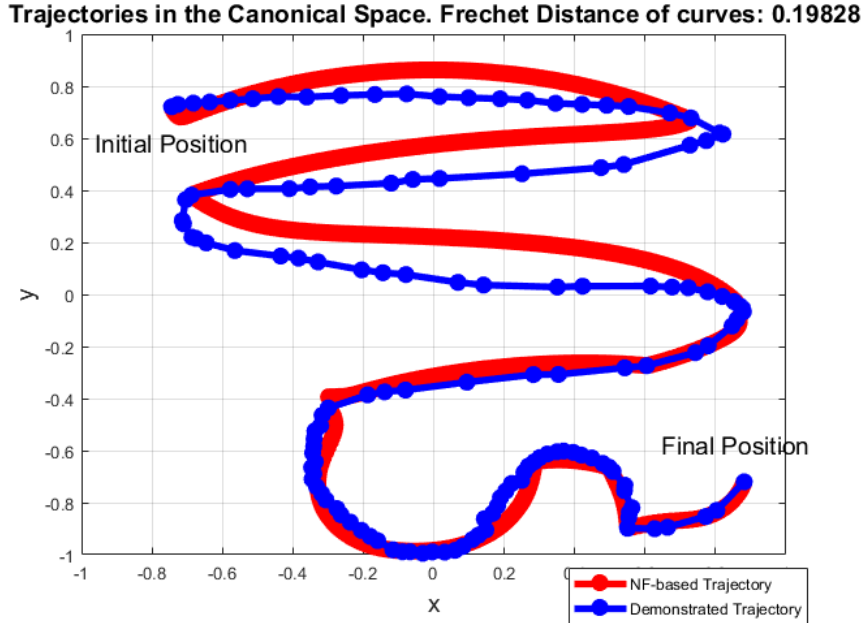


Figure 5.12: Comparison of the NF-based produced trajectory (red line) w.r.t. the carer’s demonstration (blue line) in the canonical space, based on the Fréchet distance metric.

from the preliminary results presented in this Section, that the NF learning method can be used as an alternative to the DMP approach and encode complex motions with a flexible representation, which has the potential to be applicable in different settings.

An immediate improvement to the learning procedure of the NF learning approach is to use an iterative algorithm which uses a branch procedure and computes all such possible obstacle trajectory combinations, since in the current learning procedure the GA in essence simply “decides” if the trajectory passes right or left from an obstacle. Moreover, in the current version, the number of the obstacles is set by the user. Despite the fact that a GA approach could use an open number of obstacles, this choice would drastically make its efficacy lower. Hence, an approach in which the number of obstacles is estimated by an efficient algorithmic process based on the experimental data would be beneficial. Furthermore, a more extensive experimental validation on different interactive actions that include a periodic component, would also provide a more clear view on the potential of the method on motion encoding and reproduction from demonstration.

### 5.3 Adaptation of Motion Primitives to Dynamic Surfaces

In this Section, we present an experimental evaluation of the adaptation method of primitive washing motions, focusing on a surface wiping task, which is learned by demonstration, using data from the publicly available KIT whole-body motion database. The proposed leader-follower hierarchical system considers the discrete part of the wiping action as the leader and the periodic pattern as the follower. An experimental setup (Fig. 5.13), suitable for validating the performance of the proposed approach with similar configuration to the I-Support system, is employed that includes a single Kinect-v2 camera providing depth data for the back region of the subject, with accuracy analyzed in [245]. The segmentation of the washing surface is implemented, for the purposes of the following experiments with a color filter to the pixels of the image obtained from Kinect-v2 camera. The setup also

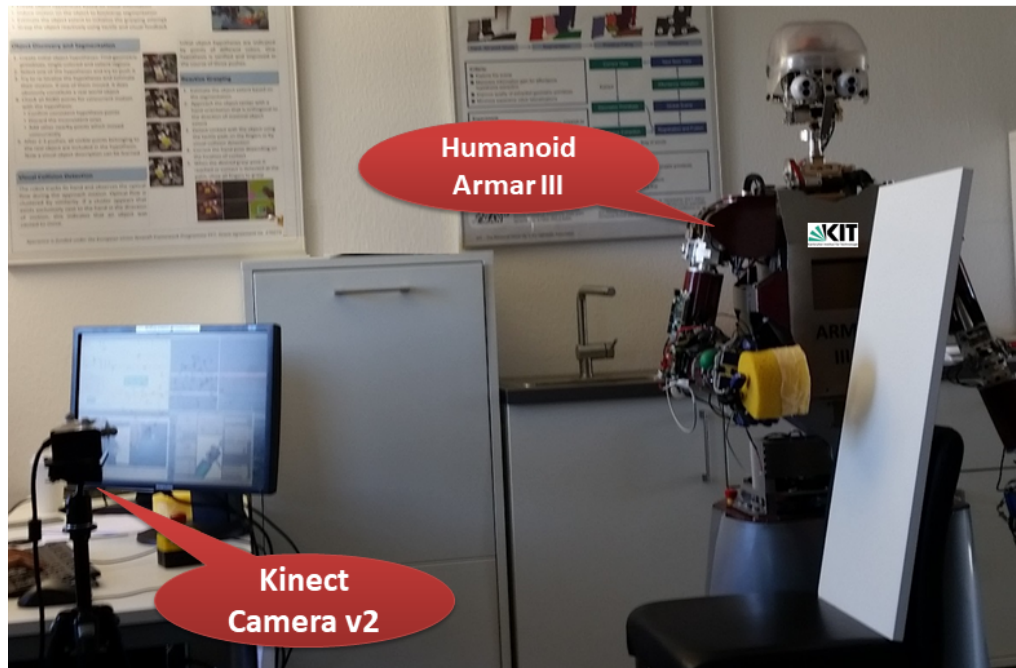


Figure 5.13: The experimental setup includes a single Kinect-v2 camera providing depth data and an ARMAR-III robot developed at KIT.

includes an ARMAR-III robot developed at KIT [256], in order to take advantage of its known kinematics structure for accurate execution of the generated actions.

### 5.3.1 Experimental Scenarios

In order to test the integrated perception-based interaction system, we consider the following experiments:

- **Scenario I:** ARMAR-III wipes a static whiteboard. The discrete part of this washing action is a vertical top-down movement. Obstacle avoidance is demonstrated in this experiment, Fig. 5.14.
- **Scenario II:** ARMAR-III wipes a dynamic whiteboard, which is held by a person and rotated/translated from time to time, Fig. 5.15.
- **Scenario III:** ARMAR-III wipes a male subject's back. He is moving his back during the experiment to demonstrate the adaptation of the robot motion to the subject's movement. For safety reasons, ARMAR-III has no real contact with the person, Fig. 5.18- 5.19.

We choose a whiteboard for this experimental procedure in order to bypass difficulties imposed by image segmentation, which is out of the scope of this thesis, and as a reference surface for validation purposes.

### 5.3.2 Experimental Results & Discussion

In Figures 5.14 – 5.19, the results of all experimental scenarios are presented. ARMAR-III uses all 7 DOFs of its right arm and its hip yaw joint to generate functional washing actions.

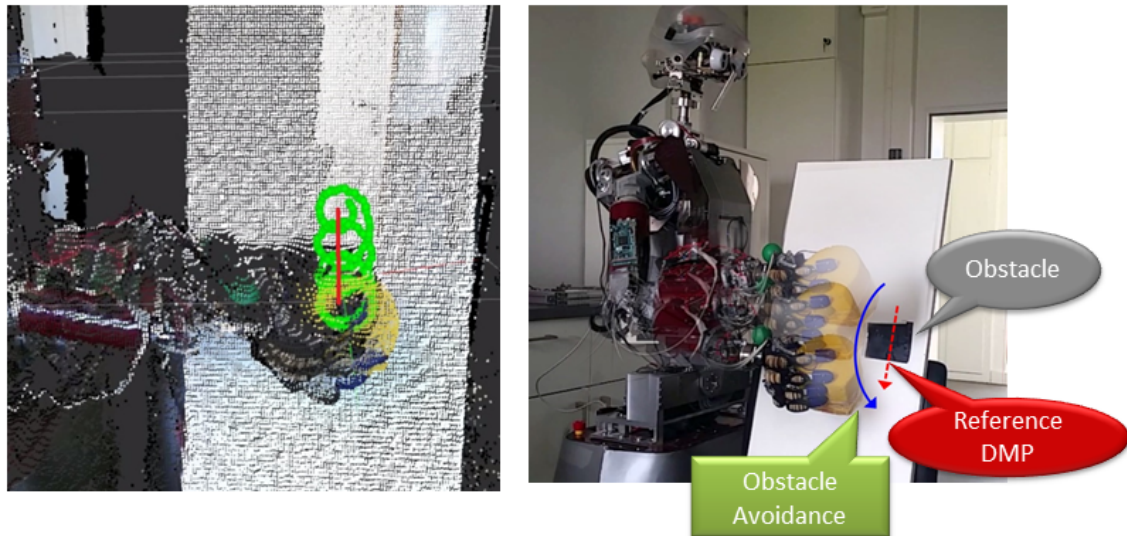


Figure 5.14: **Scenario I:** ARMAR-III wipes a static whiteboard. **Left:** Execution of a wiping motion, which constitutes of a linear leader DMP path (red) and a periodic circular motion (green), depicted from the system's camera perspective in Point-Cloud view. **Right:** An obstacle area (e.g. injury depicted with black patch) is detected in the Task space and transformed back to the Canonical space. The leader DMP path (red) leads to the target point. The controllers output is the blue path and is executed by the robot, avoiding the sensitive injured area. After the obstacle avoidance the end-effector's motion converges to the indicated linear motion primitive.

A washing task with obstacle avoidance (Scenario I) is demonstrated in Fig. 5.14, in which an obstacle area indicated with a black patch (e.g. an injury on the back region) intersects with the motion of the robot if a leader top-down path (red) is directly executed. In particular, the injured area is visually perceived and is transformed back to the Canonical space using the inverse  $T_1$  and  $T_2$  transformations. This information is inserted into the Navigation function, maximizing the values of the potential field in the corresponding coordinates. As soon as the leader DMP path (red) is defined, an attractive vector field is formed and leads to the target point. The robot executes a modified path (blue) and avoids to wash the obstacle area.

In addition, the results of Scenario II are intuitively visualized in the top of Fig. 5.15, using the Point cloud view provided by the Kinect camera and a sequence of green points showing the evolution of the circular motion and its adaptation to the movement of the whiteboard. In order to validate the performance of the robot during the periodic action, we compared the reference path computed by the washing system with the end-effector path calculated from the robot's forward kinematics. More specifically, Figures 5.16–5.17 depict the time evolution of the reference pose (position & orientation quaternion) and the executed robot end-effector pose during the wiping motion of the planar surface for Scenario I and II is presented. It is apparent, that the robot manages to follow the surfaces pose compensating with it's motion and simultaneously execute the wiping action. Furthermore, the executed path quickly converges to reference with bounded error both in position and orientation.

In Scenario III, the robot executes the washing trajectory over the back region of a male subject. In more detail, in Fig. 5.18 the subject moves to the right, while in Fig. 5.19



he moves backwards. In both cases the robot with the aid of the proposed motion planning approach manages to compensate with the movement of the subject, without interrupting

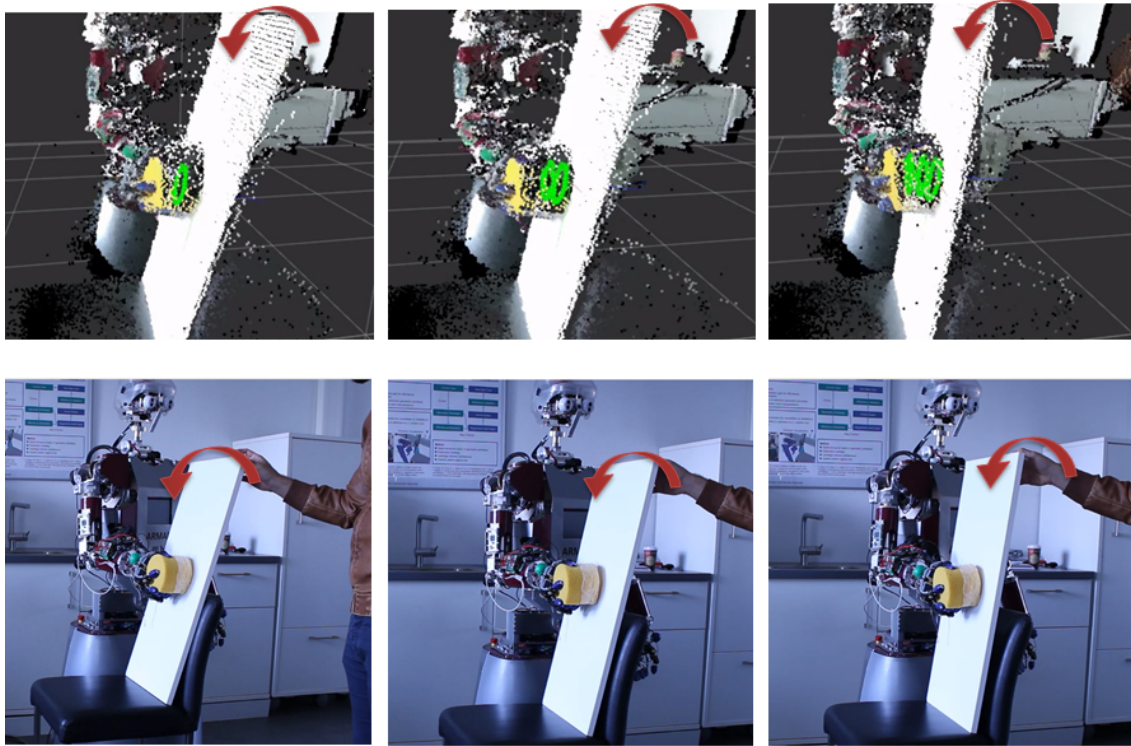


Figure 5.15: **Scenario II:** ARMAR-III is wiping a dynamic whiteboard and a person moves the board. ARMAR-III is holding a yellow sponge, which keeps contact with the surface. The wiping movement is adapted to the surface's motion. **Top:** PointCloud view of the whiteboard and the robot's end-effector showing instances of the adaptation of the wiping motion with the green trajectory. **Bottom:** Side camera view of the wiping action indicating with the red arrow the motion of the whiteboard implied by the human.

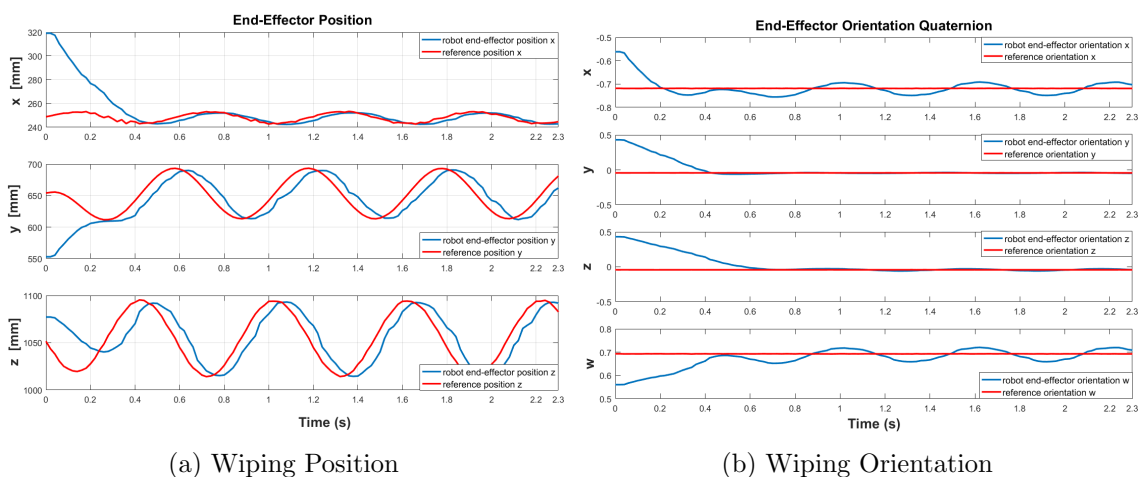


Figure 5.16: Evolution of the reference position and orientation for the wiping motion and the executed robot end-effector position, during **Scenario I** that involves a static planar surface.

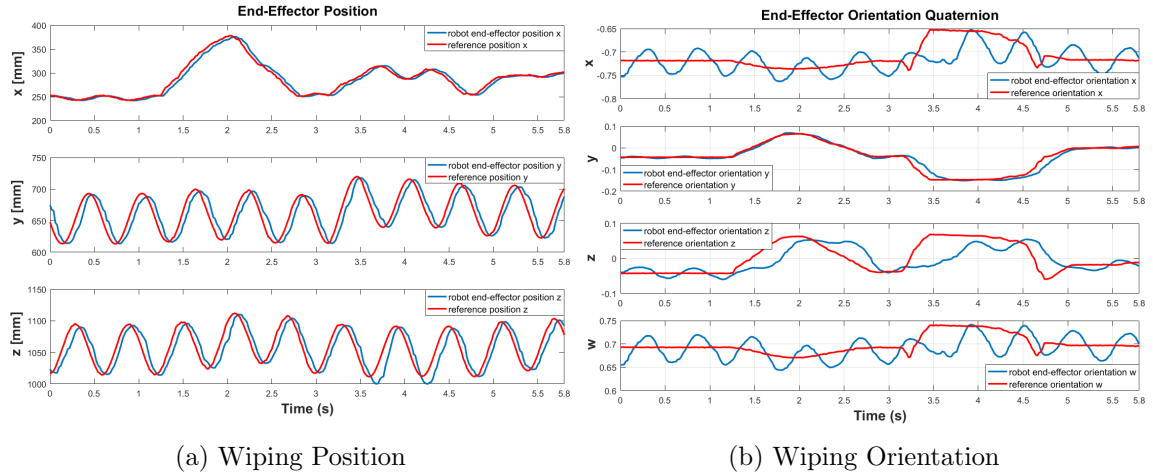


Figure 5.17: Evolution of the reference position and orientation for the wiping motion and the executed robot end-effector position, during **Scenario II** that involves a moving planar surface.

the washing task indicating the applicability of this approach to real life scenarios.

The experimental results indicate that the proposed vision-based washing system is capable of adapting the motion of a robotic end-effector to a moving and non-rigid surface, such as the back region of a person. This goal is achieved by merging two methods, a leader-follower motion primitive framework (CC-DMP) with a visual perception based controller. This fusion carries out human-friendly washing tasks with imitation learning techniques, while enabling on-line adaptation to dynamic moving and deformable objects (in our case, body parts). Using this flexible leader-follower framework it is easy to expand the repertoire of learned washing actions and smoothly integrate them to a bathing robotic system. We can also make the system more interactive by applying shared control techniques and by letting the user adjust on the fly the parameters of the robotic motion and the contact forces according to his/her feeling, affecting only the time scaling parameters of the trained DMPs.

The former remark confirms that, the choice of a learning from demonstration method among other learning techniques as described in Sec. 1.3.3, can incorporate effectively the expertise of health-care experts only from a few examples. However, pure DMPs have a limitation of flexibility for the new environment and can reproduce noise from the demonstration. To overcome these issues, the developed system integrates a visual information with an interactive DMP representation like CC-DMP.



Figure 5.18: **Scenario III:** ARMAR-III is wiping a male subject's back region. The subject is moving to the right and the robot follows the motion. **Left:** Side camera view of the subject performing a translation to the right. **Right:** Zoomed Point cloud view of the experiment highlighting the adaptation of the wiping motion (green trajectory) to the movement of the subject. Safe distance is kept between the back and ARMAR-III's end-effector.



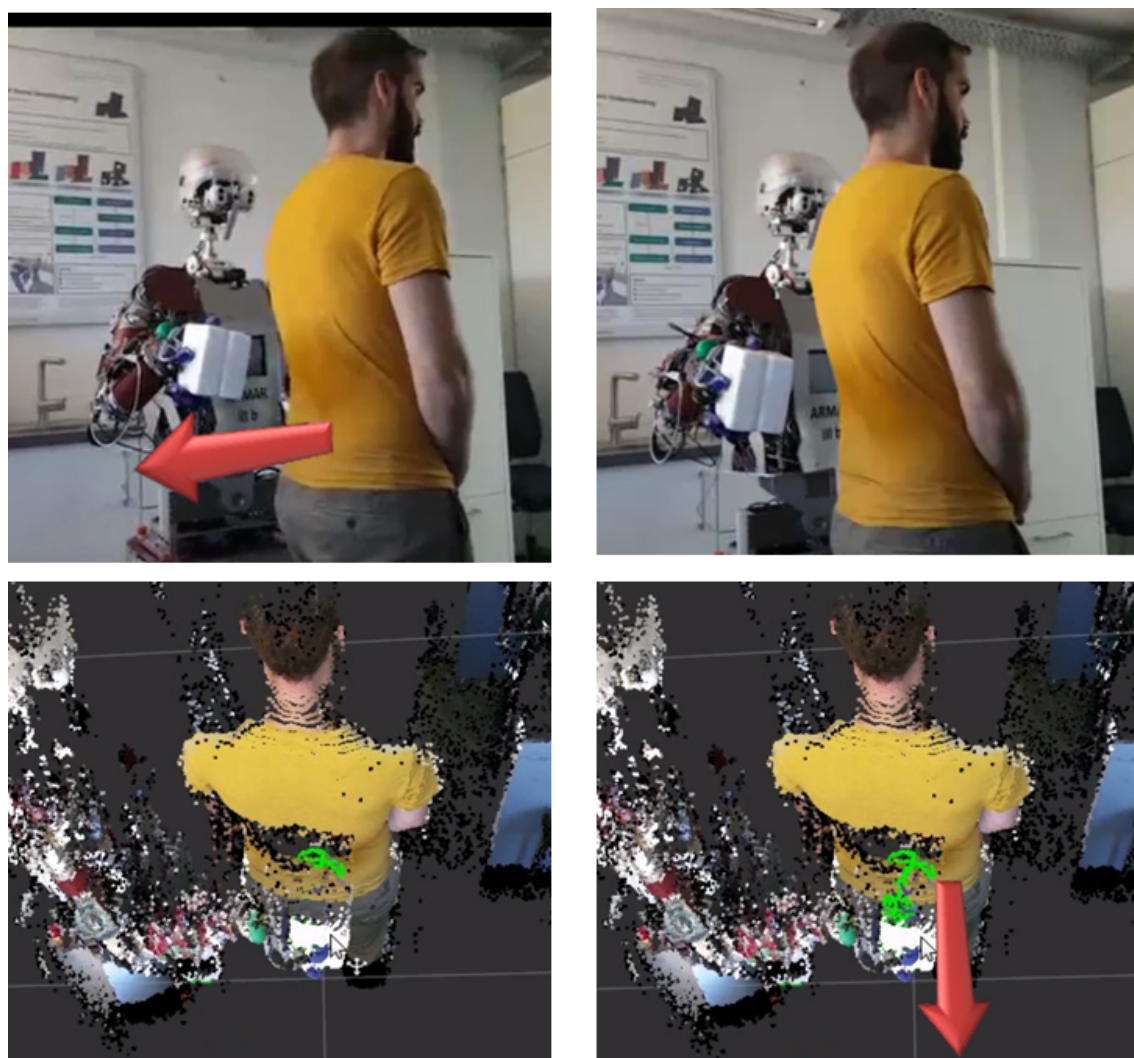


Figure 5.19: **Scenario III:** ARMAR-III is wiping a male subject's back region. The subject is moving backwards and the robot follows the motion. **Top:** Side camera view of the subject performing a translation backwards. **Bottom:** Point cloud view of the experiment highlighting the adaptation of the wiping motion (green trajectory) to the movement of the subject. Safe distance is kept between the back and ARMAR-III's end-effector.



## Chapter 6

# Experiments of Interactive Motion Planning on Deformable Surface

In this chapter, we present the experimental validation of the interaction control framework presented in Chapter 4. The goal of the conducted experiments is to assess the performance of the proposed approach in several surface interaction tasks with a deformable object. The performance criteria include interaction trajectory tracking accuracy, computational efficiency and contact force regulation. The aforementioned criteria drive our decision for choosing proper implementations of the preprocessing steps and integrate them to the overall proposed system.

### 6.1 Pre-processing Steps

The visual segmentation preprocessing step is used as an input to the deformation tracking algorithm, in order to detect the object of interest on the image plane and to reduce the number of points in the acquired point-cloud. For the implementation of this step, we employ the popular GrabCut method, implemented efficiently in GPU, described in [257]. This algorithm addresses the segmentation task as an energy minimization problem based on statistical models of the foreground and the background.

For the deformation tracking step, physics based algorithms, are more suitable for robotic interaction tasks, as described in Section 4.3. For this experimental validation we employ the FEM based method proposed in [143, 144], because it provides more accurate deformation tracking for large elastic deformations, as compared to mass-spring-damper approaches, with real-time computational performance ( $\sim 35$ fps). Moreover, this method relies on a volumetric linear FEM approach, which computes the deformation field over the elements of a known tetrahedral mesh approximating the object of interest. The use of tetrahedrons is convenient for meshing volumes with high complexity, since it offers accurate modelling and computational efficiency at the same time.

Regarding the mesh parameterization, we integrated into our system the Discrete Exponential Map (DEM) presented in [198]. DEM is a local parameterization algorithm, which focuses on the computation of normal coordinates of a discrete surface (mesh) using the Dijkstra's algorithm with very high computational efficiency ( $\sim 100$  fps).

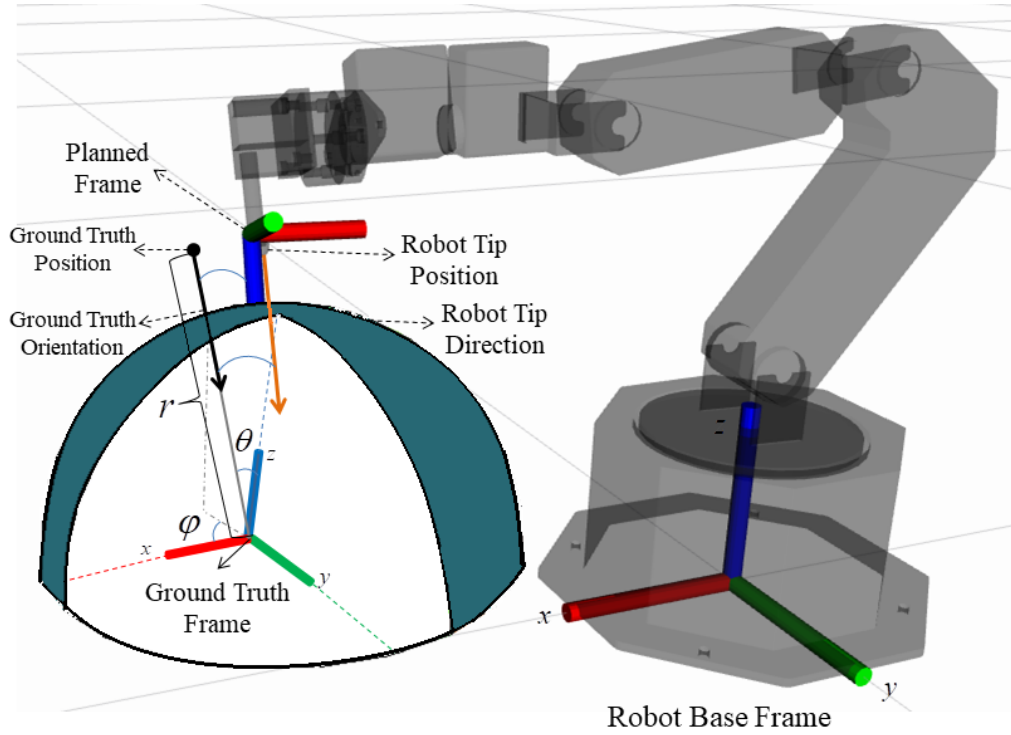


Figure 6.1: Hemispherical model with known relative position and orientation with respect to the robot's base frame. This model is used to derive ground-truth data for position and orientation accuracy evaluation both of the planned and the executed motion by the robotic manipulator.

## 6.2 Experimental Set-Up

In order to test and analyze the performance of the proposed mesh-based framework, an experimental set-up is used which includes an Intel®RealSense™ depth camera and a Widow-XL robotic manipulator by Trossen Robotics to perform the interactive tasks, as depicted in Fig. 6.2. The Widow-XL robot is a 5-DoF manipulator equipped with Dynamixel MX Series Servo motors operated in torque control mode. One of the goals of this evaluation procedure is to quantitatively measure the accuracy of planning in interactive tasks (both contact and non-contact), using our proposed framework, and of its respective execution by a robot manipulator. The planning experiments involve interactive motion tasks over an object of interest both in a stationary scenario and in a deforming scenario. In order for the generation of ground truth data to be feasible, the object's shape is required to be known at each time step, especially for the deforming scenarios. Therefore, in this experimental study, we chose to use a hemispherical model, which can undergo uniform deformations and its center (termed ground truth frame) has a known relative position and orientation with respect to the robot's base frame, as shown in Fig. 6.1.

The hemispherical model is realized with the upper part of a balloon Fig. 6.2. The shape of the balloon model is controlled with the use of a deformation control mechanism constructed for this experimental procedure. The air flow which affects the shape of the balloon model is provided by an air pump. The DC motor of the air pump is controlled by a PWM speed controller, modifying the resistance of its potentiometer. The potentiometer

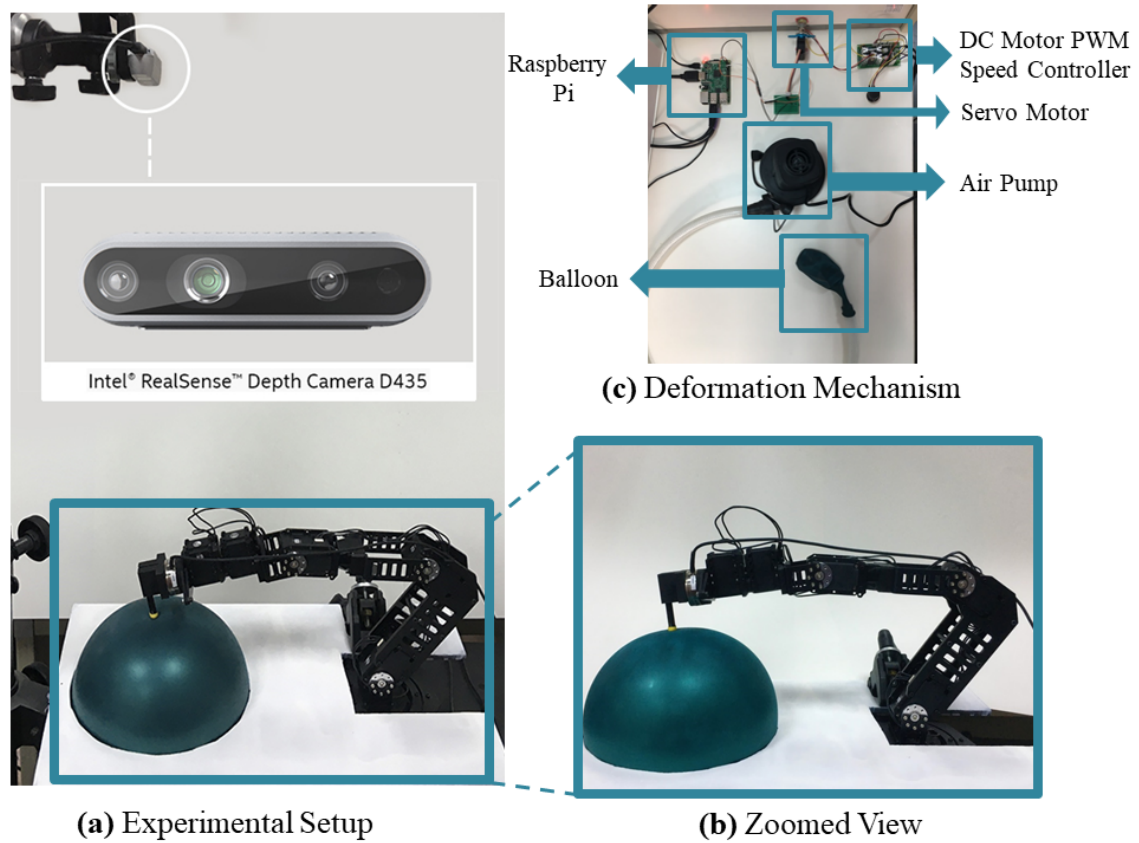


Figure 6.2: (a) The experimental setup used to test the performance of the proposed approach, which includes an Intel®RealSense™depth camera, a Widow-XL robotic manipulator by Trossen Robotics and the top side of a balloon working as a hemispherical model. (b) Zoomed aspect of the Widow-XL robotic manipulator performing an physical interaction task with a hemispherical deformable object. (c) The deformation control mechanism is constructed with air pump providing proper airflow to deform a balloon model. The DC motor of the air pump is controlled via a PWM speed controller, whose potentiometer is controlled by a servo motor. The servo motor is accurately controlled by a Raspberry Pi 3 micro-computer.

value at each time step is controlled by an algorithm executed in a Raspberry Pi 3 micro-computer, with the use of a servo motor. The angle of the servo motor linearly modifies the resistance value of the potentiometer, which modulates the PWM signal of the speed controller. With accurate speed control of the air pump’s motor, we are able to control the air flow inserted to the balloon model through a tube. However as the balloon’s pressure is increasing and becomes larger than one bar, an outgoing air current is formed which flows from the balloon to the atmosphere. Consequently, the pneumatic system finds its equilibrium and the balloons shape doesn’t change. By controlling the speed of the air pump, we are able not only to control the shape of the balloon model but also its deformation rate. The relative position of the center of the hemispherical model that is formed by the upper part of the balloon model with respect to the robot base frame is measured accurately as:  $x_c = 0.26m$ ,  $y_c = 0.025m$ ,  $z_c = 0.08m$ , denoted as Ground Truth Frame in Fig. 6.1.

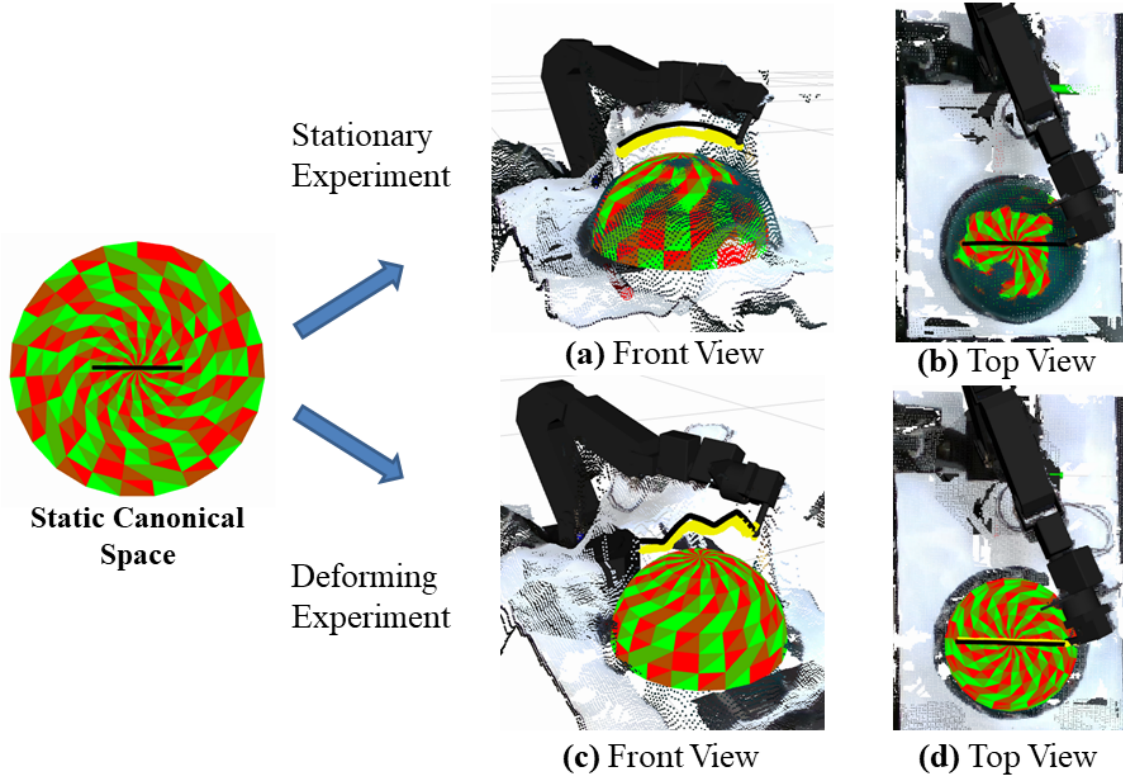


Figure 6.3: Meridian path execution in **Up**: a stationary scenario and **Down**: a deforming scenario. The interactive task is planned in the Static Canonical Space (depicted with a black colored path) and is transformed to the Physical Space with the use of the proposed framework (also depicted with a black colored path). The yellow path is the executed interactive task by the robot. (a) Front view of the stationary experiment. (b) Top view of the stationary experiment. (c) Front view of the deforming experiment. (d) Top view of the deforming experiment.

## 6.3 Experimental procedures and results

### 6.3.1 Interactive Motion Planning Accuracy

We start by expressing each interactive task in spherical coordinates following the ISO convention, i.e. denoting  $(r, \phi, \theta) : r \geq 0, 0^\circ \leq \phi \leq 360^\circ, 0^\circ \leq \theta \leq 180^\circ$ , as the radius, the azimuthal angle and the polar angle, respectively. The ground truth orientation is set, without loss of generality, to be perpendicular to the surface of the hemispherical model. Hence, it is calculated as the orientation of the vector starting from the ground truth position and passing through the model's center position, depicted with a black arrow in Fig. 6.1. The relative planned and executed robot's position is calculated with respect to the hemisphere's center and then expressed in spherical coordinates for comparison with ground truth data. Considering comparison in terms of the orientation data, the angle  $\alpha$  between the z-axis of the planned reference frame (blue vector in Fig. 6.1) and the ground truth orientation is calculated at each time step. Similarly for the robot's orientation error, the angle  $\beta$  between the z-axis of the robot's tip frame (orange arrow in Fig. 6.1) and the ground truth orientation is computed as well. Thus, with the proposed experimental protocol we are able to measure both the position and orientation errors and to properly evaluate the interactive motion planning and execution accuracy. For the



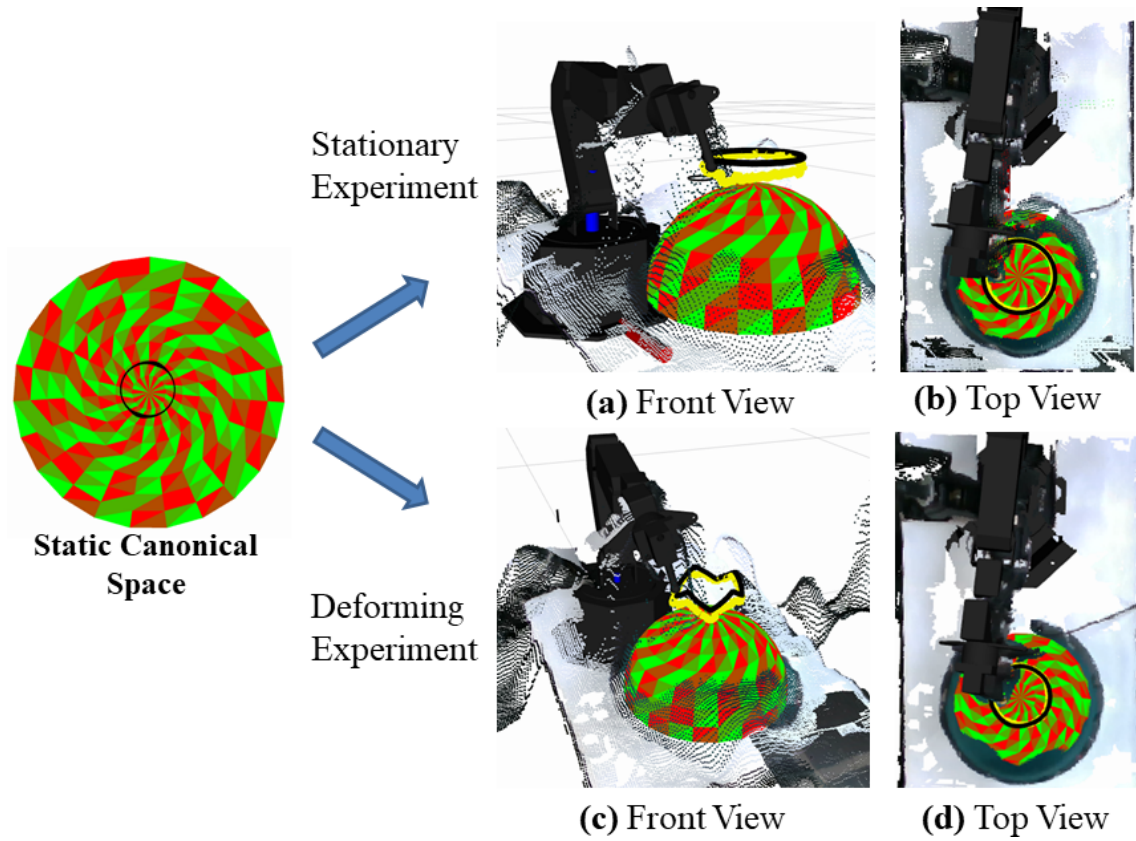


Figure 6.4: Circular path execution in **Up**: a stationary scenario and **Down**: a deforming scenario. The interactive task is planned in the Static Canonical Space (depicted with a black colored path) and is transformed to the Physical Space with the use of the proposed framework (also depicted with a black colored path). The yellow path is the executed interactive task by the robot. (a) Front view of the stationary experiment. (b) Top view of the stationary experiment. (c) Front view of the deforming experiment. (d) Top view of the deforming experiment.

deforming scenarios, the balloon model was periodically inflated and deflated between the spherical radius values  $R_{\max} = 11$  cm and  $R_{\min} = 10$  cm, using two different deformation rates of 0.25 Hz and 0.5 Hz, in two distinct experimental conditions.

To assess the performance of the proposed framework in a set of indicative experimental conditions, three different interactive tasks were planned and executed by the robotic manipulator in both stationary and deforming scenarios. More specifically, the first interactive path starts at 5 cm away from the pole of the hemispherical model, in terms of geodesic distance, crossing the pole and moving towards 5 cm on the other side. This path is denoted as **meridian path**, as depicted in Fig. 6.3. The second interactive path is a **circular path** with geodesic radius 2.5 cm away from the pole, shown in Fig. 6.4. The third interactive path is a **combined path**, comprised both of circular (with a geodesic radius of 2.5 cm) and meridian paths (of different azimuthal angles), as shown in detail in Fig. 6.5. The path requirements regarding the geodesic distance from the pole of the hemispherical model are set according to the robot kinematic constraints. They are highly important for this experimental evaluation, since they have to be respected both for the stationary and the shape deformation scenarios. As it can be deduced from the proposed evaluation protocol, the value of the polar angle  $\theta$  is indicative of the geodesic distance

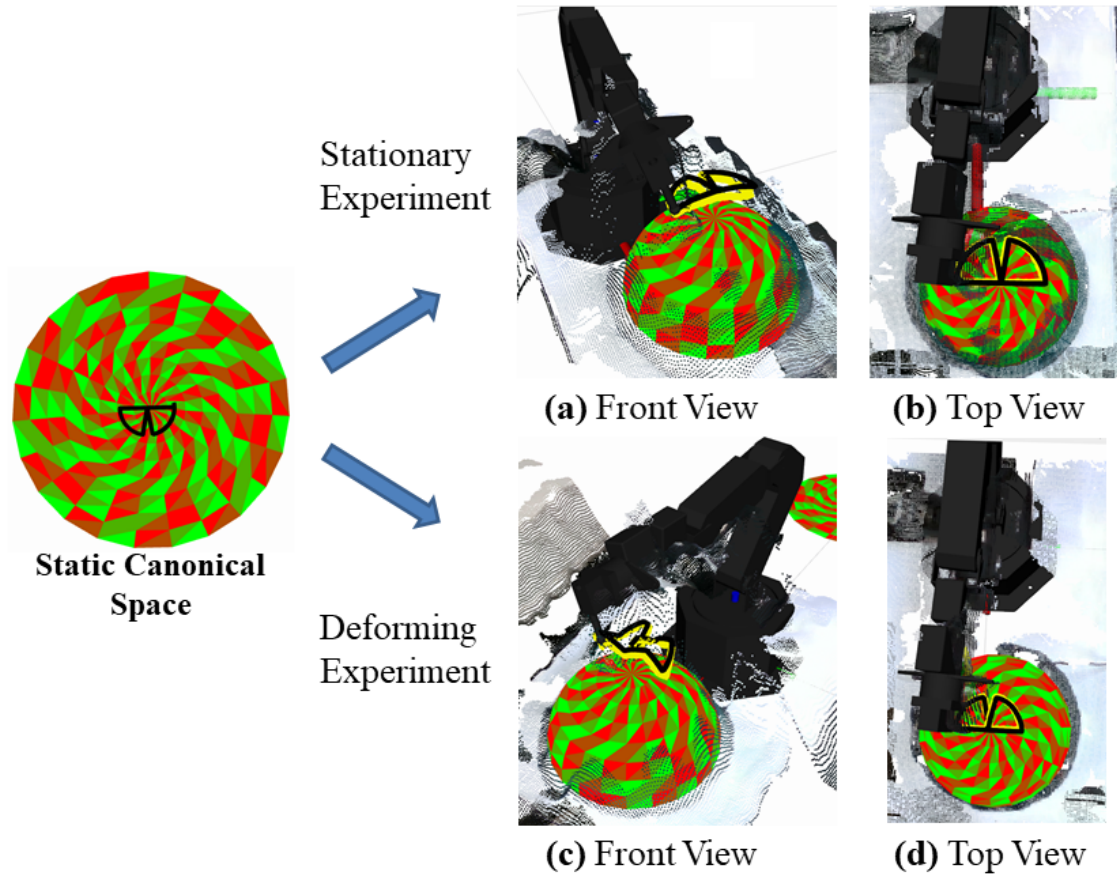


Figure 6.5: Random path execution in **Up**: a stationary scenario and **Down**: a deforming scenario. The interactive task is planned in the Static Canonical Space (depicted with a black colored path) and is transformed to the Physical Space with the use of the proposed framework (also depicted with a black colored path). The yellow path is the executed interactive task by the robot. (a) Front view of the stationary experiment. (b) Top view of the stationary experiment. (c) Side view of the deforming experiment. (d) Top view of the deforming experiment.

from the polar point, since these two values are linearly dependent with the sphere radius  $R$ . For all the tasks in these experiments, the interactive motion planning goal is to keep a constant perpendicular distance of 3 cm from the surface of the model.

Figures 6.3 to 6.5 present an overview of indicative results obtained, regarding the planning and execution of interactive paths, for the three experimental scenarios considered in this study. The paths are planned in the Static canonical frame following the requirements mentioned above. The proposed interactive motion planning framework achieves accurate transformation of the planned paths to the robot's physical space despite the visual occlusion caused by the presence of the robot in the scene, as shown by the black colored paths in the Figures. By comparing the paths executed in the stationary and deforming conditions, as depicted by the front views of the experimental scene shown in the Figures, one can clearly observe the motion adaptation performed to compensate for the surface deformation. Furthermore, the apparent path similarity between the stationary and the deforming scenarios, as shown particularly in the top views of these Figures, visually demonstrates that, by using the proposed Dynamic canonical space, the planning



Table 6.1: Planning and execution accuracy errors for three interactive trajectories (Circular, Meridian, Combined), expressed in spherical coordinates,  $r$  (cm),  $\theta$  ( $\text{rad} \times 10^{-2}$ ),  $\phi$  ( $\text{rad} \times 10^{-2}$ ), for the stationary object scenario with spherical radius values  $R_{\max} = 11$  cm and  $R_{\min} = 10$  cm. The planning errors of the current interactive mesh approach (denoted as **IMP**) are compared to the planning errors of our previous direct visual planning approach (denoted as **DVP**) and to the planning errors of our previous direct visual planning approach with occlusion from the robot motion (denoted as **DVPO**). The robot execution errors (i.e. evaluated on the path actually executed by the robotic manipulator) are denoted as **Robot**.

Stationary	Circular		Meridian		Combined		
	$R = 10\text{cm}$	$R = 11\text{cm}$	$R = 10\text{cm}$	$R = 11\text{cm}$	$R = 10\text{cm}$	$R = 11\text{cm}$	
$r$	IMP	0.25 (0.25±0.02)	0.45 (0.47±0.02)	0.24 (0.24±0.02)	0.45 (0.45±0.04)	0.23 (0.23±0.03)	0.45 (0.45±0.03)
	DVP	0.33 (0.32±0.29)	0.51 (0.15±0.69)	0.32 (0.30±0.39)	0.58 (0.13±0.66)	0.33 (0.51±0.37)	0.34 (0.19±0.54)
	DVPO	2.37 (0.64±2.28)	2.54 (1.64±1.94)	0.89 (0.80±0.39)	0.72 (0.61±0.39)	1.18 (0.78±0.89)	1.03 (0.49±0.69)
	Robot	0.97 (0.64±0.27)	1.11 (0.78±0.27)	1.03 (0.71±0.19)	1.15 (0.89±0.22)	0.90 (0.56±0.24)	1.14 (0.81±0.24)
$\theta$	IMP	1.25 (-1.23±0.25)	1.21 (-1.69±0.25)	1.27 (-1.04±0.78)	1.41 (-1.39±0.85)	1.31 (-1.17±0.58)	1.42 (-1.48±0.66)
	DVP	3.83 (-3.18±2.14)	3.52 (1.18±2.23)	4.01 (-3.03±2.63)	3.83 (0.45±2.80)	4.40 (-1.06±5.30)	3.79 (1.03±2.60)
	DVPO	9.28 (1.57±9.15)	10.1 (2.63±9.77)	12.7 (-6.89±10.7)	11.9 (-3.47±11.4)	12.5 (-3.12±12.1)	12.2 (0.57±12.2)
	Robot	3.87 (-2.90±0.90)	3.47 (-3.19±0.82)	3.28 (-2.54±4.33)	3.17 (-2.82±4.24)	4.28 (-2.63±2.93)	4.63 (-2.75±2.74)
$\phi$	IMP	1.76 (-0.56±1.03)	1.15 (-0.54±1.02)	1.61 (0.04±0.63)	1.42 (0.03±0.56)	1.84 (1.16±1.43)	1.88 (1.20±1.45)
	DVP	7.59 (-0.66±4.68)	6.95 (-1.52±6.01)	8.24 (-1.64±5.96)	7.29 (-1.79±4.73)	6.10 (2.75±7.15)	7.42 (4.23±7.70)
	DVPO	45.9 (23.8±47.0)	51.5 (21.8±56.1)	68.8 (6.26±88.7)	74.6 (6.50±84.5)	73.5 (54.2±63.6)	71.0 (39.3±71.0)
	Robot	3.87 (0.07±2.86)	3.47 (0.56±2.41)	3.28 (0.02±2.68)	3.17 (0.03±2.61)	4.28 (0.40±2.24)	4.63 (0.58±2.56)
$\alpha$	IMP	2.67 (3.67±0.91)	2.16 (4.09±0.63)	2.87 (2.68±1.05)	2.97 (3.06±1.21)	2.95 (2.78±1.01)	3.05 (3.14±1.18)
	DVP	5.59 (4.41±3.45)	5.83 (3.43±7.05)	4.33 (3.79±2.12)	3.87 (1.56±4.85)	5.35 (4.56±2.80)	4.68 (2.77±2.43)
	DVPO	24.6 (23.2±8.09)	25.0 (24.0±6.86)	26.6 (25.8±6.34)	25.9 (25.3±5.35)	21.8 (20.2±8.18)	20.6 (19.5±6.43)
$\beta$	Robot	3.82 (3.68±1.05)	3.57 (3.39±1.14)	7.63 (6.46±4.07)	7.08 (6.09±3.63)	6.07 (5.53±2.52)	5.52 (5.09±2.17)

Data presented as RMSE relative to ground truth data (mean  $\pm$  standard deviation of the error values are presented in parentheses)

procedure actually manages to properly compensate for the object deformation, despite the presence of large visual occlusions.

For the purposes of a quantitative performance evaluation, we conducted a comparative study between the proposed interactive framework and the perception-based motion planning algorithm described in 3, where a planning algorithm was proposed which uses directly the Point-Cloud data of an RGB-D Camera. The errors in position (measured in spherical coordinates) and orientation are presented comparatively in Tables 6.1 and 6.2, for the stationary and the deforming experiment, respectively. For each accuracy metric, the errors presented in the Tables are measured with respect to the ground truth position and orientation data (as explained above, in Section 6.2). The Tables present errors characterising the accuracy of motion planning in three different experimental conditions: a) using the interactive mesh approach for motion planning presented in Chapter 4 (denoted as IMP), with the robot (and the large induced occlusions) present in the scene, b) using the direct visual approach for planning from Chapter 3 (denoted as DVP), without occlusions in the scene, and c) using the previous DVP approach, further subject to occlusions from the robot (denoted as DVPO). The Tables also present results regarding the accuracy of the actual motion executed by the robot when using our proposed IMP approach (actual motion execution errors are denoted as ‘Robot’ in the Tables). The data

Table 6.2: Planning and execution accuracy errors for three interactive trajectories (Circular, Meridian, Combined), expressed in spherical coordinates,  $r$  (cm),  $\theta$  ( $\text{rad} \times 10^{-2}$ ),  $\phi$  ( $\text{rad} \times 10^{-2}$ ), for the deforming object scenario with deformation rate  $f = 0.25$  Hz &  $f = 0.5$  Hz. The planning errors of the current interactive mesh approach (denoted as **IMP**) are compared to the planning errors of our previous direct visual planning approach (denoted as **DVP**) and to the planning errors of our previous direct visual planning approach with occlusion from the robot motion (denoted as **DVPO**). The robot execution errors (i.e. evaluated on the path actually executed by the robotic manipulator) are denoted as **Robot**.

Deforming	Circular		Meridian		Combined		
	$f = 0.25$ Hz	$f = 0.5$ Hz	$f = 0.25$ Hz	$f = 0.5$ Hz	$f = 0.25$ Hz	$f = 0.5$ Hz	
$r$	IMP	0.26 (0.25±0.03)	0.26 (0.26±0.02)	0.25 (0.25±0.02)	0.25 (0.24±0.04)	0.24 (0.25±0.03)	0.24 (0.25±0.03)
	DVP	0.75 (0.35±0.75)	1.25 (0.68±0.64)	0.66 (-0.54±0.66)	0.94 (-0.53±0.79)	0.72 (-0.7±0.37)	1.04 (-0.7±0.18)
	DVPO	2.67 (0.93±2.76)	2.81 (1.93±2.47)	1.38 (0.88±0.63)	1.43 (0.83±0.5)	1.44 (0.93±0.95)	1.43 (0.69±0.72)
	Robot	0.96 (0.92±0.28)	1.03 (0.99±0.30)	1.05 (1.04±0.20)	1.05 (1.01±0.31)	0.95 (0.92±0.28)	0.95 (0.93±0.35)
$\theta$	IMP	1.22 (-1.14±0.57)	1.22 (-1.20±0.25)	1.24 (-1.03±0.68)	1.22 (-1.01±0.68)	1.27 (-1.14±0.57)	1.27 (-1.14±0.57)
	DVP	4.64 (-2.30±4.29)	7.48 (3.24±3.36)	4.27 (-3.12±3.82)	7.33 (-2.41±2.76)	5.97 (-0.25±3.28)	8.09 (-0.47±3.74)
	DVPO	9.64 (1.64±8.56)	10.5 (2.78±8.34)	13.0 (-5.13±10.35)	12.8 (-3.89±11.8)	13.0 (-3.63±12.4)	13.3 (2.17±12.6)
	Robot	2.81 (-2.45±2.91)	2.95 (-2.76±1.03)	4.73 (-2.71±3.88)	4.44 (-2.62±3.59)	3.80 (-2.45±2.91)	3.78 (-2.48±2.86)
$\phi$	IMP	2.99 (-0.25±1.61)	2.67 (0.48±0.99)	1.27 (0.32±1.18)	1.26 (0.34±1.67)	1.62 (0.38±1.19)	1.60 (-0.23±1.59)
	DVP	10.57 (-2.83±8.20)	8.95 (0.87±8.93)	7.39 (0.78±7.37)	7.94 (-3.11±7.32)	6.97 (0.79±8.34)	7.24 (0.79±8.34)
	DVPO	47.8 (28.5±48.4)	51.9 (25.7±67.6)	71.1 (7.76±85.5)	74.2 (7.52±86.5)	74.2 (56.5±63.5)	73.2 (34.2±71.5)
	Robot	5.02 (0.90±5.94)	6.45 (-5.17±3.86)	5.36 (1.42±5.63)	5.41 (2.63±7.15)	5.99 (1.37±5.85)	5.99 (2.06±8.23)
$\alpha$	IMP	2.52 (3.48±1.15)	2.50 (3.58±1.43)	2.87 (2.68±1.04)	2.83 (2.64±1.02)	2.98 (2.80±1.04)	2.97 (2.79±1.03)
	DVP	5.71 (6.38±6.24)	6.08 (4.41±7.64)	5.95 (5.19±2.93)	7.02 (4.56±6.61)	8.82 (3.45±2.49)	9.65 (3.73±3.19)
	DVPO	24.63 (26.2±8.59)	25.6 (24.7±7.13)	27.2 (26.3±6.44)	27.0 (26.3±6.02)	22.6 (20.7±8.68)	21.8 (22.0±5.13)
$\beta$	Robot	3.67 (4.66±6.78)	3.85 (4.57±6.51)	6.61 (5.74±3.30)	6.85 (5.86±3.57)	5.64 (5.18±2.24)	5.72 (5.26±2.28)

Data presented as RMSE relative to ground truth data (mean  $\pm$  standard deviation of the error values are presented in parentheses)

presented in the Tables show RMSE values evaluated relative to ground truth data, as well as as mean and standard deviation values of the errors measured along the whole duration of the interactive tasks (with the mean values denoting a positive or negative error bias during motion and the standard deviation values denoting actual error fluctuations indicating precision of motion).

Analysing more in detail the performance of the proposed IMP approach, as presented in Tables 6.1 and 6.2, it can be observed that the maximum RMSE value for the radius ( $r$ ), both in the stationary and in the deforming scenarios, is 0.45 cm, while the maximum RMSE value for the polar angle ( $\theta$ ) is  $1.42 \times 10^{-2}$  rad in the combined path of the stationary experiment with  $R = 11$  cm (resulting in 0.16 cm geodesic distance error). It is evident that the planned paths follow the requirements of the tasks, with millimeter accuracy, both in terms of the relative radial distance and the geodesic distance. Evaluating comparatively the RMSE results between the stationary and the deforming scenarios, it is clear that the changes both in radial and geodesic distances during the evolution of the deformation are effectively compensated. The orientation error  $\alpha$  of the planned motion with respect to the ground truth has the largest value of  $3.05 \times 10^{-2}$  rad (or  $1.75^\circ$ ) in the circular deforming interactive task (in the case of the higher frequency of 0.5 Hz), maintaining perpendicular orientation to the hemispherical model's surface. The errors in azimuthal

angle ( $\phi$ ) are indicative of the projection accuracy of each interactive task into the Physical space, including its timing constraints. The largest RMS error recorded for the planned motion is  $2.99 \times 10^{-2}$  rad in the circular path deforming experiment, resulting in 0.33 cm geodesic distance error (estimated for  $R_{\max}$ ). It is evident that the timing constraints of the task are respected when using the proposed IMP framework. The larger values of  $\phi$  in standard deviation comparing to the other position accuracy metrics derive from the large steps of the ISO convention followed in this analysis.

Using the planned motion at each time step, the robot is able to execute all the interactive tasks with a precision which is subject to its kinematic and joint control constraints. The implemented stiffness controller, described in Section 4.2.2, has proven convergence in the desired position for non-contact scenarios. However, the choice of its gains directly affect the robot's precision. More specifically, the quantitative analysis presented in Tables 6.1 and 6.2 shows that the maximum RMSE value for the radial motion ( $r$ ) (for all stationary and deforming scenarios) is 1.15 cm (recorded in the meridian stationary condition) and the maximum RMSE value for the polar angle ( $\theta$ ) is  $4.73 \times 10^{-2}$  rad (recorded in the meridian deforming scenario), resulting in 0.52 cm geodesic distance error. An important observation is that the robot exhibits similar behavior both in the stationary and the deforming scenarios, managing to compensate for a deformation of different frequencies between the spherical radius values  $R_{\max}$  and  $R_{\min}$ . The orientation error  $\beta$  of the robot motion relative to the ground truth has the largest RMSE value of  $7.63 \times 10^{-2}$  rad (or  $4.37^\circ$ ) in the circular deforming interactive task, deriving mainly from the robot kinematic constraints due to its 5 DoF structure. The maximum robot RMS error in azimuthal angle ( $\phi$ ) is  $6.45 \times 10^{-2}$  rad (or 0.71 cm in geodesic), which shows that the robot motion exhibits larger deviations in tracking the interactive tasks with respect to the planned motion, which was expected. Nevertheless, robot execution errors remain within acceptable margins (particularly considering the hardware limitations of the robot manipulator used in these experiments), while the performance is in any case consistent (with no significant differences) in both stationary and deforming conditions, when using the proposed IMP approach, which constitutes an important conclusive outcome of the experimental study in this Section.

Analysing further the planning accuracy of our previous approach (Chapter 3) in a scene without occlusion (indicated as DVP in Tin Tables 6.1 and 6.2), it is evident from the different error metrics shown in the Tables that the visual noise inserted by the camera reduces significantly the motion planning accuracy. More specifically, for the radial distance ( $r$ ), the largest errors are observed in the deforming scenarios (with the maximum RMSE value of 1.25 cm observed in the high frequency circular scenario). For the polar ( $\theta$ ) and azimuthal ( $\phi$ ) angles, which are characteristic values for the geodesic distances, the maximum errors are  $8.09 \times 10^{-2}$  rad (geodesic 0.89 cm) and  $10.57 \times 10^{-2}$  rad (geodesic 1.16 cm), respectively. The position planning inaccuracies occur due to depth estimation noise especially at the edge of the object despite the accurate results of the segmentation algorithm. In terms of orientation ( $\alpha$ ), the maximum error is  $9.65 \times 10^{-2}$  rad ( $5.53^\circ$ ). The overall planning performance of a direct vision-based algorithm shows that it is suitable for applications in which the visual occlusion of the surface is low and the accuracy requirements reduced. In case of larger visual occlusion of the object's surface by the motion of the robot (a condition denoted as DVPO in Tables 6.1 and 6.2), the planning accuracy is further reduced as shown by the quantitative results for the respective error metrics presented in the Tables.

In this case, the maximum RMS error values obtained for the radial distance ( $r$ ), the polar angle ( $\theta$ ) and the azimuthal angle ( $\phi$ ), are: 2.81 cm,  $13.3 \times 10^{-2}$  rad (geodesic 1.46 cm)

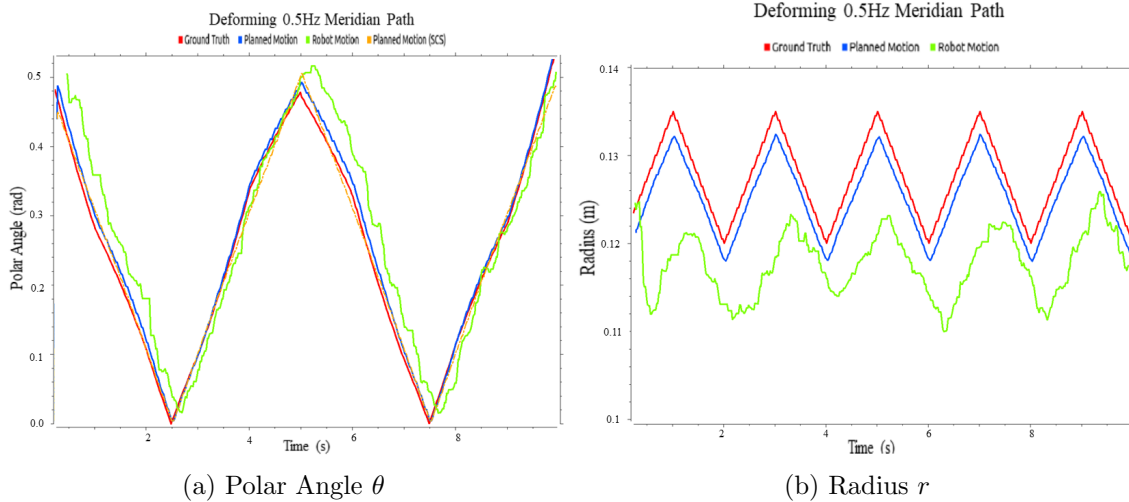


Figure 6.6: Evolution of the Ground Truth (red), the Planned (blue) and the Robot motion (green), during the execution of the **meridian** path in deforming scenario, expressed in (a) polar angle  $\theta$  representation which is indicative for the geodesic distance preservation from the pole of the hemispherical model and (b) radius  $r$  representation which is indicative for the perpendicular relative distance preservation from the surface of the hemispherical model. The orange line is the planned motion with direct transformation from the Static Canonical Space to the Physical Space. This planning strategy fails to follow the geodesic distance changes occurring in the object's surface.

and  $74.2 \times 10^{-2}$  rad (geodesic 8.16 cm), respectively. These high error values are in fact at least an order of magnitude larger than the ones obtained with the IMP approach. This result clearly reveals that a direct vision-based algorithm (based on local processing of raw depth data) indeed fails to properly plan the required interactive tasks, as opposed to the interactive mesh-based motion planning framework proposed in Chapter 4, which is able to accurately plan the required trajectories on a deformable surface even in the presence of large and persistent occlusions (in our case, induced by the robot continuously moving in front of the object surface in the scene).

In Figures 6.6 - 6.8 the evolution of the ground truth (red), the planned (blue) and the robot motion (green) expressed in polar angle and radius during the execution of each path in deforming scenario is graphically presented. In this graphical representation it is apparent that the planned motion manages to follow the desired task expressed in the ground truth graph. The executed robot motion error varies during the execution of the task showing how the kinematic constraints affect its motion. However, in polar angle representation of Fig. 6.6a, 6.7a and 6.8a the result (in orange color) of the proposed interactive framework without the use of Dynamic Canonical Space is plotted. The direct transformation from the Static Canonical Space to the Physical Space does not take into account the geodesic distance changes occurring in the surface of a deformable object, using the geodesic information captured at the time instance it was created. Thus, it fails to fulfill the geodesic distance requirements set in the interactive tasks, which is more evident in the circular path Fig. 6.7a and random path 6.8a. This comparison exhibits the necessity of Dynamic Canonical Space in the planning of interactive tasks for deformable objects in case geodesic distance requirements are set.

In order to further evaluate the motion planning accuracy of our system, we measure

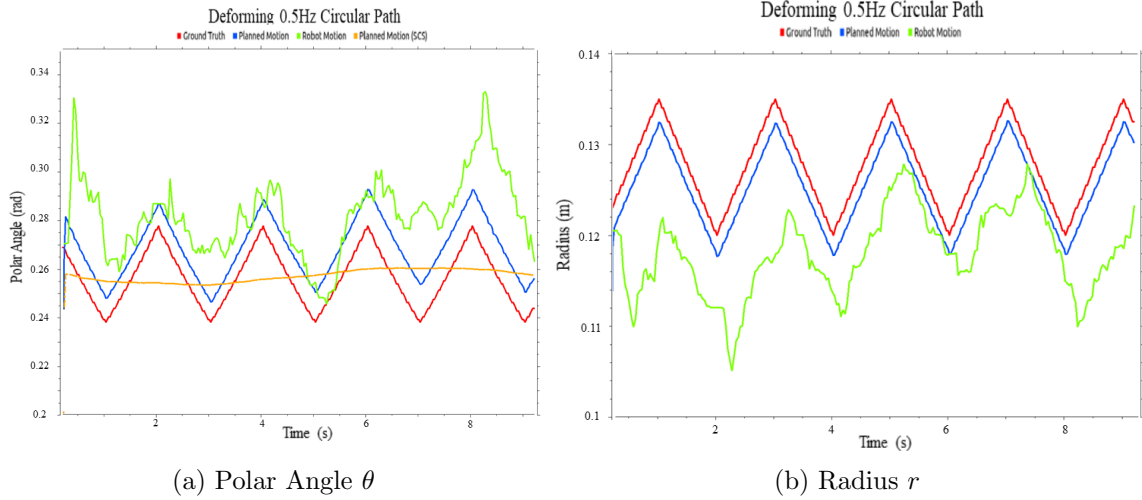


Figure 6.7: Evolution of the Ground Truth (red), the Planned (blue) and the Robot motion (green), during the execution of the **circular** path in deforming scenario, expressed in (a) polar angle  $\theta$  representation which is indicative for the geodesic distance preservation from the pole of the hemispherical model and (b) radius  $r$  representation which is indicative for the perpendicular relative distance preservation from the surface of the hemispherical model. The orange line is the planned motion with direct transformation from the Static Canonical Space to the Physical Space. This planning strategy fails to follow the geodesic distance changes occurring in the object's surface.

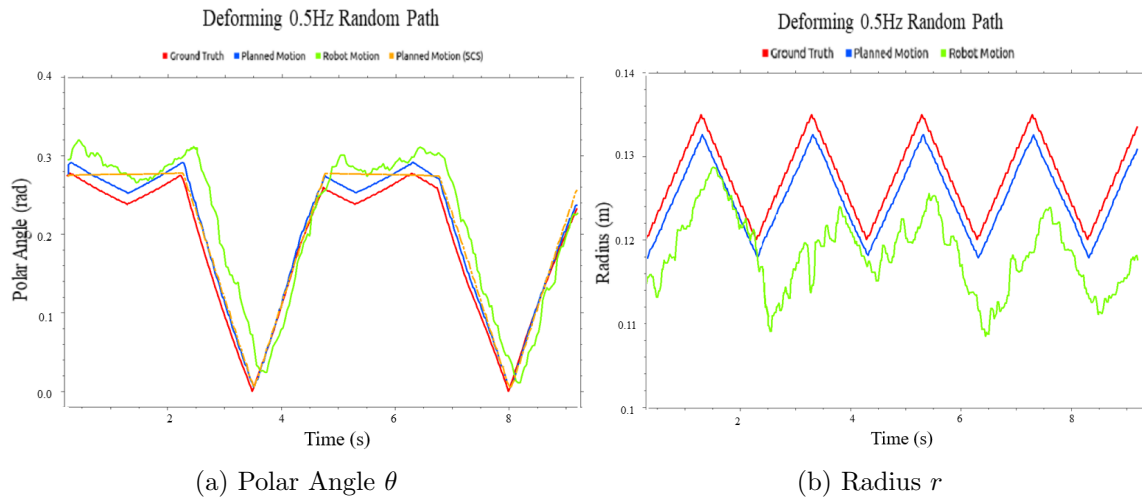


Figure 6.8: Evolution of the Ground Truth (red), the Planned (blue) and the Robot motion (green), during the execution of the **circular** path in deforming scenario, expressed in (a) polar angle  $\theta$  representation which is indicative for the geodesic distance preservation from the pole of the hemispherical model and (b) radius  $r$  representation which is indicative for the perpendicular relative distance preservation from the surface of the hemispherical model. The orange line is the planned motion with direct transformation from the Static Canonical Space to the Physical Space. This planning strategy fails to follow the geodesic distance changes occurring in the object's surface.

quantitatively the ability of the proposed framework to track a physical point on the surface

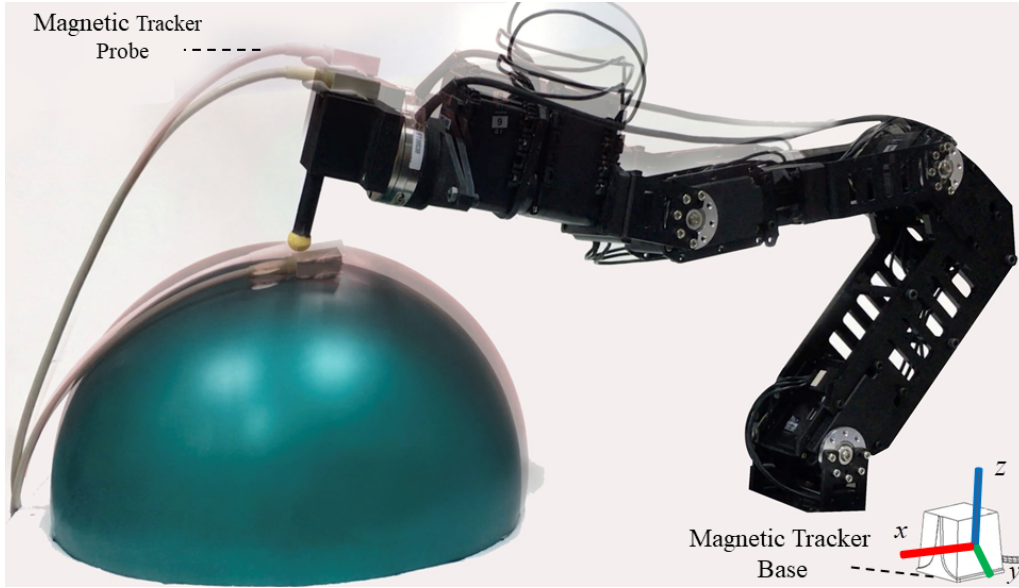


Figure 6.9: Tracking of a physical point on the surface of a deformable object. The tracking accuracy is measured with the Ascension TrakStar ATC3DGT magnetic tracker with millimeter accuracy.

of a deformable object, during the same periodic deformation scenario. In this experiment, we follow a slightly different planning strategy, in which we make use of transformation  $\zeta$  from the SCS to the Physical Space, in order to preserve the geodesic distances and track the same physical point on the object's surface. Error measurements in this experiment are realized with the use of a magnetic tracking device (an Ascension TrakStar ATC3DGT magnetic tracker), which can provide position measurements with an accuracy of one millimeter. In particular, one of the magnetic tracker probes is placed on the object surface and the other probe is attached on the robot's end-effector, as depicted in Fig. 6.9. Table 6.3 presents the results obtained regarding the relative position between the two probes along each axis of the tracker reference frame, for two object deformation frequencies. It should be pointed out here that the mean value is highly dependent on the initialization bias of each experiment (i.e. the placement of the magnetic probe on the object and the relative pose of the robot), whereas the standard deviation value characterises the motion precision thus revealing the actual position tracking performance achieved during the deformation experiments. More specifically, the maximum tracking deviation of the robot

Table 6.3: Physical point tracking errors presented along the axes of the Physical Space. The tracking error is calculated as the relative position between the magnetic tracker's probe attached on the deformable model and the tracker's probe attached on the robot's end-effector.

Tracker experiment	$x$ (cm)	$y$ (cm)	$z$ (cm)
$f = 0.25$ Hz	$2.76 \pm 0.05$	$0.74 \pm 0.13$	$3.58 \pm 0.31$
$f = 0.5$ Hz	$3.17 \pm 0.13$	$0.41 \pm 0.11$	$4.06 \pm 0.41$

Data presented as mean and standard deviation of the error values.

is 0.13 cm along  $x$ , 0.13 cm along  $y$  and 0.41 cm along  $z$ , confirming the sub-centimeter accuracy performance of the proposed framework. Larger tracking deviation values along the  $z$  axis compared to  $x$  and  $y$  axes, are observed due to the placement of the probe near the pole of the hemispherical object, whose major motion direction, caused by the object's deformation is along the  $z$  axis. Similarly to the performance assessment results presented above, the robot motion is affected by its kinematic constraints and stiffness controller gains.

### 6.3.2 Interactive Motion Demonstration

In the previous experiments, the accuracy of the proposed framework was evaluated by planning several paths in SCS and projecting the trajectories to the Physical space, over the surface of the target object, during real-time execution of the motion. In this section, we aim at evaluating the framework in a different context, that of motion programming by human demonstration. Our goal here is to showcase that the proposed framework can be effectively applied in such a context and is particularly suitable for planning (by means of human demonstration) robot manipulation tasks that involve interaction with the surface of a (potentially deformable) object.

For this purpose, we recall that, as shown in Section 4.3, each transformation (between SCS, DCS, and Physical space) is invertible; hence, using the proposed approach, interactive tasks performed on the surface of a stationary object can be transformed back to SCS during the demonstration process, as depicted in Fig. 6.10. To handle interactive trajectories which lie over or under the surface (that is, involving or not physical contact with the object during task execution), an algorithm is implemented which projects the trajectory points at each time frame on the surface of the object, using shaded normals combined with the notion of active triangle described in Section 4.3. The continuity of the demonstration trajectories ensures that, at each time frame, the motion evolves on the same active triangle or is transferred on one of its neighbors, thus reducing the search area during execution of the algorithm.

Following this process, the demonstrated task is thus recorded (and eventually encoded, for generalisation purposes) in SCS. By applying the proposed IMP approach, the trajectory can then be properly reproduced in real time and interactively at any deformation state of the target object, respecting both the time and spatial constraints (vertical and geodesic distances) of the demonstrated task. In this experiment particularly, a complex motion is demonstrated over the surface of the hemispherical model, with radius  $R = 11$  cm. In order to evaluate the accuracy of the trajectory recorded in SCS, the motion was reproduced from SCS and transformed back to Physical space. The reproduced motion was compared to the demonstrated one, as shown in Fig. 6.11, illustrating that the demonstrated path is actually reproduced quite accurately back on the physical space, using the proposed IMP framework. Specifically, the maximum planning errors, obtained for the whole duration of motion, were measured to be: 0.37 cm along  $x$ , 0.42 cm along  $y$  and 0.26 cm along  $z$  direction.

Using spherical coordinates, as described in the experiments of the previous Section, we further measured quantitatively the motion reproduction accuracy in a stationary scenario, for a hemispherical model of radius  $R = 10$  cm, as well as in a deforming scenario with two different deformation frequencies ( $f = 0.25$  Hz and  $f = 0.5$  Hz). The obtained results are shown in Table 6.4, where the maximum values observed for the motion planning RMS errors are: 0.25 cm error for the radius  $r$ ,  $1.57 \times 10^{-2}$  rad and  $1.51 \times 10^{-2}$  rad (0.16 cm geodesic) for the polar ( $\theta$ ) and azimuthal ( $\phi$ ) angles, respectively (showing in



fact similar millimeter accuracy performance as in the simpler trajectories of the previous experiments). The robot executes the reproduced trajectory relative to the target object surface, with an accuracy which is comparable to the performance achieved in the experiments of the previous section, as revealed from the values of Table 6.4.

Table 6.4: Motion reproduction errors of the demonstrated interactive trajectory, expressed in spherical coordinates  $(r, \theta, \phi)$ , for the whole duration of motion (RMSE  $\pm$  standard deviation of the error values). The motion planning errors of the proposed approach (denoted as IMP) are distinguished from the robot execution errors (evaluated on the trajectory actually executed by the robotic manipulator, denoted as Robot).

Demonstration		Stationary		Deforming	
Trajectory		$R = 10cm$	$f = 0,25Hz$	$f = 0,5Hz$	
$r$ (cm)	IMP	0.23 ( $\pm 0.04$ )	0.25 ( $\pm 0.05$ )	0.25 ( $\pm 0.05$ )	
	Robot	0.92 ( $\pm 0.27$ )	1.06 ( $\pm 1.11$ )	0.99 ( $\pm 0.88$ )	
$\theta$ (rad $\times 10^{-2}$ )	IMP	1.55 ( $\pm 0.79$ )	1.57 ( $\pm 0.89$ )	1.55 ( $\pm 0.84$ )	
	Robot	5.17 ( $\pm 3.70$ )	8.64 ( $\pm 6.02$ )	8.19 ( $\pm 7.29$ )	
$\phi$ (rad $\times 10^{-2}$ )	IMP	1.28 ( $\pm 1.25$ )	1.51 ( $\pm 1.70$ )	1.49 ( $\pm 1.49$ )	
	Robot	7.61 ( $\pm 4.92$ )	14.77 ( $\pm 9.39$ )	14.39 ( $\pm 10.37$ )	

Data presented as RMSE ( $\pm$  standard deviation of the error value).

The results also show consistent performance both for the stationary and the deforming scenarios, highlighting again the capacity of the proposed approach to compensate for the

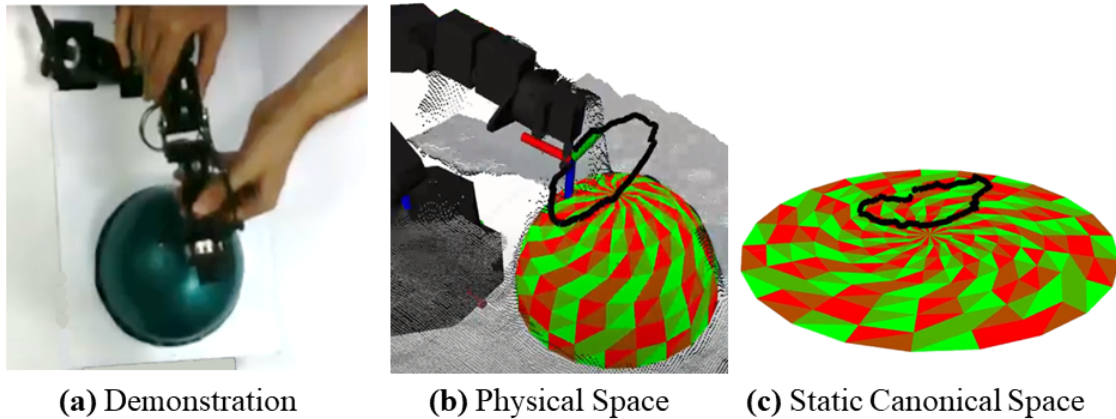


Figure 6.10: The interactive trajectory demonstration and transformation procedure. **Left:** The user is shown to move the robot over the surface of a hemispherical deformable model, in a stationary instance with radius  $R = 11cm$ , from the system's camera perspective. **Middle:** Visualization of the interactive trajectory with black line as recorded in the Physical space. At each time step the point of the trajectory is associated with the closest underlying triangle and using the proposed framework it is transformed to the Static Canonical Space. **Right:** Visualization of the interactive trajectory with black line transformed in the Static Canonical Space.



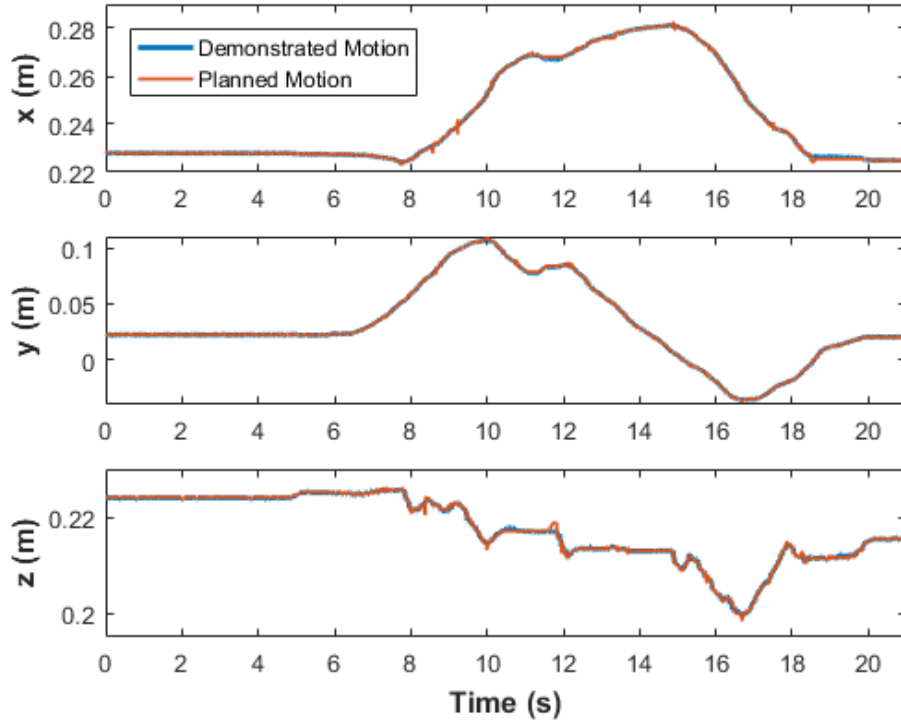


Figure 6.11: Evolution over time of the Demonstrated Motion (blue) in the 3D Physical Space, compared to the reproduced motion over a stationary hemispherical model (with the same radius  $R=11\text{cm}$  for both motions).

dynamic motions induced by the deformation of the target object surface. Furthermore, the sub-millimeter standard deviation values observed for the motion planning errors along the radial direction (IMP error values for  $r$ ), which are achieved even in the deforming scenario, show a reliable motion reproduction precision throughout the duration of the motion, demonstrating again an excellent interactive and real-time motion compensation capacity. Therefore, it can be concluded that, by applying the proposed IMP framework, a demonstrated robot manipulation task (consisting of a motion relative to a surface) can be effectively recorded and properly reproduced, interactively coping with any deformation state of the target object.

### 6.3.3 Contact Force Regulation

The previous series of experiments allowed for a thorough evaluation of motion planning accuracy for non-contact interactive tasks. The goal of this last experiment, presented in this Chapter, is to evaluate the ability of the proposed framework to regulate the contact forces during the execution of tasks that involve physical contact with the deformable object. For this purpose, an ATI Mini-40 F/T sensor is attached to the robot's end-effector, measuring the contact forces along the direction vertical to the object's surface, as depicted in Fig. 6.12. As a reminder, planning of a contact task in our approach, as has been explained in Section 4.3, is implemented indirectly through an active stiffness controller, by setting the normal offset  $d$  to negative values (thus instructing in fact the robot to move below the object's surface, as shown in Fig. 6.12).

More specifically, in this experiment, a contact task is specified such that the reference orientation remains vertical to the surface, while the normal offset linearly decreases until

a minimum value of  $d = -6$  cm (meaning that the tip of the robot, starting from initial contact, will start pushing on the deformable surface with a reference force that is linearly increasing). However, as it has already been mentioned in Section 6.2 describing the experimental setup, the deformation of the object is controlled by periodically inflating and deflating a balloon. Hence, the physical properties of the deformable model will change for different spherical radius values, since the amount of air in the balloon is different. Therefore, in order to explore the physical properties of the object, we start by applying the previously specified contact task in a stationary scenario for two different spherical radius values,  $R_{\max} = 11$  cm and  $R_{\min} = 10$  cm, as shown with dashed blue and red lines in Fig. 6.13. Several gain values for the active stiffness controller were tested and a representative behaviour is shown in the graphs for relative gain value  $k = 1$  (Fig. 6.13 top) and  $k = 1.8$  (Fig. 6.13 bottom). The coupled dynamic behavior is linear, confirming the expected ideal spring behaviour of the controller, described in Section 4.2.2. Consequently, straight lines were fitted for data presentation clarity in Fig. 6.13, to illustrate the stiffness slope margins corresponding to the two different spherical radius values.

The specified contact task was then implemented with the same controller gains, in a scenario involving a periodic deformation of the object with a spherical radius varying between the values of:  $R_{\max} = 11$  cm and  $R_{\min} = 10$  cm. Two different deformation rates were tested, 0.25 Hz and 0.5 Hz, and the obtained results are depicted with the green line plots in Fig. 6.13a and Fig. 6.13b, respectively. It is evident that the proposed interaction framework is able to compensate for the object deformation and maintain continuous contact with the object surface throughout the task, without applying excessive forces

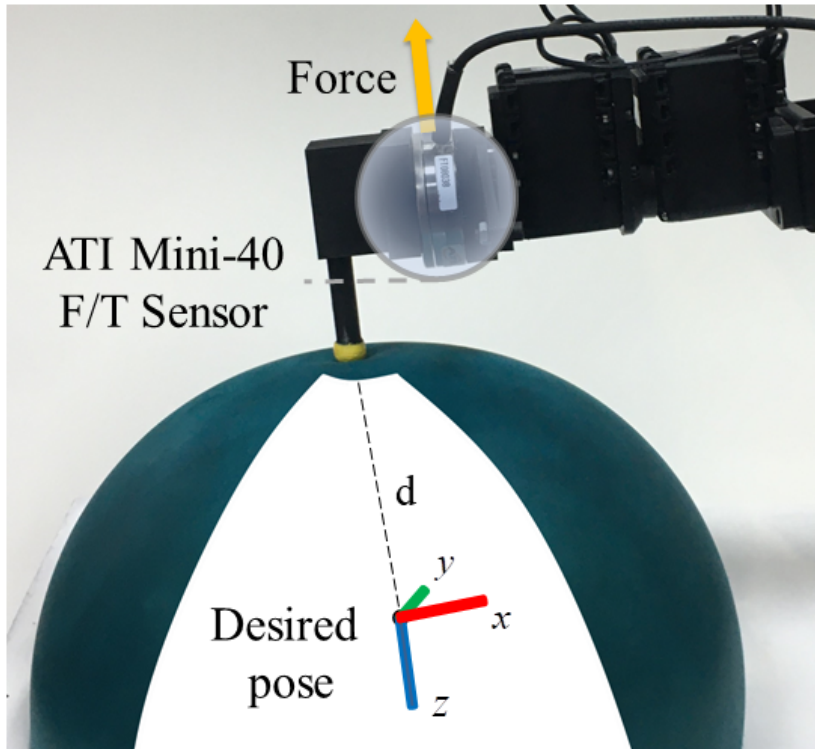


Figure 6.12: Measurement of contact forces along the vertical direction (red arrow) to the object's surface with an ATI Mini-40 F/T sensor. The planning of a contact task is implemented in our approach by setting the normal offset  $d$  to negative values, instructing the robot to move below the object's surface.

along the vertical direction. More specifically, the applied force oscillates between the expected values (as measured for  $R_{\max}$  and  $R_{\min}$ ), maintaining a quasi-static equilibrium during dynamic interaction while following the linear spring-like behaviour of the stationary scenario. This behaviour is apparently achieved by means of an accurate and reactive adaptation to the changes occurring due to object deformation.

Concluding, the interactive planning framework, which is based on visual object segmentation, FEM deformation tracking and mesh parameterization techniques, uses the barycentric coordinates of the mesh's triangles, in order to establish bijective transformations between a part of the object's surface and its planar parameterized versions (static and dynamic). With the use of these spatial transformations in combination with the preprocessing steps, we are able to reactively plan interactive trajectories with high accuracy despite the visual occlusions occurring by the robot's motion. In the conducted experimental validation with a periodically deforming hemispherical model, millimeter planning accuracy was observed for three different trajectories, showing superior performance with respect to our previous perception-based planning approach. The accuracy in tracking a physical point on the object's surface was also tested objectively with a motion tracking device, confirming the high precision performance. It is obvious that the system's accuracy is highly dependent on the performance of the algorithms used as preprocessing steps. Hence the choice and development of visual object segmentation, physics based deformation tracking and mesh parameterization algorithms is important and application dependent.

Additionally, it was shown experimentally that the proposed approach can be used for demonstration of interactive motion tasks by a human expert, in an undeformed state of the object and properly projected and saved in the Static Canonical Space. The demonstrated actions can be reproduced precisely even when the object undergoes deformation, exemplifying how a robotic system equipped with the proposed approach can work collaboratively with the user and enhance his/her ability to interact with the surface of a deformable object. Moreover, the performance of the proposed framework was further evaluated with the execution of interactive tasks in continuous contact with the surface of the object, measuring the exerted contact forces with a f/t sensor mounted on the robot. The interactive adaptation of the reference pose (through the offset values) within the proposed IMP framework, can properly regulate the contact forces within the specified range of values; a result which would not have been feasible by a straightforward implementation of a stiffness controller on a dynamically deforming surface (in which case, forces variations would largely exceed the specified range of values and might even result in complete failure during such interactive task scenarios). Therefore, by applying the proposed mesh-based framework, it is possible to accurately control interactive path following tasks on the surface of a dynamically deforming object, while also being able to properly regulate contact forces.

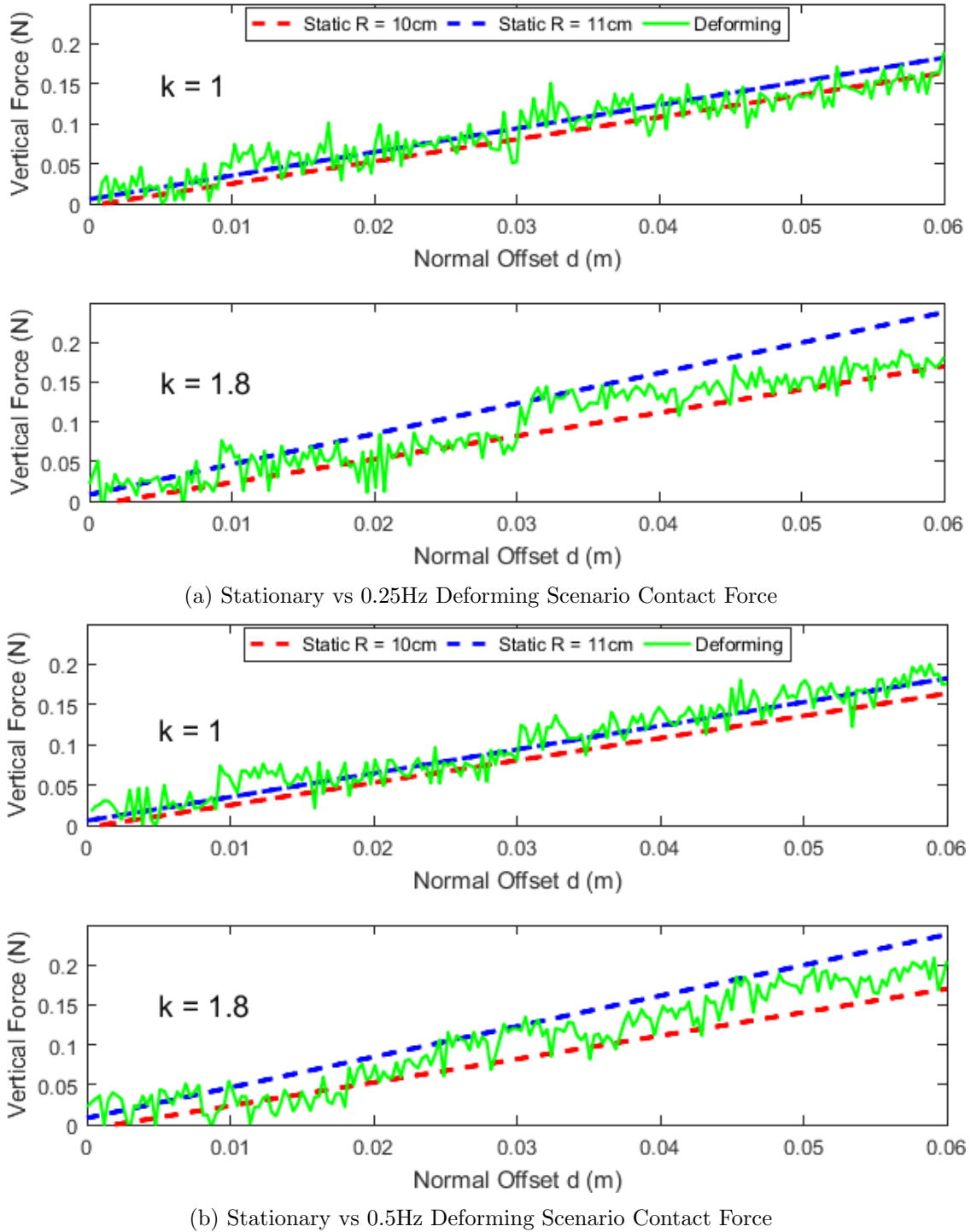


Figure 6.13: Measurement of contact forces along the vertical direction to the object's surface for a range of normal offset  $d$ . A contact task is planned such that the reference orientation is vertical to the surface and the normal offset is linearly decreased until the 6 cm value, for the stationary scenario for hemispherical radius  $R_{max} = 11\text{cm}$  and  $R_{min} = 10\text{cm}$  (dashed blue and red lines respectively) and for the deforming scenario (green solid line) with deformation rate of 0,25Hz (left) & 0,5Hz (right). Several gain values for the stiffness controller were tested and a representative behaviour is shown for relative gain value  $k = 1$  (top) and  $k = 1.8$  (bottom).

## Chapter 7

# Conclusions & Future Work

The research focus of this thesis is the development of reactive motion planning methods for robotic manipulators in assistive tasks involving human-robot physical interaction. In the context of design and development of a whole body bathing robot, the role of human - robot physical interaction in the bathing process is highly important both from system safety and from user acceptance perspective. The main challenge of such an interactive behavior is to adapt human-friendly washing actions to the deforming (due to random or systematic motion) body parts of the user. Another goal is to employ appropriate learning strategies in order to analyze and learn proper washing actions from professional caregivers incorporating their expertise into the robotic behavior. Accurate tracking of the demonstrated actions and on-line adaptation to a real washing scenario requires full cognition of the user by the system in order to achieve avoidance either of obstacle areas on user's body parts (such as injuries) and on-line adaptation of the motion's properties according to user's preferences. Contact forces are included among the user's preferences during the execution of physical interaction tasks. However, the integration of a force sensor in the soft-robotic structure and humid environment of a bathing robot is technically not feasible. Hence, robotic control techniques without the use of force feedback are required for proper execution of contact tasks, such as wiping.

### 7.1 Summary of Main Contributions

The contribution of this thesis spans a wide spectrum of research on interactive motion planning with emphasis on planning tasks on the surface of deformable objects, such as the human body parts. In particular several motion planning methodologies for robotic manipulators in interaction with their environment were investigated both analytic and learning based, while proposing reactive motion planning methodologies with novel contributions comparing with the current state of the art. The main contributions and outcomes of this thesis are summarized below:

- Development of a perception-based motion planning algorithm, which uses the visual feedback from a depth camera and the corresponding scene perception information, in order to adapt predefined, time scalable trajectories on curved and deformable surfaces, such as the human body parts, and at the same time avoid the interaction with obstacle areas, such as injuries.
- The developed algorithm was tested both in lab conditions and in a real clinical environment with elderly users in both dry and humid conditions.

- A clinical validation study conducted on the ability of elderly users to tele-operate the robot without direct visual contact and complete a washing task with the motion adaptation assistance of the developed algorithm and without it. The majority of the users found the tele-operation without motion adaptation assistance very difficult and the operation of the system with it satisfying.
- Proper washing actions from professional caregivers were recorded with the use of optical motion trackers systems (Vicon), analyzed and decomposed into primitive actions appropriate for robotic execution.
- Deployment of an integrated system based on DMP approach, which can learn and encode the demonstrated actions, imitating the human washing actions. The learned motions can then be adapted to the user's body parts compensating their motion or deformation and their execution parameters can be on-line modified in order to meet the user's requirements.
- An alternative LfD method was proposed based on Navigation functions, in order to capture the way an expert clinical carer executes the bathing activities by means of constructing repulsive potential fields ("virtual obstacles"). The bathing trajectories demonstration is realized in 3D space and are transformed to a 2D spatially normalized space by establishing appropriate transformations. In this space, a set of virtual obstacles is calculated so that the trajectory produced by the NF based planner resembles the demonstrated human trajectories.
- An efficient mesh-based integrated motion planning framework was proposed to effectively and accurately control a robotic manipulator when executing interactive tasks on the surface of a deformable object. The proposed framework integrates 3D visual object segmentation and on-line deformation modeling with real-time motion planning and interaction control. The core of the system is based on FEM deformation tracking and efficient local mesh parameterization techniques, and uses barycentric coordinates defined on the mesh triangles to establish bijective transformations between the deformable part of an object surface and its planar (static and dynamic) parameterized versions.
- The combination of these spatial transformations with the preprocessing (visual perception and deformation modeling) steps, allows for reactive planning of interactive trajectories with high accuracy, even under large and persistent visual occlusions (such as those caused by the presence of the robot manipulator in the visual scene).
- In the conducted experimental evaluation study with a periodically deforming hemispherical model, millimeter accuracy was achieved for motion planning at all conditions with three different trajectories tested, clearly showing superior performance as compared to the direct vision-based approach. The accuracy in tracking a physical point on the surface of a deforming object was also assessed objectively with a motion tracking device, confirming high precision performance. It is obvious, however, that the system accuracy is highly dependent on the performance of the algorithms used as preprocessing steps. Hence the choice and development of visual object segmentation, physics based deformation tracking and mesh parameterization algorithms is important and application dependent.
- It was also shown experimentally that the proposed IMP approach can also be effectively applied in the context of motion programming by human demonstration. It

was showcased that demonstration of an interactive motion task can be performed by a human expert in an undeformed state of the object, and this interactive motion relative to the target object surface can be properly projected and recorded in the Static Canonical Space. The demonstrated actions can then be reproduced precisely even when the object undergoes deformation, exemplifying how a robotic system equipped with the proposed IMP approach can work collaboratively with the user and eventually enhance his/her ability to perform tasks involving interaction with the surface of a deformable object.

- The performance of the proposed framework was also further evaluated with the execution of interactive tasks in continuous physical contact with the deformable surface of an object (by measuring the exerted contact forces with a f/t sensor mounted on the robot). It was shown experimentally that the proposed integrated framework manages to compensate for the object deformation and to maintain continuous contact with the target surface, while exerting contact forces that remain within a specified range of values. It can thus be concluded that, by employing the proposed integrated IMP framework, it is possible to accurately control interactive path tracking tasks on the surface of a dynamically deforming object, while also being able to effectively regulate contact forces.

## 7.2 Future Research Directions

Robotic assistants which conduct interactive tasks with the environment is an open research field. There are many research topics that have to be addressed, in order for the robotic manipulators to achieve safe and smooth physical interaction especially with the human body and ameliorate the daily lives of senior citizens facing mobility and/or cognitive impairments. Possible future research could move towards three main directions, considering more complex interactive applications with deformable environment and development of robot-centric learning algorithms, transferring the required motion skills directly to the robot's actuation. More specifically:

- A comparative study on different learning from demonstration techniques would illustrate the performance of each one in multiple interactive scenarios. The learning of primitive action relative to the environment could produce interaction primitives, which will encode both the motion and impedance parameters of the desired task.
- Towards the evolution of soft robotic technology, the development of appropriate learning approaches for direct skill transferring from human or other bio-inspired systems would increase the operability of soft robots in a larger variety of applications.
- The execution of interactive trajectories in continuous contact with a deformable object requires the exploration of impedance robot control schemes with integration of force measurements into the control loop and the deformation modeling, making the physical interaction as smooth as possible taking into account the imposed constraints. Such a task would also involve more complex contact wrench regulation in multiple directions, which combine both the manipulator's and the object deformation dynamics.

- The robotic interaction with the surface of more complex shaped objects should be examined, in order to generalize to more complex real-life scenarios.
- Further research can be conducted on the ability of the mesh based framework to directly control the object's shape and deformation or to estimate the object's physical parameters by planning appropriately the robot's motion.
- Due to the computational efficiency of the spatial transformation calculation on the mesh structure, the proposed framework can be easily extended to planning the motion of multiple robots or a robotic hand with multiple fingers for accurate grasping actions.



# Bibliography

- [1] C. Mandery, O. Terlemez, M. Do, N. Vahrenkamp, and T. Asfour, “The kit whole-body human motion database,” in *Advanced Robotics (ICAR), 2015 International Conference on*, July 2015, pp. 329–336.
- [2] J. Smith and S. Schaefer, “Bijective parameterization with free boundaries,” *ACM Transactions on Graphics (TOG)*, vol. 34, no. 4, pp. 1–9, 2015.
- [3] R. A. Guler and I. Kokkinos, “Holopose: Holistic 3d human reconstruction in-the-wild,” in *The IEEE Conference on Computer Vision and Pattern Recognition (CVPR)*, June 2019.
- [4] W. H. Organization, *World report on ageing and health*. World Health Organization, 2015.
- [5] F. Buckinx, Y. Rolland, J.-Y. Reginster, C. Ricour, J. Petermans, and O. Bruyère, “Burden of frailty in the elderly population: perspectives for a public health challenge,” *Archives of Public Health*, vol. 73, no. 1, p. 19, 2015.
- [6] S. H. Zarit, K. E. Reever, and J. Bach-Peterson, “Relatives of the impaired elderly: correlates of feelings of burden,” *The gerontologist*, vol. 20, no. 6, pp. 649–655, 1980.
- [7] S. McFall and B. H. Miller, “Caregiver burden and nursing home admission of frail elderly persons,” *Journal of Gerontology*, vol. 47, no. 2, pp. S73–S79, 1992.
- [8] D. D. Dunlop, S. L. Hughes, and L. M. Manheim, “Disability in activities of daily living: patterns of change and a hierarchy of disability,” *American Journal of Public Health*, vol. 87, pp. 378–383, March 1997.
- [9] S. Katz, A. Ford, R. Moskowitz, B. Jackson, and M. Jaffe, “Studies of illness in the aged: The index of adl: a standardized measure of biological and psychosocial function,” *JAMA*, vol. 185, no. 12, pp. 914–919, September 1963.
- [10] M. Porta, *A dictionary of epidemiology*. Oxford university press, 2014.
- [11] J. C. Millán-Calenti, J. Tubío, S. Pita-Fernández, I. González-Abraldes, T. Lorenzo, T. Fernández-Arruty, and A. Maseda, “Prevalence of functional disability in activities of daily living (adl), instrumental activities of daily living (iadl) and associated factors, as predictors of morbidity and mortality,” *Archives of gerontology and geriatrics*, vol. 50, no. 3, pp. 306–310, 2010.
- [12] S. Ahluwalia, T. Gill, D. Baker, and T. Fried, “Disaggregating activities of daily living limitations for predicting nursing home admission,” *Health Services Research*, vol. 50, pp. 560–578, 2015.

- [13] J. Wiener, R. Hanley, R. Clark, and J. Van Nostrand, "Measuring the activities of daily living: Comparisons across national surveys," *Journal of Gerontology*, vol. 45, pp. 229–237, 1990.
- [14] S. Ahluwalia, T. Gill, D. Baker, and T. Fried, "Perspectives of older persons on bathing and bathing disability: A qualitative study," *American Geriatrics Society*, vol. 58, pp. 450–456, 2010.
- [15] N. Roy, G. Baltus, D. Fox, F. Gemperle, J. Goetz, T. Hirsch, D. Margaritis, M. Montemerlo, J. Pineau, J. Schulte *et al.*, "Towards personal service robots for the elderly," in *Workshop on Interactive Robots and Entertainment (WIRE 2000)*, vol. 25, 2000, p. 184.
- [16] D. Feil-Seifer and M. J. Mataric, "Defining socially assistive robotics," in *9th International Conference on Rehabilitation Robotics, 2005. ICORR 2005*. IEEE, 2005, pp. 465–468.
- [17] P. Gerrard, "The hierarchy of the activities of daily living in the katz index in residents of skilled nursing facilities," *Journal of Geriatric Physical Therapy*, vol. 36, no. 2, pp. 87–91, 2013.
- [18] S. L. Murphy, K. A. Gretebeck, and N. B. Alexander, "The bath environment, the bathing task, and the older adult: a review and future directions for bathing disability research," *Disability and rehabilitation*, vol. 29, no. 14, pp. 1067–1075, 2007.
- [19] K. M. Vollman, "Interventional patient hygiene: Discussion of the issues and a proposed model for implementation of the nursing care basics," *Intensive and critical care nursing*, vol. 29, no. 5, pp. 250–255, 2013.
- [20] S. C. Ahluwalia, T. M. Gill, D. I. Baker, and T. R. Fried, "Perspectives of older persons on bathing and bathing disability: a qualitative study," *Journal of the American Geriatrics Society*, vol. 58, no. 3, pp. 450–456, 2010.
- [21] V. G. Duffy, "Physical and mental burden of caregivers in providing bathing assistance," in *Advances in Human Aspects of Healthcare*. CRC Press, 2012, pp. 285–291.
- [22] M.-Y. Ma, F.-G. Wu, and R.-H. Chang, "A new design approach of user-centered design on a personal assistive bathing device for hemiplegia," *Disability and Rehabilitation*, vol. 29, no. 14, pp. 1077–1089, 2007.
- [23] M. Golding-Day, P. Whitehead, K. Radford, and M. Walker, "Interventions to reduce dependency in bathing in community dwelling older adults: a systematic review," *Systematic reviews*, vol. 6, no. 1, p. 198, 2017.
- [24] K. Beedholm, K. Frederiksen, A.-M. S. Frederiksen, and K. Lomborg, "Attitudes to a robot bathtub in Danish elder care: A hermeneutic interview study," *Nursing & Health Sciences*, vol. 17, no. 3, pp. 280–286, 2015.
- [25] C.-S. Chung, H. Wang, and R. A. Cooper, "Functional assessment and performance evaluation for assistive robotic manipulators: Literature review," *The journal of spinal cord medicine*, vol. 36, no. 4, pp. 273–289, 2013.

- [26] K. Hauer, “Bewertung von aal-ambient-assisted-living-systemen bei personen mit kognitiver schädigung: Match vs. mismatch,” in *Pflegeroboter*. Springer, 2018, pp. 89–111.
- [27] T. L. Chen, M. Ciocarlie, S. Cousins, P. M. Grice, K. Hawkins, K. Hsiao, C. C. Kemp, C. King, D. A. Lazewatsky, A. E. Leeper, H. Nguyen, A. Paepcke, C. Pantofaru, W. D. Smart, and L. Takayama, “Robots for humanity: using assistive robotics to empower people with disabilities,” *IEEE Robotics & Automation Magazine*, vol. 20, no. 1, pp. 30–39, March 2013.
- [28] Z. Bien, M.-J. Chung, P.-H. Chang, D.-S. Kwon, D.-J. Kim, J.-S. Han, J.-H. Kim, D.-H. Kim, H.-S. Park, S.-H. Kang *et al.*, “Integration of a rehabilitation robotic system (kares ii) with human-friendly man-machine interaction units,” *Autonomous robots*, vol. 16, no. 2, pp. 165–191, 2004.
- [29] C. Balaguer, A. Gimenez, A. Huete, A. Sabatini, M. Topping, and G. Bolmsjo, “The mats robot: service climbing robot for personal assistance,” *Robotics Automation Magazine, IEEE*, vol. 13, no. 1, pp. 51–58, March 2006.
- [30] S. Kajikawa and K. Abe, “Development of robot hand with multi-directional variable stiffness for human-care services,” in *2012 IEEE/RSJ International Conference on Intelligent Robots and Systems*, 2012, pp. 2889–2894.
- [31] T. Mukai, S. Hirano, H. Nakashima, Y. Kato, Y. Sakaida, S. Guo, and S. Hosoe, “Development of a nursing-care assistant robot riba that can lift a human in its arms,” in *2010 IEEE/RSJ International Conference on Intelligent Robots and Systems*, 2010, pp. 5996–6001.
- [32] T. Mukai, S. Hirano, M. Yoshida, H. Nakashima, S. Guo, and Y. Hayakawa, “Tactile-based motion adjustment for the nursing-care assistant robot riba,” in *2011 IEEE International Conference on Robotics and Automation*, 2011, pp. 5435–5441.
- [33] J. Hu, A. Edsinger, Yi-Je Lim, N. Donaldson, M. Solano, A. Solochek, and R. Marchessault, “An advanced medical robotic system augmenting healthcare capabilities - robotic nursing assistant,” in *2011 IEEE International Conference on Robotics and Automation*, 2011, pp. 6264–6269.
- [34] Y. Tsumaki, T. Kon, A. Suginuma, K. Imada, A. Sekiguchi, D. Nenchev, H. Nakano, and K. Hanada, “Development of a skincare robot,” in *Robotics and Automation, 2008. ICRA 2008. IEEE International Conference on*, May 2008, pp. 2963–2968.
- [35] T. Hirose, S. Fujioka, O. Mizuno, and T. Nakamura, “Development of hair-washing robot equipped with scrubbing fingers,” in *IEEE International Conference on Robotics and Automation (ICRA)*, May 2012, pp. 1970–1975.
- [36] C.-H. King, T. L. Chen, A. Jain, and C. C. Kemp, “Towards an assistive robot that autonomously performs bed baths for patient hygiene,” in *2010 IEEE/RSJ International Conference on Intelligent Robots and Systems*. IEEE, 2010, pp. 319–324.
- [37] (2016) Oasis seated shower system. [Online]. Available: [www.adl-solutions.com/oasis/%2Dseated/%2Dshower/%2Dsystem/%2Dfor/%2Doptimal/%2Daccessible/%2Dbathing/%2Dtempe/%2Daz.html](http://www.adl-solutions.com/oasis/%2Dseated/%2Dshower/%2Dsystem/%2Dfor/%2Doptimal/%2Daccessible/%2Dbathing/%2Dtempe/%2Daz.html)

- [38] (2016) Robotics care poseidon. [Online]. Available: <http://www.roboticscare.com/robotics-care-poseidon/>
- [39] D. C. Conner, A. Greenfield, P. N. Atkar, A. A. Rizzi, and H. Choset, "Paint deposition modeling for trajectory planning on automotive surfaces," *IEEE Transactions on Automation Science and Engineering*, vol. 2, no. 4, pp. 381–392, October 2005.
- [40] C. Dornhege and A. Hertle, "Integrated symbolic planning in the tidyup-robot project," in *2013 AAAI Spring Symposium Series*, 2013.
- [41] R. Ginhoux, J. Gangloff, M. De Mathelin, L. Soler, M. M. A. Sanchez, and J. Marescaux, "Beating heart tracking in robotic surgery using 500 hz visual servoing, model predictive control and an adaptive observer," in *IEEE International Conference on Robotics and Automation (ICRA)*. IEEE, May 2004, pp. 274–279.
- [42] M. Shimizu, "Analytical inverse kinematics for 5-dof humanoid manipulator under arbitrarily specified unconstrained orientation of end-effector," *Robotica*, vol. 33, no. 4, pp. 747–767, 2015.
- [43] J. Hess, G. D. Tipaldi, and W. Burgard, "Null space optimization for effective coverage of 3d surfaces using redundant manipulators," in *2012 IEEE/RSJ International Conference on Intelligent Robots and Systems*. IEEE, 2012, pp. 1923–1928.
- [44] X. Papageorgiou, S. Loizou, and K. Kyriakopoulos, "Motion planning and trajectory tracking on 2-D manifolds embedded in 3-D workspaces," *2005 IEEE International Conference on Robotics and Automation*, pp. 501–506, 2005.
- [45] Z. Erickson, H. M. Clever, V. Gangaram, G. Turk, C. K. Liu, and C. C. Kemp, "Multidimensional capacitive sensing for robot-assisted dressing and bathing," in *2019 IEEE 16th International Conference on Rehabilitation Robotics (ICORR)*, 2019, pp. 224–231.
- [46] D. Leidner, W. Bejjani, A. Albu-Schäffer, and M. Beetz, "Robotic agents representing, reasoning, and executing wiping tasks for daily household chores," in *Proceedings of the 2016 International Conference on Autonomous Agents & Multiagent Systems*. International Foundation for Autonomous Agents and Multiagent Systems, 2016, pp. 1006–1014.
- [47] D. Leidner and M. Beetz, "Inferring the effects of wiping motions based on haptic perception," in *2016 IEEE-RAS 16th International Conference on Humanoid Robots (Humanoids)*, 2016, pp. 461–468.
- [48] D. Martínez, G. Alenya, and C. Torras, "Planning robot manipulation to clean planar surfaces," *Engineering Applications of Artificial Intelligence*, vol. 39, pp. 23–32, 2015.
- [49] R. Wagner, U. Frese, and B. Bäuml, "3d modeling, distance and gradient computation for motion planning: A direct gpgpu approach," in *2013 IEEE International Conference on Robotics and Automation*, 2013, pp. 3586–3592.
- [50] J. Li, Z. Teng, J. Xiao, A. Kapadia, A. Bartow, and I. Walker, "Autonomous continuum grasping," in *Intelligent Robots and Systems (IROS), 2013 IEEE/RSJ International Conference on*. IEEE, 2013, pp. 4569–4576.

- [51] A. Ataka, P. Qi, A. Shiva, A. Shafti, H. Wurdemann, P. Dasgupta, and K. Althoefer, "Towards safer obstacle avoidance for continuum-style manipulator in dynamic environments," in *2016 6th IEEE International Conference on Biomedical Robotics and Biomechatronics (BioRob)*, 2016, pp. 600–605.
- [52] A. Ataka, P. Qi, H. Liu, and K. Althoefer, "Real-time planner for multi-segment continuum manipulator in dynamic environments," in *2016 IEEE International Conference on Robotics and Automation (ICRA)*, 2016, pp. 4080–4085.
- [53] H. Urbanek, A. Albu-Schaffer, and P. van der Smagt, "Learning from demonstration: repetitive movements for autonomous service robotics," in *2004 IEEE/RSJ International Conference on Intelligent Robots and Systems (IROS) (IEEE Cat. No.04CH37566)*, vol. 4, 2004, pp. 3495–3500 vol.4.
- [54] P. Kormushev, D. N. Nenchev, S. Calinon, and D. G. Caldwell, "Upper-body kinesthetic teaching of a free-standing humanoid robot," in *2011 IEEE International Conference on Robotics and Automation*, 2011, pp. 3970–3975.
- [55] D. Lee and C. Ott, "Incremental kinesthetic teaching of motion primitives using the motion refinement tube," *Autonomous Robots*, vol. 31, no. 2-3, pp. 115–131, 2011.
- [56] A. Gams and A. Ude, "On-line coaching of robots through visual and physical interaction: Analysis of effectiveness of human-robot interaction strategies," in *2016 IEEE International Conference on Robotics and Automation (ICRA)*, 2016, pp. 3028–3034.
- [57] B. Nemeč and A. Ude, "Action sequencing using dynamic movement primitives," *Robotica*, vol. 30, no. 5, pp. 837–846, 2012.
- [58] A. Gams, T. Petrič, B. Nemeč, and A. Ude, "Learning and adaptation of periodic motion primitives based on force feedback and human coaching interaction," in *2014 IEEE-RAS International Conference on Humanoid Robots*, 2014, pp. 166–171.
- [59] A. Gams, T. Petrič, M. Do, B. Nemeč, J. Morimoto, T. Asfour, and A. Ude, "Adaptation and coaching of periodic motion primitives through physical and visual interaction," *Robotics and Autonomous Systems*, vol. 75, pp. 340–351, 2016.
- [60] T. Kulvicius, M. Biehl, M. J. Aein, M. Tamosiunaite, and F. Wörgötter, "Interaction learning for dynamic movement primitives used in cooperative robotic tasks," *Robotics and Autonomous Systems*, vol. 61, no. 12, pp. 1450–1459, 2013.
- [61] H. B. Amor, G. Neumann, S. Kamthe, O. Kroemer, and J. Peters, "Interaction primitives for human-robot cooperation tasks," in *2014 IEEE international conference on robotics and automation (ICRA)*. IEEE, 2014, pp. 2831–2837.
- [62] I. F. Filippidis, K. J. Kyriakopoulos, and P. K. Artemiadis, "Navigation functions learning from experiments: Application to anthropomorphic grasping," in *2012 IEEE International Conference on Robotics and Automation*, 2012, pp. 570–575.
- [63] J. Kim, N. Cauli, P. Vicente, B. Damas, F. Cavallo, and J. Santos-Victor, "'icub, clean the table!' a robot learning from demonstration approach using deep neural networks," in *2018 IEEE International Conference on Autonomous Robot Systems and Competitions (ICARSC)*, 2018, pp. 3–9.

- [64] C. Eppner, J. Sturm, M. Bennewitz, C. Stachniss, and W. Burgard, "Imitation learning with generalized task descriptions," in *2009 IEEE International Conference on Robotics and Automation*, 2009, pp. 3968–3974.
- [65] G. Martius, R. Hostettler, A. Knoll, and R. Der, "Compliant control for soft robots: Emergent behavior of a tendon driven anthropomorphic arm," in *2016 IEEE/RSJ International Conference on Intelligent Robots and Systems (IROS)*, 2016, pp. 767–773.
- [66] S. Stelter, G. Bartels, and M. Beetz, "Multidimensional time-series shapelets reliably detect and classify contact events in force measurements of wiping actions," *IEEE Robotics and Automation Letters*, vol. 3, no. 1, pp. 320–327, 2018.
- [67] M. Do, J. Schill, J. Ernesti, and T. Asfour, "Learn to wipe: A case study of structural bootstrapping from sensorimotor experience," in *2014 IEEE International Conference on Robotics and Automation (ICRA)*, 2014, pp. 1858–1864.
- [68] J. D. Langsfeld, A. M. Kabir, K. N. Kaipa, and S. K. Gupta, "Robotic bimanual cleaning of deformable objects with online learning of part and tool models," in *2016 IEEE International Conference on Automation Science and Engineering (CASE)*, 2016, pp. 626–632.
- [69] A. M. Kabir, K. N. Kaipa, J. Marvel, and S. K. Gupta, "Automated planning for robotic cleaning using multiple setups and oscillatory tool motions," *IEEE Transactions on Automation Science and Engineering*, vol. 14, no. 3, pp. 1364–1377, 2017.
- [70] V. Ortenzi, R. Stolkin, J. Kuo, and M. Mistry, "Hybrid motion/force control: a review," *Advanced Robotics*, vol. 31, no. 19-20, pp. 1102–1113, 2017. [Online]. Available: <https://doi.org/10.1080/01691864.2017.1364168>
- [71] R. V. Patel, H. A. Talebi, J. Jayender, and F. Shadpey, "A robust position and force control strategy for 7-dof redundant manipulators," *IEEE/ASME Transactions on Mechatronics*, vol. 14, no. 5, pp. 575–589, 2009.
- [72] Z. Xu, S. Li, X. Zhou, S. Zhou, and T. Cheng, "Dynamic neural networks for motion-force control of redundant manipulators: An optimization perspective," *IEEE Transactions on Industrial Electronics*, pp. 1–1, 2020.
- [73] V. Ortenzi, M. Adjigble, J. A. Kuo, R. Stolkin, and M. Mistry, "An experimental study of robot control during environmental contacts based on projected operational space dynamics," in *2014 IEEE-RAS International Conference on Humanoid Robots*, 2014, pp. 407–412.
- [74] F. Sato, T. Nishii, J. Takahashi, Y. Yoshida, M. Mitsuhashi, and D. Nenchev, "Experimental evaluation of a trajectory/force tracking controller for a humanoid robot cleaning a vertical surface," in *2011 IEEE/RSJ international conference on intelligent robots and systems*. IEEE, 2011, pp. 3179–3184.
- [75] D. P. Le, J. Choi, and S. Kang, "External force estimation using joint torque sensors and its application to impedance control of a robot manipulator," in *2013 13th international conference on control, automation and systems (ICCAS 2013)*. IEEE, 2013, pp. 1794–1798.

- [76] C. Laschi, B. Mazzolai, and M. Cianchetti, “Soft robotics: Technologies and systems pushing the boundaries of robot abilities,” *Science Robotics*, vol. 1, no. 1, p. eaah3690, 2016.
- [77] G. S. Chirikjian and J. W. Burdick, “A hyper-redundant manipulator,” *IEEE Robotics & Automation Magazine*, vol. 1, no. 4, pp. 22–29, 1994.
- [78] A. Stilli, L. Grattarola, H. Feldmann, H. A. Wurdemann, and K. Althoefer, “Variable stiffness link (vsl): Toward inherently safe robotic manipulators,” in *2017 IEEE International Conference on Robotics and Automation (ICRA)*, 2017, pp. 4971–4976.
- [79] S. Sanan, M. H. Ornstein, and C. G. Atkeson, “Physical human interaction for an inflatable manipulator,” in *2011 Annual International Conference of the IEEE Engineering in Medicine and Biology Society*. IEEE, 2011, pp. 7401–7404.
- [80] J. Kim, A. Alspach, and K. Yamane, “3d printed soft skin for safe human-robot interaction,” in *2015 IEEE/RSJ International Conference on Intelligent Robots and Systems (IROS)*, 2015, pp. 2419–2425.
- [81] M. Manti, V. Cacucciolo, and M. Cianchetti, “Stiffening in soft robotics: A review of the state of the art,” *IEEE Robotics & Automation Magazine*, vol. 23, no. 3, pp. 93–106, 2016.
- [82] M. T. Gillespie, C. M. Best, and M. D. Killpack, “Simultaneous position and stiffness control for an inflatable soft robot,” in *2016 IEEE International Conference on Robotics and Automation (ICRA)*, 2016, pp. 1095–1101.
- [83] G. Pavlakos, X. Zhou, K. G. Derpanis, and K. Daniilidis, “Coarse-to-fine volumetric prediction for single-image 3d human pose,” in *The IEEE Conference on Computer Vision and Pattern Recognition (CVPR)*, July 2017.
- [84] J. Shotton, M. Johnson, and R. Cipolla, “Semantic texton forests for image categorization and segmentation,” in *2008 IEEE Conference on Computer Vision and Pattern Recognition*, 2008, pp. 1–8.
- [85] B. Fulkerson, A. Vedaldi, and S. Soatto, “Class segmentation and object localization with superpixel neighborhoods,” in *2009 IEEE 12th International Conference on Computer Vision*, 2009, pp. 670–677.
- [86] J. Shotton, J. Winn, C. Rother, and A. Criminisi, “Textonboost for image understanding: Multi-class object recognition and segmentation by jointly modeling texture, layout, and context,” *International journal of computer vision*, vol. 81, no. 1, pp. 2–23, 2009.
- [87] J. Carreira, R. Caseiro, J. Batista, and C. Sminchisescu, “Semantic segmentation with second-order pooling,” in *European Conference on Computer Vision*. Springer, 2012, pp. 430–443.
- [88] P. Krähenbühl and V. Koltun, “Efficient inference in fully connected crfs with gaussian edge potentials,” in *Advances in neural information processing systems*, 2011, pp. 109–117.
- [89] L. Ladický, C. Russell, P. Kohli, and P. H. S. Torr, “Associative hierarchical crfs for object class image segmentation,” in *2009 IEEE 12th International Conference on Computer Vision*, 2009, pp. 739–746.

- [90] J. Carreira and C. Sminchisescu, “Cpmc: Automatic object segmentation using constrained parametric min-cuts,” *IEEE Transactions on Pattern Analysis and Machine Intelligence*, vol. 34, no. 7, pp. 1312–1328, 2012.
- [91] A. Krizhevsky, I. Sutskever, and G. E. Hinton, “Imagenet classification with deep convolutional neural networks,” in *Advances in neural information processing systems*, 2012, pp. 1097–1105.
- [92] C. Szegedy, W. Liu, Y. Jia, P. Sermanet, S. Reed, D. Anguelov, D. Erhan, V. Vanhoucke, and A. Rabinovich, “Going deeper with convolutions,” in *The IEEE Conference on Computer Vision and Pattern Recognition (CVPR)*, June 2015.
- [93] D. Erhan, C. Szegedy, A. Toshev, and D. Anguelov, “Scalable object detection using deep neural networks,” in *Proceedings of the IEEE conference on computer vision and pattern recognition*, 2014, pp. 2147–2154.
- [94] S. Ren, K. He, R. Girshick, and J. Sun, “Faster r-cnn: Towards real-time object detection with region proposal networks,” in *Advances in neural information processing systems*, 2015, pp. 91–99.
- [95] G. Papandreou, I. Kokkinos, and P.-A. Savalle, “Modeling local and global deformations in deep learning: Epitomic convolution, multiple instance learning, and sliding window detection,” in *Proceedings of the IEEE Conference on Computer Vision and Pattern Recognition*, 2015, pp. 390–399.
- [96] L. Chen, G. Papandreou, I. Kokkinos, K. Murphy, and A. L. Yuille, “Deeplab: Semantic image segmentation with deep convolutional nets, atrous convolution, and fully connected crfs,” *IEEE Transactions on Pattern Analysis and Machine Intelligence*, vol. 40, no. 4, pp. 834–848, 2018.
- [97] X. Chen, R. Mottaghi, X. Liu, S. Fidler, R. Urtasun, and A. Yuille, “Detect what you can: Detecting and representing objects using holistic models and body parts,” in *Proceedings of the IEEE Conference on Computer Vision and Pattern Recognition*, 2014, pp. 1971–1978.
- [98] S. Chandra, N. Usunier, and I. Kokkinos, “Dense and low-rank gaussian crfs using deep embeddings,” in *Proceedings of the IEEE International Conference on Computer Vision*, 2017, pp. 5103–5112.
- [99] A. Bulat and G. Tzimiropoulos, “Human pose estimation via convolutional part heatmap regression,” in *European Conference on Computer Vision*. Springer, 2016, pp. 717–732.
- [100] A. Newell, K. Yang, and J. Deng, “Stacked hourglass networks for human pose estimation,” in *European conference on computer vision*. Springer, 2016, pp. 483–499.
- [101] S. E. Wei, V. Ramakrishna, T. Kanade, and Y. Sheikh, “Convolutional pose machines,” in *The IEEE Conference on Computer Vision and Pattern Recognition (CVPR)*, June 2016, pp. 4724–4732.
- [102] V. Belagiannis and A. Zisserman, “Recurrent human pose estimation,” in *2017 12th IEEE International Conference on Automatic Face Gesture Recognition (FG 2017)*, 2017, pp. 468–475.



- [103] J.-C. Latombe, *Robot motion planning*. Springer Science & Business Media, 2012, vol. 124.
- [104] O. Khatib, “Real-time obstacle avoidance for manipulators and mobile robots,” in *Autonomous robot vehicles*. Springer, 1986, pp. 396–404.
- [105] —, “The potential field approach and operational space formulation in robot control,” in *Adaptive and Learning Systems*. Springer, 1986, pp. 367–377.
- [106] J. . Kim and P. K. Khosla, “Real-time obstacle avoidance using harmonic potential functions,” *IEEE Transactions on Robotics and Automation*, vol. 8, no. 3, pp. 338–349, 1992.
- [107] C. I. Connolly and R. A. Grupen, “The applications of harmonic functions to robotics,” *Journal of robotic Systems*, vol. 10, no. 7, pp. 931–946, 1993.
- [108] R. Volpe and P. Khosla, “Manipulator control with superquadric artificial potential functions: theory and experiments,” *IEEE Transactions on Systems, Man, and Cybernetics*, vol. 20, no. 6, pp. 1423–1436, 1990.
- [109] E. Rimon and D. E. Koditschek, “Exact robot navigation using artificial potential functions,” *IEEE Transactions on Robotics and Automation*, vol. 8, no. 5, pp. 501–518, 1992.
- [110] D. E. Koditschek, “Autonomous mobile robots controlled by navigation functions,” in *Proceedings. IEEE/RSJ International Workshop on Intelligent Robots and Systems '89 (IROS '89) 'The Autonomous Mobile Robots and Its Applications*, 1989, pp. 639–645.
- [111] G. Lionis, X. Papageorgiou, and K. J. Kyriakopoulos, “Locally computable navigation functions for sphere worlds,” in *Proceedings 2007 IEEE International Conference on Robotics and Automation*, 2007, pp. 1998–2003.
- [112] —, “Towards locally computable polynomial navigation functions for convex obstacle workspaces,” in *2008 IEEE International Conference on Robotics and Automation*, 2008, pp. 3725–3730.
- [113] D. E. Koditschek and E. Rimon, “Robot navigation functions on manifolds with boundary,” *Advances in applied mathematics*, vol. 11, p. 412, 1990.
- [114] I. Filippidis and K. J. Kyriakopoulos, “Adjustable navigation functions for unknown sphere worlds,” in *2011 50th IEEE Conference on Decision and Control and European Control Conference*, 2011, pp. 4276–4281.
- [115] I. F. Filippidis and K. J. Kyriakopoulos, “Navigation functions for everywhere partially sufficiently curved worlds,” in *2012 IEEE International Conference on Robotics and Automation*. IEEE, 2012, pp. 2115–2120.
- [116] A. J. Ijspeert, J. Nakanishi, and S. Schaal, “Movement imitation with nonlinear dynamical systems in humanoid robots,” in *Proceedings 2002 IEEE International Conference on Robotics and Automation (Cat. No.02CH37292)*, vol. 2, 2002, pp. 1398–1403 vol.2.

- [117] A. J. Ijspeert, J. Nakanishi, and S. Schaal, "Learning rhythmic movements by demonstration using nonlinear oscillators," in *Proceedings of the IEEE/RSJ Int. Conference on Intelligent Robots and Systems (IROS2002)*, no. CONF, 2002, pp. 958–963.
- [118] A. Ude, A. Gams, T. Asfour, and J. Morimoto, "Task-specific generalization of discrete and periodic dynamic movement primitives," *IEEE Transactions on Robotics*, vol. 26, no. 5, pp. 800–815, 2010.
- [119] S. Schaal, P. Mohajjerian, and A. Ijspeert, "Dynamics systems vs. optimal control—a unifying view," *Progress in brain research*, vol. 165, pp. 425–445, 2007.
- [120] S. Schaal and C. G. Atkeson, "Constructive incremental learning from only local information," *Neural computation*, vol. 10, no. 8, pp. 2047–2084, 1998.
- [121] T. Petrič, A. Gams, A. J. Ijspeert, and L. Žlajpah, "On-line frequency adaptation and movement imitation for rhythmic robotic tasks," *The International Journal of Robotics Research*, vol. 30, no. 14, pp. 1775–1788, 2011.
- [122] A. Gams, A. J. Ijspeert, S. Schaal, and J. Lenarčič, "On-line learning and modulation of periodic movements with nonlinear dynamical systems," *Autonomous Robots*, vol. 27, no. 1, pp. 3–23, 2009.
- [123] A. Nealen, M. Müller, R. Keiser, E. Boxerman, and M. Carlson, "Physically based deformable models in computer graphics," in *Computer graphics forum*, vol. 25, no. 4. Wiley Online Library, 2006, pp. 809–836.
- [124] P. Moore and D. Molloy, "A survey of computer-based deformable models," in *International Machine Vision and Image Processing Conference (IMVIP 2007)*. IEEE, 2007, pp. 55–66.
- [125] A. Myronenko and X. Song, "Point set registration: Coherent point drift," *IEEE Transactions on Pattern Analysis and Machine Intelligence*, vol. 32, no. 12, pp. 2262–2275, Dec 2010.
- [126] R. Szeliski and D. Tonnesen, *Surface modeling with oriented particle systems*. ACM, 1992, vol. 26, no. 2.
- [127] F. F. Khalil and P. Payeur, "Dexterous robotic manipulation of deformable objects with multi-sensory feedback—a review," in *Robot Manipulators Trends and Development*. IntechOpen, 2010.
- [128] F. Nadon, A. J. Valencia, and P. Payeur, "Multi-modal sensing and robotic manipulation of non-rigid objects: A survey," *Robotics*, vol. 7, p. 74, 2018.
- [129] J. Sanchez, J.-A. Corrales, B.-C. Bouzgarrou, and Y. Mezouar, "Robotic manipulation and sensing of deformable objects in domestic and industrial applications: a survey," *The International Journal of Robotics Research*, vol. 37, no. 7, pp. 688–716, 2018.
- [130] M. Zollhöfer, M. Nießner, S. Izadi, C. Rehmann, C. Zach, M. Fisher, C. Wu, A. Fitzgibbon, C. Loop, C. Theobalt *et al.*, "Real-time non-rigid reconstruction using an rgb-d camera," *ACM Transactions on Graphics (ToG)*, vol. 33, no. 4, p. 156, 2014.

- [131] A. Tsoli and A. A. Argyros, "Tracking deformable surfaces that undergo topological changes using an rgb-d camera," in *2016 Fourth International Conference on 3D Vision (3DV)*. IEEE, 2016, pp. 333–341.
- [132] M. Famouri, A. Bartoli, and Z. Azimifar, "Fast shape-from-template using local features," *Machine Vision and Applications*, vol. 29, no. 1, pp. 73–93, 2018.
- [133] B. Willimon, S. Hickson, I. Walker, and S. Birchfield, "An energy minimization approach to 3d non-rigid deformable surface estimation using rgb-d data," in *2012 IEEE/RSJ International Conference on Intelligent Robots and Systems*. IEEE, 2012, pp. 2711–2717.
- [134] B. Willimon, I. Walker, and S. Birchfield, "3d non-rigid deformable surface estimation without feature correspondence," in *2013 IEEE International Conference on Robotics and Automation*. IEEE, 2013, pp. 646–651.
- [135] A. Jordt, I. Schiller, J. Bruenger, and R. Koch, "High-resolution object deformation reconstruction with active range camera," in *Joint Pattern Recognition Symposium*. Springer, 2010, pp. 543–552.
- [136] A. Jordt and R. Koch, "Direct model-based tracking of 3d object deformations in depth and color video," *International journal of computer vision*, vol. 102, no. 1-3, pp. 239–255, 2013.
- [137] F. F. Khalil, P. Curtis, and P. Payeur, "Visual monitoring of surface deformations on objects manipulated with a robotic hand," in *2010 IEEE international workshop on robotic and sensors environments*. IEEE, 2010, pp. 1–6.
- [138] F. Hui, P. Payeur, and A.-M. Cretu, "Visual tracking of deformation and classification of non-rigid objects with robot hand probing," *Robotics*, vol. 6, no. 1, p. 5, 2017.
- [139] C. M. Mateo, P. Gil, D. Mira, and F. Torres, "Analysis of shapes to measure surfaces: An approach for detection of deformations," in *2015 12th International Conference on Informatics in Control, Automation and Robotics (ICINCO)*, vol. 2. IEEE, 2015, pp. 60–65.
- [140] J. Tian and Y.-B. Jia, "Modeling deformations of general parametric shells grasped by a robot hand," *IEEE Transactions on Robotics*, vol. 26, no. 5, pp. 837–852, 2010.
- [141] B. Tawbe and A.-M. Cretu, "Acquisition and neural network prediction of 3d deformable object shape using a kinect and a force-torque sensor," *Sensors*, vol. 17, no. 5, p. 1083, 2017.
- [142] J. Schulman, A. Lee, J. Ho, and P. Abbeel, "Tracking deformable objects with point clouds," in *2013 IEEE International Conference on Robotics and Automation*. IEEE, 2013, pp. 1130–1137.
- [143] A. Petit, V. Lippiello, and B. Siciliano, "Real-time tracking of 3d elastic objects with an rgb-d sensor," in *2015 IEEE/RSJ International Conference on Intelligent Robots and Systems (IROS)*, Sep. 2015, pp. 3914–3921.
- [144] A. Petit, V. Lippiello, G. A. Fontanelli, and B. Siciliano, "Tracking elastic deformable objects with an rgb-d sensor for a pizza chef robot," *Robotics and Autonomous Systems*, vol. 88, pp. 187–201, 2017.

- [145] F. Ficuciello, A. Migliozi, E. Coevoet, A. Petit, and C. Duriez, “Fem-based deformation control for dexterous manipulation of 3d soft objects,” in *2018 IEEE/RSJ International Conference on Intelligent Robots and Systems (IROS)*. IEEE, 2018, pp. 4007–4013.
- [146] J. Das and N. Sarkar, “Planning and control of an internal point of a deformable object,” in *2010 IEEE International Conference on Robotics and Automation*. IEEE, 2010, pp. 2877–2882.
- [147] D. Navarro-Alarcón, Y.-H. Liu, J. G. Romero, and P. Li, “Model-free visually servoed deformation control of elastic objects by robot manipulators,” *IEEE Transactions on Robotics*, vol. 29, no. 6, pp. 1457–1468, 2013.
- [148] D. Berenson, “Manipulation of deformable objects without modeling and simulating deformation,” in *2013 IEEE/RSJ International Conference on Intelligent Robots and Systems*. IEEE, 2013, pp. 4525–4532.
- [149] L. Zaidi, J. A. Corrales, B. C. Bouzgarrou, Y. Mezouar, and L. Sabourin, “Model-based strategy for grasping 3d deformable objects using a multi-fingered robotic hand,” *Robotics and Autonomous Systems*, vol. 95, pp. 196–206, 2017.
- [150] H. Lin, F. Guo, F. Wang, and Y.-B. Jia, “Picking up a soft 3d object by “feeling” the grip,” *The International Journal of Robotics Research*, vol. 34, no. 11, pp. 1361–1384, 2015.
- [151] A. R. Fugl, A. Jordt, H. G. Petersen, M. Willatzen, and R. Koch, “Simultaneous estimation of material properties and pose for deformable objects from depth and color images,” in *Joint DAGM (German Association for Pattern Recognition) and OAGM Symposium*. Springer, 2012, pp. 165–174.
- [152] B. Frank, C. Stachniss, R. Schmedding, M. Teschner, and W. Burgard, “Learning object deformation models for robot motion planning,” *Robotics and Autonomous Systems*, vol. 62, no. 8, pp. 1153–1174, 2014.
- [153] A. Petit, F. Ficuciello, G. A. Fontanelli, L. Villani, and B. Siciliano, “Using physical modeling and rgb-d registration for contact force sensing on deformable objects,” in *ICINCO 2017-14th International Conference on Informatics in Control, Automation and Robotics*, vol. 2, no. 978-989-758-263-9. ScitePress; Springer, 2017, pp. 24–33.
- [154] S. Caccamo, P. Güler, H. Kjellström, and D. Kragic, “Active perception and modeling of deformable surfaces using gaussian processes and position-based dynamics,” in *2016 IEEE-RAS 16th International Conference on Humanoid Robots (Humanoids)*. IEEE, 2016, pp. 530–537.
- [155] P. Güler, A. Pieropan, M. Ishikawa, and D. Kragic, “Estimating deformability of objects using meshless shape matching,” in *2017 IEEE/RSJ International Conference on Intelligent Robots and Systems (IROS)*. IEEE, 2017, pp. 5941–5948.
- [156] L. Maier-Hein, P. Mountney, A. Bartoli, H. Elhawary, D. Elson, A. Groch, A. Kolb, M. Rodrigues, J. Sorger, S. Speidel, and D. Stoyanov, “Optical techniques for 3d surface reconstruction in computer-assisted laparoscopic surgery,” *Medical Image Analysis*, vol. 17, no. 8, pp. 974 – 996, 2013. [Online]. Available: <http://www.sciencedirect.com/science/article/pii/S1361841513000480>

- [157] T. R. dos Santos, A. Seitel, T. Kilgus, S. Suwelack, A.-L. Wekerle, H. Kenngott, S. Speidel, H.-P. Schlemmer, H.-P. Meinzer, T. Heimann *et al.*, “Pose-independent surface matching for intra-operative soft-tissue marker-less registration,” *Medical image analysis*, vol. 18, no. 7, pp. 1101–1114, 2014.
- [158] N. Haouchine, J. Dequidt, I. Peterlik, E. Kerrien, M.-O. Berger, and S. Cotin, “Image-guided simulation of heterogeneous tissue deformation for augmented reality during hepatic surgery,” in *2013 IEEE international symposium on mixed and augmented reality (ISMAR)*. IEEE, 2013, pp. 199–208.
- [159] N. Haouchine, J. Dequidt, M.-O. Berger, and S. Cotin, “Monocular 3d reconstruction and augmentation of elastic surfaces with self-occlusion handling,” *IEEE transactions on visualization and computer graphics*, vol. 21, no. 12, pp. 1363–1376, 2015.
- [160] A. Malti, A. Bartoli, and T. Collins, “Template-based conformal shape-from-motion from registered laparoscopic images.” in *MIUA*, vol. 1, no. 2, 2011, p. 6.
- [161] M. N. Cheema, A. Nazir, B. Sheng, P. Li, J. Qin, J. Kim, and D. Feng, “Image-aligned dynamic liver reconstruction using intra-operative field of views for minimal invasive surgery,” *IEEE Transactions on Biomedical Engineering*, 2018.
- [162] M. Hu, G. P. Penney, D. Rueckert, P. J. Edwards, F. Bello, R. Casula, M. Figl, and D. J. Hawkes, “Non-rigid reconstruction of the beating heart surface for minimally invasive cardiac surgery,” in *International Conference on Medical Image Computing and Computer-Assisted Intervention*. Springer, 2009, pp. 34–42.
- [163] R. Richa, A. P. Bó, and P. Poignet, “Towards robust 3d visual tracking for motion compensation in beating heart surgery,” *Medical Image Analysis*, vol. 15, no. 3, pp. 302–315, 2011.
- [164] D. Stoyanov and G.-Z. Yang, “Soft tissue deformation tracking for robotic assisted minimally invasive surgery,” in *2009 annual international conference of the IEEE engineering in medicine and biology society*. IEEE, 2009, pp. 254–257.
- [165] V. Kraevoy and A. Sheffer, “Cross-parameterization and compatible remeshing of 3d models,” *ACM Transactions on Graphics (TOG)*, vol. 23, no. 3, pp. 861–869, 2004.
- [166] B. Purnomo, J. D. Cohen, and S. Kumar, “Seamless texture atlases,” in *Proceedings of the 2004 Eurographics/ACM SIGGRAPH symposium on Geometry processing*, 2004, pp. 65–74.
- [167] S. Saba, I. Yavneh, C. Gotsman, and A. Sheffer, “Practical spherical embedding of manifold triangle meshes,” in *International Conference on Shape Modeling and Applications 2005 (SMI’ 05)*, 2005, pp. 256–265.
- [168] N. Ray, W. C. Li, B. Lévy, A. Sheffer, and P. Alliez, “Periodic global parameterization,” *ACM Transactions on Graphics (TOG)*, vol. 25, no. 4, pp. 1460–1485, 2006.
- [169] Y. T. P. A. D. Cohen and S. M. Desbrun, “Designing quadrangulations with discrete harmonic forms,” in *Eurographics symposium on geometry processing*, 2006, pp. 1–10.

- [170] M. S. Floater and K. Hormann, “Surface parameterization: a tutorial and survey,” in *Advances in multiresolution for geometric modelling*. Springer, 2005, pp. 157–186.
- [171] A. Sheffer, E. Praun, and K. Rose, “Mesh parameterization methods and their applications,” *Foundations and Trends® in Computer Graphics and Vision*, vol. 2, no. 2, pp. 105–171, 2006.
- [172] A. Sheffer, K. Hormann, B. Levy, M. Desbrun, K. Zhou, E. Praun, and H. Hoppe, “Mesh parameterization: Theory and practice,” *ACM SIGGRAPH, course notes*, vol. 10, no. 1281500.1281510, 2007.
- [173] J. Maillot, H. Yahia, and A. Verroust, “Interactive texture mapping,” in *Proceedings of the 20th annual conference on Computer graphics and interactive techniques*, 1993, pp. 27–34.
- [174] Xianfeng Gu, Yalin Wang, T. F. Chan, P. M. Thompson, and Shing-Tung Yau, “Genus zero surface conformal mapping and its application to brain surface mapping,” *IEEE Transactions on Medical Imaging*, vol. 23, no. 8, pp. 949–958, 2004.
- [175] S. Haker, S. Angenent, A. Tannenbaum, R. Kikinis, G. Sapiro, and M. Halle, “Conformal surface parameterization for texture mapping,” *IEEE Transactions on Visualization and Computer Graphics*, vol. 6, no. 2, pp. 181–189, 2000.
- [176] V. Kraevoy and A. Sheffer, “Template-based mesh completion.” in *Symposium on Geometry Processing*, vol. 385. Citeseer, 2005, pp. 13–22.
- [177] P. Alliez and C. Gotsman, “Recent advances in compression of 3d meshes,” in *Advances in multiresolution for geometric modelling*. Springer, 2005, pp. 3–26.
- [178] P. Alliez, G. Ucelli, C. Gotsman, and M. Attene, “Recent advances in remeshing of surfaces,” in *Shape analysis and structuring*. Springer, 2008, pp. 53–82.
- [179] W.-C. Li, N. Ray, and B. Lévy, “Automatic and interactive mesh to t-spline conversion,” in *Proceedings of the fourth Eurographics symposium on Geometry processing*. Eurographics Association, 2006, pp. 191–200.
- [180] J. Mitani and H. Suzuki, “Making papercraft toys from meshes using strip-based approximate unfolding,” *ACM transactions on graphics (TOG)*, vol. 23, no. 3, pp. 259–263, 2004.
- [181] M. do Carmo, “Differential geometry of curves and surfaces,” *Prentice-Hall International Englewood Cliffs*, 1976.
- [182] W. T. Tutte, “How to draw a graph,” *Proceedings of the London Mathematical Society*, vol. 3, no. 1, pp. 743–767, 1963.
- [183] M. Eck, T. DeRose, T. Duchamp, H. Hoppe, M. Lounsbery, and W. Stuetzle, “Multiresolution analysis of arbitrary meshes,” in *Proceedings of the 22nd annual conference on Computer graphics and interactive techniques*, 1995, pp. 173–182.
- [184] M. S. Floater *et al.*, “Parametrization and smooth approximation of surface triangulations,” *Computer aided geometric design*, vol. 14, no. 3, pp. 231–250, 1997.
- [185] M. S. Floater, “Mean value coordinates,” *Computer aided geometric design*, vol. 20, no. 1, pp. 19–27, 2003.

- [186] B. Lévy, S. Petitjean, N. Ray, and J. Maillot, “Least squares conformal maps for automatic texture atlas generation,” *ACM transactions on graphics (TOG)*, vol. 21, no. 3, pp. 362–371, 2002.
- [187] M. Desbrun, M. Meyer, and P. Alliez, “Intrinsic parameterizations of surface meshes,” in *Computer graphics forum*, vol. 21, no. 3. Wiley Online Library, 2002, pp. 209–218.
- [188] N. Ray and B. Levy, “Hierarchical least squares conformal map,” in *11th Pacific Conference on Computer Graphics and Applications, 2003. Proceedings.*, 2003, pp. 263–270.
- [189] K. Hormann and G. Greiner, “Mips: An efficient global parametrization method,” ERLANGEN-NUERNBERG UNIV (GERMANY) COMPUTER GRAPHICS GROUP, Tech. Rep., 2000.
- [190] A. Sheffer and E. De Sturler, “Surface parameterization for meshing by triangulation flattening,” in *Proc. 9th International Meshing Roundtable*. Citeseer, 2000.
- [191] A. Sheffer, B. Lévy, M. Mogilnitsky, and A. Bogomyakov, “Abf++: fast and robust angle based flattening,” *ACM Transactions on Graphics (TOG)*, vol. 24, no. 2, pp. 311–330, 2005.
- [192] M. Floater and K. Hormann, “Parameterization of triangulations and unorganized points,” in *Tutorials on multiresolution in geometric modelling*. Springer, 2002, pp. 287–316.
- [193] P. Degener, J. Meseth, and R. Klein, “An adaptable surface parameterization method.” *IMR*, vol. 3, pp. 201–213, 2003.
- [194] P. V. Sander, J. Snyder, S. J. Gortler, and H. Hoppe, “Texture mapping progressive meshes,” in *Proceedings of the 28th annual conference on Computer graphics and interactive techniques*, 2001, pp. 409–416.
- [195] G. Zigelman, R. Kimmel, and N. Kiryati, “Texture mapping using surface flattening via multidimensional scaling,” *IEEE Transactions on Visualization and Computer Graphics*, vol. 8, no. 2, pp. 198–207, 2002.
- [196] K. Zhou, J. Snyder, B. Guo, and H.-Y. Shum, “Iso-charts: stretch-driven mesh parameterization using spectral analysis,” in *Proceedings of the 2004 Eurographics/ACM SIGGRAPH symposium on Geometry processing*, 2004, pp. 45–54.
- [197] L. Liu, L. Zhang, Y. Xu, C. Gotsman, and S. J. Gortler, “A local/global approach to mesh parameterization,” *Computer Graphics Forum*, vol. 27, no. 5, pp. 1495–1504, 2008. [Online]. Available: <https://onlinelibrary.wiley.com/doi/abs/10.1111/j.1467-8659.2008.01290.x>
- [198] R. Schmidt, C. Grimm, and B. Wyvill, “Interactive decal compositing with discrete exponential maps,” in *ACM SIGGRAPH 2006 Papers*, 2006, pp. 605–613.
- [199] R. Schmidt, “Part-based representation and editing of 3d surface models,” Ph.D. dissertation, University of Toronto, Canada, 2010.

- [200] D. M. DeTurck and J. L. Kazdan, “Some regularity theorems in riemannian geometry,” in *Annales scientifiques de l’École Normale Supérieure*, vol. 14, no. 3, 1981, pp. 249–260.
- [201] S. Schaal, “Dynamic movement primitives—a framework for motor control in humans and humanoid robotics,” in *Adaptive Motion of Animals and Machines*. Springer, 2006, pp. 261–280.
- [202] Y. Zhou, M. Do, and T. Asfour, “Coordinate change dynamic movement primitives—a leader-follower approach,” in *Intelligent Robots and Systems (IROS), 2016 IEEE/RSJ International Conference on*. IEEE, 2016, pp. 5481–5488.
- [203] M. Stommel, M. Beetz, and W. Xu, “Inpainting of missing values in the kinect sensor’s depth maps based on background estimates,” *IEEE Sensors Journal*, vol. 14, no. 4, pp. 1107–1116, 2014.
- [204] L. Petrescu, A. Morar, F. Moldoveanu, and A. Moldoveanu, “Kinect depth inpainting in real time,” in *International Conference on Telecommunications and Signal Processing (TSP)*. IEEE, June 2016, pp. 697–700.
- [205] D.-H. Park, H. Hoffmann, P. Pastor, and S. Schaal, “Movement reproduction and obstacle avoidance with dynamic movement primitives and potential fields,” in *Humanoids 2008-8th IEEE-RAS International Conference on Humanoid Robots*. IEEE, 2008, pp. 91–98.
- [206] P. Pastor, H. Hoffmann, T. Asfour, and S. Schaal, “Learning and generalization of motor skills by learning from demonstration,” in *2009 IEEE International Conference on Robotics and Automation*. IEEE, 2009, pp. 763–768.
- [207] M. Chi, Y. Yao, Y. Liu, and M. Zhong, “Learning, generalization, and obstacle avoidance with dynamic movement primitives and dynamic potential fields,” *Applied Sciences*, vol. 9, no. 8, p. 1535, 2019.
- [208] T. Eiter and H. Mannila, “Computing discrete fréchet distance,” Tech. Rep., 1994.
- [209] L. Hasdorff, “Gradient optimization and nonlinear control,” 1976.
- [210] M. Pak, “Fast c implementation of the discrete fréchet distance computation for matlab mex,” Available at [https://github.com/mp4096/discrete-frechet-distance\(15/9/2017\)](https://github.com/mp4096/discrete-frechet-distance(15/9/2017)).
- [211] Z. Michalewicz, *Genetic Algorithms + Data Structures = Evolution Programs*, 3rd ed. Springer, 1996.
- [212] J. Burkardt, “A simple genetic algorithm,” Available at [https://people.sc.fsu.edu/~jburkardt/cpp\\_src/simple\\_ga/simple\\_ga.html\(15/9/2017\)](https://people.sc.fsu.edu/~jburkardt/cpp_src/simple_ga/simple_ga.html(15/9/2017)).
- [213] A. Billard and D. Kragic, “Trends and challenges in robot manipulation,” *Science*, vol. 364, no. 6446, 2019.
- [214] V. E. Arriola-Rios, P. Guler, F. Ficuciello, D. Kragic, B. Siciliano, and J. L. Wyatt, “Modeling of deformable objects for robotic manipulation: A tutorial and review,” *Frontiers in Robotics and AI*, vol. 7, p. 82, 2020. [Online]. Available: <https://www.frontiersin.org/article/10.3389/frobt.2020.00082>



- [215] H. G. Tanner, K. J. Kyriakopoulos, and N. J. Krikelis, “Modeling of multiple mobile manipulators handling a common deformable object,” *Journal of Robotic Systems*, vol. 15, no. 11, pp. 599–623, 1998.
- [216] H. G. Tanner, “Mobile manipulation of flexible objects under deformation constraints,” *IEEE transactions on robotics*, vol. 22, no. 1, pp. 179–184, 2006.
- [217] Y. Li, Y. Wang, M. Case, S.-F. Chang, and P. K. Allen, “Real-time pose estimation of deformable objects using a volumetric approach,” in *2014 IEEE/RSJ International Conference on Intelligent Robots and Systems*. IEEE, 2014, pp. 1046–1052.
- [218] Y. Li, D. Xu, Y. Yue, Y. Wang, S.-F. Chang, E. Grinspun, and P. K. Allen, “Re-grasping and unfolding of garments using predictive thin shell modeling,” in *2015 IEEE International Conference on Robotics and Automation (ICRA)*. IEEE, 2015, pp. 1382–1388.
- [219] Y. Li, Y. Yue, D. Xu, E. Grinspun, and P. K. Allen, “Folding deformable objects using predictive simulation and trajectory optimization,” in *2015 IEEE/RSJ International Conference on Intelligent Robots and Systems (IROS)*. IEEE, 2015, pp. 6000–6006.
- [220] A. Doumanoglou, J. Stria, G. Peleka, I. Mariolis, V. Petrik, A. Kargakos, L. Wagner, V. Hlaváč, T.-K. Kim, and S. Malassiotis, “Folding clothes autonomously: A complete pipeline,” *IEEE Transactions on Robotics*, vol. 32, no. 6, pp. 1461–1478, 2016.
- [221] A. Doumanoglou, A. Kargakos, T.-K. Kim, and S. Malassiotis, “Autonomous active recognition and unfolding of clothes using random decision forests and probabilistic planning,” in *2014 IEEE International Conference on Robotics and Automation (ICRA)*. IEEE, 2014, pp. 987–993.
- [222] D. Triantafyllou, I. Mariolis, A. Kargakos, S. Malassiotis, and N. Aspragathos, “A geometric approach to robotic unfolding of garments,” *Robotics and Autonomous Systems*, vol. 75, pp. 233–243, 2016.
- [223] A. Namiki and S. Yokosawa, “Robotic origami folding with dynamic motion primitives,” in *2015 IEEE/RSJ International Conference on Intelligent Robots and Systems (IROS)*. IEEE, 2015, pp. 5623–5628.
- [224] X. Li, X. Su, and Y. Liu, “Cooperative robotic soldering of flexible pcbs,” in *2017 IEEE/RSJ International Conference on Intelligent Robots and Systems (IROS)*. IEEE, 2017, pp. 1651–1656.
- [225] I. Leizea, H. Álvarez, I. Aguinaga, and D. Borro, “Real-time deformation, registration and tracking of solids based on physical simulation,” in *2014 IEEE International Symposium on Mixed and Augmented Reality (ISMAR)*. IEEE, 2014, pp. 165–170.
- [226] R. E. Goldman, A. Bajo, and N. Simaan, “Algorithms for autonomous exploration and estimation in compliant environments,” *Robotica*, vol. 31, no. 1, pp. 71–87, 2013.
- [227] S. Patil and R. Alterovitz, “Toward automated tissue retraction in robot-assisted surgery,” in *2010 IEEE International Conference on Robotics and Automation*. IEEE, 2010, pp. 2088–2094.

- [228] M. Dominici, P. Poignet, R. Cortesão, E. Dombre, and O. Tempier, “Compensation for 3d physiological motion in robotic-assisted surgery using a predictive force controller. experimental results,” in *2009 IEEE/RSJ International Conference on Intelligent Robots and Systems*. IEEE, 2009, pp. 2634–2639.
- [229] L. Cheng, J. Fong, and M. Tavakoli, “Semi-autonomous surgical robot control for beating-heart surgery,” in *2019 IEEE 15th International Conference on Automation Science and Engineering (CASE)*. IEEE, 2019, pp. 1774–1781.
- [230] A. Ruszkowski, C. Schneider, O. Mohareri, and S. Salcudean, “Bimanual teleoperation with heart motion compensation on the da vinci® research kit: Implementation and preliminary experiments,” in *2016 IEEE International Conference on Robotics and Automation (ICRA)*. IEEE, 2016, pp. 4101–4108.
- [231] S. Leonard, K. L. Wu, Y. Kim, A. Krieger, and P. C. Kim, “Smart tissue anastomosis robot (star): A vision-guided robotics system for laparoscopic suturing,” *IEEE Transactions on Biomedical Engineering*, vol. 61, no. 4, pp. 1305–1317, 2014.
- [232] J. D. Langsfeld, A. M. Kabir, K. N. Kaipa, and S. K. Gupta, “Integration of planning and deformation model estimation for robotic cleaning of elastically deformable objects,” *IEEE Robotics and Automation Letters*, vol. 3, no. 1, pp. 352–359, 2017.
- [233] S. Lee, “Development of a new variable remote center compliance (vrcc) with modified elastomer shear pad (esp) for robot assembly,” *IEEE Transactions on Automation Science and Engineering*, vol. 2, no. 2, pp. 193–197, 2005.
- [234] L. Villani and J. De Schutter, “Force control,” *Springer handbook of robotics*, pp. 161–185, 2008.
- [235] B. Siciliano, L. Sciavicco, L. Villani, and G. Oriolo, *Robotics: modelling, planning and control*. Springer Science & Business Media, 2010.
- [236] B. Zhao, J. Feng, X. Wu, and S. Yan, “A survey on deep learning-based fine-grained object classification and semantic segmentation,” *International Journal of Automation and Computing*, vol. 14, no. 2, pp. 119–135, 2017.
- [237] N. M. Zaitoun and M. J. Aqel, “Survey on image segmentation techniques,” *Procedia Computer Science*, vol. 65, pp. 797–806, 2015.
- [238] A. Bartoli, V. Gay-Bellile, U. Castellani, J. Peyras, S. Olsen, and P. Sayd, “Coarse-to-fine low-rank structure-from-motion,” in *2008 IEEE Conference on Computer Vision and Pattern Recognition*. IEEE, 2008, pp. 1–8.
- [239] R. A. Newcombe, D. Fox, and S. M. Seitz, “Dynamicfusion: Reconstruction and tracking of non-rigid scenes in real-time,” in *Proceedings of the IEEE conference on computer vision and pattern recognition*, 2015, pp. 343–352.
- [240] A. Weiss, D. Hirshberg, and M. J. Black, “Home 3d body scans from noisy image and range data,” in *2011 International Conference on Computer Vision*. IEEE, 2011, pp. 1951–1958.
- [241] C. Elbrechter, R. Haschke, and H. Ritter, “Bi-manual robotic paper manipulation based on real-time marker tracking and physical modelling,” in *2011 IEEE/RSJ International Conference on Intelligent Robots and Systems*. IEEE, 2011, pp. 1427–1432.

- [242] C. Wang, Z. Liu, and L. Liu, "As-rigid-as-possible spherical parametrization," *Graphical models*, vol. 76, no. 5, pp. 457–467, 2014.
- [243] P. Kyriakis and G. Moustiris, "Terrain following for fixed-wing unmanned aerial vehicles using feedback equivalence," *IEEE Control Systems Letters*, vol. 3, no. 1, pp. 150–155, 2019.
- [244] L. Yang, J. Qi, D. Song, J. Xiao, J. Han, and Y. Xia, "Survey of robot 3d path planning algorithms," *Journal of Control Science and Engineering*, vol. 2016, 2016.
- [245] L. Yang, L. Zhang, H. Dong, A. Alelaiwi, and A. El Saddik, "Evaluating and improving the depth accuracy of kinect for windows v2," *IEEE Sensors Journal*, vol. 15, no. 8, pp. 4275–4285, 2015.
- [246] N. AG, "Katana user manual and technical description."
- [247] D. Kim, R. Hazlett-Knudsen, H. Culver-Godfrey, G. Rucks, T. Cunningham, D. Portee, J. Bricout, Z. Wang, and A. Behal, "How autonomy impacts performance and satisfaction: Results from a study with spinal cord injured subjects using an assistive robot," *IEEE Transactions on Systems, Man, and Cybernetics - Part A: Systems and Humans*, vol. 42, no. 1, pp. 2–14, 2012.
- [248] N. Koceska, S. Koceski, P. Beomonte Zobel, V. Trajkovik, and N. Garcia, "A telemedicine robot system for assisted and independent living," *Sensors*, vol. 19, no. 4, p. 834, 2019.
- [249] H. Yu, M. Spenko, and S. Dubowsky, "An adaptive shared control system for an intelligent mobility aid for the elderly," *Autonomous Robots*, vol. 15, no. 1, pp. 53–66, 2003.
- [250] F. I. Mahoney and D. W. Barthel, "Functional evaluation: the barthel index: a simple index of independence useful in scoring improvement in the rehabilitation of the chronically ill." *Maryland state medical journal*, 1965.
- [251] M. F. Folstein, S. E. Folstein, and P. R. McHugh, "'mini-mental state': a practical method for grading the cognitive state of patients for the clinician," *Journal of psychiatric research*, vol. 12, no. 3, pp. 189–198, 1975.
- [252] J. R. Lewis, "Ibm computer usability satisfaction questionnaires: psychometric evaluation and instructions for use," *International Journal of Human-Computer Interaction*, vol. 7, no. 1, pp. 57–78, 1995.
- [253] J. Brooke *et al.*, "Sus-a quick and dirty usability scale," *Usability evaluation in industry*, vol. 189, no. 194, pp. 4–7, 1996.
- [254] A. Bangor, P. Kortum, and J. Miller, "Determining what individual sus scores mean: Adding an adjective rating scale," *Journal of usability studies*, vol. 4, no. 3, pp. 114–123, 2009.
- [255] L. Skedung, C. El Rawadi, M. Arvidsson, C. Farcet, G. S. Luengo, L. Breton, and M. W. Rutland, "Mechanisms of tactile sensory deterioration amongst the elderly," *Scientific reports*, vol. 8, no. 1, pp. 1–10, 2018.

- 
- [256] T. Asfour, K. Regenstein, P. Azad, J. Schröder, N. Vahrenkamp, and R. Dillmann, “ARMAR-III: An Integrated Humanoid Platform for Sensory-Motor Control,” Genova, Italy, December 2006, pp. 169–175.
- [257] C. Rother, V. Kolmogorov, and A. Blake, “Grabcut: Interactive foreground extraction using iterated graph cuts,” in *ACM transactions on graphics (TOG)*, vol. 23, no. 3. ACM, 2004, pp. 309–314.

# Appendix A

## Glossary

ADL	Activities of Daily Living	Δραστηριότητες Καθημερινότητας
ASQ	After Scenario Questionnaire	Μετασεναριακό Ερωτηματολόγιο
ANN	Artificial Neural Network	Τεχνητό Νευρωνικό Δίκτυο
CNN	Convolutional Neural Network	Συνελικτικό Νευρωνικό Δίκτυο
CPM	Convolutional Pose Machines	Συνελικτικές Μηχανές Πόζας
DCNN	Deep Convolutional Neural Network	Βαθιά Συνελικτικά Δίκτυα
RNN	Recurrent Neural Network	Επαναλαμβανόμενο Νευρικό Δίκτυο
DBN	Dynamic Bayesian Network	Δυναμικό Μπευζιανό Δίκτυο
RGB-D	Red Green Blue Depth	Κοκκινου Πρασινου Μπλε Βάθους
DMP	Dynamic Motion Primitives	Δυναμικές Πρωτογενείς Κινήσεις
CC-DMP	Coordinate Change DMP	ΔΠΚ με αλλαγή συντεταγμένων
DCS	Dynamic Canonical Space	Δυναμικός Κανονικοποιημένος Χώρος
SCS	Static Canonical Space	Στατικός Κανονικοποιημένος Χώρος
SVM	Support Vector Machine	Διανυσματική Μηχανή Υποστήριξης
SVR	Support Vector Regression	Παλινδρόμηση Διανυσματων Υποστηριξής
HRI	Human Robot Interaction	Αλληλεπίδραση Ανθρώπου-Ρομποτ
ICT	Information Communication Technology	Τεχνολογίες Επικοινωνιών Πληροφορίας
DoF	Degrees of Freedom	Βαθμοί Ελευθερίας
LfD	Learning from Demonstration	Μάθηση από Επίδειξη
GMM	Gaussian Mixture Model	Μίξη Μοντέλων Γκάους
GMR	Gaussian Mixture Regression	Παλινδρόμηση Μοντέλων Γκάους
GPR	Gaussian Process Regression	Παλινδρόμηση Μεθόδου Γκάους
HMM	Hidden Markov Model	Κρυφό Μαρκοβιανό Μοντέλο
MPC	Model Predictive Control	Έλεγχος Προβλεπτικού Μοντέλου
NF	Navigation Function	Συναρτήσεις Πλοήγησης
KIT	Karlsruhe Institute of Technology	Ινστιτούτο Τεχνολογίας Καρλσρούης
MSD	Mass Spring Damper	Μάζας Ελατηρίου Αποσβεστήρα
FEM	Finite Element Method	Μέθοδος Διακριτών Στοιχείων
DEM	Discrete Exponential Map	Διακριτός Εκθετικός Χάρτης
IMU	Inertial Measurement Unit	Μονάδα Μέτρησης Αδρανείας
SUS	System Usability Scale	Κλίμακα Χρηστικότητας Συστήματος
GA	Genetic Algorithm	Γενετικός Αλγόριθμος



# Appendix B

## List of Publications

### B.1 Publications in Peer-reviewed International Journals

- J1 **Athanasios C. Dometios**, You Zhou, Xanthi S. Papageorgiou, Costas S. Tzafestas and Tamim Asfour, "Vision-Based Online Adaptation of Motion Primitives to Dynamic Surfaces: Application to an Interactive Robotic Wiping Task," in *IEEE Robotics and Automation Letters*, vol. 3, no. 3, pp. 1410-1417, July 2018, doi: 10.1109/LRA.2018.2800031.
- J2 Athanasia Zlatintsi, **Athanasios C. Dometios**, Nikos Kardaris, Isidoros Rodomagoulakis, Petros Koutras, Xanthi Papageorgiou, Petros Maragos, Costas S. Tzafestas, Panagiotis Vartholomeos, Klaus Hauer, Christian Werner, Roberta Annicchiarico, Maria G. Lombardi, Fulvia Adriano, Tamim Asfour, Andrea M. Sabatini, Cecilia Laschi, Mateo Cianchetti, Alp Güler, Iasonas Kokkinos, Barbara Klein, Rafa López, I-Support: A robotic platform of an assistive bathing robot for the elderly population, *Robotics and Autonomous Systems*, Volume 126, 2020, 103451, ISSN 0921-8890, <https://doi.org/10.1016/j.robot.2020.103451>.
- J3 Christian Werner, **Athanasios C. Dometios**, Costas S. Tzafestas, Petros Maragos, Jürgen M. Bauer, Klaus Hauer (2020) Evaluating the task effectiveness and user satisfaction with different operation modes of an assistive bathing robot in older adults, *Assistive Technology*, DOI: 10.1080/10400435.2020.1755744
- J4 **Athanasios C. Dometios**, Costas S. Tzafestas "Interaction Control of a Robotic Manipulator with the Surface of Deformable Object" *IEEE Transactions on Robotics* (submitted)

### B.2 Publications in Peer-reviewed International Conferences

- C1 Xanthi S. Papageorgiou, George P. Moustris, Vassilis Pitsikalis, Georgia Chalvatzaki, **Athanasios Dometios**, Nikolaos Kardaris, Costas S. Tzafestas, Petros Maragos, "User-Oriented Cognitive Interaction and Control for an Intelligent Robotic Walker", Workshop of the 2015 7th International Conference on Social Robotics, "Improving the quality of life in the elderly using robotic assistive technology: benefits, limitations, and challenges", 26 - 30 October 2015, Paris, France.
- C2 Costas S. Tzafestas, Xanthi S. Papageorgiou, George P. Moustris, Georgia Chalvatzaki, **Athanasios Dometios**, "User-Oriented Human-Robot Interaction for an

Intelligent Walking Assistant Robotic Device”, Workshop of the 2015 IEEE/RSJ International Conference on Intelligent Robots and Systems, Invited Session: ”Cognitive Mobility Assistance Robots: Scientific Advances and Perspectives”, Hamburg, Germany, September 28 - October 02, 2015.

- C3 George Moustiris, **Athanasios C. Dometios**, Costas S. Tzafestas, ”User Front-Following Behaviour for a Mobility Assistance Robot: A Kinematic Control Approach. Proceedings of the 8th International Conference on Integrated Modeling and Analysis in Applied Control and Automation, Bergeggi, Italy, September 21 - 23, 2015 (**Best Paper Award**).
- C4 **Athanasios C. Dometios**, Xanthi S. Papageorgiou, Costas S. Tzafestas, Panagiotis Vartholomeos, ”Towards ICT-supported bath robots: Control architecture description and localized perception of user for robot motion planning,” 2016 24th Mediterranean Conference on Control and Automation (MED), Athens, 2016, pp. 713-718, doi: 10.1109/MED.2016.7535954.
- C5 Xanthi S. Papageorgiou, Georgia Chalvatzaki, **Athanasios C. Dometios**, Costas S. Tzafestas, and Petros Maragos. 2017. Intelligent Assistive Robotic Systems for the elderly: Two real-life use cases. In Proceedings of the 10th International Conference on Pervasive Technologies Related to Assistive Environments (PETRA '17). Association for Computing Machinery, New York, NY, USA, 360–365.  
DOI:<https://doi.org/10.1145/3056540.3076184>
- C6 **Athanasios C. Dometios**, Xanthi S. Papageorgiou, Antonis Arvanitakis, Costas S. Tzafestas and Petros Maragos, ”Real-time end-effector motion behavior planning approach using on-line point-cloud data towards a user adaptive assistive bath robot,” 2017 IEEE/RSJ International Conference on Intelligent Robots and Systems (IROS), Vancouver, BC, 2017, pp. 5031-5036, doi: 10.1109/IROS.2017.8206387.
- C7 **Athanasios C Dometios**, Antigoni Tsiami, Antonis Arvanitakis, Panagiotis Giannoulis, Xanthi S Papageorgiou, Costas S Tzafestas, Petros Maragos ”Integrated Speech-based Perception System for User Adaptive Robot Motion Planning in Assistive Bath Scenarios.” Multi-Learn workshop of European Conference on Signal Processing EUSIPCO, Kos, 2017.
- C8 Athanasia Zlatintsi, Isidoros Rodomagoulakis, Petros Koutras, **Athanasios Dometios**, Vasilis Pitsikalis, Costas Tzafestas, Petros Maragos, ”Multimodal Signal Processing and Learning Aspects of Human-Robot Interaction for an Assistive Bathing Robot,” 2018 IEEE International Conference on Acoustics, Speech and Signal Processing (ICASSP), Calgary, AB, 2018, pp. 3171-3175, doi: 10.1109/ICASSP.2018.8461568.
- C9 Xanthi S. Papageorgiou, Georgia Chalvatzaki, **Athanasios C. Dometios**, Costas S. Tzafestas. ”Human-centered service robotic systems for assisted living,” In Proc. International Conference on Robotics in Alpe-Adria Danube Region 2018 (RAAD 2018), Jun 6 (pp. 132-140), Springer.
- C9 Xanthi S. Papageorgiou, Georgia Chalvatzaki, **Athanasios C. Dometios**, Costas S. Tzafestas. ”Human-centered service robotic systems for assisted living,” In Proc. International Conference on Robotics in Alpe-Adria Danube Region 2018 (RAAD 2018), Jun 6 (pp. 132-140), Springer.



- C10 Moustris George, Nikolaos Kardaris, Antigoni Tsiami, Georgia Chalvatzaki, Petros Koutras, **Athanasios C. Dometios**, Paris Oikonomou et al. The i-Walk Assistive Robot: a Multimodal Intelligent Robotic Rollator Providing Cognitive and Mobility Assistance to the Elderly and Motor-Impaired. 13th International Workshop on Human-Friendly Robotics (HFR 2020) October 22-23, 2020, Innsbruck.
- C11 Xanthi S. Papageorgiou, **Athanasios C. Dometios**, Costas S. Tzafestas “Towards a User Adaptive Assistive Robot: Learning from Demonstration Using Navigation Functions” 2021 IEEE/RSJ International Conference on Intelligent Robots and Systems (IROS) (Under Review)

